CHEMICAL REVIEWS

Synthesis of Semiconductor Nanocrystals, Focusing on Nontoxic and Earth-Abundant Materials

Peter Reiss,*,†,‡,§ Marie Carrière,†,|| Christophe Lincheneau,†,‡,§ Louis Vaure,†,‡,§ and Sudarsan Tamang⊥

†Université Grenoble Alpes, INAC-SyMMES, F-38054 Grenoble Cedex 9, France
‡CEA, INAC-SyMMES-STEP/LEMOH, 17 rue des Martyrs, F-38054 Grenoble Cedex 9, France
§CNRS, SPrAM, F-38054 Grenoble Cedex 9, France
||CEA, INAC-SyMMES-CIBEST/LAN, 17 rue des Martyrs, F-38054 Grenoble Cedex 9, France
⊥Department of Chemistry, Sikkim University, Sikkim 737102, India

ABSTRACT: We review the synthesis of semiconductor nanocrystals/colloidal quantum dots in organic solvents with special emphasis on earth-abundant and toxic heavy metal free compounds. Following the Introduction, section 2 defines the terms related to the toxicity of nanocrystals and gives a comprehensive overview on toxicity studies concerning all types of quantum dots. Section 3 aims at providing the reader with the basic concepts of nanocrystal synthesis. It starts with the concepts currently used to describe the nucleation and growth of monodisperse particles and next takes a closer look at the chemistry of the inorganic core and its interactions with surface ligands. Section 4 reviews in more detail the synthesis of different families of semiconductor nanocrystals, namely elemental group IV compounds (carbon nanodots, Si, Ge), III−V compounds (e.g., InP, InAs), and binary and multinary metal chalcogenides. Finally, the authors' view on the perspectives in this field is given.

CONTENTS

1. INTRODUCTION

Colloidal semiconductor nanocrystals (NCs) have drawn significant research interest since the discovery of their size-dependent optical and electronic properties more than 30 years ago.[1−4] These small, inorganic crystallites of nanometric size, containing hundreds to thousands of atoms and covered with organic surfactant molecules (ligands), present a high interest for fundamental science: they are also known as "quantum dots" (QDs) or "artificial atoms", whose unique properties can be adjusted with size, composition, shape and surface state.[5] At the same time these nano-objects have a strong potential for use in many types of applications, particularly in optoelectronics (display, lighting, photovoltaics, etc.), as well as in biological imaging and detection. Many of these applications rely on the fluorescence emission of the QDs, and by proper surface engineering quantum yields approaching unity are now being achieved with type II−VI NCs based on CdSe. Figure 1 gives an overview of the emission ranges reported for different types of QDs. The development of chemical synthesis methods has received particular attention, as it is of prime importance to be able to synthesize NCs of precisely controlled dimensions, shape, and composition. A pronounced distribution in these parameters directly affects their physical properties; one example is the fluorescence emission line width, which strongly depends on the size distribution of the NCs. In reality, the size distribution of a colloidal sample cannot be reduced to zero, and it is common practice to term a sample showing a size distribution of 5% or less as being "monodisperse".

The increase of the band gap with decreasing particle size induced by the quantum confinement effect strongly influences the suitability of different types of QDs for various applications. Indium phosphide, for example, has an optimal bulk band gap for photovoltaics (E_g = 1.35 eV) but may no longer be suitable for this application when the size is below 10 nm. InP QDs are indeed mainly investigated for use in visible light emitting devices or in biological imaging applications. Similarly, narrow band gap semiconductors such as InAs and InSb (E_g = 0.35 and 0.23 eV, respectively) may have optimal band gaps for photovoltaic applications or as near-infrared active materials in form of colloidal QDs.[7]

The chemical synthesis of semiconductor NCs has been reviewed in several papers and book chapters appearing in the last two decades.[8−20] Additionally, a number of reviews focus on the synthesis of specific families of materials, which are cited in the appropriate subsections of the present work, and on their applications such as biological imaging/detection,[21−25] light-emitting devices,[26] photovoltaics,[27−29] and optoelectronics in general.[10] In contrast to prior reports, here we focus on the synthesis of NCs constituted of nontoxic and earth-abundant

materials. The precise definition of the terms "non-toxic" and "earth-abundant" NCs is not straightforward, even though they are used abundantly in research papers. When discussing NCs' toxicity, one has to distinguish between effects coming from the toxic effects of the constituting elements, as well as those induced by the small dimensions of the particles. For example, the latter influences their circulation in the body and uptake in different organs. Furthermore, the high surface/volume ratio can be at the origin of catalytic reactions, leading to the formation of reactive molecules, such as reactive oxygen species (ROS). The intrinsic toxicity of the constituting elements depends on their chemical environment. If they are strongly bound in a crystal, which is then covered with another inorganic shell material, even Cd- and Pb-containing NCs are not expected to exhibit toxic effects directly related to these elements. This supposes however that the inorganic shell prevents from dissolution and release of highly toxic Cd^{2+} and Pb^{2+} ions. Nonetheless, NCs containing elements notoriously known for their toxicity and banned by legal regulations are out of the scope of this review. This applies in particular to Cd-, Pb- and Hg-based materials, for which a huge body of work exists and which have been already reviewed extensively elsewhere. The contents of theses elements, as well as those of hexavalent chromium, polybrominated biphenyls (PBB) and polybrominated diphenyl ethers (PBDE), in (opto-)electronic consumer products are severely restricted by the RoHS (Restriction of Hazardous Substances) regulation, in vigor in the EU since July 2006. For all substances the maximum concentration values by weight in homogeneous materials are fixed to 0.1%, except for Cd where the limit is set 1 order of magnitude lower (0.01%). Similar regulations exist in a number of other countries, including South Korea and China. The currently available data on the toxicity of NCs suffers from the multiplicity of experimental procedures and conditions, including large differences in the investigated samples, which hampers on the comparison of the results and the establishment of global statements. It appears, therefore, appropriate to start this article with a short, yet comprehensive overview of the data related to the toxicity of semiconductor NCs (section 2).

The earth abundance of the elements can first be judged by their abundance in the Earth's upper crust, as depicted in Figure 2. However, this chart only partially reflects the effective usable abundance of the elements, as becomes clear when looking at the particular situation of the rare earth elements (REE). Even though a number of them are as earth-abundant as common metals such as nickel or copper, REE do not generally concentrate in exploitable ore deposits, and by consequence, the world's supply relies on a small number of sources.[30] Furthermore, the extraction of these deposits and the REE separation bear environmental and regulatory problems. All of these factors contribute to an apparent scarcity of REE and to their elevated prices; Eu, Tm and Lu metal reach prices of several thousands of euros per kg. As visible in Figure 2, the semimetal tellurium is one of the rarest elements on Earth. By consequence, Te-based NCs do in principle not fall into the scope of the present review. However, for the sake of completeness metal telluride NCs are included. Indium, being a main constituent of InP and chalcopyrite-type semiconductors, like $CuInS_2$ and $CuInSe_2$, is an element of particular interest for this article, as these compounds are considered to range among the most promising ones for replacing toxic Cd- and Pb-based NCs. While widely considered as a "rare" metal, the abundance of indium in the
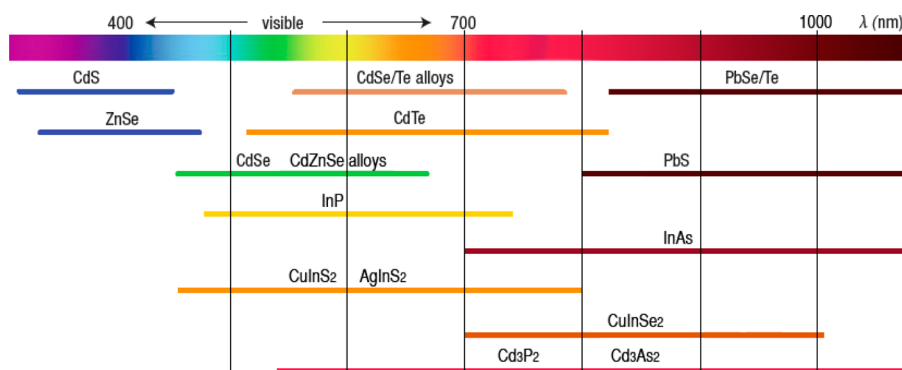
Figure 1. Spectral range of emission for the most widely studied types of semiconductor NCs. Reprinted from ref 6. Copyright 2013 Cambridge University Press.

earth crust is roughly as high as 1.6×10^{-5} %, similar to that of cadmium and twice as high as that of silver. However, In does not naturally occur in the native state but can be found at ppm levels in base metal ores (e.g., zinc, lead, tin, copper). It has to be separated from these ores at the base metal smelter using complex procedures, then concentrated and purified in indium refineries.[19] An important factor contributing to an apparent scarcity of this element is its strongly increasing use as a constituent of transparent conducting oxides (TCO) in optoelectronics. Around 50% of the produced indium is transformed into ITO (indium tin oxide), used as transparent electrode material in LCD and other types of flat panel display technologies. A continuous trend in this direction could lead to the limited availability of indium in the near future. Therefore, processes for the recycling of ITO and the recovery of indium are currently being developed, which show increasing maturity and efficiency. Nonetheless, indium-based compounds are not economically viable in applications requiring huge amounts of these materials, such as for example photovoltaics.[31] While excellent power conversion efficiencies reaching up to 21% are obtained with CIGS (Cu(In,Ga)Se$_2$) thin film solar cells,[32] a lot of research efforts are being devoted to the development of indium-free alternative materials. Cu$_2$ZnSn(S,Se)$_4$ (CZTS) is one of the most promising candidates, even though the efficiencies lack behind CIGS. This is due to the difficulties in controlling the crystalline phases, which form during the transformation of the starting compounds into thin films. In this context, NCs can play an important role, as they allow for the ex situ control of size, composition, and crystalline phase prior to their processing as thin films.[33]

In summary, we do not exclude materials from discussion on the basis of the smaller earth abundance of their constituting elements (e.g., indium in InP NCs). On the other hand, we explicitly exclude materials containing the three toxic elements Cd, Pb, and Hg. The compound semiconductor NCs based on these metals are already largely covered by earlier studies, describing in details their synthesis and physical properties. From a more applied point of view, their use in most applications is severely restricted by many national and international regulations. One exception from this rule is section 2 dealing with toxicity studies, as the main body of work has been carried out on CdSe-based NCs.[34] This section would lose its interest when restricting it to Cd-free materials. The semiconductor materials covered within this review possess a bulk band gap <3 eV. Zinc sulfide with a band gap of 3.9 eV is also included, as this material has a prototype character for the synthesis of other metal chalcogenide NCs and it serves as the

major material for preparing an inorganic shell passivating core NCs. Such core/shell systems, earlier reviewed in refs[35,36] are directly integrated in the discussion of the relevant core materials' families. The main emphasis is put on the solution-phase synthesis of spherical NCs in organic solvents. 1D Rod/wire- and 2D platelet/sheet-shaped particles are also discussed for specific materials, which show a high tendency to form these structures. On the other hand, aqueous syntheses and methods based on cation exchange and the preparation of doped systems are not covered here, as dedicated reviews in this Special Issue deal with these topics.

The review is structured as follows: First, aspects related to the toxicity of semiconductor NCs are summarized, including: toxicity assessment, impact and translocation of NCs to primary and secondary target organs, and the mechanisms underlying NC toxicity (section 2). Next, the basic concepts of NC synthesis are discussed, with emphasis on nontoxic materials and on recent progress in the understanding of reaction mechanisms (section 3). In the following, the synthesis of NCs of different material families is reviewed, starting with group IV elemental semiconductors, continuing with binary III–V compounds and metal chalcogenides, and finishing with ternary and multinary compounds (section 4). Finally, we give our view on the perspectives of this currently strongly expanding field.
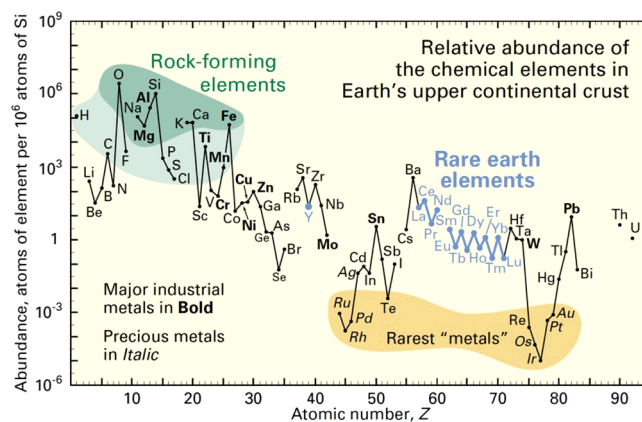

Figure 2. Abundance (atom fraction) of the chemical elements in Earth's upper continental crust.[30] Major industrial metals attain a global production exceeding ~3×10^7 kg/year. The six platinum group elements plus Au, Re, and Te (a metalloid) form the nine rarest "metals". Credit: U. S. Geological Survey.

2. TOXICITY OF SEMICONDUCTOR NANOCRYSTALS

2.1. Definition of Risk and Toxicity; Toxicity Assessment

Health risk associated with exposure to a chemical substance or a nanoparticle (NP) is classically defined as the combination of hazard and exposure (Figure 3). Hazard is an inherent property
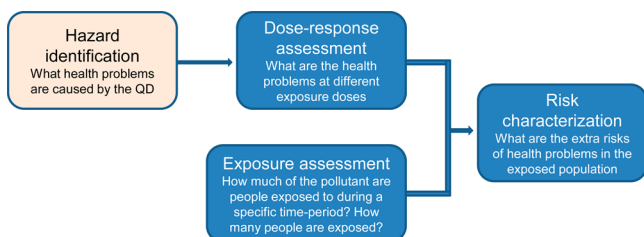

Figure 3. Steps of the risk assessment process. Chart adapted from the U.S. Environmental Protection Agency (EPA), http://www.epa.gov/risk/conducting-human-health-risk-assessment.

of the chemical element or NP, and this parameter is usually measured using toxicity assays. Exposure is defined as the quantity of a chemical element or NP to which a person or a population is exposed, as well as the frequency of that exposure.

Studies dedicated to risk assessment for NPs have emerged since the early 2000s and have increased exponentially to the present day. Many of the current studies in the literature have focused on identifying potential hazards, and although recent advances have demonstrated substantial progress within the field, current knowledge still needs to be refined. With regard to QDs, risk assessment studies have mainly focused on CdTe and CdSe, while there are fewer studies reporting on the toxicological impact of other types of QDs, such as InP or $CuInS_2/CuInSe_2$.

To appropriately assess the risk associated with the use of QDs, it is thus necessary to (i) address exposure, (ii) verify the presence and quantify QDs in the considered object, (iii) quantify the release of QDs from this object, and (iv) identify the state of the released QDs. Indeed, NP transformation in biological or environmental matrices has been demonstrated as having significant effects on its biological impact. Consequently the state of the NP, i.e., still pristine or aged (partly dissolved, surface passivated etc.), greatly impacts the outcome of toxicity assays.

Second, risk assessment necessitates the identification of the route of exposure, which defines the primary target organs. If QDs translocate to internal tissues, i.e., cross the physiological barriers of skin, lungs, or intestine, accumulate in secondary target organs and are finally released via urinary excretion or in the feces, then toxicity toward the secondary target organs, as well as kidneys and/or the liver also has to be evaluated. A series of toxicity end points have to be addressed by carrying out toxicity assays on these defined organs using laboratory

models (in vivo experimental animals or in vitro cell lines) exposed to realistic concentrations of this QD, either pristine or aged. An important issue to be considered when performing toxicity assays is the interference of QDs while interpreting results. Most QDs are fluorescent, and many toxicity assays rely heavily on measuring the absorbance or fluorescence of a reagent, which may also be excited by QDs and/or emit in the same range of wavelength as QDs. This interference must thus be characterized and therefore only non-interfering QD/toxicity assay pairs may be used to assess risk. Only by using this experimental strategy can potential risk be appropriately identified.

2.2. Who Are the Exposed Populations?

Two populations are at risk when it comes to QD toxicological impact, since exposure may occur during the whole life cycle of QD-containing products (Figure 4). First, workers in QD production plants may be exposed during raw material processing, manufacturing, and final product assembly, especially if they are not properly protected. Occupational exposure primarily consists of cutaneous and ocular exposure (i.e., skin and cornea). QDs are mainly produced in the liquid phase, thus minimizing the probability of their release in ambient air and possible exposure via inhalation, however, the risk of inhalation (i.e., lung exposure) still exists. Ingestion via oral exposure through hand-to-mouth contact is also a major route of exposure.

The general population may be exposed in a direct way during the use of products containing QDs, as well as indirectly through environmental contamination following the disposal of the products, unless properly treated and recycled. To illustrate this last point: What happens when the consumer upgrades to a new system (e.g., TV set, mobile phone, and so on) and the old one is thrown in a landfill, where it breaks open and gets rained upon? The materials inside of it will surely be washed into the environment. For this population, the general route of exposure depends on the consumer product and/or application for which QDs are used. Briefly, the applications and consumer products that already/will soon contain QDs are (i) medical/clinical applications (fluorescent labels for site-specific medical imaging, vectors for drug delivery, etc.), (ii) solar cells, (iii) color converters, and (iv) light emitting diodes (LEDs). In terms of risk, medical applications differ from the other application domains. Medical applications imply that pristine QDs are directly delivered to patients, possibly by intravenous injection. Here "exposure" is maximal, and the strategy is to minimize toxicity and/or to promote the rapid release of QDs out of the patient's body. For the other three applications mentioned, "exposure" is far less important and depends on the life cycle of the product containing QDs, as well as the method and intensity of its usage. Within this population, the major exposure route is skin contact through the release of aged QDs or QDs embedded in a polymeric matrix. Based on these
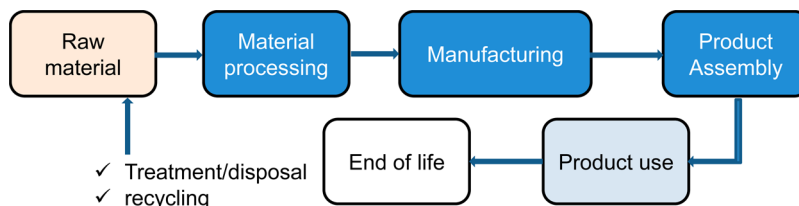

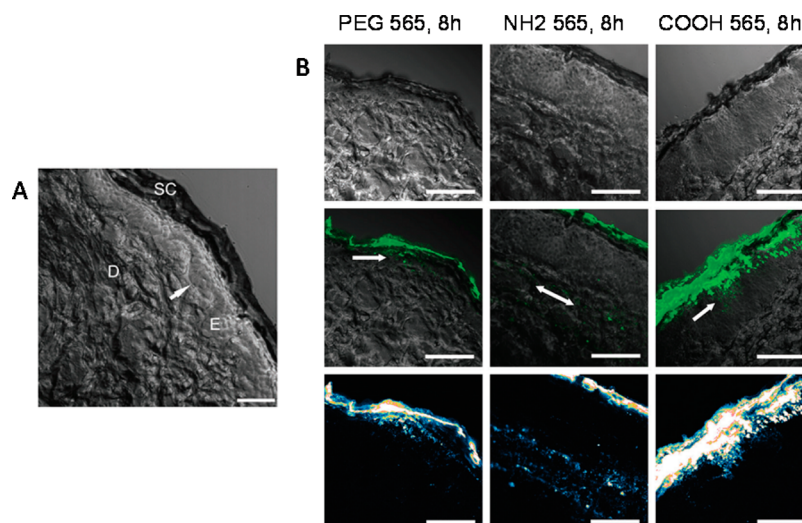**Figure 4.** QD life cycle assessment.

Figure 5. Penetration of QDs through intact skin. (A) structure of the skin, treated with buffer only for 8 h; SC, stratum corneum; E, epidermis; D, dermis. (B) confocal scanning microscopy of skin treated for 8 h with PEG, PEG-amine (NH_2), or carboxylic-acid (COOH) coated QD 565. Top row: confocal-DIC channel only allows an unobstructed view of the skin layers. Middle row: confocal-DIC overlay with the fluorescence channel (green) shows QD localization in the skin layers. Arrows indicate QD localization in the epidermis or dermis. Bottom row: fluorescence intensity scan of QD emission. QDs 565 are localized in the epidermis (PEG and COOH coatings) or dermal (NH_2 coating) layers by 8 h. Scale bar (lower right corners): 50 μm. Reproduced with permission from ref 37. Copyright 2006 Oxford University Press.

conclusions, it can be predicted that the primary target organs of possible QD toxicity are the skin and eyes, followed by the gastrointestinal (GI) tract, and finally, the lungs.

2.3. Impact and Translocation of QDs on/through the Primary Target Organs

2.3.1. Translocation through the Skin. Translocation of CdSe QDs through intact skin was first demonstrated by the team of Monteiro-Riviere, where they demonstrated that QDs could penetrate the outer stratum corneum (SC) layer of porcine skin. Using a flow-through diffusion model, this group demonstrated that the level of skin penetration is based on QD shape (spherical, ellipsoid or nail-shaped) and QD surface coating [(-PEG or -PEG-amine or -carboxylic acid), and/or QD charge (neutral, positive or negative charge)], dictating how deeply the QDs can localize within the skin (Figure 5). This demonstrates the role of their physicochemical characteristics on the deepness and rate of QD skin penetration.[37,38]

QDs were never detected in the perfusate of the flow-through diffusion cell, suggesting that they may not reach the bloodstream via this exposure route.[37,38] However, skin penetration demonstrates exposure of QDs to keratinocytes. A subsequent study from the same team addressed cytotoxicity and release of pro-inflammatory cytokines in vitro by human epidermal keratinocytes when exposed to some of these QD formulations. None of the QDs induced overt cytotoxicity and only COOH-coated QDs induced a pro-inflammatory response, suggesting that surface charge modulates the pro-inflammatory potential of QDs.[39] To reduce potential risks associated with the exposure to QDs, larger QDs with neutral surface charge, such as those coated with PEG which were also used in these studies, would appear be the best formulation, as they seem to minimally penetrate the skin barrier. Mortensen et al. applied DHLA-coated CdSe/ZnS QDs topically on mice, which had been previously exposed to UVB irradiation. As expected, UVB irradiation caused significant damage and barrier impairment to murine skin, and thus promoted deeper penetration of QDs. Moreover, Cd accumulation in the liver

and lymph nodes of exposed mice was detected, which was also related to the inflammatory response of skin cells.[40]

To conclude, CdSe/ZnS QDs penetrate the first layers of undamaged skin, but do not appear to translocate to the systemic circulation. Conversely, following skin injury, QDs (or Cd ions released from their surface) can penetrate much deeper and can be translocated to secondary organs, the liver and the lymph nodes.

2.3.2. Translocation through the Intestine. When considering the GI tract as a route of exposure, no translocation was observed for a variety of QDs, including hydrophobic CdSe/ZnS core/shell QDs without any other surface modification,[41] as well as hydrophilic CdSe/ZnS QDs coated with mercaptocarboxylic acids or encapsulated in a silica shell.[42] Depending on their surface properties, these QDs progressively degraded along the GI tract, more or less quickly. Hydrophobic CdSe/ZnS QDs were completely degraded in under an hour, while CdSe/ZnS QDs coated with hydrophilic thiols were only partially degraded within 4 h.[41,42] Conversely, hydrophilic CdSe/ZnS QDs, coated with a shell of silica, appeared to be resistant to degradation and were rather eliminated in the feces of exposed animals.[42] It has also been reported that InP QDs have the capacity to degrade in physiological fluids, mainly in gastric fluid.[43] Most importantly, progressive degradation of QDs along the GI tract suggests the release of Cd and In ions in the intestinal lumen, which may also allow them to localize within internal organs. This hypothesis is further confirmed by the observation of oxidative damage in the kidneys and spleen of animals exposed to hydrophobic CdSe/ZnS QDs.[41] In addition, the resistance of several formulations of CdSe/ZnS QDs toward reconstituted GI fluids has been assessed in vitro. The ZnS shell is not resistant to the acidic and enzymatic environment of these GI fluids, even when QDs are further coated with polyethylene glycol (PEG350 or PEG5000).[44] An attractive strategy to render them more resistant is to coat them with so-called "proton-sponge" polymers, such as polyethylenimine (PEI). This strategy efficiently enhances the resistance of QDs against the gastro-intestinal environment. However,
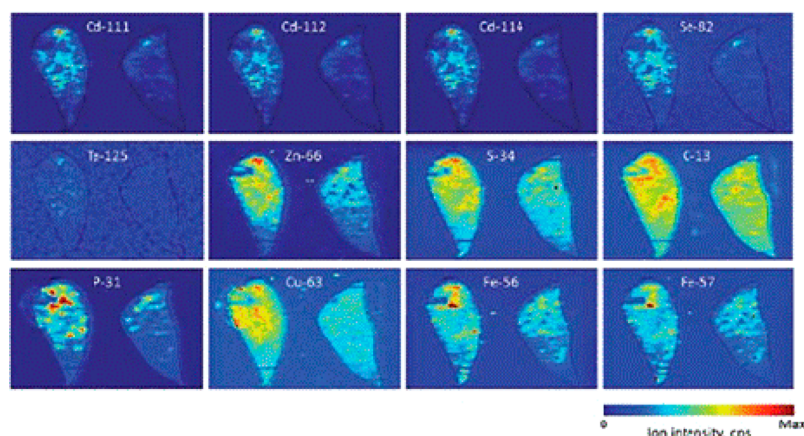
Figure 6. Co-localization of Cd with Se, Zn, and S in slices of lungs from animals exposed to CdSe/ZnS QDs by intratracheal instillation. Laser-ablation inductively coupled plasma mass spectroscopy (LA-ICP-MS) mapping images. Reproduced with permission from ref 46. Copyright 2013 Royal Society of Chemistry.
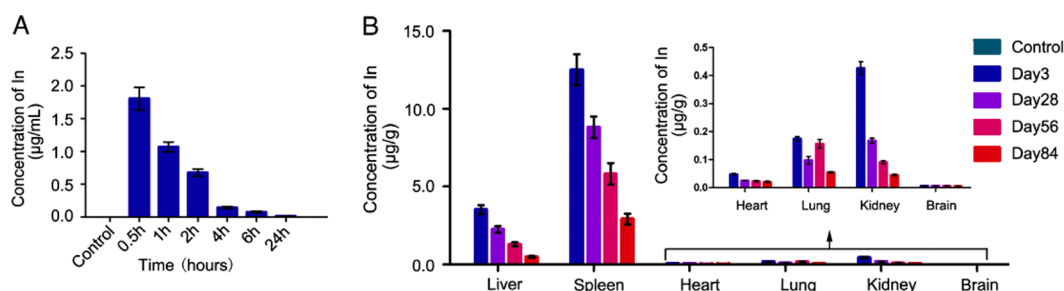

Figure 7. ICP-MS analysis of In content in the blood and major organs of mice treated with InP/ZnS QDs encapsulated in PEGylated phospholipids. A: ICP-MS analysis of blood samples at 0.5, 1, 2, 4, 6, and 24 h postinjection. B: In vivo biodistribution of In in liver, spleen, heart, lung, kidney, and brain at indicated time-points. Values are means $\pm$ SD, n = 3. Reproduced with permission from ref 52. Copyright 2015 Elsevier Inc.

CdSe/ZnS QDs coated with PEG-grafted PEI retain only 70% of their fluorescence in vitro after 1 h of incubation in simulated GI fluids.[45] Based on the current literature, the best alternative for CdSe/ZnS QDs to resist degradation in the GI environment, and consequently to avoid the release of toxic Cd and Se ions, is to coat them with a shell of silica or PEG−PEI.

2.3.3. Translocation through the Lung. Regarding translocation through the lung, two studies report the fate of QDs administered to mice by intratracheal instillation,[46] and to rats by inhalation, using head-nose exposure.[47] Hsieh and collaborators showed that over 17 days neither obvious translocation through the lung barrier nor degradation of CdSe QDs in the lung took place, as attested by Cd and Se being closely colocalized in specific lung regions, with no evidence of the presence of isolated Cd atoms (Figure 6).

One way the authors could have validated their findings would be to quantify Cd and Se using a sensitive method, such as ICP-MS, thus confirming the absence of QD degradation, and translocation of Cd or Se soluble species. The authors show that QDs accumulate in the bronchiolar region of the lung, colocalized with lymphocytes, suggesting that they cause inflammation.[46] In the study by Ma-Hock et al., QD or soluble Cd species translocation through the lung was shown to be minimal, and the authors indicate that Cd found in the rats' livers and kidneys may result from oral ingestion of the QDs deposited in the nose and mouth at the time of administration and/or due to mucociliary clearance and/or contaminated fur cleaning.[47] Here, translocation through the lung barrier is not

definitely demonstrated under these conditions. The authors show no obvious toxicity of QDs, except lung inflammation that partially regresses after a recovery period of 3 weeks.[47] To our knowledge, no article reports the impact of InP-based QDs after lung exposure. Several studies have been conducted with microparticulate forms of InP. InP microparticles cause severe pulmonary inflammation and fibrotic changes after inhalation or oropharyngeal aspiration, as well as pleural effusion.[48,49] Even if the impact of nano- vs microparticle is not comparable, it is important to note that the International Agency for Research in Cancer (IARC) concluded that there was "clear evidence" of carcinogenic activity of InP microparticles in rats, based on a 2-year inhalation study, thus classifying InP in Group 2A (probable) carcinogens.[50]

From these studies, it is rather clear that the translocation of CdSe/ZnS QDs through physiological barriers and further redistribution through the body via the bloodstream is minimal, if not absent. Consequently, systemic toxicity in these exposure scenarios would also be low or absent. Acute toxicity primarily consists of local inflammation. Yet QD translocation and toxicity resulting from chronic exposure is still poorly documented and now has to be considered for a proper risk analysis.

2.4. Secondary Target Organs after Translocation, Primary Target Organs after Intravenous Administration, Clearance

Several studies, mainly using intravenous (IV) or intra-peritoneal (IP) administration, have addressed the biodistribution (the organs in which QDs accumulate) and biokinetics
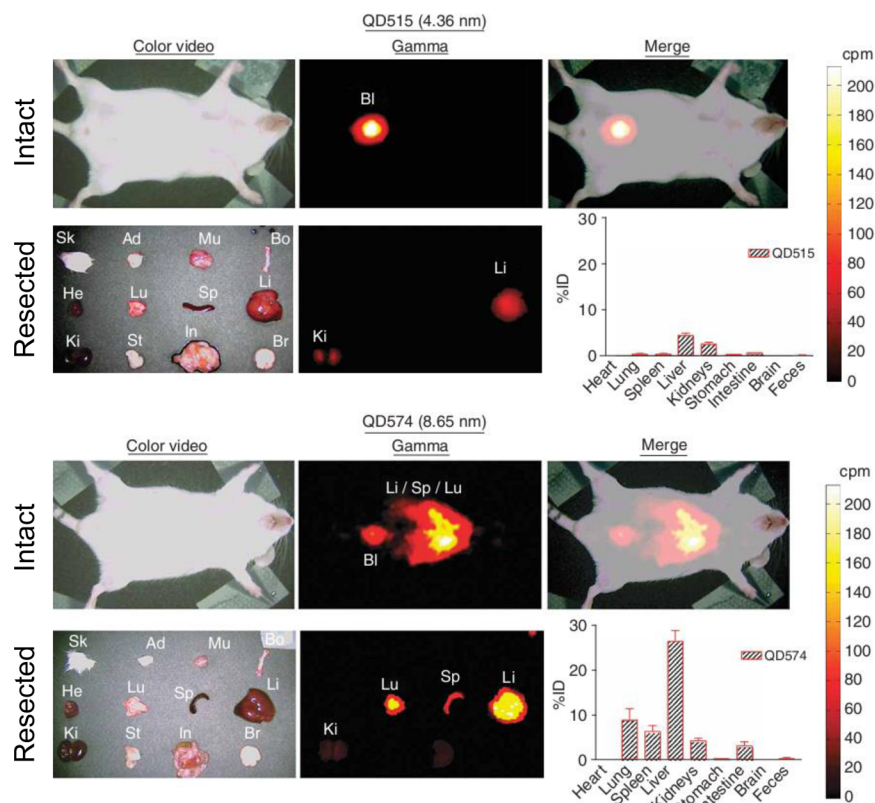
Figure 8. Biodistribution of CdSe QD515 (4.36 nm) and 574 (8.65 nm) in rats after intravenous injection. Rats were treated with ^{99}Tc-radiolabeled QDs, either QD515 (up) or QD574 (down), then animals were sacrificed after 4 h. Color video (left) and Anger camera gamma X-ray images (middle) of the intact animal immediately after sacrificed (top row), and of organs after resection (bottom row). Merged color video and gamma images (top right) and quantitative distribution of ^{99}Tc in all organs after well counting (bottom right). Sk, skin; Ad, adipose; Mu, muscle; Bo, bone; He, heart; Lu, lung; Sp, spleen; Li, liver; K_i, kidney; St, stomach; In, intestine; Br, brain; Bl, bladder. Each point represents the mean ± s.d. of N = 5 animals. Reproduced with permission from ref 60. Copyright 2007 Macmillan Publishers Ltd.

(the time scale of retention/clearance) of QDs out of the body. Most of them were short-term studies, conducted after a single IV or IP injection. However, recently there have been findings focusing more on chronic exposure, thus demonstrating the limited view of the chronic effects of QDs.

As observed with most of the NPs, primary target organs and retention time of QDs in the body depend on their size (i.e., primary diameter and/or agglomeration state), surface charge, and surface coating. The largest or agglomerated NPs are recognized by scavenger receptors of cells from the mononuclear phagocytic system, which eventually transfer NPs to the lymph nodes, liver and spleen.[51] This pattern has been proposed for QDs as well. Biodistribution of InP/ZnS QDs with 58 nm hydrodynamic diameter, encapsulated in PEGylated phospholipids and IV injected into mice (25 mg/kg) show accumulation in the spleen and liver, with progressive clearance from these organs. Still considerable amounts of QDs with intact fluorescence remain 12 weeks postinjection (Figure 7).[52] These QDs do not appear to cause any visible acute toxicity in the animals.[52]

Upon subcutaneous (SC) injection in mice, CuInS$_2$/ZnS QDs emitting in the near-infrared region rapidly distributed to lymph nodes.[53,54] Their toxicity was compared to that of CdTeSe/CdZnS QDs, also administered by subcutaneous injection. The authors observed the onset of an inflammatory response within the axillary lymph nodes, occurring at only 10 pmol of CdTeSe/CdZnS QDs while it rather occurred at 100 pmol of CuInS$_2$/ZnS.[54] This pro-inflammatory response of the

Cd-based QDs was attributed to the release of Cd and/or Te. Moreover, CuInS$_2$/ZnS QDs did not induce any hemolysis in vitro up to 150 nM, while 28% of hemolysis was already reported when red blood cells were incubated with 25 nM of CdTeSe/CdZnS QDs. In vitro, this higher toxicity of CdTeSe/CdZnS QDs was confirmed in MRC-5 human fibroblasts.[53] In this cell line, the cytotoxicity index, i.e., the QD concentration leading to 50% of cell death, ranges between 8 and 21 nM for CdTeSe/CdZnS QDs while it ranges between 76 and 108 nM for CuInS$_2$/ZnS QDs.[53] Together, these data demonstrate that QDs made of CuInS$_2$/ZnS are less toxic than those made of CdTeSe/CdZnS.

Generally speaking, upon IV administration, most CdSe/ZnS and CdTe/ZnS QDs, whatever their surface coating, show rapid blood clearance and accumulate primarily in the lung, liver, spleen and kidneys at early time points. CdSe/ZnS QDs coated either with carboxylic acid or with amine were shown to induce vascular thrombosis via activation of the coagulation cascade in the pulmonary circulation upon IV injection.[55] Accumulation in the lungs may thus result from coagulation, leading to deposition in the lung microvasculature. To a lesser extent, they accumulate in the carcass, heart, muscles, and occasionally the brain. The kinetics of blood clearance, exact distribution and retention time in organs, clearance from the body, depend upon the surface coating of the QD. This distribution pattern was observed in mice,[56−59] rats,[60,61] and rhesus macaques primates[62] exposed to CdSe QDs either noncoated[58] or coated with several ligands. Among these

ligands, mercaptopropionic acid (MPA) or thioglycolic acid (TGA);[56,57] methoxy-polyethylene glycol (methoxy-PEG);[59] dihydrolipoic acid (DHLA), cysteamine, cysteine or DHLA-PEG;[60] bovine serum albumin (BSA), octadecylamine grafted on poly(acrylic acid) (PAA) or PEG-3000;[61] or phospholipid micelles[62] have been tested. Most of the studies reporting similar biodistribution pattern also encountered increased Cd content in the kidneys at later time points, suggesting redistribution of Cd from other organs up to kidneys over time. It was suggested that this redistribution to the kidneys originates from the degradation and release of Cd ions from QDs in the hepatic tissue. Cd ions would then be complexed by metallothioneins (MTs), which are small thiol-containing proteins that complex ions as a means of detoxification. These complexes would further be transferred to kidneys, as demonstrated in animals treated with CdCl$_2$.[59] CdTe-ZnS QDs indeed were rapidly degraded in the liver, as shown by Liu et al., by the evolution of the Cd:Te ratio in this organ during the 28-day course of their experiment.[56] In contrary to what was observed in animals treated with CdCl$_2$, Yeh et al. observed no induction of MTs in the liver 28 days after IV injection. This team also previously reported intact fluorescence of QDs in the liver in the same exposure conditions with the same QD formulation,[58] suggesting that these QDs did not degrade in the liver. Relocated Cd may thus result from the transfer of QDs from other tissues where they accumulated earlier, i.e., the lungs, the brain, and/or the muscles.[59] Using CdSe/ZnS QDs coated with mPEG-5000, Fitzpatrick et al. observed primary distribution in the liver, spleen, and lymph nodes, but not in kidneys.[63] QDs were retained in these organs for up to two years, and exhibited emission spectra with blue-shifted emission peaks and increased bandwidth in mouse tissues, also suggesting that they had degraded.[63] In contrast small CdSe/ZnS QDs coated with cysteine (zwitterionic, 4.36, 4.99, and 5.22 nm) were cleared in mice via urine excretion after a single IV injection at 300 pmol of ^{99}Tc-labeled CdSe/ZnS QDs (Figure 8).[60]

Finally, several of these studies also indicate that QDs may translocate to the brain,[56,62,64,65] and potentially induce adverse effects on the central nervous system. For instance, Gao et al. exposed rats for 7 days to CdSe/ZnS QDs coated with streptavidin (15−20 nm, injection of 0.25 or 5 pmole of QD) by IP injection, and they observed Cd accumulation in the hippocampus of animals as measured by ICP-MS, as well as localized oxidative stress. The authors observe signs of enhanced synaptic transmission, as well as impairment of synaptic plasticity in exposed animals, while rats' spatial memory is altered.[64] ICP-MS is a very sensitive technique, but it does not indicate whether this Cd is in the form of QDs or if the migration of Cd ions released by QDs occurs upon partial dissolution. Whether these effects are due to QD accumulation in brain tissues or to the accumulation of toxic ions released from QDs upon degradation is not demonstrated.

As summarized from these studies, QDs generally show long-time retention in the body of exposed animals, with low (if any) clearance in the urine and feces, except for very small QDs coated with specific ligands. For instance CdSe/ZnS QDs with primary diameter <5.5 nm, coated with DHLA-PEG or cysteine,[60] would be good candidates. The kidneys, spleen and liver are consequently the most potent secondary target organs that may be damaged by QDs. The fate of QDs in the body, especially their degradation largely depends on their size, composition and surface coating. Their persistence as QDs (or

as their composing elements) in these organs justifies the necessity to prove their innocuousness by using chronic, long-term exposure systems.

2.5. Mechanisms Driving QD Toxicity

2.5.1. Release of Toxic Ions from QDs. Concerning the toxicity of QDs, the primary mode of action described to date is the release of toxic ions from the core of the QD, principally Cd, Se, In, and Te. The toxicity of Cd and Se are very well documented and are known to depend upon the speciation of the ion. The release of these ions from QD cores is attributed to oxidation of chalcogenide atoms (S and Se) by O$_2$ from air; these atoms then form oxides (SO$_4^{2-}$, SeO$_2$) that desorb from the QD surface, leaving free reduced Cd atoms that eventually leach from the surface of the QD core (Figure 9). This release is amplified upon UV irradiation[66] and in the presence of Cd-binding ions such as chloride.[67]
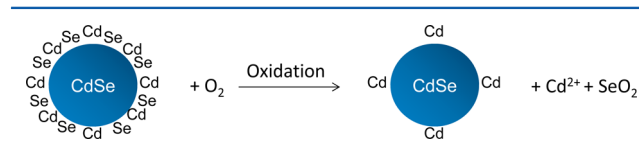
Figure 9. Mechanism of toxic ion release from QD core. Adapted from ref 66. Copyright 2004 American Chemical Society.

In addition to dissolution caused by air oxidation, the oxidative degradation of QDs in vitro by reactive oxygen intermediates (ROI), especially HOCl and H$_2$O$_2$, has been reported by Mancini et al.[68] For any kind of surface coating, including MPA, polyethylenimine (PEI) graft PEG, PAA graft dodecylamine (DDA), or lipid-PEG, CdSe-(CdS-ZnS) core−shell QDs are rapidly etched by these molecules, leading to loss of fluorescence intensity and a blue shift in the exciton peak, suggesting a decreased QD size. This leaching of toxic ions is efficiently reduced by coating QDs with an inorganic shell (such as a shell of ZnS), or small organic ligands, or cross-linked organic shells deposited on the core.[66] For better stability, double inorganic shells are also employed, such as ZnSe/ZnS or CdS/ZnS shells. In these systems, the intermediate shell, acting as a "crystal lattice adapter",[35] enables the growth of a thicker and hence more protective outer ZnS shell. While they do not totally protect the QD core from degradation upon exposure to UV radiation[66] and in acidic environments,[44] double shells on CdSe and InP QDs[69] help to efficiently reduce their toxicity. At the cellular level, UV irradiation is improbable (unless used as a recreational or therapeutic option), whereas acidic conditions are encountered within lysosomes (pH 5), where QDs are stored after intracellular accumulation by endocytosis.[70,71] QDs might thus degrade in these compartments. Moreover, the presence of ROI inside the cell resulting from other unresolved stresses, would amplify the QD dissolution process.

While cells have evolved mechanisms to regulate the intracellular concentration of toxic chemical elements, including efflux of toxic ions, scavenging by metallothioneins (MTs) or other thiol-containing ligands, such as glutathione, this is not the case for NPs. Indeed, Cd ions are usually transported inside cells by hijacking membrane transporters dedicated to the internalization of essential elements. Generally they enter cells via DMT1 which is a transporter of iron, Zrt/Irt-related proteins which are zinc transporters, but also amino-acid or organic cation/anion transporters.[72] Upon reaching the cytoplasmic compartment, these ions are captured by MTs

Figure 10. Oxidative stress, pro-oxidants (orange) and antioxidants (green).

Figure 11. Impact of the °OH radical on the backbone of DNA.

that sequester them, limiting their reactivity and thus their potential toxic impact. Conversely, NPs are internalized in cells mostly via endocytosis and accumulate in endosomes and/or lysosomes.[51] Soluble NPs would then progressively dissolve in these cytoplasmic compartments which would serve as r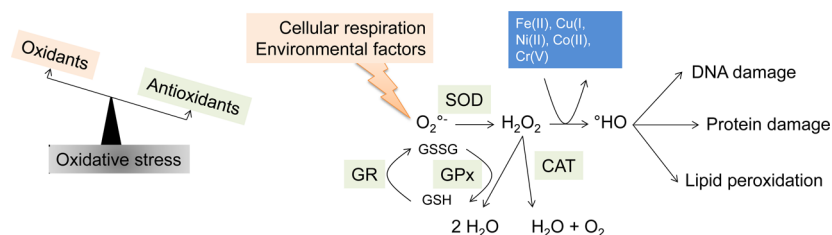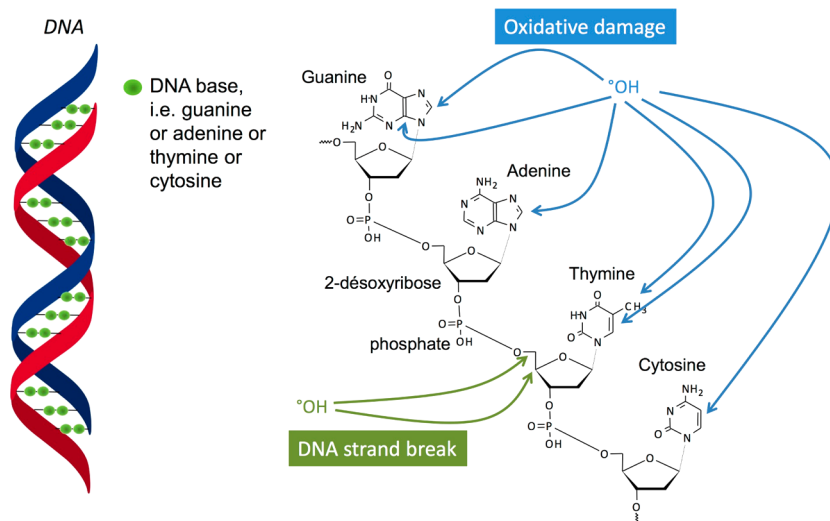eservoirs that progressively release toxic ions that cells cannot appropriately regulate. This was first hypothesized by Limbach et al.[73] and then demonstrated for Ag-NPs, ZnO-NPs, and CuO-NPs;[74] it certainly also applies for QDs. A recent study shows that both CdSe/ZnS and InP/ZnS QDs accumulate in the same amount in two cell types, where they release comparable amounts of Cd and In ions, respectively, but only CdSe/ZnS QDs induce cell mortality.[69] Assuming that QD toxicity is caused only by toxic ion release, the authors concluded that In ions show less intrinsic toxicity than Cd ions.[69]

2.5.2. Oxidative Stress. The toxicity of QD core elements is well documented, especially that of Cd.[75] It has primarily been related to the induction of oxidative stress, observed in the liver shortly after exposure of the animals, then in the kidneys. Cd ions induce extreme overexpression of genes encoding MTs. Oxidative stress is a situation resulting from a misbalance between the amount of ROIs present in the cell and the cell's capacity to eliminate them (Figure 10). ROIs may accumulate upon exposure to QDs; this is not a guarantee of oxidative stress and its consequences, especially if ROIs are appropriately handled by the cell's antioxidant systems, including reduced glutathione (GSH) or antioxidant enzymes, such as superoxide dismutase (SOD) or catalase (CAT). If these antioxidant systems are overwhelmed, then ROIs can oxidize biomolecules, including proteins, lipids from extra- and intracellular membranes, as well as DNA. Oxidative DNA damage can

also be amplified by inhibition of DNA repair, as demonstrated with Cd ions.[76]

Several studies published to date relate the potentiality that QDs per se produce ROIs. This was demonstrated for InP/ZnS QDs exposed to visible light. ROI generation was halved when InP QDs were coated with a double-shell of ZnS, as compared to a single-shell. It mainly consisted of superoxide production, as well as the generation of a small amount of hydroxyl radicals. Generation of these radicals was directly correlated with cell death induced by these QDs; this cytotoxicity, tested on five different cell lines, was low and significantly lower than that induced by CdSe/ZnS or CdTe QDs.[77] In the study by Brunetti et al., CdSe/ZnS QDs (double shell of ZnS) were shown to induce cell mortality, oxidative stress and increased intracellular Ca^{2+} content in two cell types, while InP/ZnS (double shell of ZnS) did not.[69] Early in vitro acellular studies using electron paramagnetic resonance (EPR) showed that CdSe/ZnS QDs produced ROIs, both in the dark and under UV irradiation, which were shown to attack the backbone of DNA.[78] The authors explained that the generation of ROIs in QDs which were not light exposed or photoactivated was caused by generation of sulfur free radical species from the ZnS shell via exposure to air and water.[78] In another study, CdS and CdSe QDs were shown to produce ROIs when UV-irradiated, while CdSe/ZnS QDs did not.[79] The same QDs did not produce any EPR signal when manipulated in the dark.[79] Anas et al. used DNA as a probe of ROI generation by CdSe/ZnS QDs upon photoactivation under different lighting conditions and showed induction of oxidative DNA damage only when QDs were photoactivated, compared to QDs not exposed to light.[80]

In vivo induction of oxidative stress has been demonstrated in animals dosed with CdSe/Te-based QDs. For instance, Lin et al. demonstrated that, upon IV injection in mice, CdSe/Te-ZnS QDs coated with methoxy-PEG-5000 accumulated in the liver, where they caused time- and dose-dependent elevation of MT contents, as well as increased expression of several markers of oxidative stress and inflammation (hemoxygenase 1, interleukin 6, and TNF-alpha).[81]

2.5.3. Damage to DNA. In addition to oxidative stress, Lin et al. reported that CdSe/Te-ZnS QDs coated with methoxy-PEG-5000 caused oxidative DNA damage through generation of the signature lesion, the oxidized derivative of guanine (8-oxo-dGuo).[81] Khalil et al.[82] also reported oxidative DNA damage in the liver and bone marrow of animals exposed at much higher doses of CdSe QDs, as well as chromosomal damage. As previously mentioned, if not appropriately handled by cells, ROIs, especially the hydroxyl radical °OH, may attack DNA and generate both oxidized DNA bases and DNA strand breaks (Figure 11). These bases are efficiently repaired by the base-excision repair (BER) pathway. However, if these lesions are not properly repaired, they have been shown to have mutagenic properties.

More generally, QD genotoxicity has been demonstrated in several in vivo and in vitro studies. In vivo, Aye et al. showed that CdSe/ZnS QDs, encapsulated in phospholipids, caused DNA strand breaks in the liver and brain of exposed animals (exposure via IP injection at 0.55, 0.05, or 0.005 μg/kg body weight, with DNA damage analysis at 24 h postinjection). These QDs also caused chromosomal aberration on blood reticulocytes, as determined by the micronucleus assay.[83] Interestingly, the authors also monitored oxidative stress, inflammation (TNF-α), Hsp70, and apoptosis (Caspase-3), but did not observe any significant modulation of these markers in the organs of exposed animals. Genotoxicity may thus be caused by both oxidative stress and other mechanisms. From in vitro experiments, the mechanisms of QD genotoxicity have been deeply investigated, and while oxidative stress plays a major role,[79,84] it was also shown that QDs may directly induce DNA strand breaks after entering the nucleus via nuclear pore complexes.[78,85,86] Moreover, since Cd ions have been shown to promote the accumulation of DNA damage via inhibition of DNA repair mechanisms,[87] QDs that dissolve and release Cd ions may have the same effect, although this has not been mentioned in the current literature.

2.6. What Would Be the Profile of Safer-by-Design QDs?

As described earlier in this chapter, risk results from the combination of hazard and exposure. Limitation of exposure derives from QD surface modification or limitation of dissolution. For example, coating QDs with a shell of PEG render them furtive or coating them with a shell of amorphous silica would limit their dissolution, even in harsh conditions, such as low pH. The last option would be to embed them in an insoluble, inert and robust matrix, such as polymeric matrix. Considering the already acquired knowledge relative to QD toxicity, the ideal candidate for safer QDs would not contain any heavy metals, or would contain the least toxic metal possible (reduction of hazard). These QDs would be coated so that they do not translocate through physiological barriers (reduction of exposure), and/or would minimally dissolve (reduction of hazard and exposure to toxic ions that would be released). Lastly their dissolution products would show low toxicity. New generations of QDs are composed of In or Cu/In

rather than Cd. This is an important step toward safer QDs, yet the toxicity of In might also be significant, even if it is lower than that of Cd, as demonstrated some years ago with indium—tin-oxide microparticles[88] and InP microparticles.[50] Replacement of In by another chemical element would thus also be valuable, as long as QD properties are preserved. Among such examples, zinc phosphide has been proposed in recent years, which has a direct band gap of 1.5 eV in the bulk. Despite the fact that only a handful of synthetic methods for colloidal Zn_3P_2 NCs have been reported, steady progress in this field gives now access to samples of low polydispersity in different size regimes. In the 2—3 nm size range they exhibit clear excitonic absorption features indicative of band gap energies of 2.3—2.9 eV,[89] while 8 nm sized Zn_3P_2 NCs showed a band gap of 2 eV.[90] Another option would be to reduce as much as possible the In content in QDs, for instance by substituting it or doping it with another chemical element that would be less toxic and would enhance the optical properties of QDs. This option is already tested in the strategies aiming at doping ZnS, ZnSe and InP QDs with, for example, Mn or Cu ions. However, it must be kept in mind that the chemical elements used as dopants may also exert some toxic action under certain conditions. Finally QDs that would not contain any possibly toxic elements would be even better options, and it is certainly the case of the NCs of the elemental semiconductors Si and Ge. These alternative QDs show promising luminescence properties; their syntheses and properties will be discussed in details in section 4.1. A recent review summarizes the findings relative to the toxicity and biodegradability of Si NCs.[91] Very few articles describe the toxicity of Ge NCs; the vast majority of them report very low toxicity.[92] As for Cd- and In-based QDs, their toxicity depends on their surface coating, charge and size,[93] and indirectly on their in vivo degradation. However, toxic effects appear at much lower concentrations of these QDs compared to Cd- or In-based QDs. In vivo, their biodistribution is comparable to that of other QDs, except that they degrade much more rapidly if not appropriately surface-coated. But contrary to Cd- and In-based QDs, the degradation of Si NCs leads to the release of silicic acid in the bloodstream, which is not toxic and is rapidly released out of the body via renal excretion. Combined to the high natural abundance of Si, these properties place Si NCs among the most promising QDs for medical applications, provided their optical properties can be improved to similar quality as those of established QDs. Indeed they have already been tested in vivo, coated with phospholipid-PEG micelles and targeted to tumors via RGD ligands, and proved to be efficient for subcutaneous tumor imaging.[94]

3. BASIC CONCEPTS IN NANOCRYSTAL SYNTHESIS

3.1. Introduction

The introduction of a high temperature synthesis method in organic solvents in 1993 by Murray, Norris, and Bawendi was one of the most important steps toward the preparation of monodisperse NCs.[95] It described the synthesis of cadmium chalcogenides (CdE, E = S, Se, and Te), and since then CdSe NCs serve as the work horse for a huge number of studies. Monodispersity is of paramount importance for fundamental studies aimed at understanding the optoelectronic properties of nanostructures but also for applications, as NCs show more uniform optical and improved electrical transport properties and better pack into 2D films or 3D solids. Before going into details of the discussion of different families of materials, this
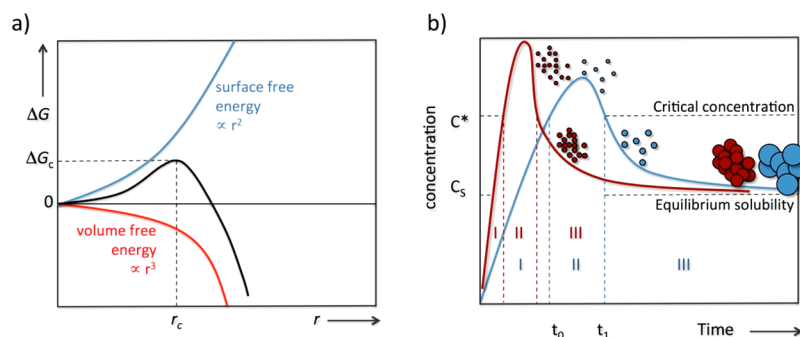
Figure 12. Nucleation and growth of NCs. (a) Contribution of the volume free energy (red) and surface free energy (blue) to the total free energy change (black) as a function of nucleus size (adapted from ref 102). The critical radius r_c indicates the minimum size for which the nuclei do not redissolve spontaneously. (b) LaMer diagram: prenucleation stage (I) nucleation (II) and growth (III) phases as a function of the reaction time. Nucleation takes place when the monomer concentration exceeds C*. Highly reactive precursors, which undergo conversion to monomers in stage I with a fast rate, yield a larger number of NCs of smaller final size (red curve) than less reactive precursors (blue curve).

section aims at giving an overview of the main synthetic schemes for the preparation of monodisperse NCs as well as of the underlying physicochemical models.

3.2. Physicochemical Principles of Nucleation and Growth

### 3.2.1. Homogeneous and Heterogeneous Nucleation.
Classical studies of LaMer and Dinegar predict that the temporal separation of nucleation and growth is necessary for obtaining colloidal solutions of NCs showing narrow size distribution.[96] In other words, the nucleation event ("burst") should be as short as possible with no more new nuclei formed in later stages of particle growth. The qualitative validity of this model has been experimentally verified in many examples. Its limitations and extensions will be discussed in the next paragraphs. Separation of nucleation and growth can be achieved in different ways, and it is helpful to divide the cases of heterogeneous and homogeneous nucleation. Zsigmondy introduced the "seeded growth" method, which is a prototype reaction for heterogeneous nucleation.[97] Here the seed particles are first formed and isolated and then injected into the reaction medium containing appropriate precursors and stabilizers for the growth, while being in a regime of concentration, which does not induce further nucleation of seeds. In particular this early example concerned the synthesis of monodisperse Au nanoparticles by reducing chloroauric acid with formaldehyde in the presence of 3 nm seed particles, namely Faraday's gold sols.[97,98] More recently seeded growth has turned out to be a powerful method for the synthesis of spherical core/elongated shell semiconductor heterostructures, giving an unprecedented control of diameter and length in CdSe/CdS NCs.[99,100] Heterogeneous nucleation occurs at preferential sites of surfaces and requires lower activation energy then homogeneous nucleation. Both processes have been treated in the framework of classical nucleation theory (CNT), which is based on the principle that the thermodynamic system tends to minimize its Gibbs free energy.[101] Upon nucleation the Gibbs free energy change is the sum of a negative term, describing the energetic gain due to bond formation, and a positive term arising from the increase of the Gibbs free surface energy (eq 1).[102]

$$\Delta G = -\frac{4}{3}\pi r^3 |\Delta G_V| + 4\pi r^2 \gamma \tag{1}$$

$$\text{for } \frac{d\Delta G}{dr} = 0 \rightarrow r_c = \frac{2\gamma}{|\Delta G_V|} \tag{2}$$

with r being the nucleus radius, G_V the Gibbs bulk free energy per unit volume, and γ the surface free energy per unit area. The maximum in the plot of ΔG vs r corresponds to the minimum critical radius for nucleation r_c, and the corresponding energy barrier, the activation energy ΔG_c (Figure 12a). Only nuclei larger than r_c enter the growth stage, while smaller ones redissolve.

In homogeneous nucleation the formation of the solute ("monomer") from the precursors precedes the NCs' nucleation and growth, as demonstrated by Steckel et al.,[103] Liu et al.,[104] and Abe et al.[105] Importantly the precursor transformation to monomers is often irreversible and the conversion rate is not affected by the concentration of monomers or NCs. Therefore, the whole process can be summarized as follows:[105,106]

$$\text{precursors} \rightarrow \text{monomers} \rightleftharpoons \text{nanocrystals}$$
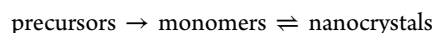
Recent synthetic methods adjust the precursor conversion rate in a way that it limits the crystallization step. By consequence this rate can be used to tune the number of NCs produced during nucleation, which allows the design of syntheses showing close to quantitative chemical yield for a desired NC size.

3.2.2. LaMer Model and Its Extensions.
The LaMer model links nucleation and growth of colloidal particles in homogeneous solution and represents, despite some shortcomings,[107] the most widely applied model for describing the formation of NCs. Figure 12b depicts the LaMer diagram for the cases of high (red) and low (blue) precursor-to-monomer conversion rate. Fast nucleation of a large number of seeds leads to a larger number of particles of smaller final size and vice versa. In any case the reaction can be divided into three phases:[96] In stage I the concentration of the solute/monomers is built up by the addition of precursors or change in the reaction parameters (e.g., T, p). When the monomer supersaturation reaches the level of the critical concentration C* nucleation sets in (stage II). The nucleation process continues until the monomer of the growing nuclei exceeds the monomer production by precursor conversion ($C_{mon} < C^*$), terminating this stage. In the subsequent growth stage (stage III), ideally the balance of monomer consumption and production maintains a high supersaturation. If this is not the case, growth from solution can be accompanied and/or followed by another growth process termed Ostwald ripening. This phenomenon is triggered by the larger solubility of the
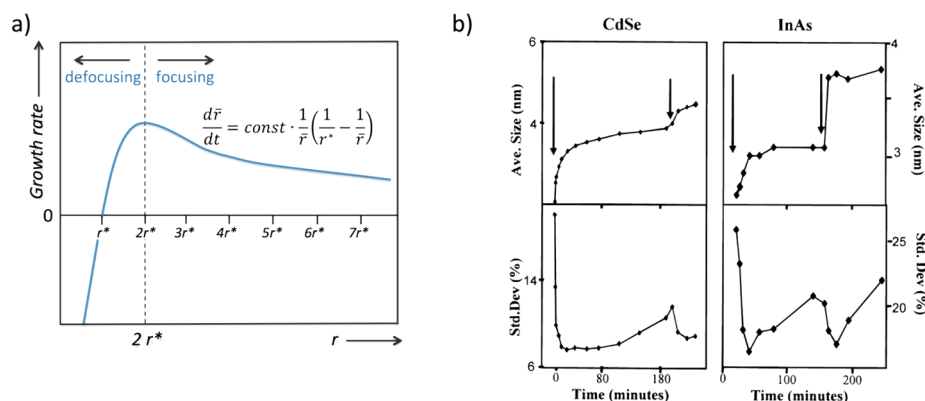
Figure 13. (a) Size-dependent growth rate for diffusion-controlled growth. For the average radius $\bar{r} > 2r^*$ size focusing occurs, while for $\bar{r} < 2r^*$ the size distribution broadens. r^* indicates for a given concentration the equilibrium size with zero growth rate [neither negative (dissolution) nor positive (growth)]. (b) Mean size and size distribution extracted from the PL line width of aliquots taken during the synthesis of CdSe and InAs NCs. Arrows indicate the injection of stock solutions containing the Cd and Se or In and As precursors into the hot reaction medium. Reproduced with permission from ref 111. Copyright 1998 American Chemical Society.

smaller particles in an ensemble (Kelvin effect), which can lead to a broadening of the size distribution. The dissolved matter is redeposited on the larger particles, leading finally to a smaller number of particles of increased diameter.[108] To prevent the formed crystallites from irreversible coagulation/aggregation, the addition of stabilizing molecules (ligands, surfactants) is mandatory when working in organic solvents. These molecules have to be chosen in a way that they provide sufficient steric repulsion to ensure colloidal stability of the NCs. In many cases they contain long alkyl chains (e.g., trioctylphosphine oxide, oleate, oleylamine). When the synthesis is carried out in aqueous media stabilization is facilitated through long-range electrostatic repulsion forces between particles, around which an electric double layer forms. The repulsive forces are function of the zeta potential and Debye length. One limitation of the LaMer model is that it does not describe the evolution of the size distribution during the growth stage. When considering the seeded-growth approach, size focusing is supposed to occur during growth, decreasing the initial size dispersion of the seeds. The growth stage comprises the sequence of monomer diffusion to the surface and the reaction of the monomer on the surface. Depending on the diffusion coefficient and rate constant for the surface reaction the growth can be limited by one or the other process leading to diffusion-controlled or reaction-controlled growth. When surface reaction is the rate-limiting step and the growth rate is proportional to the surface area, the increase in radius of each particle of the ensemble is equal, inducing a decrease of the relative size distribution with growth. For the diffusion-controlled case H, Reiss developed a model for predicting the evolution of the NC size distribution.[109] It takes into account nanoparticle assemblies and supposes that the growth rate of spherical particles only depends on the supplied monomer flux. As a consequence, smaller particles grow faster than larger ones in the assembly. This leads, like in the case of reaction-limited growth to size-focusing, yet with an even faster narrowing of the size distribution. On the other hand, this model does not consider competing processes like aggregation or Ostwald ripening, which can lead to a broadening of the size distribution. Sugimoto included dissolution processes in the model of Reiss, which led to the definition of a size-dependent growth rate.[110] One important outcome of this extended model was shown that under low supersaturation, namely for $\bar{r}/r^* < 2$ the size

distribution increases ($\bar{r}$, mean particle radius; r^*, particle radius in equilibrium with the bulk solution, i.e., particles of $r < r^*$ dissolve due to the Kelvin effect, particles of $r > r^*$ grow). On the other hand, the size distribution becomes narrower for the situation of $\bar{r}/r^* > 2$. This means that size focusing can be achieved during particle growth under the condition that the supersaturation is kept high enough with respect to the solubility of the particles of the mean size (Figure 13a). However, it has to be taken into account that r^* increases under the depletion of the monomer reservoir during particle growth. Therefore, it can practically be necessary to supply additional monomers during the growth stage to prevent from size defocusing. Experimentally, this model has first been validated by Peng, Wickham and Alivisatos who demonstrated size focusing regimes upon repeated injection of the precursor mixtures in the synthesis of CdSe and InAs NCs.[111] This approach can be considered as a variant of the seeded-growth method. One notes in Figure 13b that the achievable size range is much smaller and the size distribution significantly broader in the case of InAs. These features unfortunately characterize the majority of reported syntheses of III–V semiconductor NCs, and their origin will be discussed in the last part of this section.

3.2.3. Separation of Nucleation and Growth: Hot-Injection and Heat-Up Methods. Two main NC synthesis methods in organic solvents have been developed, which give access to monodisperse particles through the separation of nucleation and growth: the hot-injection (HI) and the heat-up method (HU). Both have been reviewed independently by Donega et al.[112] and Jasieniak and co-workers[19] and have also been compared to each other in another review by Kwon and Hyeon.[13] In case of the HI method, the separation of nucleation and growth can be achieved by the rapid injection of the reagents into the hot solvent, which raises the concentration in the reaction flask above the nucleation threshold. The hot injection leads to a nucleation burst, which is quickly quenched by two factors: (i) the fast cooling of the reaction mixture, enhanced by the fact that the solution to be injected is at room temperature; (ii) the decreased supersaturation due to precursor/monomer consumption during nucleation. Another possibility, realized in the HU method, relies on attaining the degree of supersaturation necessary for homogeneous nucleation via the in situ formation of reactive species upon supply of thermal energy. While

initially this method was more widely used in the synthesis of metallic nanoparticles, more recently a strongly increasing number of examples of semiconductor NCs prepared by this approach can be found. From the practical point of view and with regard to the scale-up of syntheses, the HU method has obvious advantages over the HI method, which typically translate into higher reproducibility and lower risks. The characteristic temporal evolution of the prominent reaction parameters during the HU synthesis is depicted in Figure 14.[19]
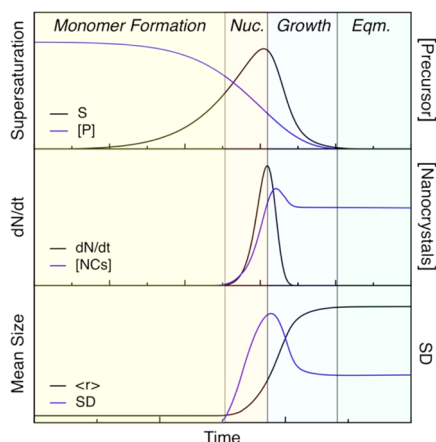

Figure 14. Simulated evolution of the characteristic reaction parameters during the heat-up synthesis of NCs. The temperature is ramped at constant rate to the nucleation temperature during the yellow stage and then left constant for the rest of the simulation. Reproduced with permission from ref 19. Copyright 2015 American Chemical Society [*Chem. Mater.* **2015**, 27(7), 2246−2285].

The top panel in this figure shows that the evolution of the supersaturation follows the LaMer model (cf. Figure 12b), however, with a prolonged nucleation stage (vide infra). In the first stage (yellow), the precursors are transformed to monomers of the compound to be formed and concomitantly the precursor concentration [P] is going down. Monomer accumulation takes place until the critical temperature and critical concentration for homogeneous nucleation are reached (orange stage). The nucleation rate dN/dt reaches a maximum, as does the particle size distribution, characterized by its standard deviation SD. The decline of the nucleation rate marks the beginning of the growth stage (blue). The high supersaturation in the initial growth stage favors size focusing, which leads to a drop of the SD. In the equilibrium stage (green), the mean size and size distribution remain nearly constant, although Ostwald ripening could lead to size broadening in the case of prolonged heating.

Even though the HI synthesis can in principle be schematized with a similar diagram replacing the yellow monomer formation/accumulation phase by the fast injection of precursors, van Embden et al. pointed out differences between both methods.[19] The nucleation period, as a key feature of the HU method, is much longer than in the HI method. The prolonged nucleation stage in the HU method arises from the progressive monomer generation, which is accelerated during the temperature rise and subsequent heating stage. Therefore, even after the nucleation is triggered, a high supersaturation is maintained for an extended period. The overlap of nucleation and growth stages leads to an initially broadened size distribution. On the other hand, the continuous monomer formation and supply assures a high growth rate of

the nuclei, fulfilling the above-mentioned condition $\bar{r} > 2r^*$ for size focusing. The most important factors governing the heat-up synthesis are the choice of the precursors and stabilizers as well as the heating rate. Increasing the heating rate leads to a decrease of the mean NC size, which is accompanied by an increase of the NC concentration, like in the case of fast precursor conversion depicted in Figure 12b. In addition, fast heating rates favor the decrease of the size distribution by ensuring a high growth rate of the nuclei. The choice of precursors and adjusting their reactivity is the second factor impacting strongly the size and size distribution of the obtained NCs. Moderately reactive precursors are the best choice, which offer a balanced monomer formation rate during heating, control over the nucleation and growth stages at high temperature as well as negligible nucleation at room temperature. In case of highly reactive precursors (e.g., organometallic-type compounds like R_xM or $E(SiMe_3)_x$, R = Me,Et; M = metal; E = pnictogen or chalcogen; x = 2,3), monomer formation occurs at room temperature, which triggers nucleation already at a mild increase of temperature. Simultaneous high nucleation and growth rates lead to broad size distributions in this case. Too low precursor reactivity in turn leads to delayed monomer formation and small growth rates of the nuclei. Ostwald ripening becomes the predominant growth mechanism in this case, leading once again to a broadened size distribution. By consequence, the fine-tuning of the precursor reactivity is a crucial step in the HU method, which explains why for some materials so far the HI method yields higher quality NCs. In both methods the rather restricted libraries of pnictide and chalcogenide precursors currently explored (cf. section 4) constitute a bottleneck for the development of synthesis methods for materials less mastered today, calling for the design of tailor-made compounds. One exception of this rule is the recent work of Hendricks et al., who prepared a library of differently substituted thioureas, which showed tailored reactivity and conversion rates controllable over several orders of magnitude.[106] This enabled the synthesis of monodisperse metal sulfide NCs of desired size under simultaneous optimization of the reaction yield.

3.3. Chemistry of the Inorganic Core, Interaction with Organic Surface Ligands

The goal of this subsection is to provide the reader with some useful concepts for understanding the underlying chemistry governing the synthesis reactions for different families of semiconductor NCs as well as their interactions with the surface ligands. We start from the inorganic core and draw parallels of the observed differences in reactivity and precursor chemistry with the fractional ionic/covalent character of bonding (concept of ionocovalency) of the different compounds. These are metal chalcogenides on the one hand, and metal pnictides as well as silicon and germanium on the other hand. When looking at the NC as a whole, surface−ligand interactions have to be considered. In this context the hard and soft acids and bases (HSAB) principle is very helpful for classifying affinities between different kinds of metal ions (Lewis acids) and ligands (Lewis bases). For both the inorganic core and organic ligand shell, we further highlight recent developments in advanced characterization techniques allowing for the real-time assessment of the nucleation and growth kinetics and the precise description of the surface state. Finally, we draw attention to an often-neglected step in NC synthesis, namely purification, i.e. the separation of the NCs from the

reaction medium, remaining precursors, excess ligands and eventual side products. Although the purification procedure has important consequences on the final properties of the NCs (e.g., colloidal stability, fluorescence emission, surface reactivity), its description is in many cases treated stepwise.

3.3.1. Closer Look at Different Semiconductor Families. As mentioned before, most of the studies related to the factors governing nucleation and growth of semiconductor NCs have been conducted on CdSe. While the elaborated principles apply in general also for the synthesis of NCs of other II−VI and IV−VI compounds of similar bonding nature (e.g., CdS, CdTe, PbS, and PbSe), the III−V compounds and elemental group IV semiconductors do not follow the same behavior. Their nature of bonding does not facilitate the identification of suitable precursors and reaction conditions enabling the separation of nucleation and growth and diffusion-controlled growth from solution. One way to classify the different classes of materials with regard to their bonding is by means of their lattice ionicity. From the crystallographic point of view all II−VI and III−V semiconductors exhibit tetrahedral bonding geometry and realize the zinc blende or wurtzite crystal structure. IV−VI compounds such as the lead chalcogenides differ from this pattern, crystallizing in the cubic rocksalt structure with octahedral 6-fold coordination. Common to all these families is that the chemical nature of bonding has both covalent and ionic contributions, which has been quantified by Phillips in form of the fractional ionic character f_i (Table 1).[113]

Table 1. Fractional Ionic Character of Bonding f_i, Band Gap Energies and Structural Properties of Different Families of Compound Semiconductors[113,114]

family	material	f_i	E_g at 300 K (eV)	crystal structure (most stable form at 300 K)	lattice parameter (Å)
III−V	InN	0.58	0.8	wurtzite	3.545/5.703
	InP	0.42	1.35	zinc blende	5.869
	InAs	0.36	0.35	zinc blende	6.058
	InSb	0.32	0.23	zinc blende	6.479
	GaN	0.50	3.44	wurtzite	3.188/5.185
	GaP	0.33	2.27 (ind.)	zinc blende	5.45
	GaAs	0.31	1.42	zinc blende	5.653
	GaSb	0.26	0.72	zinc blende	6.096
II−VI	ZnS	0.62	3.54	zinc blende	5.41
	ZnSe	0.63	2.69	zinc blende	5.668
	ZnTe	0.61	2.26	zinc blende	6.104
	CdS	0.69	2.49	wurtzite	4.136/6.714
	CdSe	0.70	1.74	wurtzite	4.3/7.01
	CdTe	0.72	1.43	zinc blende	6.482
IV−VI	PbS	0.77	0.41	rocksalt	5.936
	PbSe	0.72	0.28	rocksalt	6.117
	PbTe	0.63	0.31	rocksalt	6.462

One first qualitative observation is that the III−V compounds show a much higher fraction of covalent bonding ($f_i < 0.5$ except for InN) than the II−VI and IV−VI compounds ($f_i > 0.6$). Heath and Shiang demonstrated that lattice covalency and hence the fractional ionic character of bonding is strongly correlated with the onset and magnitude of quantum size effects.[115] As we will see in the following, the extent of lattice covalency also correlates with the availability of chemical synthesis methods giving access to monodisperse NCs of a given compound. In particular the synthetic challenges related to the group IV elemental semiconductor NCs Si and Ge (diamond cubic structure, $f_i = 0$) and to the III−V compounds are directly related to their (more) covalent character. It implies the use of precursors of higher reactivity and higher reaction temperatures than in the case of metal chalcogenide NCs. These requirements make it generally difficult to establish reaction conditions yielding monodisperse NCs.

3.3.2. Investigation of the Evolution of the NC Core during Synthesis. For the real-time assessment of the nucleation and growth stages in NC synthesis discussed in Section 3.1, appropriate in situ characterization methods should be applied. This type of study gives access to the reaction kinetics and, depending on the used technique, to the evolution of the crystal structure and habit with reaction time.[116,117] However, suitable in situ methods are scarce due to the limited choice of observable and stringent requirements related to the chemical synthesis of NCs (e.g., high temperature, inert atmosphere, fast kinetics).[14] Furthermore, one critical issue related to in situ methods is that the measurement must not disturb the observed reaction. This criterion is difficult to fulfill when working with high-energy electron beams or X-ray radiation. For in situ (scanning) transmission electron microscopy investigations, special sample holders have been designed, using for example silicon nitride or graphene sheets as window materials.[118,119] The nucleation within the precursor solution placed in these holders can be triggered thermally or by means of the electron beam. The technique, also called liquid transmission electron microscopy (LTEM), is therefore especially well suited to syntheses relying on the heat-up strategy. It allows for the direct real-time observation of the nucleation and growth stages and is a potent tool for the verification of the models proposed for describing these processes.[120] So far, except for PbS NCs, mainly metal nanoparticles have been investigated,[121] but this approach is currently being applied to many other systems.[122] In comparison to metal nanoparticles, semiconductor NCs possess the huge advantage of exhibiting size-dependent optical properties for in situ studies. In particular, due to the quantum confinement effect, the onset of their absorption spectrum shifts gradually to longer wavelengths with increasing reaction time (and hence NC size). This can be exploited in in situ UV−vis spectroscopy studies of the growth kinetics.[123] Due to the fast measurement, the temporal resolution can be as low as microseconds.[124] Both the reaction kinetics and structural properties can be assessed in real time by in situ X-ray diffraction. Small-angle X-ray scattering (SAXS) gives access to precursor or monomer organization in prenucleation stages and to the average size and autoassembly of NCs in postnucleation stages. Wide-angle studies (WAXS), in turn, shed light on the formed crystal structures and their evolution. In contrast to these techniques, which are angular dispersive, X-ray absorption fine structure (XAFS) spectroscopy is energy dispersive and therefore requires a polychromatic X-ray beam. XAFS is very sensitive to the absorption of X-rays near and above the core-level binding energies of the atom. Consequently this technique allows the probing of the local environment of atoms, such as coordination chemistry, nearest neighbor distances and formal oxidation state. Another advantage of this technique is that it does not require the sample to be crystalline, which enables, for example, the study of amorphous surface layers on nanoparticles formed upon partial oxidation. The XAFS spectrum is divided into two regions: one within 50 eV above the main

absorption edge (X-ray absorption near-edge spectroscopy, XANES) and one within 50−1000 eV above (extended X-ray absorption fine-structure spectroscopy, EXAFS). Figure 15 summarizes the different X-ray techniques used for the investigation of the different stages of nanoparticle crystallization.
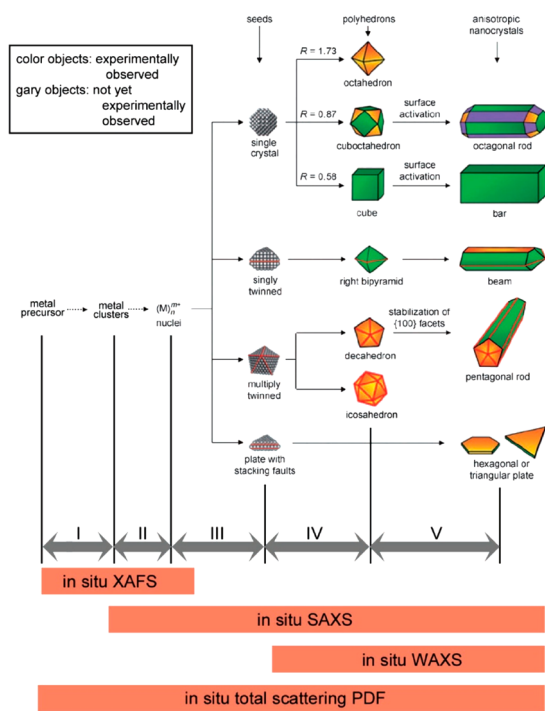

Figure 15. Processes in the growth of shape-controlled face-centered cubic metal nanoparticles and capabilities of different in situ X-ray techniques for investigating these processes. Reproduced with permission from ref 125. Copyright 2013 WILEY-VCH Verlag GmbH & Co. KGaA.

Samples for such experiments are generally enclosed or flown through glass capillaries or specially designed reaction flasks, and high-energy synchrotron radiation is required to obtain sufficient signal intensity.[125,126] Sample damage can be avoided by beam shutters and by the use of short acquisition times. Depending on the used detectors, SAXS measurements can be performed as fast as in tens of milliseconds, while WAXS measurements require usually at least seconds. Initially applied to Ag[125] and Au[127] nanoparticles, such methods have more recently also been used to investigate the pre- and postnucleation stages of metal chalcogenide synthesis NCs, in particular of CdSe. Examples are in situ EXAFS and XAFS measurements performed on CdSe and ZnSe NCs, respectively.[128,129] Abécassis and co-workers made a combined real-time SAXS/WAXS study on CdSe QDs, which gave a number of interesting novel elements for the understanding of their crystallization process (Figure 16).[130] In particular, while LaMer-type behavior was observed, the nucleation stage was longer than theoretically predicted (10 s vs 1 s) and the data suggested a relatively low energetic barrier for nucleation. The authors attributed the apparent lowering of the Gibbs free energy to (i) the decrease of the solid/liquid surface tension in the presence of surfactants/ligands; (ii) the low solubility of monomers in nonpolar organic solvents like 1-octadecene. The observed growth rate in these experiments was 8 orders of magnitude lower than the theoretically expected one for diffusion-limited growth, which confirmed that NC growth was limited by the precursor conversion kinetics.

3.3.3. Metal−Stabilizing Ligand Interactions. Stabilizing ligands have several crucial roles in NC synthesis: (i) in the complexation step they transform the starting chemicals into molecular precursors, which further evolve into "monomers"; (ii) they prevent from the uncontrolled aggregation of the monomers and nuclei formed in solution, but allow for NC growth at elevated temperature; (iii) they regulate the nucleation and growth kinetics, enabling the control of size and shape; (iv) they stabilize the NCs in colloidal form once the reaction is finished, providing sufficient repulsive forces of steric or electrostatic nature; (v) they passivate the coordination sphere of surface atoms, ideally preventing from the formation of deep trap states, which are detrimental for the luminescence properties. It is obvious that it is difficult to identify for a given synthesis one single molecule fulfilling all these requirements, and therefore in the majority of examples two or more ligands are applied simultaneously. For syntheses in organic solvents, stabilizing ligands are of surfactant type and consist of a polar headgroup (e.g., carboxylic or phosphonic acid, thiol, amine), which shows an affinity for the NC surface and one or several apolar/lipophilic moieties (e.g., alkyl chains). Co-ligands, which do not bind to the surface but influence the reaction mechanism, may also be applied. Furthermore, the solvent can play the role of ligand, and therefore act as a coordinating solvent. Trioctylphosphine oxide is certainly the most well-known representative of this kind,[95] although other examples exist, such as oleylamine[131] or dioctylether.[132] In aqueous syntheses, the lipophilic moiety is replaced by a lipophobic/hydrophilic one (e.g., carboxylate, amino, etc.), generally separated from the surface anchoring function by a hydrocarbon spacer.

When designing the synthesis method, the appreciation of the ligand interaction with the precursors and with the NC surface is fundamental. In our case, we are mainly interested in the interaction of ligands with metal ions and with pnictogen or chalcogen atoms. (The coordination chemistry of carbon, silicon and germanium differs significantly from that of the compound semiconductor NCs and will be discussed directly in the relevant part of section 4.) Pearson's concept of hard and soft acids and bases (HSAB) is widely used for explaining the observed trends.[133] It classifies Lewis acids, i.e. electrophilic atoms or groups (e.g., metal atoms), according to their polarizability: a small size and high positive charge results in "hard" acids of low polarizability, while "soft" acids are characterized by large size and/or low or zero oxidation state. The same concept can be applied to neutral Lewis bases (e.g., amines, phosphines, and so on). However, in the case of ionic bases a strong solvent dependence of their binding strength has to be considered. With this classification at hand (cf. Figure 17), the Pearson principle can be simply summarized as follows: hard acids prefer to associate with hard bases, soft acids prefer soft bases, just like in the expression birds of a feather flock together. This concept is particularly useful for predicting ligand affinities for metal ions in the design of synthesis methods and ligand exchange reactions. As already stated in the original work,[133] polarizability may only be one property among others characterizing the reactivity and binding of Lewis acids and bases. The fractional ionic/covalent character of (σ-)binding, π-bonding contributions and solvation effects are expected to add to the observed behavior and the relative
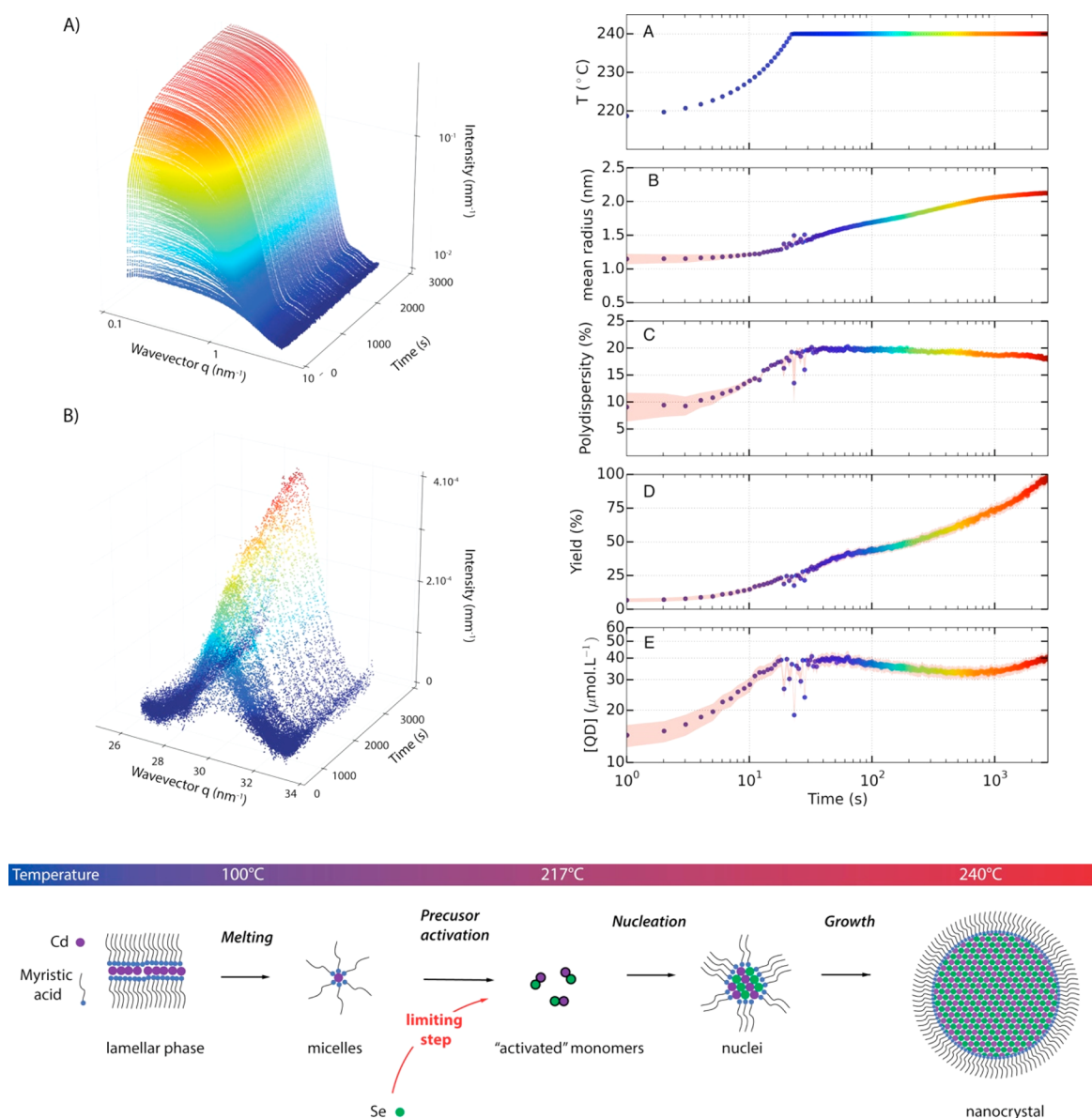
Figure 16. Synchrotron in situ SAXS/WAXS study of the formation of CdSe NCs. Top left: Time series of SAXS (A) and WAXS (B) patterns. Top right: Temporal evolution of the imposed temperature and of different characteristic parameters obtained from Monte Carlo fitting of the X-ray data. Bottom: Scheme summarizing the different steps of QD formation. Reproduced with permission from ref 130. Copyright 2015 American Chemical Society.

contributions of these different effects depend on the system under study. Solvents may equally be classified as hard or soft.[133] The former ("hard"), e.g., water, HF and hydroxylic solvents, strongly solvates hard bases, such as OH- or other oxygen anions as well as fluoride. Polar aprotic solvents ("soft") like dimethyl sulfoxide or dimethylformamide preferentially solvate soft bases/large anions. Neutral solutes are affected to a lesser extent.

Despite the usefulness of the HSAB principle for guiding the choice of ligand combinations in the synthesis of NCs of a desired material, it does however not describe the actual nature of the surface–ligand interaction and the change it induces to the electronic structure of the NC. Recent combined theoretical and experimental studies aim at the understanding of the NC surface at an atomic level, but are far from being generalized due to the large demand of computation resources.[134] While in initial syntheses the interaction of the NC surface with organic

ligands was generally described as a dative bond between a neutral electron donor (Lewis base) with the metal atom, e.g. in the case of TOPO molecules bound to cadmium surface atoms in CdE (E = S, Se, and Te).[95] In the meantime it has been demonstrated and recognized that also neutral acceptors, bound ion pairs and ionic species can act as surface ligands. In this context, the covalent bond classification method proposed by Green,[135] whose application is promoted by Owen and others in the field of QDs, is very useful for classifying ligands and describing their exchange reactions on NC surfaces (Figure 18).

3.3.4. Progress in the Understanding of the Surface State and Reaction Mechanism. Understanding the chemical transformations of all ingredients of the reaction medium (precursors, stabilizing ligands, additives, solvent(s)) at any stage of the reaction is an important step enabling the optimization of synthesis methods and the development of new

Figure 17. Classification of Lewis acids and bases relevant in NC synthesis according to the Pearson HSAB principle.

ones. Furthermore, in many cases the fortuitous discovery of secondary products or of "impurities" and the identification of their role in the reaction mechanism has led to breakthroughs in the synthesis of semiconductor NCs and to paradigm shifts. To give an example, the identification and intentional use of the impurities contained in 90% and even in 99% purity trioctylphosphine oxide (TOPO), widely used as a coordinating solvent, has led to novel synthetic schemes for a large variety of spherical and of anisotropically shaped metal chalcogenide NCs.[124,137−141]

NMR and FTIR spectroscopic techniques are methods of choice for investigating the chemical transformations of the organic compounds involved in NC synthesis. These techniques are also extremely useful for the in-depth characterization of the surface state of the obtained NCs. The organic ligand shell governs their physicochemical properties (colloidal stability in a given solvent, reactivity) and, through the passivation of surface electronic states, influences their optoelectronic properties. As highlighted by Hens and Martins, advanced proton and carbon NMR studies (e.g., DOSY, NOESY) allow for the identification of ligand dynamics at the NC surface, distinguishing bound from free ligands, and for analyzing binding strengths of competitive ligands.[142] These

techniques are of course also routinely used for the determination of ligand exchange yields. In this context, Owen and co-workers made a significant contribution by putting into evidence that carboxylate terminated metal chalcogenide NCs (ME, with M = Cd, Pb and E = S, Se) are subject of metal carboxylate complex displacement when exposed to various Lewis bases such as alkylamines or phosphines.[143] Their results indicate that the Lewis bases cooperatively complex the displaced metal ion as well as the NC. The process is accompanied by a strong decrease of the fluorescence QY, which is reversible upon rebinding of metal oleate. Using the Green formalism[135] this can be described as L-type donors displacing reversibly Z-type carboxylate ligands, which leads to variations in the NC stoichiometry for a given core size. Another accurate way for quantifying the ligand coverage of QDs has been proposed by Knittel et al., who used tritium-labeled oleic acid and scintillation counting.[144] One result of this study was the assessment of the strength of various competing ligands with regard to their ability for displacing oleic acid from the QD surface. These ligands are added in controlled excess to the NCs covered with tritiated oleic acid, and scintillation counting is used for measuring the decrease of the radioactivity borne by the QDs. As shown in Figure 19, also L-type ligands (neutral donors) replace X-type oleate ligands, though to a lesser extent than oleic or stearic acid, which undergo fast exchange.

In terms of mechanistic understanding, analysis of the ^1H, ^{13}C, and ^{31}P NMR spectra gave access to the molecular mechanism of precursor evolution in the synthesis of Zn- and Cd-chalcogenide NCs.[139,145−147] The obtained knowledge from such experiments about reaction pathways and rate limiting steps is obviously extremely valuable for the fine-tuning and development of synthesis methods. For the moment, the large majority of studies have focused on metal chalcogenide NCs, in particular on CdSe and to a lesser extent on PbSe.

3.3.5. When Synthesis Is Over: Purification—An Often Neglected Step. High quality NCs are generally synthesized in organic media in the presence of ambipolar organic ligands or surfactants containing long hydrocarbon tails and polar headgroup.[148] During the synthesis ligands have various roles including solubilization of the precursor, controlling of size and size dispersion and the shape. Post synthesis, these ligands provide the NCs colloidal stability and functionality. However, excess of ligand is usually not desirable for the subsequent use
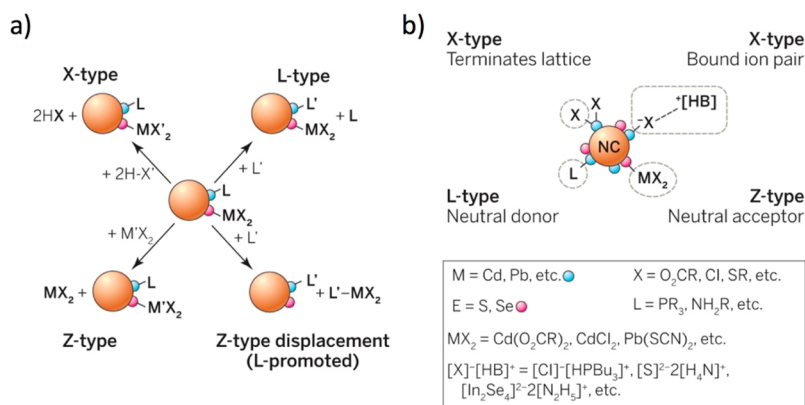

Figure 18. (a) Example of ligand exchange reactions on NCs. (b) Coordination of different types of ligands to metal chalcogenide NCs. Reproduced with permission from ref 136. Copyright 2015 American Association for the Advancement of Science (AAAS).
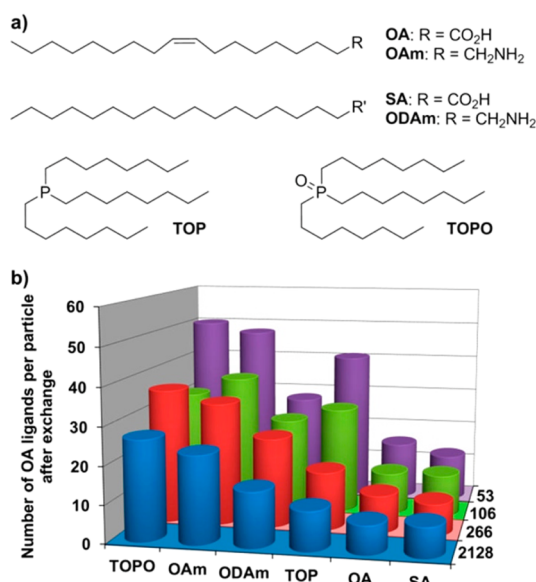
a)

b)

Figure 19. Displacement strength of various ligands with respect to the initial capping ligand, tritium-labeled oleate, on the surface of CdSe QDs. (a) Chemical structures of the competing ligands; (b) number of remaining labeled oleate ligands per NC after exchange with an excess of 53 (purple), 106 (green), 266 (red), or 2128 (blue) competing ligands per nm^2 of QD surface. Reproduced with permission from ref 144. Copyright 2013 American Chemical Society.

of the NCs as the ligands unpredictably affect the chemical composition of the surface,[149] the optical and electrical properties,[150−154] functionalities[155−157] and processability of these NCs.[158,159] Therefore, a purification step invariably follows the synthesis of colloidal quantum dots. The most commonly employed purification technique is based on centrifugation. Typically, an excess amount of a polar nonsolvent such as methanol, ethanol, acetone, acetonitrile etc. is added to the colloidal quantum dots dispersed in organics. The nonsolvent precipitates the sterically stabilized NCs and upon centrifugation they form pellets at the bottom of the tube while free ligands remain in the solution. By discarding the supernatant unbound free ligands could be removed. This method has been largely successful in removing excess ligands, remaining precursors and secondary reaction products. However, the efficiency of this procedure strictly depends on the solubility of the free ligands or other impurities in the mixture of solvent/nonsolvent. As it has been found in the case of InAs NCs, the usual purification process cannot remove the excess Indium precursor effectively.[160] Another drawback of this purification technique is that controlling the surface ligand coverage and surface properties are rather difficult.[149,151] The decrease of dispersibility of NCs in apolar organic solvents with an increasing number of purification cycles is widely observed, but a more quantitative description of this phenomenon has not been achieved until recently. Hens and co-workers demonstrated that short chain alcohols like methanol and ethanol, which are widely used for purification, can induce the release of X-type ligands like alkylcarboxylates (oleate ligands) from the NC surface.[161] This is accompanied by a decrease of the fluorescence QY due to the formation of surface trap states. On the opposite, acetonitrile used as the nonsolvent did not show this behavior, indicating that the protic character of the alcohols is at the origin. To avoid protonation and desorption of the carboxylate ligand, the authors advised the use of aprotic

solvents for NC purification. Shakeri and Meulenberg investigated the influence of the choice of the nonsolvent (methanol or ethanol) and number of washing cycles on the surface state of CdSe NCs, which were initially capped with a mixture of stearic acid and TOPO.[162] They found that L-type TOPO ligands are removed in the first purification steps, while the removal of stearate ligands reaches a plateau, resulting in QDs with very low organic mass fraction (13%) while still stable in colloidal form. Pansu et al. showed by means of NMR and time-resolved PL studies that in the case of a ligand shell composed of oleylamine, stearic acid and TOP (in average 144, 93, and 13 molecules per NC), even simple dilution with toluene can have dramatic consequences on the PL decay behavior.[163] This has been rationalized by the generation of 3 quenching sites per NC on average caused by the removal of TOP. While the above examples deal with CdSe and PbSe NCs, it is evident that the influence of purification processes on the surface state and optical properties has also to be taken account for in the case of the nontoxic NCs in the focus of this article.

Alternatively, purification techniques based on chromatography and electrophoresis,[159,164−166] allow a more precise control over surface ligand coverage. However, the challenge with chromatographic or electrophoretic separation is to find a suitable stationary phase compatible with the quantum dots in a nonpolar solvent. Recently, Shen et al. have successfully demonstrated purification of colloidal quantum dots from hydrophobic solvents using gel permeable chromatography with polystyrene as stationary phase.[159]

4. SYNTHESIS OF DIFFERENT FAMILIES OF SEMICONDUCTOR NANOCRYSTALS

This section first reviews the progress in the development of synthesis methods for the group IV elemental semiconductor NCs Si and Ge, carbon nanodots are also briefly discussed. Due to their peculiar bonding and coordination chemistry, their synthesis methods differ significantly from the subsequently discussed compound semiconductors. They crystallize in the diamond cubic structure with lattice parameters of 5.43 Å (Si) and 5.66 Å (Ge), showing tetrahedral bonding. The binary compound semiconductors covered in the following subsection of this review are composed of a main group or transition metal and a pnictogen (N, P, As, and Sb) or a chalcogen (S, Se, and Te). Most of them crystallize either in the cubic zinc blende (ZB) or in the hexagonal wurtzite (W) structure. Both are four-coordinate and vary in the layer stacking along (111), showing an ABCABC or an ABAB sequence, respectively (Figure 20).

The room temperature ground state structures and lattice parameters of a number of binary semiconductors are given in
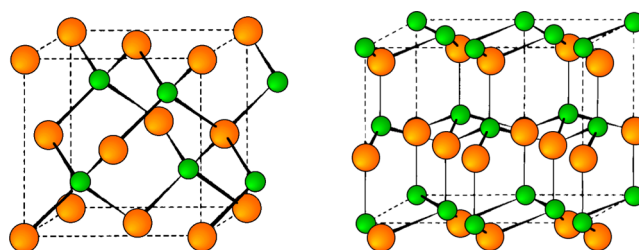

Figure 20. Zinc blende (left) and wurtzite (right) crystal structures realized by most of the binary semiconductors. The diamond cubic structure is identical with zinc blende, but with equal atoms on each site (e.g., Si and Ge).

Table 1. The presented synthesis methods are classified according to the applied pnictogen or chalcogen precursor. As mentioned before, the relatively restricted libraries of currently explored anionic precursors are a bottleneck in NC synthesis. Finally, an overview of the strongly expanding family of ternary and multinary metal chalcogenide NCs is given. Their structural properties are directly discussed in section 4.3.

4.1. Elemental Group IV Semiconductors

4.1.1. Introduction. Colloidal NCs of the group IV elemental semiconductors silicon and germanium have been studied to a much less extent than compound semiconductors. In the case of silicon, this stands out against the ubiquitous use of this material in modern electronics and the fact that it is with 27% the second most abundant element in the earth crust after oxygen. Furthermore, several studies indicate the nontoxicity and biodegradability of Si nanoparticles.[94,167] Both materials have a narrow, indirect band gap of 1.12 eV (Si) and 0.66 eV (Ge) and crystallize in diamond cubic structure with lattice parameters of 5.43 Å (Si) and 5.66 Å (Ge), showing tetrahedral bonding.[168] As indirect semiconductors, they are poor light emitters in the bulk; however, on the nanoscale efficient emission has been observed. In particular, the seminal work of Canham in 1993 on porous silicon, demonstrating intense and blue-shifted emission, stimulated considerable research activity.[169] One of the biggest differences with respect to the more widely studied compound semiconductors is the covalent nature of binding in Si and Ge requiring high temperatures to form crystalline nuclei.[115] The bond dissociation energies are 327 and 274 kJ/mol, respectively, and both elements form stable amorphous phases. In addition they have a strong propensity toward binding with oxygen with dissociation energies of 798 kJ/mol (Si − O) and 662 kJ/mol (Ge − O). These factors combined with marked differences in surface ligand chemistry with respect to compound semiconductor NCs make the chemical synthesis of Si and Ge NCs challenging. As by definition the oxidation state of the atoms composing elemental semiconductor NCs is zero, their synthesis methods are more similar to those of metal nanoparticles than those used for compound semiconductor NCs. As an example, one of the main ways to synthesize them is via reduction of their halides. Despite all aforementioned problems in recent years, significant progress has been made. Nowadays the research is not only focused on the design and optimization of synthetic methods, but continuous efforts are being made also toward the understanding of the optical and electronic properties of the NCs. Triggered by Canham's work,[169] a huge number of studies have demonstrated the complex mechanisms underlying the photoluminescence of Si NCs. They put into evidence the dependency on several parameters such as size effects,[170−172] surface effects,[173,174] and defect states.[175,176] The observed emission wavelength of Si NCs prepared by solution routes covers the spectral region from blue[177,178] to the near IR.[170,177,179−181] Kovalev and co-workers reviewed the optical properties of Si NCs and concluded that their bright and tunable photoluminescence arises from exciton confinement with the confinement energy exceeding 1 eV for small particles.[182] However, even nanometer-size crystals do not become a direct semiconductor. The theoretical framework has been elaborated by Delerue and co-workers who investigated the size-dependent properties of both Si and Ge NCs (Figure 21).[183,184]
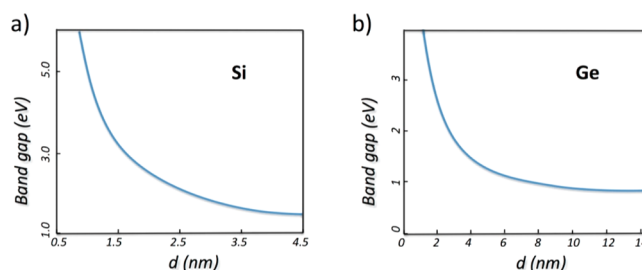
Figure 21. Calculated optical band gap energies vs diameter d (a) Si NCs, using the linear combination of atomic orbitals (LCAO) approach (data from ref 183). The band gap follows approximately a $d^{-1.39}$ law. The effective mass approximation predicts an exponent of 2, which is only reached for large diameters. (b) Ge NCs, using the tight binding approach (data from ref 184).

On the experimental side, as most synthesis methods yield Si NCs of relatively broad size distribution, the analysis of size-dependent effects is hampered and the characteristic features are averaged. Therefore, postsynthetic size selection procedures have been applied to separate the initial sample into fractions of narrow size distribution, namely size-selective precipitation[185] and density gradient ultracentrifugation (Figure 22).[186] As one
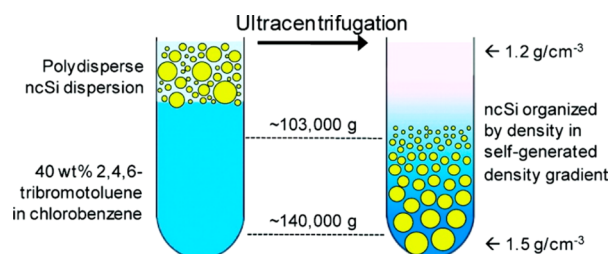
Figure 22. Principle of density gradient ultracentrifugation for the separation of a polydisperse sample of Si NCs into sharp size fractions. Reproduced with permission from ref 186. Copyright 2011 American Chemical Society.

example of the importance of size fractionation, Ozin and co-workers were able to show that the PL QY and the lifetime monotonically decreased with decreasing Si NC size in a range of 1−5 nm, indicating that in their case nonradiative surface defects and vibrational effects dominate over spatial confinement effects favoring radiative recombination.[187] The same group also reported size-dependent oxidation of Si NCs after their size fractionation using size-selective precipitation.[185] Due to the higher surface-to-volume ratio and surface curvature, which induces a less dense packing of organic surface capping groups, the smaller NCs (around 1.5 nm) were more prone to surface oxidation and its associated loss of PL QY.

4.1.2. Carbon Nanodots. Strictly speaking, NCs of carbon are not in the scope of this article, as this element, in its bulk form, is not a semiconductor. Its well-known allotrope diamond shows tetrahedral coordination and sp3 hybridization of the C atoms. Diamond is an electrical insulator with a band gap of approximately 5.5 eV. Even though bright visible light emission can be observed in the case of nanometer-sized diamond crystals (nanodiamonds), this effect is not the consequence of a reduction of band gap or quantum size effects, but arises from color centers in the crystal structure, formed for example by nitrogen atoms close to a vacancy in the lattice (N−V center).[188] The second allotrope of carbon, graphite, has a layered structure of sp2 hybridized C atoms arranged in a
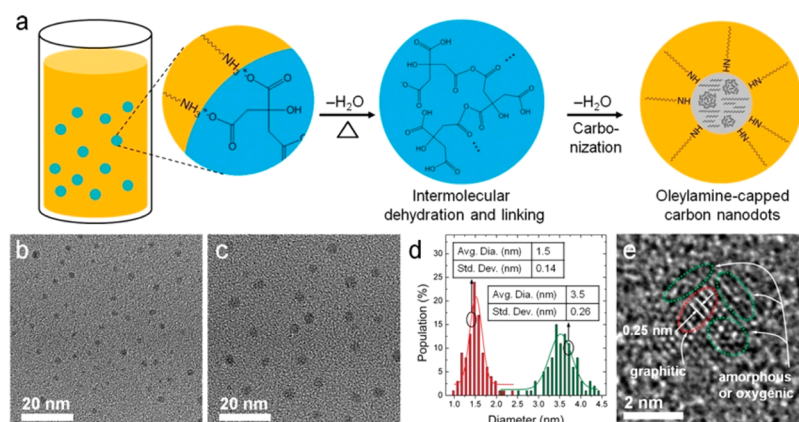
Figure 23. (a) Synthesis scheme for carbon nanodots using a microemulsion technique. (b–d) TEM analysis of the obtained particles. (e) High-resolution image indicating graphitic clusters distributed in an amorphous matrix, probably containing oxygenated species like carbonyl or carboxyl groups. Reproduced with permission from ref 204. Copyright 2013 Wiley-VCH Verlag GmbH & Co. KGaA.

honeycomb lattice and is an electrical conductor. A new era started with the discovery of the new allotrope fullerene in 1985,[189] which triggered an unprecedented research interest in carbon nanostructures based on the graphitic motive. These have turned out to exhibit many unique and unexpected properties. Fullerenes as the first representative are closed cage structures consisting of three-coordinated carbon atoms in sp^2 hybridization, just as in graphite, however arranged in both hexagonal and pentagonal rings. Buckminsterfullerene C_{60} exhibits a band gap of 1.86 eV and its bigger brother "rugbyballene" C_{70} of 1.56 eV.[190] Just a few years later, multiwall (1991)[191] and single-walled (1993)[192,193] carbon nanotubes (CNTs) have been reported, representing a further novel allotropes of carbon. CNTs consist of a single graphitic sheet folded resulting in a cylindrical nanostructure. They can be metallic or semiconducting depending on the diameter and helicity of the graphitic rings.[194] More recently, a flat single graphitic sheet, much better known now as graphene, has been isolated in 2003.[195] Graphene is an extremely good conductor with electron mobilities as high as 15 000 cm^2 V^{-1} s^{-1}. It exhibits a particular band structure where the conduction and valence band meet at six Dirac points, making it a zero band gap semiconductor. On the other hand, the opening of a band gap can be achieved by controlled hydrogen adsorption[196] or by using appropriate substrates for the growth.[197] As excitons in graphene have an infinite Bohr radius, fragments of any size show quantum confinement effects. Experimentally, several methods for cutting fragments of graphene have been developed, giving access to nanostructures of various sizes and shapes called graphene quantum dots (GQDs).[198] They can show strong luminescence with reported QYs up to 28% with the emission peak centered at 360 nm for GQDs of 13 nm average diameter.[199] Surface and/or edge states are involved in the PL mechanism, as the band gap energies of GQDs with diameters exceeding 5 nm have been calculated to be not higher than 1.0 eV.[200] GQDs constitute one example of the larger family of 0D carbon nanostructures, which comprises also carbon nanodots (C-dots) and polymer dots (PDs).[201] PDs have been the least investigated so far and are prepared by dehydration, condensation, carbonization or assembly routes from conventional, i.e., nonconjugated polymers.[201] The enhancement of the PL properties in these systems has been attributed to the decreased vibrational and rotational freedom of organic chromophores in the aggregated state within the

nanometers sized dots, a phenomenon termed cross-linked enhanced emission (CEE).[202] C-dots, finally, are the type of carbon nanostructures coming most closely to the other types of semiconductor NCs in the scope of this review. They are characterized by strong luminescence properties, biocompatibility, and chemical and photostability and can be prepared from a surprisingly large variety of resources from every-day life such as ground coffee, boiled tea, candle soot, and grass.[203] Their size is usually below 10 nm and recent studies indicate that they possess a complex structure composed of graphitic domains in amorphous carbon as well as oxygenated species like carbonyl and carboxyl groups (Figure 23).[204] Many synthesis methods are top-down approaches like arc-discharge,[205] laser ablation,[206] electrochemical or combustion routes,[207] and will not be discussed here. Solution synthesis is mainly carried out in aqueous solvents, for example by means of dehydratation of carbohydrates like glucose, fructose, starch and so on using concentrated mineral acids (e.g., sulfuric or nitric acid).[208] Eventually stabilizers like poly(ethylene) glycols can be added before or after the reaction and the acid treatment can be assisted by ultrasound treatment[209] or replaced by microwave heating[210,211] for triggering the formation of the C-dots. One rare example of synthesis in organic solvent has been proposed by Kwon et al., who used nanometer-sized water droplets in a microemulsion containing of 1-octadecene and oleylamine as reactors for C-dot formation.[204] Cytric acid was solubilized in these droplets, which were subsequently dehydrated by heating at 250 °C. The size of the obtained C-dots could be tuned by varying the amount of oleylamine used in the reaction. After exchange of the oleylamine surface ligands with aromatic amines PL QYs up to 40–60% have been obtained in the blue region (400–500 nm), however, with a broad emission line width and a dependence of the PL with the excitation wavelength.

The detailed understanding of the emission mechanisms in C-dots is subject of current research and debate. Nonetheless, ten years after their discovery[212] a common consensus has been found concerning several distinct contributions to their luminescence, whose relative weights depend on the structure and surface state of the investigated sample.[201,203] First, the blue emission (around 450 nm) is attributed to intrinsic quantum confined states, which are related to the dimensions of the sp^2 hybridized (graphitic) domains in the core of the C-dots, with a characteristic decay time of 5 ns.[213] Second, the

emissions at longer wavelengths, mostly observed in the green range, are ascribed to extrinsic states involving in particular carbon−oxygen species like carbonyl or carboxyl groups with longer characteristic decay times of 5−10 ns.[213] This feature is common to C-dots and GQDs and the mentioned common origin of the green luminescence observed in both cases has been unraveled by Wang et al. using ultrafast transient absorption spectroscopy.[214] An intriguing feature is the marked dependence of the PL signal position and intensity on the excitation wavelength. This can be seen in Figure 24 showing
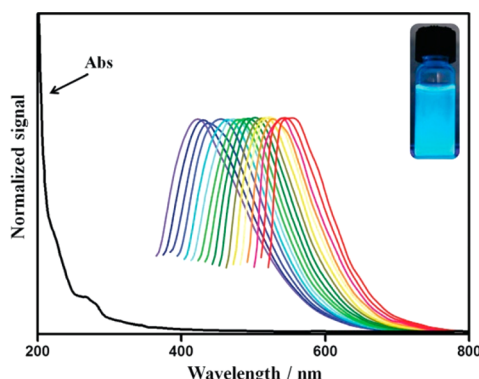

Figure 24. Absorption and normalized PL spectra of C-dots, using increasingly longer excitation wavelengths starting with 350 nm in 15 nm increments. Inset: colloidal solution of C-dots under UV light. Reproduced with permission from ref 215. Copyright 2012 Royal Society of Chemistry.

the absorption and PL emission spectra of 5 ± 2 nm C-dots prepared by calcination of coffee grounds at 300 °C in air, followed by extraction with ethanol.[215] The excitation wavelength dependence of PL is usually attributed to the size distribution of the C-dots and/or to the distribution of emissive trap states.[212]

4.1.3. Synthesis of Si and Ge NCs. Most solution synthesis routes have been developed in parallel for both silicon and germanium NCs. At a first glance both elements share some similarities such as the diamond cubic crystal structure and covalent nature of bonding. However, within column IVA (14) of the periodic table of elements the chemical reactivity of germanium resembles more to that of carbon than that of silicon, as can be seen in the reduction behavior of the halogenides, the hydrolysis of tetrahydrides, and the reaction of Ph_3EH (E = C, Si, or Ge) with organolithium compounds. As mentioned above, a large research interest has been devoted to the study of silicon NCs with the goal of exploiting their luminescence properties. Their appealing features of natural abundance, nontoxicity and chemical inertness place them very well for a range of potential applications. To give some examples, Si NCs have been proposed for use in biological imaging, LEDs, photodetectors as well as in form of electrode material in energy storage devices.[170,176,177,180] Veinot (2006) and later Tilley (2014) and co-workers reviewed the chemical synthesis and the applications of silicon NCs.[176,216] Likewise, in 2013 Vaughn and Schaak published a comprehensive review on colloidal germanium, germanium chalcogenide NCs and other types of nanostructures.[217] In the following chapter, we will divide the reported methods into three main groups, namely the reduction of the group IV salts, mainly halides, which represents by far the most employed method, the metathesis reactions and finally the thermal decomposition of organo-

silanes or -germanes. For each method, first the reports on Si NCs and then those on Ge NCs will be discussed. Table 2 gives an overview of the applied methods and reaction conditions.

The reduction of Ge(IV) and Si(IV) halides is the most widely used approach for synthesizing NCs of these elements. In the case of germanium, also the use of Ge(II) precursors is becoming popular. These show a more positive reduction potential than the Ge(IV) precursors (+0.247 and +0.124 V vs SHE, respectively).[257] Therefore, Ge(II) precursors are more reactive and convert to Ge(0) under milder conditions (e.g., lower temperature) than Ge(IV) compounds. Analogous progress has not yet been reported with Si(II) compounds, due to their challenging preparation, low yield, low stability and hence difficulties to isolate them. Nonetheless recent advances in the synthesis of silylenes with high yield pave the way for the exploration of these systems.[258]

4.1.3.1. Reduction of Ge and Si Salts Initiated by Organoalkali or Alkali Metals. Only few reports concern the reduction of $SiCl_4$ by alkali metals, due to the harsh conditions (temperature and pressure), which have to be used to obtain crystallization of the particles. Heath reported the first wet-chemical route synthesis of silicon NCs in 1992.[224] $SiCl_4$ was mixed with RCl_3 (R = H or octyl) and sodium and stirred in a reactor under pressure (>100 atm) for 3 to 7 days at 385 °C. The obtained nanoparticles were extremely polydisperse (5 to thousands of nanometers) but showed good crystallinity as evidenced by TEM analysis. An FTIR study of the crystals was used to probe their surface state, revealing Si−H, Si−O and Si−Cl bonds. As the required conditions of pressure and temperature were uneasy to reach and to control during the reaction, the development of solution syntheses based on the reduction of silanes with alkali metals was not further pursued. In contrast, the same strategy turned out to be more promising for the synthesis of germanium nanoparticles, as already mentioned in Heath's work. Weller and co-workers first reported the room temperature reduction of $GeCl_4$ with lithium naphthalide ($C_{10}H_8Li$) in THF in 1993.[238] The reaction was terminated by addition of Me_3SiCl to the mixture, which reacts with excess naphthalide and passivates surface atoms. The obtained particles were amorphous and could be crystallized under laser illumination. Several reactions derived from this early work, aiming at directly obtaining crystalline particles. Kauzlarich and co-workers used sodium naphthalide and butyl-Grignard ($nBuMgCl$) to terminate the reaction.[241] The obtained alkyl-capped particles were crystalline as demonstrated by electron diffraction with an average size of 4.5 nm and relatively large polydispersity. The organic polymeric side product generated in this reaction could be removed by heating the oily reaction product to 300 °C under vacuum. This heating step resulted also in a reduction of the size distribution affording a mean size of 5.1 nm, albeit yielding particles in the amorphous state. Further heating to 500−600 °C induced a reverse amorphous−crystalline transition accompanied by particle ripening to 7.6 nm and broadening of the size distribution. Melting of the Ge NCs was observed at 925 °C. Lee and co-workers used a similar approach for their synthesis, and obtained amorphous butyl-capped Ge NCs of 10 nm average size by reacting $GeCl_4$ with Na naphthalide in diglyme.[231] In this work, the butyl ligands were coming from $nBuLi$, injected into the mixture to catalyze the reaction. No recrystallization steps were attempted and the obtained particles were explored as anode materials for Li-ion secondary batteries. Heath and co-workers used the same type of reaction

Table 2. Representative Overview of the Solution-Phase Synthesis Methods for Si and Ge NCs[a]

			Si nanoparticles				
			synthesis conditions				
refs	method	Si precursor	other reagents	ligands	solvent(s)	temp. (°C)	size (nm)
174,179,218,219	reduction	$SiCl_4$	$LiAlH_4$, (TOAB)	heptane	toluene, hexane	RT	1.8
				allylamine	water		1−10
171	reduction	$SiCl_4$	$LiAlH_4$	H	octane, decane	RT	1.8−10
220	reduction	$SiCl_4$	$LiAlH_4$, C12E5	alkyl, amines	hexane	RT	1.6
			$LiBH(Et)_3$, C12E5				1.8
			$LiBH_4$, $C1_2E5$				2.2
			NaBH4, $C1_2E5$				2.5
221	reduction	SiCl4	$LiAlH_4$, TOAB	dodecyl, tetradecyl, hexadecyl	toluene	RT	1.8
222	reduction	SiBr4	TOAB, $C1_2E5$	allylamine, hexadiene	hexane, toluene	RT	3.7
180	reduction	APTMS	trisodium citrate dihydrate	"hydrophilic amino groups"	water	160	2.2
223	reduction	APTMS	1,8-naphthalimide	1,8-naphthalimide	water	RT	2.3
224	reduction	$SiCl_4$, $HSiCl_3$, octyl-$SiCl_3$	Na	octyl	toluene	385	5−3000
173	sol−gel	Allyl-$SiCl_3$, $SiCl_4$	$LiAlH_4$	alkane-thiols	toluene	RT	3.7
172	sol−gel	HSQ	HF, HCl	dodecene, ODE		1100−1400	3.1−12.8
225	sol−gel	$HSiCl_3$	HF	H	water	1100−1400	4, 4.5
185	sol−gel	$HSiCl_3$	HF, allylphenylsulfide	allylphenylsulfide	toluene	1100	1−10
178	metathesis	$SiCl_4$	Mg2Si, glyme, MeLi	methyl	hexane	RT	3.2
				ethyl			3.1
				n-butyl			3.7
				n-octyl			4.4
226	decomposition	$Si(Ph)_2$	octanol	octanol	octanol	500	1.5
			octanol, Hexane		octanol, hexane		2.5−3.5
170,227	decomposition	SiH_4	HF, HNO3	PAAc	water	850	3−5
228	decomposition	SiH_4		H	EG	860	3−8
229	decomposition	SiH_4	HF, HNO_3	styrene, ODE, Ethyl undecylenate	chloroform	RT	4
175	decomposition	HSQ	HF	dodecyl		1100	3.5

			Ge nanoparticles				
			synthesis conditions				
refs	method	Ge precursor	other reagents	ligands	solvent(s)	temp. (°C)	size (nm)
230	reduction	$GeCl_4$	$LiAlH_4$	H	octane	RT	2−10
231	reduction	$GeCl_4$	Na naphtalide, n-BuLi	butyl	glyme	RT	10
232	reduction	GeCl4, n-butyl-$GeCl_3$	n-BuLi	butyl	hexane	RT	4
233	reduction	$GeCl_4$	$LiAlH_4$, THDAB	allylamine	toluene	RT	3−12
234	reduction	$GeCl_4$	$LiAlH_4$, TOAB	heptane	toluene	RT	3
			$LiBH(Et)_3$, TOAB				4.1
			$LiBH_4$, TOAB				4.7
			$Li(CH(CH_3)CH_2CH_3)_3BH$, TOAB				5.1, 11.7
		$GeBr_4$	$LiAlH_4$, TOAB				4
			$LiBH(Et)_3$, TOAB				4.5
			$LiBH_4$, TOAB				5.4
			$Li(CH(CH_3)CH_2CH_3)_3BH$, TOAB				11.4
235	reduction	$GeCl_4$	$LiAlH_4$, TBAB	allylamine	toluene	RT	3.5
			$LiAlH_4$, THAB				3.7
			$LiAlH_4$, TOAB				4.1
			$LiAlH_4$, TKAB				4.5
236	reduction	$GeCl_4$	$NaBH_4$, NaOH, HCl, PVP	PVP	water	60	3.8
			PVP, triglyme	PVP	EG	RT	3.9
237	reduction	$GeCl_4$	$NaBH_4$, triglyme	PVP	EG	RT	3.7
238	reduction	$GeCl_4$	Li naphtalide, CH_3(Si)	CH3(Si)	THF	60	2
239	reduction	GeO_2	$NaBH_4$, NaOH, HCl, PVP	PVP	water	60	3

Table 2. continued

			Ge nanoparticles				
			synthesis conditions				
refs	method	Ge precursor	other reagents	ligands	solvent(s)	temp. (°C)	size (nm)
240	reduction	GeO2	NaBH4, PVP, NaOH, HCl	PVP	water	80	3−7
241	reduction	GeCl4	Na naphtalide, n-BuMgCl	butyl	glyme	300	4−5
242	reduction	GeCl4, Ph-GeCl3	NaK	Cl	heptane	270	6, 10, 20
243	reduction	Ph3PC(CH3)2·GeH2·BH3	1-dodecene, diphenylether	1-dodecyl	1-dodecene, diphenylether	100−250	5.3 10.1
			3-dimethylamino-1-propyne	dimethylamine	3-dimethylamino-1-propyne		5.4
244	reduction	GeI4	OLA, OA, HMDS	OLA	OLA, OA	260	6, 12, 22
245	reduction	GeI2	OLA	OLA	OLA	300	4.8
246	reduction	GeBr2	OLA	OLA	OLA	260	10
247	reduction	GeI2	OLA	DDT	OLA	210	3.7, 5.4, 9.7
248	reduction	GeI2	OLA	OLA	OLA	210	2.9, 4.8, 5, 5.1
		GeI2, GeI4					3.5, 5.6, 10
249	reduction	GeI2, GeI4	OLA	DDT	OLA	210	3.9, 5.3, 7.5
250	reduction	GeI2, GeI4	n-BuLi	HDA, ODE	HDA, ODE	300	2.3−11.3
181	sol−gel	(C3H5)GeCl3		H		400	12
		(C7H7)GeCl3				450	11
		(Et)GeCl3				400	22
		(n-Bu)GeCl3				300	15
		(HOOCC2H4)GeCl3				350	12
251	sol−gel	Ph-GeCl3	IPA	oxides, hydroxides	water	525	5.5
252	metathesis	GeCl4	NaGe, KGe, Mg2Ge, alkyllithium, Grignard reagent	butyl, methyl, octyl	glyme	84	6.2−6.5
					diglyme	162	
					triglyme	216	
253	decomposition	Ge(Et)4	nonanoic acid	H, C	toluene, hexane	430	5−30
254	decomposition	Ge(Et)4	scCO2, octanol	octanol	scCO2, octanol	500	5.6
		Ge(Ph)2					10.1
255	decomposition	HGeCl3	TOA	TOA	TOA	385	1−2
		HGe(Bu)3	squalene	squalene	squalene	410	2−7
							4−15
256	decomposition	TOG	OLA, OA, TOA	OLA, OA, TOA	OLA, OA, TOA	360	5.2, 9.5, 20.4

[a]RT: room temperature (298 K), Me: Methyl, Et: Ethyl, Bu: Butyl, Ph: Phenyl, ODE: Octadecene, OLA: Oleylamine, TOA: Trioctylamine, HDA: Hexadecylamine, DDT: Dodecanethiol, OA: Oleic Acid, THF: Tetrahydrofuran, EG: Ethylene Glycol, IPA: Isopropyl Alcohol, Glyme: Dimethylglycol, Diglyme: Dimethyldiglycol, Triglyme: Dimethyltriglycol, C12E5: Pentaethylene glycol monododecyl ether, PAAc: Polyacrylic Acid, PVP: polyvinylpyrrolidone, THAB: tetrahexylammonium bromide, TOAB: Tetraoctyl ammonium bromide, THDAB: tetrahexadecylammonium bromide, TBAB: tetrabutylammonium bromide, TKAB: tetrakis(decyl)ammonium bromide, Li(CH(CH3)CH2CH3)3BH: Lithium tri-sec-butylborohydride, scCO2: supercritical CO2, APTMS: (3-Aminopropyl)trimethoxysilane, HSQ: Hydrogen Silsesquioxane, HMDS: Hexamethyldisilazane, TOG: tetra-cis-9-octadecenoic germanium

in 1994, but replaced the organoalkali compound by NaK, a liquid alloy made of sodium and potassium dispersed in heptane.[242] GeCl4 was mixed with PhGeCl3 and the NaK reducing agent and followed by ultrasonication which allowed the authors to reduce the reaction time to minutes. The obtained amorphous particles of 10 nm mean size were crystallized through annealing under pressure at 270 °C for 24 to 48h. Summarizing, all described reactions for the synthesis of Ge NCs through reduction of Ge halides by means of organoalkali compounds or alkali metals were conducted at room temperature, but further thermal and chemical treatments were necessary to crystallize the nanoparticles and passivate their surface.

No annealing step was required in a method reported by Carolan and Doyle:[232] GeCl4 was added to butyl trichlorogermane (nBuGeCl3) in hexane. The reduction of both reagents was achieved by injecting dropwise n-butyllithium to

the mixture and the excess of reducing agent was quenched by addition of methanol, affording Ge nanoparticles with a size of 3.9 ± 0.5 nm. One particular interest of this procedure among others is that it directly produces Ge NCs of low polydispersity and good crystallinity. Furthermore, a high PL QY of 37% has been observed; the PL decay was characterized by two lifetime components of 2.5 and 9.1 ns. The emission peak maximum showed several spectral contributions and a marked dependence on the excitation wavelength (Figure 25), arising from the size distribution and/or from surface states involved in the luminescence mechanism.

Veinot et al. recently reported a method based on the reduction of the germanium dihydride (Wittig reagent) adduct, compound 1 in Figure 26,[243] precedently isolated by Rivard and co-workers.[259,260] The hot injection method (HI) is compared to microwave irradiations of the reagent after optimization of the reaction temperature and precursor
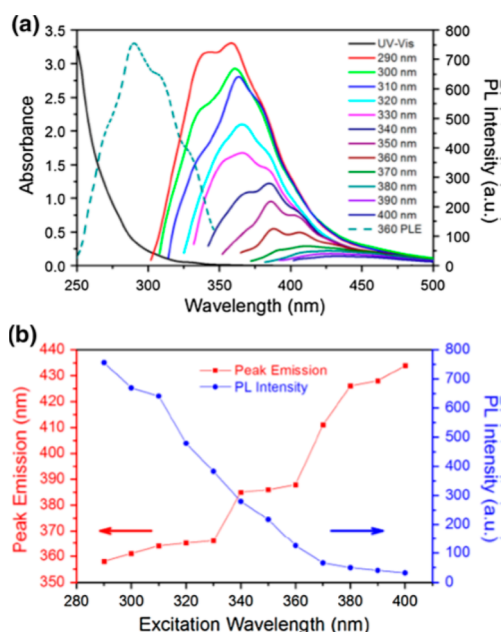
Figure 25. (a) UV−vis, PL and PLE spectra of 3.9 nm Ge NCs in chloroform. (b) PL peak maximum (red squares) and intensity (blue circles) versus excitation wavelength. Reproduced with permission from ref 232. Copyright 2014 Springer Science+Business Media Dordrecht 2014.

concentration. The obtained roughly spherical particles are crystalline and show low polydispersity with diameters of 10 ± 1.5 nm for the HI method and 5 ± 1 nm for the microwave irradiation method. Hydrophobic particles were obtained by reaction of the Ge precursor with 1-dodecene and diphenylether while the reaction with 3-dimethylamino-1-propyne yielded hydrophilic particles.

4.1.3.2. Reduction Initiated by Hydrides. Wilcoxon et al. proposed in 1999 a synthetic route for silicon NCs[171] and a very similar approach for germanium, which will be described later.[261] Silicon tetrachloride was reduced by LiAlH$_4$ within inverse micelles formed by nonionic aliphatic polyethers or cationic quaternary ammonium salts (surfactants) in octane (continuous phase). It is worth emphasizing that in contrast to other works describing NC synthesis in reverse micelles (water droplets in oil), which have been in particular conducted in the initial discovery stages of this field,[262,263] the present system is characterized by the complete absence of water. Anhydrous compounds are required to avoid hydrolysis of the Si precursor into SiO$_2$. The latter is completely insoluble in organic solvents such as octane or decane, and therefore the reaction takes place inside the reverse micelle formed by the surfactant, which acts as a microreactor confining the size of the obtained particles in a range of 1.8 to 10 nm depending on the conditions. Room temperature PL emission in the range of 350 to 700 nm has been observed with a maximum QY of 4%. The discussion of the emission peak positions and their correlation with NC size was once again complicated by the potential overlap of optical transitions, inherent to the particle volume, which are expected to be modified by quantum confinement effects, and transitions involving surface states. It has to be noted that the authors pointed out later in an erratum serious safety issues with the described reaction, as it produces highly toxic and pyrophoric silane (SiH$_4$) gas.[264] Tilley and co-workers further explored the microemulsion method using reducing agents of variable

strength.[179,220,265] In order to increase M-H bond lability and hence reducing strength, sodium borohydride (NaBH$_4$), lithium borohydride (LiBH$_4$), superhydride (LiBHEt$_3$), and lithium aluminum hydride (LiAlH$_4$) have been compared, while keeping the other synthetic conditions identical. The stronger the hydride, the smaller and the less polydisperse the obtained Si nanoparticles; the size range was 1.6 to 2.5 nm. In accordance with these findings, lithium aluminum hydride is the most widely used reducing agent in the microemulsion synthesis of Si NCs. In the final step, the hydrogen-terminated particles were capped with amine groups using hexachloroplatinic acid as a catalyst and UV irradiation to diminish the reaction time of grafting. Although being substantially smaller than the exciton Bohr radius of 4−5 nm,[266] again no pronounced size-dependent optical properties have been seen: the PL peak position just shifted by 5 nm from 347 to 352 nm when exciting the 1.6 and 2.5 nm Si NCs at 325 nm (Figure 27). Also, a marked red-shift of the PL signal with increasing excitation wavelength was noted, which indicates surface states to be involved in the emission process, similar as in the reports cited above. The size distribution is another factor, which can contribute to this behavior.

A modified version of Tilley's method[265] has been developed by Zuilhof and co-workers who used sonication at all reaction steps.[221] The size distribution of the NCs remained narrow (1.57 ± 0.21 nm), and as a major advantage this method allowed synthesizing quasi-gram quantities of crystalline silicon NCs (Figure 28). This represents approximately a 100-fold increase compared to the above-cited microemulsion methods.

Another variant of the microemulsion method has been proposed by Cheng et al., who used allyltrichlorosilanes in addition to SiCl$_4$ within a sonication-assisted reaction (Figure 29).[173] The allyltrichlorosilanes acted as both secondary Si source and surfactant/capping ligand. The obtained alkene-capped NCs were then reacted with various functional ligands via the versatile, efficient and specific thiol−ene click chemistry, upon 254 nm UV-light illumination. Terminal amine, carboxylate, and sulfonate groups as well as alkyl chains were successfully introduced in this manner.

The optical properties of the as-synthesized particles remain very similar to the ones described before with an absorption onset below 400 nm, and an emission peak at 375 nm with a fwhm of 70 nm. The observed spectral shifts upon surface functionalization were attributed to the differences in the electron donating or withdrawing character of the involved groups, which may lead to a change of the energy levels of the quantum confined states within the Si QDs. The influence of the differing dielectric environment of the nanoparticles, which are surrounded by functional groups and solvents of various polarity, is another possible origin of the observed behavior.[267] Apart from microemulsion syntheses based on Si halides, Zhong et al. proposed two methods for the reduction of (3-aminopropyl)trimethoxysilane (APTMS). In the first method, trisodium citrate dihydrate was used as the reducing agent in aqueous solution under microwave heating at 160 °C, yielding 0.1 g of 2.2 nm Si nanoparticles, which showed blue luminescence (QY: 20−25%).[180] More recently the same group reported a mild photochemical reduction method, resulting in large amounts (10 g) of fluorescent Si NCs (QY: 25%) with tunable emission in the 470−560 nm range.[223] In this case APTMS was mixed with 1,8-naphthalimide in aqueous solution and submitted to UV irradiation at 365 nm for different reaction times (15−40 min). In the proposed reaction
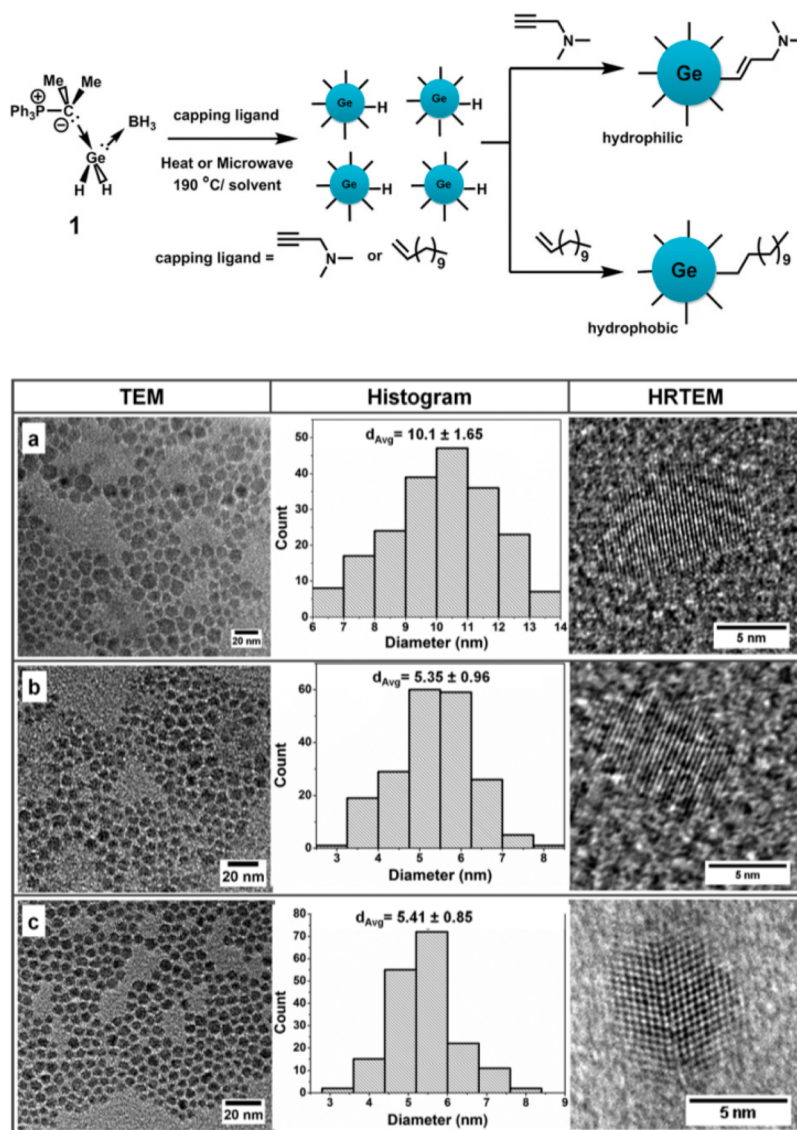
Figure 26. Top: Synthetic pathway leading to hydrophilic or hydrophobic germanium nanoparticles by thermal decomposition of $Ph_3PCMe_2 \cdot GeH_2 \cdot BH_3$ in the presence of appropriate capping agents. Bottom: TEM images and size distribution histograms of the obtained germanium NCs. (a) Dodecyl-capped Ge NCs obtained via hot injection; (b) dodecyl-capped Ge NCs synthesized using microwave irradiation; (c) dimethylamino-capped Ge NCs obtained by microwave irradiation. Reproduced with permission from ref 243. Copyright 2015 Royal Society of Chemistry.
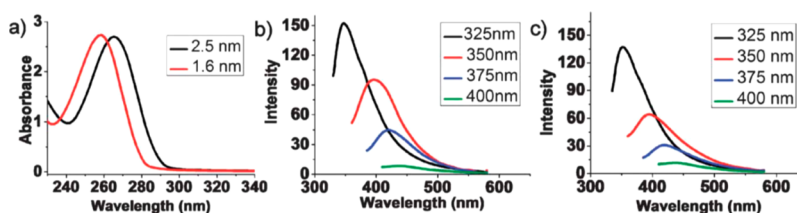
Figure 27. (a) Absorption spectra of hydrogen-terminated Si nanoparticles. (b) PL spectra of 1.6 nm particles and (c) of 2.5 nm particles using the indicated excitation wavelengths. Reproduced with permission from ref 220. Copyright 2012 Royal Society of Chemistry.

mechanism, APTMS first undergoes hydrolysis to form (3-aminopropyl)trihydroxysilane and is then photochemically reduced by 1,8-naphthalimide. PL studies indicate that this molecule is also involved in the formation of a charge-transfer complex with the Si NCs, leading to an enhanced emission with increasing amount of 1,8-naphthalimide.

For Ge NCs, the described microemulsion technique was applied in a similar way. Initially, Wilcoxon and co-workers

reduced $GeCl_4$ solubilized in the above-mentioned water-free surfactant/solvent system known to form reverse micelles by using $LiAlH_4$.[261] Similar safety issues as in the case of the reduction of $SiCl_4$ exist, here of course related to the formation of toxic and pyrophoric germane (GeH_4) gas.[268] The initially polydisperse samples with sizes ranging from 2 to 10 nm were fractionated by the means of high-pressure liquid chromatography (HPLC). The hydrogen-terminated Ge NCs showed PL
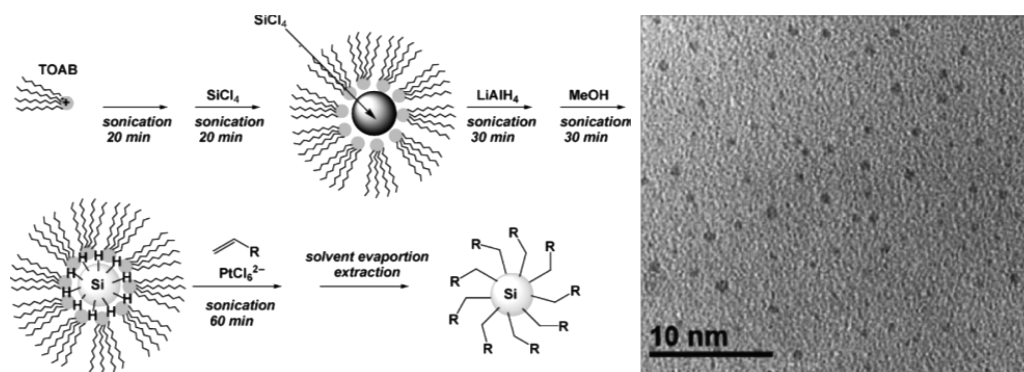
Figure 28. Left: Synthetic pathway for the microemulsion synthesis of alkyl-capped Si NCs using ultrasonication. Right: TEM image of the obtained 1.57 ± 0.21 nm NCs. Reproduced with permission from ref 221. Copyright 2008 Wiley-VCH Verlag GmbH & Co. KGaA.

Figure 29. Top: One-pot synthesis of alkene coated Si NCs and post functionalization via thiol−ene click chemistry. Middle: PL spectra showing the emission of Si NCs capped with different surface groups (a−e) excited at 320 nm. Bottom: photograph taken under UV (365 nm) illumination showing the change of the emission color and hydrophobicity/philicity of the particles as a function of the surface groups. Each vial contains hexane (upper layer) and H_2O (lower layer). Reproduced with permission from ref 173. Copyrights 2008 Royal Society of Chemistry.

Figure 30. (a/b) UV−vis, PL and PLE spectra of 3.9 nm (a) and 6.8 nm (b) Ge NCs obtained by the reduction of $GeCl_4$ by $LiAlH_4$ in inverse micelles formed by mixing tetrahexadecylammonium bromide with toluene. (c/d) Excitation−emission scanning matrices for 3.9 (c) and 6.8 nm (d) Ge NCs. Reproduced with permission from ref 233. Copyright 2015 Royal Society of Chemistry.

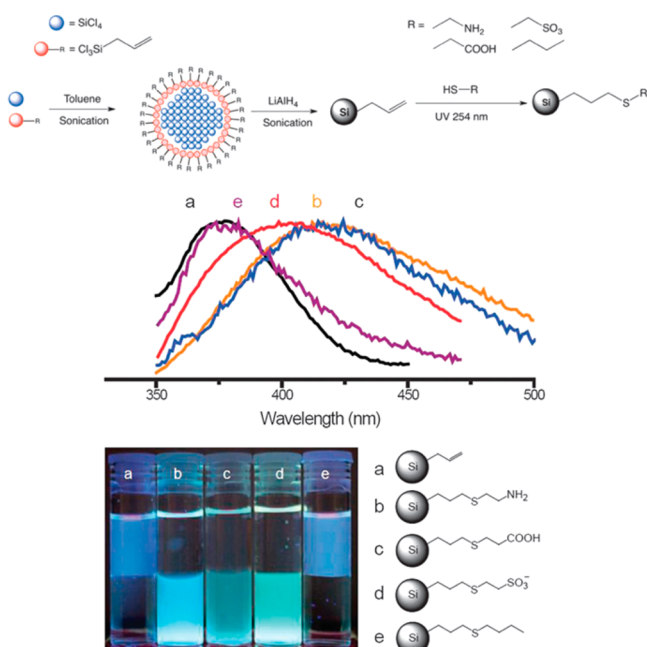emission centered at 480 nm for 2 nm and at 615 nm for 5 nm sized particles, indicating quantum confinement effects. The latter are expected in view of the large exciton Bohr radius in Ge of around 24 nm.[269] More recently, Carolan and Doyle expanded Wilcoxon's approach, focusing on the choice of the cationic quaternary ammonium surfactants used to form the reverse micelles, which led to an improved control of the PL properties with size-dependent emission in the visible range and QY values reaching 20% (Figure 30).[233−235] On the other hand, the initial broad size distribution of 6.4 ± 2.0 nm first had to be split into more narrow size fractions by centrifugation.[233]

GeO_2 has been explored as an alternative germanium precursor by several groups in syntheses taking place in aqueous media.[236,239,240] In a first step, GeO_2 was dissolved in a NaOH solution under ultrasonication to form aqueous

Na_2GeO_3 whose pH was adjusted with HCl to 6.5. In the second step, this mixture was injected into a solution of the reducing agent $NaBH_4$ and the polyvinylpyrrolidone (PVP), which acts as a stabilizer. The Ge NCs formed under heating to 60−80 °C for several hours (3−8). The obtained particles showed high PL QY up to 26%, however, no shift of the emission peaks located in the UV/blue region with changing size was observed, indicating that interfacial defects or surface oxides are involved in the fluorescence process. The powder X-ray diffractograms obtained with these methods show only two broad peaks, which resolve to the characteristic pattern of crystalline Ge after annealing at 600 °C. On the other hand, the visibility of lattice fringes in high-resolution TEM images already before annealing suggests the crystalline character of the as-synthesized Ge nanoparticles. In a modified polyol process taking place at room temperature, Schaak and co-workers used the same stabilizer (PVP) and reducing agent ($NaBH_4$) but $GeCl_4$ as germanium precursors and a mixture of ethylene glycol and triethylene glycol dimethyl ether (triglyme) as reaction medium.[270] Amorphous Ge nanoparticles of 5.1 ± 1 nm were obtained, emitting at 352 nm when excited at 310 nm. By changing the reaction conditions other sizes were also

accessible in a range of 2−50 nm, the biggest cube-shape particles were constituted of aggregates of smaller particles. A similar method was followed by Karatutlu and co-workers in 2015, who bubbled a mixture of H_2/Ar (5%/95%) instead of pure Ar through the reaction mixture.[237] The obtained 3.9 ± 0.6 nm Ge NCs exhibited a shoulder in the UV−vis absorption spectrum at around 400 nm and a strongly red-shifted PL emission centered at 680 nm (ex. wavelength: 473 nm). The structural and optical properties were described on the basis of a model implying a crystalline core and an amorphous shell of the particles.

4.1.3.3. One Pot Reduction Using Oleylamine. Oleylamine (OLA) has become a very widely applied starting compound in NC synthesis, which can have a triple role of solvent, surfactant/ligand and reducing agent with the additional advantages of being liquid at room temperature and having a high boiling point (~350 °C).[271] In particular it can act as a mild reducing agent for Ge halides, being itself oxidized to imine or nitrile as evidenced by FTIR spectroscopy.[272] Adapting the heat-up method widely use to synthesize metal or chalcogenides NCs (cf. section 3), Schaak and co-workers synthesized germanium NCs with a good control of the size and shape by heating GeI_4 with oleylamine, oleic acid and hexamethyldisilazane (HMDS) at 260 °C for 30 min.[244] By changing the concentration of germanium precursor the size of the obtained particles could be varied from 6 to 22 nm. While the precise role of HMDS was not identified, it is suggested that initially a Ge-HMDS complex is formed as the reactive species. Wan and co-workers used oleylamine as solvent and reducing agent for $GeBr_2$ without additional stabilizers, obtaining after heating to 260 °C for 2 h Ge nanoparticles of 10 nm average diameter.[246] In a similar approach Shirahata used GeI_2 in oleylamine, heated up to 300 °C.[245] Solubilization of the Ge precursor at 120 °C indicates adduct formation with OAm. The disproportionation of GeI_2 into Ge and GeI_4, is proposed as alternative reaction pathway. Polydispersity is still quite large (1−12 nm), but most of the crystals are found to be in the range of 4.8−5 nm. Yet, oleylamine capped germanium NCs have the tendency to degrade over time upon exposure to ambient conditions, with a loss of solubility and a diminution of their photoluminescence properties. As one possible solution, Kauzlarich and co-workers used thiols to replace oleylamine at the surface of the synthesized Ge NCs.[247] Similar as in prior work,[248] the synthesis was carried out by reducing GeI_2 with oleylamine in a microwave reactor at 210 °C for 1 h. After purification, the NCs were treated with hydrazine to remove the initial oleylamine ligands from their surface. This step was performed at room temperature (1 h) and monitored by FTIR spectroscopy. Then NCs were mixed with dodecanethiol (DDT) and heated in the microwave reactor at a 150 °C for 1 h. A slight increase of the crystallite size was observed by XRD. All the result of surface photovoltage voltammetry (SPV) and contact potential difference indicate a n type conduction of the charge carriers (electrons) and quantum confinement, i.e. increasing band gap with decreasing size). Beside the fact that DDT capped NCs exhibit a better colloidal stability than the oleylamine capped ones, they also show a larger negative contact potential difference (CPD). Control experiments indicated that this better charge separation was neither related to the shorter chain length of the DDT ligands, nor to ligand− substrate interactions, but rather to the nature of the thiol anchoring group itself, passivating the surface of the Ge NCs. The size-dependent band gap of the thiol and oleylamine

capped Ge NCs was investigated in another work from the same authors, confirming quantum confinement effects:[249] For oleylamine capped crystals, the band gap determined from UV−vis spectra, equals 1.30 eV for 3.87 nm, and 1.00 eV for 7.54 nm Ge NCs, in accordance with previous studies (Figure 31).[250] The corresponding DDT capped samples exhibited
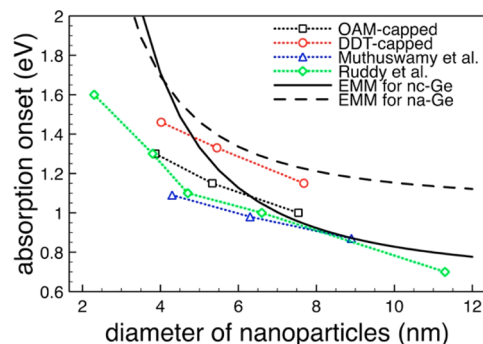
Figure 31. Band gap as a function of size for Ge NCs. Lines with symbols: experimental data from ref 249 (black diamond, OAM = oleylamine, red circle, DDT = dodecanethiol), ref 248 (blue triangle), ref 250 (green diamond); black solid line: theoretical behavior of Ge NCs (nc) according to the effective mass model, compared to nanoamorphous (na) Ge (black dashed line).[273] Reproduced with permission from ref 249. Copyright 2015 American Chemical Society.

larger values of 1.46 and 1.15 eV, respectively. In cyclic voltammetry studies the oleylamine capped NCs showed weak but distinguishable signals, however, no redox signals could be detected after exchange with DDT. This suggests that oxidation of the NCs was prohibited after DDT capping and likely occurred through surface defects in the case of oleylamine ligands. The passivation of surface trap states would also explain the observed widening of the band gap for DDT capped particles.

4.1.3.4. Thermal Reduction of Organogermanes and Organosilanes, Sol−Gel Methods. The use of sol−gel methods in the synthesis of Si and Ge NCs gives access to a large range of controlled sizes and narrow size distributions. The sol−gel process is generally used for building up solid materials such as metal oxides from molecular precursors in a controlled way through the stages of sol formation, gelation/ polycondensation, aging and drying.[274] Veinot and co-workers proposed to translate silicate sol−gel chemistry to the synthesis of Si nanoparticles by carrying out the thermal treatment under reducing atmosphere.[275] Either commercial silsesquioxanes of the general formula $RSiO_{1.5}$ (R = H, alkyl, silyl, aromatic) such as $H_8Si_8O_{12}$ (HSQ)[275] or tailor-made polymers obtained for example by the hydrolysis of trichlorosilane[225] can be used as the sol−gel precursors. They are submitted to thermal processing under reducing atmosphere, which leads to the diffusion of Si atoms in the formed thermodynamically stable SiO_2 matrix, clustering of Si-rich domains, and crystallization of Si nanoparticles. In one example Si NCs embedded in the sol− gel matrix were formed by heating the precursor in a furnace to 1100−1400 °C for 1−10 h under reducing atmosphere (5% H_2/95% Ar).[225] The particles were removed from the matrix by etching with HF yielding hydride termination of their surface, which opens the way for functionalization with alkenes. Korgel and co-workers built on this method and achieved accurate size control in a range of 3 to 13 nm (standard deviation: 10−19%) by varying the reaction temperature from 1100 to 1350 °C
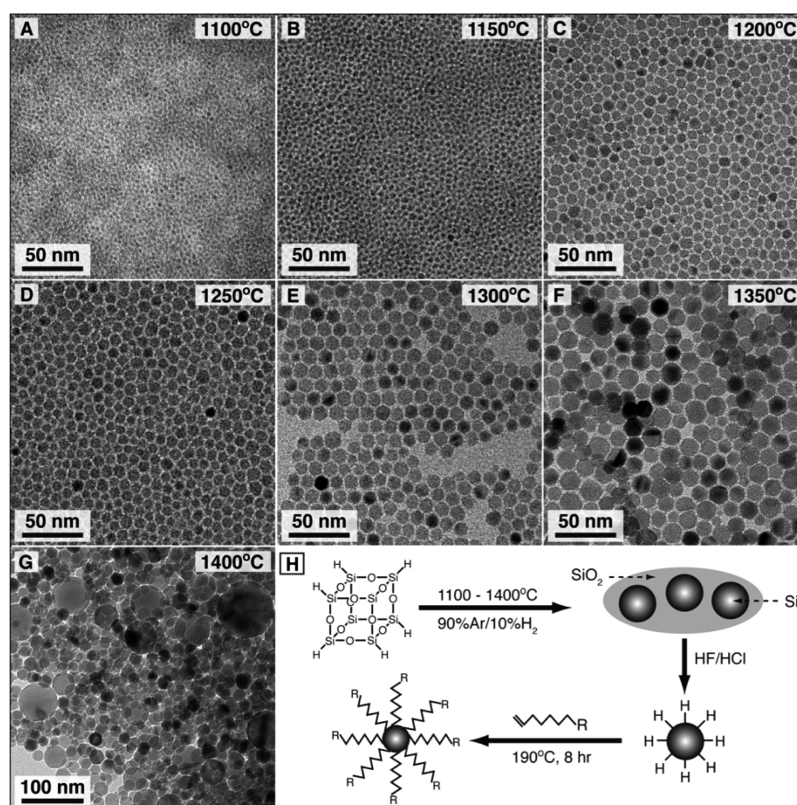
Figure 32. Synthesis of Si NCs by means of the sol−gel method starting from hydrogen silsesquioxane (HSQ) and using different decomposition temperatures. (A−G) TEM images; (H) reaction pathway. After HF-etching and alkene-functionalization, free-standing particles are obtained, dispersible in solvents that match the polarity of the substituent R. Reproduced with permission from ref 172. Copyright 2012 Amercian Chemical Society.

under more strongly reducing atmosphere (10% H2/90% Ar) (Figure 32).[172] Heating to 1400 °C leads to very polydisperse nanoparticles in a range of 18−90 nm.

In addition to the mentioned hydrosilylation reactions for the surface functionalization involving alkenes, several studies report the use of polymeric ligands or the polymerization of suitable monomers on the NC surface. Such approaches can further enhance the surface passivation, stability and functionality of the NCs. As an example, in an earlier study Li and Ruckenstein polymerized acrylic acid on the surface of silicon nanoparticles upon UV illumination, which led to water dispersible NCs of high colloidal stability while maintaining their PL properties.[227] The obtained particles were used as fluorescent probes in cellular biological imaging. Instead of directly grafting the hydrophilic polymer on the surface, Erogbogbo et al. used amphiphilic polyethylene glycol (PEG) substituted phospholipids to encapsulate alkyl capped Si nanoparticles in a micellar approach.[229] The surface of the phospholipid micelles can serve as a platform for the introduction of additional functional groups enabling the grafting or targeting of biomolecules. For applications in this field the postsynthetic purification steps deserve special attention to prevent toxicity from unreacted precursors or excess capping agents, which potentially exceeds that of the Si nanoparticle itself.

In an extension of the sol−gel approach to Ge nanoparticles Veinot and co-workers investigated the use of phenyl trichlorogermane as a precursor for sol−gel polymerization.[251] PhGeCl₃ was first hydrolyzed by addition of isopropyl alcohol in water under inert atmosphere, and then heated at 60 °C for 24 h to ensure complete condensation. The obtained sol−gel polymer $(PhGeO_{1.5})_n$ was then heated to 500−550 °C under reducing atmosphere (5% He/95% Ar) leading to the formation of Ge NCs within a GeO_2 matrix. In contrast to SiO_2, GeO_2 is hydrosoluble, and therefore the matrix can simply be dissolved in warm water (60 °C). The average diameter of the obtained nanoparticles was 5.5 nm, with a relatively low polydispersity. By changing the substituent on the trichlorogermane precursor, the same group later showed that lower reaction temperatures could be used (300−400 °C), and larger average sizes of the Ge NCs could be obtained in a range of 11−22 nm.[181]

4.1.3.5. Zintl Salt Metathesis Reactions. Starting from 1996, Kauzlarich and co-workers reported several metathesis reactions for the synthesis of Si and Ge NCs. These approaches rank among the first solution phase syntheses performed at comparably low temperature. As a common feature these reactions imply Zintl compounds such as NaE, KE or Mg_2E "(E = Si, Ge)" as precursors, which are a special class of intermetallic phases of unusual bonding, structural properties and oxidation states.[276] They are reacted with silicon, germanium, transition metal or ammonium halides, and the driving force for the metathesis is the formation of the alkaline (earth) metal halide. Initially NaSi and KSi have been applied in a metathesis reaction with $SiCl_4$, leading to polydisperse Si nanoparticles.[277] Later Mg_2Si has been used in combination with $SiCl_4$ to produce 2−5 nm nanoclusters of crystalline silicon.[178] In this case, the Zintl salt was mixed with glyme (ethylene glycol dimethyl ether), dissolved gradually after addition of $SiCl_4$, and the mixture was refluxed for 36−48 h

Table 3. Synthesis Conditions and Outcome (Size and Shape of Ge NCs) of the Thermal Decomposition of Organogermanes in High Boiling Point Solvents[255a]

germanium precursor	decomposition temperature (°C)	solvent	reaction temperature (°C)	mean size (nm)	comments
trichlorogermane	140	trioctylamine	384	1−2	mainly amorphous. crystalline fractions after longer times (30 min)
		squalene	410	2−7	uniform, highly crystalline particles
tributylgermane	390	squalene	410	4−15	
triethylgermane	420	squalene	410	~10 nm diameter	nanowires
		octacosane	429		

[a]A novel type of organogermane precursor was proposed by Jiang and co-workers in 2006: tetra-*cis*-9-octadecenoic germanium (TOG) was obtained in a simple way by the reaction of GeCl$_4$ with oleylamine.[256] TOG was dissolved in trioctylamine and injected into a mixture of trioctylamine, oleic acid and oleylamine at 200 °C. The mixture was then refluxed at 360 °C for 15 min, 30 min or 1 h, yielding Ge nanoparticles of 5, 10, and 20 nm, respectively, and of narrow size distribution (Figure 33).
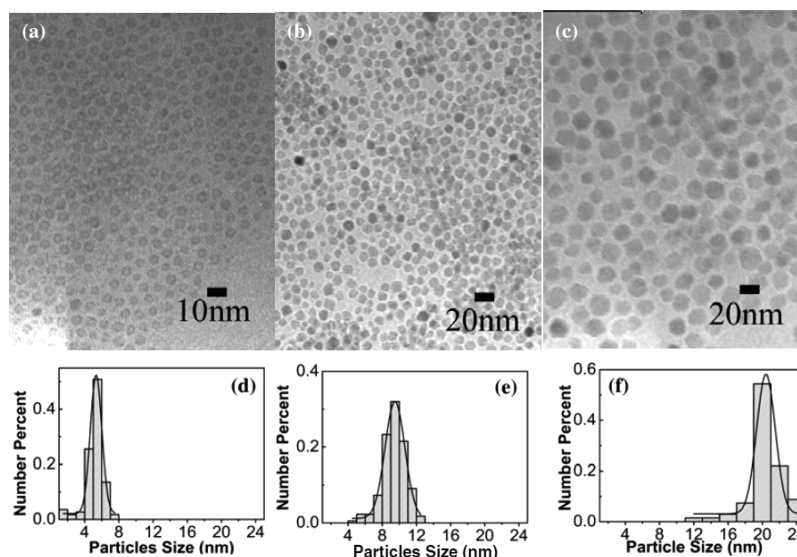
Figure 33. TEM images and size distribution of Ge NCs obtained by thermal decomposition of tetra-*cis*-9-octadecenoic germanium after 15 min (a, d), 30 min (b, e), and 60 min (c, f) reaction time at 360 °C. Reproduced with permission from ref 256. Copyright 2006 IOP Publishing Ltd.

under inert atmosphere. Finally the Si−Cl bonds at the surface of the NCs were replaced by alkyl chains after reaction with various Grignard reagents or alkyllithium leading to NCs soluble in organic solvents like hexane. The yield of the metathesis reaction could be increased by adding a phase-transfer catalyst such as (*n*-octyl)$_4$NBr, to facilitate the solubilization of Mg$_2$Si in refluxing glyme. The metathesis method was further optimized by reacting NaSi with NH$_4$Br in dimethoxyethane at 80 °C or in dioctylether at 260 °C affording 4.95 ± 1.23 nm and 3.85 ± 1.03 nm H-terminated Si NCs.[278] Si nanoparticles obtained by these methods have been applied in hyperpolarized magnetic resonance imaging[279] and as anode material in Li-ion batteries.[280]

Also in the case of germanium NCs metathesis reactions of Zintl salts such as NaGe, KGe and Mg$_2$Ge have been explored.[252,281] The Zintl compounds were added to a large amount of glyme, diglyme or triglyme (mono-, di-, or triethylene glycol dimethyl ether) and stirred for several hours under reflux. Upon addition of 3-fold excess of GeCl$_4$ with respect to the Zintl salt and further reflux, Ge NCs were obtained with sizes depending on the heating time (4−120 h). Surface modification has been achieved as mentioned before using BuLi, MeLi or Grignard reagents. Methyl capped NCs were found to be better soluble in polar solvents such as

methanol, whereas butyl and octyl capped ones showed higher solubility in apolar solvents such as toluene or hexane.

4.1.3.6. Thermal Decomposition of Organosilanes and Organogermanes. Early syntheses based on the thermal decomposition of silanes, i.e. molecules composed exclusively of Si and H, have been reported by Brus and co-workers in 1993.[228,282] In their work, silicon NCs were synthesized using an aerosol system for the pyrolysis of silanes in the gas phase and collected in ethylene glycol. Due to the required high temperatures to form crystalline nuclei and with the goal to find easier to manipulate precursors for synthesis, organosilanes have replaced the pyrophoric and low boiling point silanes in subsequent studies. Their thermal decomposition under supercritical conditions has been developed by Korgel and co-workers who heated diphenylsilane with octanol and hexane in a sealed reactor to 500 °C at 34.5 MPa.[226] 1.5 nm diameter Si NCs were obtained in pure octanol and a radical mechanism was claimed for the decomposition of diphenylsilane. Octanol passivated the NC surface and prevented from further growth or aggregation of the particles, which was observed when using ethanol instead. When replacing some of the octanol by supercritical hexane, larger particles were obtained in a range of 2.5 to 3.5 nm. Those particles showed green photo-luminescence with a QY of 23%, while the 1.5 nm particles exhibited blue emission, indicating the presence of quantum

size effects. One drawback of this method is the relatively low reaction yield, because only 0.5−5% of the initially introduced Si precursor is converted into Si NCs. Organogermane precursors have likewise been decomposed thermally. In an earlier report by Gerion and co-workers tetraethylgermane is heated to 430 °C during 1−30 min in a sealed pressure reactor.[253] TEM and X-ray diffraction confirm that crystalline Ge NCs in diamond cubic phase have been obtained. Depending on the reaction conditions (addition of toluene, hexane, reaction time), their size could be varied in a range of 5−30 nm and also different shapes have been obtained (dots, pyramids, cubes, wires, etc.). Nonetheless the precise control of size and shape was not possible with this method, and a large amount of residual byproducts was observed. On the other hand, the obtained products have been found to be air stable for months, without sign of surface oxidation. Lu and co-workers used a similar method to synthesize Ge NCs in supercritical CO$_2$ (sc-CO$_2$) in a sealed reactor at 500 °C.[254] The conditions were similar to those used by Holmes et al. for the above-described synthesis of Si NCs[226] and in addition to tetraethylgermane diphenylgermane was also explored. The germanium precursor was mixed with octanol and sc-CO$_2$ and heated to 500 °C in the sealed vessel at high pressure (27.6 MPa). However, as before the size distribution remains broad and hardly controllable with this way of synthesis and the separation of the NCs from byproducts was challenging. A better control of the size and morphology of the Ge NCs has been achieved by Zaitseva and co-workers who carried out the thermal decomposition of organogermanes at ambient pressure.[255] The authors used different high-boiling point organic solvents, which were adapted to the decomposition temperature of the used Ge precursor. As seen in Table 3, Ge nanoparticles in a size range of 1−15 nm were obtained from trichlorogermane, triethylgermane, and tributylgermane in trioctylamine, squalene, and octacosane. The reactions of triethylgermane in squalene or octacosane led to the formation of Ge nanowires growing in the [110] direction. A vapor−liquid−solid (VLS) growth mechanism was suggested on drops of the boiling solvent condensed on the walls of the reaction flask.

4.2. III−V Semiconductor NCs

4.2.1. Introduction. III−V semiconductors are crystalline binary compounds formed by combining metallic elements from group IIIA (13) and nonmetallic elements from group VA (15) of the periodic table. They are used for high performance optoelectronic devices due to their unique properties such as high electron mobility, direct band gap, low exciton binding energy, and bulk band gap values covering a wide range of spectra from ultraviolet to infrared region. Despite of their dominance in bulk form both Si and III−V semiconductors have been outperformed by more polar II−VI and IV−VI semiconductor based QDs mainly due to synthetic challenges associated with these systems. As reflected in their fractional ionic character of bonding (Table 1), except for some nitrides most III−V semiconductors have smaller lattice ionicity than II−VI and IV−VI semiconductors. Compared to ionic reactions, more covalent bond formation usually requires harsher reaction conditions marked by higher reaction temperature, longer reaction time and more reactive precursors.[283] These conditions are generally not favorable for the precise control of size and size distribution of the NCs. The precursor reactivity and reaction conditions have to be

carefully optimized to obtain high quality materials. Furthermore, the III−V semiconductor NCs such as InP are much more air-sensitive than their II−VI counterparts (e.g., CdSe), so that most syntheses require air-free conditions. The nitrides are different from the other III−V compounds with regard to their crystal structure (wurtzite) and their comparably low thermal stability, which complicates high temperature syntheses. Indium nitride single crystal films of 200−300 nm thickness, for example, undergo thermal decomposition under dinitrogen desorption at 500−550 °C.[284] In form of NCs with diameters of a few nm, this process is likely to appear at much lower temperature. For the metal nitrides in particular, but also for the NCs of the other pnictides, the identification of suitable group V precursors is the key challenge in chemical synthesis. Due to the comparably low electron affinity of group V elements, it is difficult to find appropriate precursors in the oxidation state −III. By consequence common group V precursors involve reactive compounds with highly electro-positive elements like H, Na, Si. Some examples are Na$_3$P, H$_3$P, (Me$_3$Si)$_3$As, (Me$_3$Si)$_3$P, Li$_3$N, (Me$_3$Si)$_3$N, etc. Table 4 outlines

Table 4. Physical Properties of III−V Semiconductors[a]

material	ε[286]	$\mu_e(m_0)$[285]	$\mu_h(m_0)$[285]	E_g (eV)[287]	exciton Bohr radius (nm)	exciton binding energy (meV)
InN	5.5	0.12	0.5	0.8	3.0	43.5
InP	12	0.077	0.6	1.35	9.3	6.44
InAs	12.3	0.022	0.4	0.35	31.2	1.87
InSb	15.6	0.014	0.4	0.23	60.9	0.75
GaN	5.8	0.18	0.54	3.44	2.3	54.5
GaP	8.5	0.35	0.5	2.27(i)	2.2	38.7
GaAs	10.9	0.067	0.5	1.42	12.9	3.87
GaSb	14.4	0.041	0.28	0.75	21.3	2.34

[a]All values are calculated for room temperature (300 K).

the basic properties of III−V semiconductors. Baring few most III−V semiconductors are direct band gap semiconductors. Both the exciton Bohr radius and exciton binding energy give a useful perspective on the length scale where these materials deviate from the bulk materials and exhibit size dependent optical and electrical properties.

The exciton Bohr radius can be calculated using the equation:

$$r_B = \frac{\epsilon m_0}{\mu} a_o \text{ where } a_o = \frac{4\pi\epsilon_0 \hbar^2}{m_0},$$

$$\epsilon = \text{dielectric constant}, \quad \epsilon_0 = \text{vacuum permittivity},$$

$$\hbar = \frac{h}{2\pi}, \quad m_0 = \text{free electron mass}, \quad \mu = \text{effective mass}$$

The dielectric constant is frequency-dependent. Consequenty, the exciton Bohr radius and exciton binding energy values reported in the literature may slightly vary from each other due to discrepancies in the dielectric constant value used. For simplicity we have used high frequency optical dielectric constants (ϵ_∞) for our calculation. This gives a qualitative idea about the quantum confinement and binding energies of the exciton in various III−V semiconductors and hence helps us in judging the suitability of a material in various applications. The exciton binding energy has been calculated using the following

equation, $E_{Bind} = \frac{\mu}{\epsilon^2 m_0} R_y$ where R_y = Rydberg constant (13.6 eV).[285]

Due to the large exciton Bohr radius in GaSb, InAs, and InSb a wider size range of NCs exhibiting quantum confinement effects can be prepared with these materials. In contrast, InN, GaP, and GaN have a very small Bohr exciton radius. Therefore, ultrasmall particles have to be synthesized to observe quantum confinement with these materials. As we will see in the following discussion, syntheses of quantum-confined NCs in colloidal form with these materials are sparse.

4.2.2. Indium Nitride. For a long time it was believed that the fundamental band gap of InN was 1.9 eV. However, more recent studies on higher quality films of this material have unambiguously shown that the true value of its direct band gap lies at 0.8 eV,[288] making it a very promising compound for optoelectronic applications. In bulk form the band gap can be tuned by forming alloys with other materials such as GaN and AlN. For example, the band gap energy of aluminum gallium indium nitride (AlGaInN) can be tuned between 6.2 and 2.0 eV by changing the composition. Consequently, these semiconductors can be used for red- to ultraviolet-emitting devices.[289] In quantum confinement regimes, the band gap can be further tuned by changing the size and shape of the NCs, even though the Bohr exciton radius is with 3 nm rather small (vide supra). InN NCs are potentially important for a wide range of applications including solid-state lighting, biological imaging and photovoltaic applications. Several wet-chemical synthesis strategies such as solvothermal synthesis, thermolysis of precursors, and dehalosilylation reactions using $N(SiMe_3)_3$ have been used to obtain InN in colloidal form. However, to date the optical properties in terms of size-tunable absorption and emission spectra and fluorescence quantum yield, are not of comparable quality to those obtained with more established types of NCs. In the solvothermal method the synthesis is conducted in an autoclave at elevated pressure. Like in a pressure cooker used in the kitchen, in the hermetically closed system of the autoclave the boiling temperatures of the solvents can be elevated by increasing the vapor pressure. Bai et al. synthesized InN by autoclaving Li_3N and $InCl_3$ in xylene at 250 °C for 24h.[290] Crystalline InN nanoparticles were also synthesized by autoclaving InI_3 with $NaNH_2$ in benzene at different temperatures (180, 210, 230 °C).[291] Depending on the reaction time and temperature the particle size could be controlled. For example, higher temperature and longer reaction time yielded larger sized particles. Other examples of solvothermal syntheses are reactions between $NaNH_2$ and In_2S_3,[292] as well as autoclaving of a mixture of M_2S_3 (M= In, Ga, Al), NH_4Cl, CS_2, and I_2 in water.[293] Neale and co-workers synthesized oleylamine capped colloidal InN of 4−10 nm diameter by reacting $NaNH_2$ and In_2S_3.[294] The obtained InN NCs exhibited a visible absorption onset (~1.8 eV) and a strong localized surface plasmon resonance absorption in the mid infrared (~3000 nm). Other attempts to synthesize InN NCs include thermal decomposition of precursors and dehalosilylation reactions between $InCl_3$ and $N(SiMe_3)_3$ in a non-coordinating solvent using myristic acid as ligand.[295] However, these methods usually resulted in polydisperse NCs. Recently, nearly monodisperse InN NCs dispersible in various organic solvents have been synthesized by combining solution and vapor phase methods. First colloidal myristic acid capped In_3O_2/SiO_2 core/shell NCs were grown, which were subsequently annealed at 500−700 °C under NH_3 flow to obtain InN NCs with an average size of 5.7 ± 0.6 nm.[296]

4.2.3. Gallium Nitride. Nitrides of gallium and indium have first been synthesized using solvothermal methods. Xie et al. obtained GaN crystallites of 30 nm average size with this approach.[297] The reaction was carried out at 280 °C in benzene (Boiling point: 80.1 °C at 1 atm) by using $GaCl_3$ and Li_3N as gallium and nitrogen precursors, respectively.

$$GaCl_3 + Li_3N \rightarrow GaN + 3LiCl$$
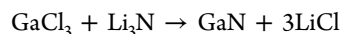
The product mainly crystallized in the wurtzite (hexagonal) form with some traces of rocksalt GaN. The PL spectra showed a broad emission peak at 370 nm, which is characteristic of bulk GaN. As evident from the synthetic scheme, the above method does not use a capping ligand. Rao and co-workers have synthesized GaN particles of 2.5 nm average diameter by using N-cetyl-N,N,N-trimethylammonium bromide (CTAB) as the capping ligand (Cupferron stands for 3 equiv of N-nitroso-N-phenylhydroxylamine):[298]

$$Ga\ cupferron + (CH_3)_3SiNHSi(CH_3)_3$$
$$\xrightarrow{CTAB} GaN\ (4\ nm) + (CH_3)_3SiOSi(CH_3)_3 + H_2$$
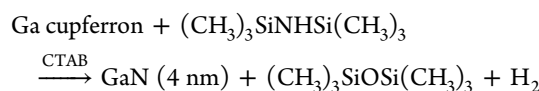
The reaction was carried out for 2 h in toluene at 250 °C in a Teflon-lined steel autoclave. In the absence of the capping agent, NCs of bigger particle size (4 nm) have been obtained. In the same report, the authors demonstrate the size-dependency in GaN NCs, resulting from quantum confinement. The PL emission band at 265 nm exhibited by 2.5 nm quantum dots red-shifted to 315 nm for 4 nm particles. The first article on the synthesis of GaN stable in colloidal form came up in 1999.[299] Mićić et al. reported the synthesis of 2 nm sized GaN NCs using a polymeric gallium imide as the precursor and trioctylamine as ligand and high boiling solvent (boiling point: 365 °C) to facilitate the pyrolysis of the precursor at 360 °C (reaction time: 24 h). Addition of the less sterically hindered ligand hexadecylamine (HDA) improved the capping robustness and hence colloidal stability. At low temperature, the PL spectrum showed several emission peaks in the range of 3.0−3.8 eV. The polymeric precursor gallium imide, $[Ga(NH)_{3/2}]_n$, was first shown to yield cubic/hexagonal GaN particles via pyrolysis by Wells and co-workers.[300] It was suggested that this precursor yields GaN via stepwise deamination reactions:

$$Ga(NH_2)_3 \xrightarrow{\Delta(-NH_3)} Ga(NH)_2NH \xrightarrow{\Delta(-\frac{1}{2}NH_3)} Ga(NH)_{3/2}$$
$$\xrightarrow{\Delta(-\frac{1}{2}NH_3)} GaN$$
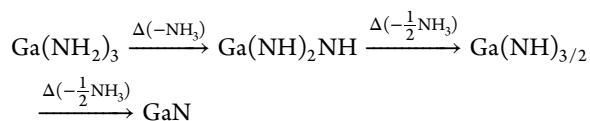
Pan et al. proposed a modification to the above reaction strategy.[301] They showed that the dimeric amidogallium precursor $(Ga_2[N(CH_3)_2]_6)$, which upon reaction with ammonia gas generates the polymeric precursor gallium imide $[Ga(NH)_{3/2}]_n$, can be converted directly to GaN through pyrolysis without the need for the polymeric intermediate. This strategy therefore does not require the use of gaseous ammonia. In addition to an improved reaction yield, the authors also demonstrate the importance of the used capping ligand for the production of stable colloidal QDs. No GaN was produced in the absence of the capping ligand HDA, which suggests a possible transamination reaction. However, the reaction time was still at least 24 h. Manz et al. reported the synthesis of GaN NCs at remarkably low temperature (220 °C) and low reaction

time (15−300 min) in triglyme solution using the following organometallic azide precursors: $[Et_2Ga(N_3)]_3$, $(N_3)_2Ga$-$[(CH_2)_3NMe_2]$ and $(Et_3N)Ga(N_3)$.[302] Depending on the reaction conditions, several sizes in the range of 2.5 nm up to 500 nm have been obtained. However, the lower annealing time and lower temperature is at the cost of the crystalline quality of the GaN NCs; X-ray diffraction revealed that they were of amorphous nature.

4.2.4. Indium Phosphide. The interest in synthesizing InP NCs mainly stems from their tunable emission in the visible and NIR range making them a direct alternative for CdSe-based QDs. Colloidal InP NCs were first synthesized by reacting chloroindium oxalate with tris(trimethylsilyl) phosphine (P-$(SiMe_3)_3$, also abbreviated as $P(TMS)_3$) in trioctylphosphine oxide (TOPO) at 270−360 °C for 3 days.[303] This reaction is based on the dehalosilylation reaction developed by Wells and co-workers and already mentioned for the nitrides. Since this seminal work, $P(SiMe_3)_3$ has become the most commonly used phosphorus source for the synthesis of InP NCs. In this reagent, the phosphorus atom bonded to the highly electropositive Si imparts the necessary driving force to react with cationic In(III) precursors to form InP. Heath and co-workers modified the original procedure of Mićić by replacing the chloroindium oxalate with $InCl_3$ and reported size-dependent optical properties. While they employed postsynthesis size selective precipitation techniques to improve the size dispersions, they were still broader (∼20%) compared to CdSe (∼5%) NCs. In addition, the InP NCs also showed poor photoluminescence properties (QY < 1%). Surface treatment of the InP NCs with HF or NH_4F was shown to drastically improve the quantum yield up to 30%.[304] With further optimization of the HF treatment under light irradiation a QY as high as ∼40% at room temperature has been achieved.[305] In this study Adam and co-workers also investigated the underlying mechanism of the HF treatment (Figure 34): by
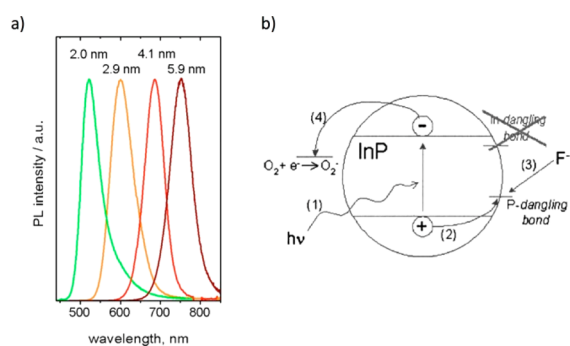

Figure 34. (a) Normalized photoluminescence spectra of size-selected InP NCs after photoassisted etching of their surface with HF. (b) The four steps of the photoetching mechanism: (1) photon absorption and exciton formation; (2) capture of the hole by a P surface bond; (3) nucleophilic attack of photoactivated P atom with fluorine ions; (4) electron reaction with acceptors from solution. Reproduced with permission from ref 305. Copyright 2005 American Institute of Physics.

means of high-resolution synchrotron XPS spectroscopy they showed that HF removed unpassivated P atoms, which induced trap states within the band gap of InP, responsible for the low initial PL QY. The reconstructed surface was mainly terminated by TOPO-passivated In atoms. The same work also provides the correlation of size and molar extinction coefficient of the

NCs, which greatly simplifies the determination of the concentration of colloidal solutions of InP QDs.

Alternatively, as in the case of II−VI semiconductor NCs the concept of inorganic shell growth on the emissive core particle has also been developed for InP QDs in order to improve their QY, chemical and photostability.[35] Nozik and co-workers first synthesized lattice-matched $InP/ZnCdSe_2$ core/shell NCs and achieved an improvement of the PL QY up to 5−10%.[306] Following this work, Haubold et al. synthesized InP/ZnS core/shell NCs with a maximum QY of 20%.[307] Despite of 7.7% lattice mismatch between the InP core and the ZnS shell, zinc sulfide is the most widely used shell material for InP NCs due to the lower QY obtained with ZnSe (lattice mismatch 3.3%) and $ZnCdSe_2$. On the other hand, Kim and co-workers successfully used ZnSe as a lattice adaptor between the InP core and the ZnS outer shell, which enables achieving higher shell thicknesses (∼1.9 nm) and enhanced photochemical stability.[308] Recently, an optimized synthesis of an InP/ZnSeS core/shell system with compositional gradient shell has yielded a PL QY as high as 81%.[309] The highest value reported so far (85%) has been obtained for the InP/GaP/ZnS system with a very thin GaP interlayer.[310] GaP presents a relatively large lattice mismatch of 7.0% with InP but is almost lattice matched with ZnS (mismatch: 0.2%). It should also be noted that zinc acetate was used during core synthesis, improving the PL QY to around 15% with respect to syntheses without zinc (QY < 1%). Several studies demonstrate that the addition of zinc complexes does not only improve the surface passivation (e.g., of phosphorus dangling bonds) but that zinc can be actually incorporated into the InP core, leading to alloyed InZnP NCs.[311,312] In the example of Kim et al.[310] the authors proposed that GaP growth occurred on the InP core via the cation exchange reaction between In^{3+} and Ga^{3+} ions. This is consistent with the observed blue-shift of 5−15 nm and concomitant increase of PL QY from 15% to 30%. Overcoating this structure with a ZnS shell led to the observed high QY. In addition to these core/shell syntheses implying two steps, the core preparation followed by shell growth, Li et al. reported a single-step one-pot heat-up method yielding high PL QY up to 70% and relatively narrow emission line width of 40−60 nm fwhm (Figure 35).[313] In this simple procedure both the core (indium myristate, $P(SiMe_3)_3$) and the shell (zinc stearate, DDT) precursors are mixed and then heated to 300 °C. Due to the difference in reactivity during the temperature increase first the InP precursors react followed by the ZnS precursors. A high-resolution synchrotron XPS study of the obtained NCs indicated that the core consisted of an alloyed InPZnS structure, covered with a thin layer of ZnS.[314] Table 5 gives an overview of representative synthesis methods for highly luminescent InP-based core/shell NCs.

One of the most important turning points in the synthesis of InP NCs came when coordinating solvents such as TOPO were replaced with a noncoordinating solvent, viz. 1-octadecene (ODE), in combination with fatty acid type stabilizers.[317] In this case, the size of the NCs could be controlled by varying the concentration and alkyl chain length of the fatty acid ligand. Under optimized conditions myristic acid (C_{14}) and palmitic acid (C_{16}) were found to be the best ligands for InP NCs synthesis in ODE, yielding the narrowest size distribution. The main achievements of this approach are thus marked by the reduction in reaction time from 3 to 7 days to 3−60 min and by the reduction of the size distribution of the as-synthesized InP NCs (15−20% vs 25−30% in the case of syntheses in TOPO).
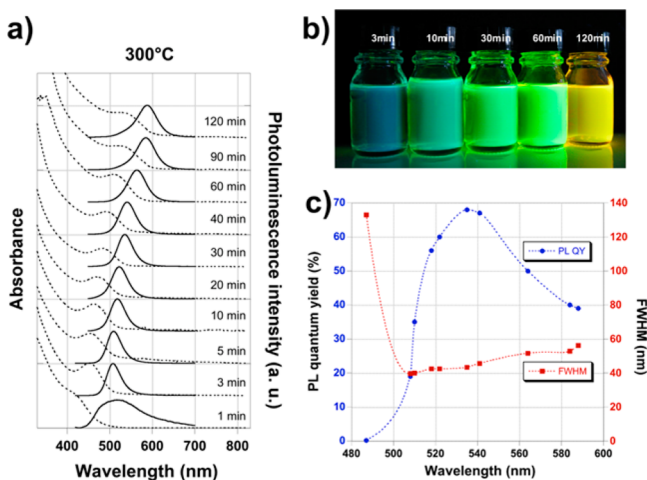
Figure 35. (a) Evolution of the PL (excitation: 400 nm) and absorption spectra with reaction time in a single-step one-pot synthesis of InP/ZnS NCs. (b) Photographs of the different sized samples under UV illumination. (c) Variation of the PL QY and line width (fwhm) with reaction time. Reproduced with permission from ref 313. Copyright 2008 American Chemical Society.

Further improvements could be made by the use of reaction additives. Short chain alkylamines like octylamine, for example, have been shown to enable a decrease of the reaction temperature to around 190 °C.[315] On the other hand, the simultaneous use of alkylamines and fatty acids precludes reaction temperatures as high as 250−300 °C, as under these conditions amide formation takes place as a side reaction.[318] This process is accompanied by the in situ generation of water, which leads to the concurrent formation of indium oxide. As mentioned before the addition of Z-type zinc complex ligands, e.g., zinc stearate[319] or zinc undecylenate,[316] is widely used for improving the PL QY of the InP core NCs. In this context Delpech, Nayral and co-workers showed that fatty acids, used as a complexing agent for both indium and zinc, can undergo, at elevated temperature, a decarboxylative coupling reaction (ketonization) under release of water, once again inducing undesired surface oxidation of the InP or InP/ZnS NCs.[320,321]

Despite of the outlined remarkable progress in $P(SiMe_3)_3$ based synthesis of InP QDs, current studies seek to explore alternative phosphorus precursors.[366] The motivations for such a quest arise from the current understanding of InP formation in noncoordinating solvents. Further drawbacks of $P(SiMe_3)_3$ are related to its pyrophoric nature, high cost and hazardous reagents and secondary products involved in its production. Current studies have linked polydispersity in the case of InP NCs to the rapid depletion of molecular phosphorus species following nucleation.[322] It has been therefore suggested that the growth of InP NCs is a non-molecular ripening mechanism.

Rapid precursor depletion is also attributed to be at the origin of the apparent difficulty in synthesizing larger sized (>4 nm) InP NCs with this precursor. In another study, the protic fatty acid ligands are also linked to the polydispersity of the NCs as they promote rapid side reactions of the phosphorus precursors.[323] Joung et al. replaced $P(SiMe_3)_3$ with more stable $P(SiMe_2(t\text{-}Bu))_3$ to achieve larger sized NCs without compromising on the particle size dispersion.[324] More recently, precursors with decreased reactivity such as $P(GeMe_3)_3$ and $P(SnMe_3)_3$ have been prepared and used for the synthesis of InP NCs.[325] However, only modest success in improving size dispersion was achieved. Replacing Si in the Si−P bond with Ge or Sn reduces the reactivity of the precursor by decreasing the polarity of the bond. Currently, tris(dimethylamino) phosphine $(P(NMe_2)_3)$ has been identified as a potential phosphorus precursor.[326−329] Although this compound was commercially available for a long time, its successful use in InP NC synthesis has only been reported in recent years, as its reactivity in the "standard" synthesis with indium myristate or palmitate in ODE is too low. Song et al. applied oleylamine as the solvent/ ligand and reacted $InCl_3$ with $P(NMe_2)_3$ in the presence of $ZnCl_2$. The as-synthesized core NCs do not exhibit any photoluminescence. After coating with a ZnS shell, however, the obtained InP/ZnS NCs showed a PL QY (51−53%) and emission line width (60−64 nm fwhm) comparable to those synthesized using $P(SiMe_3)_3$ (Figure 36).[326]
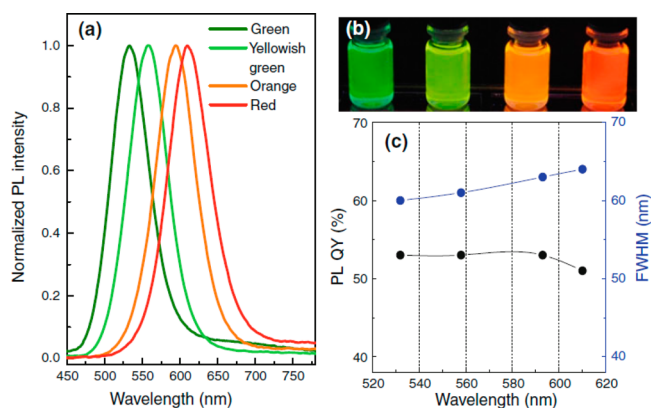
Figure 36. InP/ZnS NCs synthesized using $P(NMe_2)_3$ as the phosphorus precursor. (a) PL spectra; (b) photograph of different sized samples; (c) variation of the PL QY and fwhm as a function of the emission wavelength. Reproduced with permission from ref 326. Copyright 2013 Springer Science+Business Media Dordrecht.

This method was further developed by Hens and co-workers to obtain narrower emission line widths (46−63 nm) and higher QYs (up to 60%) at quasi-quantitive reaction yield.[329] In the latter case, the size of the InP NCs was controlled by using

Table 5. Representative Articles on the Synthesis of Highly Luminescent InP Based NCs

		core synthesis						
year	method	precursors	ligands/additives	temp (°C)	time (min)	shell material	max. PL QY	ref
2007	hot injection	P(TMS)₃/In(OAc)₃	MA/octylamine	188−178	60	ZnS	40%	315
2008	hot injection	P(TMS)₃/InCl₃	SA, HDA/zinc undecylenate	280−220	20	ZnS	60%	316
2008	heat up	P(TMS)₃/In(OAc)₃	MA/zinc stearate	25−300	3−20	ZnS	70%	313
2012	hot injection	P(TMS)₃/In(OAc)₃	PA/Zn(OAc)₂	300−230	120	GaP/ZnS	85%	310
2012	hot injection	P(TMS)₃/In(OAc)₃	MA/octylamine	200	60	ZnSe/ZnS	55%	308
2013	hot injection	P(TMS)₃/InCl₃	oleic acid/zinc oleate	280	10	ZnSeS	81%	309

different In halides, namely $InCl_3$, $InBr_3$ and InI_3. InI_3 gave the smallest size while larger sized InP NCs were obtained with $InCl_3$. The InP NCs were overcoated with both ZnS and ZnSe shells and the authors reported that the ZnS shell resulted in a broader emission line width but larger QY compared to the ZnSe shell. This difference was attributed to the larger lattice mismatch between InP and ZnS compared to InP and ZnSe (vide supra).[329] There are several other synthetic schemes alternative to the $P(SiMe_3)_3$ method in the literature and a few of them, affording precise control over the size and hence the optical properties of the InP NCs, will be presented here. For more details the interested reader is referred to three review papers focusing on III−V semiconductor NCs.[330,331,366] Liu et al. obtained size-tunable InP NCs based on coreduction of indium acetate and phosphorus trichloride using $LiBHEt_3$ as reducing agent in ODE in the presence of stearic acid.[332] Another example is the slow and continuous injection of PH_3 gas into a ODE solution containing indium acetate and myristic acid.[319] With this method larger sized InP NCs with an emission up to 750 nm could be synthesized.[333] Quantum-dots with absorption/emission in the near-infrared (NIR) window (700−1600 nm) are important for applications in in vivo biological imaging, solar cells and telecommunications. As pointed out earlier, the synthesis of larger sized (>5 nm) InP NCs is a synthetic challenge. Strategies to overcome this problem include the use of more stable P precursors,[324,325] the increase in ligand concentration,[315] the use of multiple precursor injections[316] as well as transmetalation reactions.[334] In the latter case, applicable to different types of III−V compounds, first elemental In or Ga is produced through the reaction of the metal chloride with butyllithium. In the second step, Mg_3P_2 or Mg_3As_2 undergo the transmetalation to afford the according III−V compound NCs. Interestingly, the InP NCs obtained by the transmetalation method were in the size range 8−9 nm, which presents the largest size reported for this system. However, the optical properties of the as-synthesized NCs were poor; size selective precipitation methods had to be used to obtain better defined absorption spectra and HF-etching to reveal a broad photoluminescence with a PL QY of 10%.[334] It should be underlined that the described transmetalation method is one of the very rare wet-chemical syntheses giving access to colloidal GaAs NCs. Furthermore, the obtained size distribution is lower than with previously reported methods, many of which rely on highly reactive and pyrophoric precursors.

4.2.5. Gallium Phosphide. Historically, Dougall and co-workers first reported size-dependent optical properties of GaP NCs synthesized in zeolite by reacting Me_3Ga and PH_3 gas.[335] Nozik and co-workers synthesized for the first time colloidally stable GaP QDs by carrying out Wells' dehalosilylation reaction between $GaCl_3$ and $P(SiMe_3)_3$ in a mixture of TOPO and TOP heated to 270−320 °C. The synthesized NCs were amorphous and in order to improve crystallinity, the amorphous material in TOPO was heated at 360 °C for 3 days.[336] There are several other reports on the solution synthesis of GaP NCs via reaction between $GaCl_3$ and (Na/K)$_3$P or $P(SiMe_3)_3$, summarized in ref 331. Nearly monodisperse GaP NCs have been obtained through the ion-exchange reaction between Cd_3P_2 QDs and Ga^{3+} ions in TOP.[337] In the transmetalation method mentioned above, Lauth et al. synthesized crystalline GaP NCs of low size distribution by reacting Mg_3As_2 with in situ generated Ga(0) species, prepared from n-butyllithium and $GaCl_3$.[334]

4.2.6. Indium Arsenide. An alternative III−V semiconductor material for NIR applications is InAs, which has a smaller band gap than InP (Table 4) and gives access to a spectral range of emission of approximately 700−1400 nm. Once again Wells' dehalosilylation reaction has been successfully applied in initial syntheses. Alivisatos and co-workers prepared InAs NCs by reacting $InCl_3$ and $As(SiMe_3)_3$ in TOP at elevated temperature (240−265 °C).[338] Following post-synthetic size-selective precipitation, they obtained InAs NCs with sizes ranging from 2.5 to 6 nm and with a size distribution of 10−15%. In parallel to the development observed in the case of InP, Battaglia and Peng later also introduced the non-coordinating solvent ODE in the InAs NC synthesis.[317] The obtained absorption spectra, with excitonic peaks in the range of around 650−800 nm exhibited also features from excited states at higher energy, indicating a narrow size distribution, albeit the description was extremely brief. As described in subsequent studies of the same group, the direct translation of the synthetic scheme used for InP NCs in InAs, resulted to the initial formation of small "magic-sized" nanoclusters (<1 nm).[339] Similar to the case of $P(SiMe_3)_3$, used as the pnictogen precursor in InP syntheses, $As(SiMe_3)_3$ decomposes very quickly in the initial stages of the reaction and Ostwald ripening becomes the predominant growth mechanisms. Therefore, the accessible size range of the obtained InAs NCs is very restricted. A way to circumvent this shortcoming is by maintaining a high monomer concentration via secondary injection of precursor solution during the growth stage of the NCs.[89] Under optimized conditions size focusing occurs and with this strategy the size distribution of InAs NCs could be improved from initial 20% to 8.7%.[89,340] As discussed in section 3.1, under diffusion controlled growth of the NCs, size focusing occurs when the concentration of monomers is high enough to promote growth of smaller NCs at a higher rate than that of the larger particles.[110] In this case, the longer growth stage and profuse monomer supply allow the smaller NCs to "catch up" with the larger ones. However, when the monomer concentration is low, Ostwald ripening leads to the broadening of the size distribution, defocusing occurs.[341] The concept of generating monodisperse NCs by manipulating the growth kinetics was further explored by Xie and Peng by introducing the so-called "self-focusing" concept.[339,342,343] In this technique, a high particle concentration is maintained to force the diffusion spheres of adjacent particles overlap. Consequently, slightly higher monomer concentration near the surface of the smaller "shrinking" NCs should rapidly move toward the surface of the larger ones due to the concentration gradient. The smaller NCs are therefore forced to dissolve completely while the larger ones grow at a relatively slow rate resulting in nearly monodisperse particles. By optimizing the concentration of the initially formed InAs nanoclusters and reaction temperature, InAs NCs in a size range of 1−3 nm and with an emission range of 700−1400 nm were obtained.[339] The PL QY of the latter could be improved from <1% to 90% by growing a shell of lattice-matched CdSe on their surface. Prior to this, Cao and Banin had systematically investigated various shell materials with InAs core NCs, including III−V (InP and GaAs) and II−VI (CdSe, ZnSe, and ZnS) semiconductors.[344] Enhancement of the QY up to 8% for InAs/ZnS and 20% for InAs/ZnSe or InAs/CdSe were observed (lattice mismatch: 10.7%, 6.4%, 0). PL quenching was observed with InP (lattice mismatch 3.1%) whereas the optical results of GaAs were not discussed. Zimmer et al. synthesized water-soluble NIR

emitting InAs/ZnSe core/shell NCs with small hydrodynamic diameter and performed in vivo studies in mice.[345] With the goal of reducing the lattice mismatch and hence strain in the core/shell system, the same group developed the synthesis of alloyed $InAs_xP_{1-x}$/InP/ZnSe core/shell NCs with tunable emission in the NIR region suitable for biological imaging.[346] Following the same strategy, Peng et al. introduced a single-pot synthesis of InAs/InP/ZnSe core/shell/shell NCs, with PL QY in the range 40%−90%.[347] One advantage of InAs-based NCs over InP-based ones for in vivo biological imaging applications is that, due to their smaller band gap, NIR emission can be achieved at lower particle sizes. Furthermore, with InAs QDs wavelengths in the range of 650−900 nm are easily accessible where light absorption and scattering by hemoglobin and water are minimized, enabling larger imaging depths.[348] Optimization of the hydrodynamic diameter is extremely important for in vivo applications as NCs circulation in the body and clearance depend on their hydrodynamic size.[349] In particular, an upper cutoff level for renal clearance of 5.5 nm hydrodynamic diameter has been identified.[350] InAs NCs have also been considered as a potential absorber material for photovoltaic applications due to their narrow band gap, which can be tuned to meet the optimum range (1.1−1.4 eV) desired for solar cells.[7] In this context, InAs NCs are also a potential candidate for multiple exciton generation showing a low threshold for carrier multiplication (CM), i.e., the generation of more than one electron per incident photon. The CM threshold is expected to be even smaller in InSb based materials due to a further decrease in the ratio m_e/m_h (∼0.03).[351]

4.2.7. Indium Antimonide. InSb is in several respects an outstanding III−V compound: it exhibits the largest electron mobility (78 000 cm^2 V^{-1} s^{-1}) and exciton Bohr radius (60 nm), narrowest band gap (0.18 eV at 300 K), and a high static dielectric constant (17.9). By consequence InSb is an ideal candidate for mid-IR optoelectronic applications, in replacement of Cd-, Pb-, and Hg-based materials. As we have seen above, the majority of successful synthesis schemes for obtaining high quality InP and InAs NCs are based on Wells dehalosilylation reaction. However, due to the decreased stability and tedious synthesis of $Sb(SiMe_3)_3$ the preparation of InSb NCs using this Sb source has not become popular. Attempts by Evans et al. did not succeed in obtaining InSb NCs showing the expected optical and structural properties.[352] On the other hand, it has been shown that both PH_3 and AsH_3 gas constitute suitable pnictogen precursors for the synthesis of InP and InAs NCs.[319,353] Following this route, Maurice et al. used SbH_3 gas (stibine) as Sb source to obtain well-crystallized InSb NCs of around 8−9 nm diameter.[354] However, no photoluminescence signal could be obtained presumably due to surface oxidation. Talapin and co-workers developed a method to obtain crystalline, monodisperse InSb NCs with well-defined optical properties using antimony amido complexes.[355] Their synthesis involved simultaneous coreduction of $Sb(N(SiMe_3)_2)_3$ and $InCl_3$ in oleylamine in the presence of a strong reducing agent, $LiEt_3BH$. After size-selective precipitation it could be shown that the excitonic peak position varied from 1200 to 1750 nm for NC sizes increasing from 3.3 to 6.5 nm. Two amido precursors, namely $In(N(SiMe_3)_2)_3$ and $Sb(NMe_2)_3$, have been combined in the method reported by Yarema and Kovalenko, also yielding sub-10 nm InSb NCs.[356] Here no additional reducing agent is required and a weak PL signal peaking at 1900 nm has been observed for 8.5 nm InSb NCs. The authors also report a zinc blende/wurtzite poly-morphism, which can be controlled by changing the In/Sb precursor molar ratio. Both of the above methods use silylamides which are not commercially available. Tamang et al. recently demonstrated that InSb NCs can be synthesized by directly reacting the commercially available precursors $InCl_3$ and $Sb(NMe_2)_3$ in the presence of an activating base for the In precursor, such as $LiN(SiMe_3)_2$ or $nBuLi$.[357]

4.3. Metal Chalcogenide NCs

Throughout this section the abbreviations in Table 6 will be used for the chemical compounds occurring repeatedly.

Table 6

compound	abbr.	compound	abbr.
1-octadecene	ODE	trioctylphosphine	TOP
oleic acid	OA	trioctylphosphine oxide	TOPO
oleylamine	OLA	dodecanethiol	DDT
hexadecylamine	HDA	thioacetamide	TAA

4.3.1. Chalcogenide Precursors. Compared to the pnictogens discussed above, a much larger variety of anionic precursors have been developed in the case of metal chalcogenide NCs. In the simplest form, powders of elemental S, Se, or Te are applied, generally after "solubilization" in appropriate organic compounds. Elemental (yellow) sulfur occurs in its main allotrope as S_8 rings, while (gray) selenium and tellurium consist of polymeric chains. To transform them into soluble molecular precursors, they are usually mixed and eventually heated with a Lewis base like OLA or TOP. Unsaturated organic solvents, such as ODE, can also transform elemental chalcogens into reactive species, and even saturated solvents react upon heating. In the following we give a short overview of these different reactions, many of which have been discussed in details by Owen and co-workers.[358] Their knowledge is fundamental for the understanding of the syntheses methods for metal chalcogenide NCs described subsequently.

4.3.1.1. Reaction of S, Se, and Te with Tertiary Phosphines. Tertiary phosphines R_3P (R = octyl, butyl) are very popular compounds for the preparation of chalcogenide precursors due to the facile approach and their physicochemical properties (low melting point, high boiling point). However, they also present some drawbacks such as air-sensitivity and high price, which can become limiting when the scale-up of syntheses is required. In the case of elemental sulfur and selenium, the oxidation to afford the desired phosphine chalcogenides $R_3P=E$ (E = S and Se) takes place within minutes (S) or hours (Se).[359,360] Often the parent phosphine is used in excess in NC synthesis; this excess influences the reaction kinetics. In the case of phosphine tellurides, an equilibrium between R_3PTe and elemental Te is established within hours, which depends on the nature of the substituents R; by consequence pure trialkyl- and triarylphosphine tellurides are unstable.[361] The binding strength and hence reactivity of the three tertiary phosphine chalcogenides follows the trend expected from the overlap of the implied atomic and molecular orbitals $R_3PTe < R_3PSe < R_3PS$. For R = butyl, P=E bond dissociation energies of 52, 75, and 96 kcal/mol have been reported for E = Te, Se, and S, respectively,[359] and the P=E bond length determined from single crystal structures situates itself between a single and a double bond. The $R_3P=E$ species can coordinate Lewis acids like metal atoms through the chalcogen atom in an unidentate

or bridging (between two metal centers) way, which causes a decrease in the P=E bond strength.[358] Cleavage of the P=E bond occurs via two pathways: (i) in an acid/base mechanism, E^{2-} is transferred while the remaining phosphine is oxidized to phosphine oxide;[103,104,362] (ii) Elemental E^0 is transferred in a redox mechanism. In the first case, the cleavage of the TOP=Se bond in the presence of cadmium carboxylate or phosphonate has been studied by means of NMR investigations, showing that the conversion increased from 70 to 80% in anhydrous conditions to 100% upon addition of a controlled amount of water.[104] In the second case, the metal atom is formally in the zero oxidation state right from the beginning (e.g., metal carbonyl complexes) or reduced to this form (e.g., decomposition of metal alkyls, chemical reduction) prior to reaction with R_3PE, affording $ME + R_3P$.[358,363]

4.3.1.2. Reaction with Primary Amines. As mentioned already in section 4.1, OLA has become a very versatile reagent in NC synthesis, which can serve as solvent, ligand and sometimes as reducing agent in the reaction.[271] Nonetheless investigations of the compounds formed upon "dissolving" the chalcogens in OLA are scarce. Ozin and co-workers used 1D and 2D NMR experiments for the identification of the formed products in mixtures of sulfur and octylamine, acting as a higher purity (99%) model for OLA (70%).[364] They showed that at low temperatures (<80 °C, sonication), octylammonium polysulfides were formed. Upon heating to 130 °C for 2 h, four new products have been detected (Figure 37).
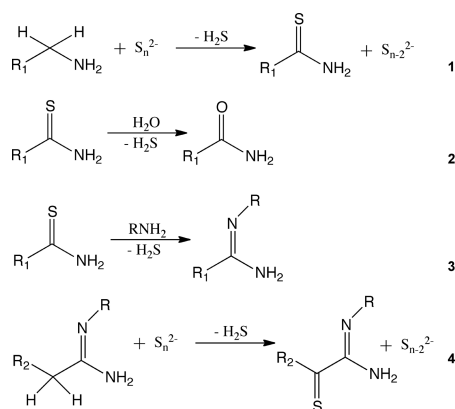

Figure 37. Reaction pathways for an octylamine/sulfur mixture heated to 130 °C for 2h (R: C_8H_{17}, R_1: C_7H_{15}, R_2: C_6H_{13}). Reproduced with permission from ref 364. Copyright 2011 American Chemical Society.

In particular, octanethioamide (**1**) is formed, which hydrolyses in the presence of water traces to yield octaneamide (**2**). Excess octylamine reacts with octanethioamide to form N-octyaloctanamidine (**3**). The latter can react with polysulfide ions to afford α-thioketoamidine (**4**). All these reactions form H_2S, which is considered as the actual sulfur source for metal sulfide NC formation using this approach. In another study Peng and co-workers confirmed H_2S generation in the course of the reduction of elemental sulfur with octylamine, and the synthesis of CdS NCs of low size distribution could be achieved at lower temperature (100 °C) in toluene.[365]

4.3.1.3. Reaction with ODE and Other Types of Hydrocarbon Solvents.[358] The reduction of elemental sulfur in alkanes and alkenes proceeds via several steps involving radical dehydrogenation, and thiol−ene addition and elimination reactions leading to oligosulfides, hydrogen sulfide and

thiophene derivatives (Figure 38). The conversion rate depends on the strength of the involved C−H bonds; therefore alkenes
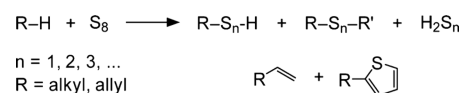
Figure 38. Reduction of elemental sulfur by hydrocarbons. Reproduced with permission from ref 358. Copyright 2013 American Chemical Society.

react faster than alkanes. The reaction is also accelerated in the presence of Lewis acidic substrates absorbing H_2S, like zinc oxide.

Heating of elemental selenium in hydrocarbon solvents like ODE, OA, hexadecane, paraffin or TOPO produces H_2Se gas. Therefore, the loss of H_2Se influences the reactivity of the remaining Se precursor solution. It has been observed that after prolonged heating for 4 h to 200 °C gradual deactivation occurred.[367] Nonetheless the initially prepared solution showed higher reactivity than TOPSe in CdSe NC synthesis.[368] Activation of tellurium in ODE has not been reported.

4.3.1.4. Alkylthiols. Alkylthiols have become an increasingly popular sulfur source due to the ready commercial availability of a large palette of compounds. In addition, if the organic substituent is properly chosen, they can also act as the reaction (co)solvent and as stabilizing ligand for the NC surface. Playing this triple role, DDT has encountered a large success in the synthesis of ternary $CuInS_2$ NCs.[369] In the first step of the reaction with a metal the alkylthiol forms the corresponding metal thiolate, which can then undergo thermal decomposition at higher temperatures to afford the desired metal sulfide.[370] In the case of $CuInS_2$ NCs, DDT also helps mediating the reactivities of the two metal precursors. Heat-up approaches are well adapted for this kind of reaction. The decomposition temperature of the metal thiolate depends on the nature of the metal: softer Lewis acids interact more strongly with the thiolate group and hence weaken the C−S bond, which results in lower temperatures of decomposition (e.g., < 200 °C for Cu^+ and Ag^+). To the contrary harder Lewis acids like Zn^{2+} require higher reaction temperatures.

4.3.1.5. Dithiocarbamates and Xanthates. Dithiocarbamates and xanthates coordinate metal centers in a similar way through their carbodithioate function and differ in the carbon substituent: alkoxy in the case of xanthates, primary or secondary amine in the case of dithiocarbamates (Figure 39). They are of great importance for the preparation of single-molecular precursors, as after coordination of a metal atom,
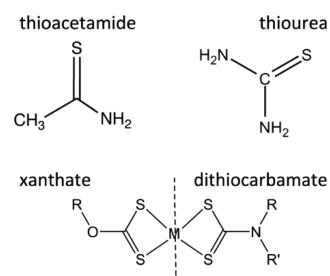
Figure 39. Top: Structures of thioacetamide and thiourea used as sulfur precursors in metal sulfide NC synthesis. Bottom: Xanthate and dithiocarbamate coordination of a metal ion M (R, R′ = alkyl or aryl group, R′ can also be H).

they can simply be decomposed thermally to afford the desired metal sulfide NCs.[371] In principle, aliphatic or aromatic substituents could also be used, however, their air-sensitivity and more complex preparation constitute drawbacks with respect to xanthates and dithiocarbamates.[372] The same applies for the corresponding Se- or Te-based compounds; reactions for synthesizing selenoxanthates or diselenocarbamates generally imply the use of highly toxic starting reagents like carbon diselenide, CSe_2.

4.3.1.6. Other Types of Chalcogen Precursors. Ammoniumsulfide "dissolved" in OLA has been proposed by Robinson and co-workers 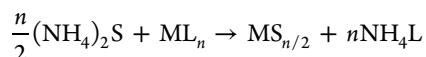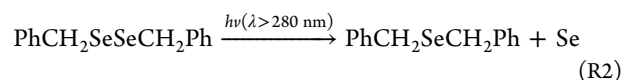as sulfur source.[373] In contrast to the above-discussed transformation of elemental sulfur by primary amines, the authors proposed a direct salt elimination without implication of OLA as the mechanism:

$$\frac{n}{2}(NH_4)_2S + ML_n \rightarrow MS_{n/2} + nNH_4L$$

On the other hand, more detailed investigations of the precursor solution and its transformation upon heating were not provided. This sulfur source turned out to be highly reactive toward various metal salt solutions, giving access to metal sulfide NCs of low size distribution and high reaction yields.

SeO_2 has a polymeric structure and has been proposed in combination with ODE for the synthesis of CdSe NCs by Cao and co-workers.[374] A stock solution of SeO_2 prepared by heating with ODE at 240 °C has been found to be stable for months. The detailed mechanism of SeO_2 activation is unknown, but reduction to $Se^{(0)}$ by ODE is presumed. Bis(trimethylsilyl)chalcogenides are highly reactive chalcogen sources, which readily react with many transition and main group metal salts M–X (X = halide, acetate, and so on). The energetically favorable formation of the Si–X bond is the driving force in these reactions, just like in Wells' dehalosilylation reaction for producing metal pnictides, discussed above. One drawback of these compounds is their air- and moisture sensitivity, and the tellurium species decomposes even when stored under inert atmosphere at −20 °C in the dark. $Te(SiMe_2{}^tBu)_2$ can be used as a more stable alternative.[375] Thiourea (Figure 39) and selenourea are common chalcogen precursors for NC preparation in aqueous media where the hydrolysis of the C–S or C–Se bonds is accelerated under basic conditions. Fewer reports on their use in dry organic media exist, mainly for zinc and cadmium chalcogenide nanostructures. One notable recent study concerns the use of a library of differently substituted thioureas whose conversion rate could be controlled over several orders of magnitude giving access to synthetic schemes for monodisperse NCs in a large range of sizes obtained in quantitative yield.[106] Thioacetamide (TAA) is a very well-known chemical used in place of gaseous H_2S in the practical work of undergraduate chemistry classes for precipitating more than 20 metal sulfides. Its hydrolysis in aqueous solution is controlled by heating. TAA can also be used in organic solvents and dissolves in Lewis bases like OLA or TOP. Its decomposition implies the release of H_2S and acetonitrile as possible side products. It has been successfully applied for example in the synthesis of SnS NCs. Diorganyl dichalcogenides (R–E–E–R, where E = S, Se, or Te and R = alkyl, allyl, benzyl, or aryl) have emerged as alternate chalcogenide precursors and their use in NC synthesis has been reviewed by Brutchey in 2015.[376] Ph_2Se_2 and Ph_2Te_2 have first been

applied in the synthesis of SnSe and SnTe nanoparticles in 2002.[377] In the meantime a large number of papers has described the use of differently substituted diorganyl dichalcogenides in the synthesis of binary, ternary and multinary metal chalcogenide NCs of controlled size and shape. The decomposition of the precursors can be triggered thermally (R1) or photolytically (R2):[376]

$$Ph_2CHSeSeCHPh_2 \xrightarrow{\Delta} Ph_2CHCHPh_2 + 2Se \qquad (R1)$$

$$PhCH_2SeSeCH_2Ph \xrightarrow{h\nu(\lambda>280\ nm)} PhCH_2SeCH_2Ph + Se \qquad (R2)$$

These reactions yield elemental selenium, monoselenide and organic side products through the radical scission of the Se–Se and Se–C bonds. Vela and co-workers reported a combined experimental and DFT study correlating the bond strengths in the precursor molecules with the size and shape of the obtained CdSe and CdS NCs.[378] They demonstrated that the carbon–chalcogen bond determines the reactivity of the dichalcogenide precursor, while the chalcogen–chalcogen bond strength remains essentially constant within the disulfide or diselenide series. Among the molecules studied, the phenyl substituted dichalcogenides exhibited the strongest carbon–chalcogen bonds and hence least reactivity, while the weakest bonds were observed in allyl-substituted compounds. Among the advantages of this type of precursors is the fact that a broad variety of differently substituted dichalcogenides are commercially available. Furthermore, they constitute the only family of precursors, which can be used for the synthesis of all types of chalcogenide compounds, i.e., metal oxides, sulfides, selenides, and tellurides.[376]

4.3.2. Binary Metal–Chalcogenide NCs. Binary metal–chalcogenide semiconductors of general formula M_xE_y (M = Cd, Hg, Pb, Zn, Ag, Cu, Mn, Sn, Ni, Bi, Eu, and so on, and E = S, Se, and Te) constitute a large class of materials, and for numerous examples, syntheses in the form of colloidal NCs have been reported. Since the pioneering works performed by Ekimov,[379] Efros,[380] and Brus[381] on Cd-chalcogenides in the early 1980s, it has been shown that metal chalcogenide NCs exhibit unique chemical and physical properties, which have enabled their utilization in various applications including electroluminescent devices,[5,382] solar cells,[383] photodetectors,[384,385] and catalysis.[386] More recently, the development of efficient approaches for the functionalization of NCs has allowed the increase of the range of their applications to chemo-sensing[387,388] and biomedical imaging.[389,390] Until today CdS, CdSe, and CdTe NCs remain the most widely studied representatives of this family, due to their range of emission covering the whole visible and NIR region, their high PL quantum yields approaching unity after surface passivation, their high photostability, and, as discussed in section 3, their relative ease in preparation. With the increasing maturity of NC based applications the demand for nontoxic compounds complying with national and international regulations is rising. This is surely one of the reasons for the strongly growing research interest in the development of alternative materials; binary and multinary metal chalcogenide NCs play an important role in this field. Due to the chemical similarities between various transition metals, it can be anticipated that the preparation of NCs of other types of metal chalcogenides ME is achievable using similar synthetic pathways as in case of Cd- and Pb-based compounds. Historically, the synthesis of

Table 7. Overview of the Principal Synthesis Methods Used for the Preparation of Binary Metal Chalcogenide NCs[a]

compound	crystalline phase	method	reagents	temp	nanocrystal shape and size	ref
ZnS	ZB	HU	ZnCl2;S; OLA	340 °C	spherical: 8–11 nm	398
		HU	Zn(OA)2; OLA; DDT	310 °C	spherical: 7–10 nm	371
	WZ	HU	Zn-(DDTC)2; OA, OLA, ODE	300 °C	spherical: 9.5 nm	399
	H	HU	Zn-(DDTC)2; OLA, ODE	300 °C	nanowires: 300 × 4.4 nm	400
	ZB	HU	Zn-(PhDTC)-Phen/Pyr TOP, HDA	180–220 °C	spherical: 2.9–3.5 nm	401
	N.A.	HU	Zn-(HTC/HDX)2 HDA	125/70 °C	spherical: 4.5 nm	402
	ZB+WZ	HI	ZnCl2, S, DDT, OLA/OA	200 °C	spherical: 2.2–7 nm	403
	ZB	HI	Zn(OA)2, DDT, ODE	260 °C	N.A.	
	WZ/ZB+WZ	HI	ZnCl2, DDT, ODE			
MnS	WZ	HU	MnCl2;S; OLA; (M/E = 1:1)	240–280 °C	nanorods: 20 × 37–20 × 60 nm	398
		HU	MnCl2;S; OLA; (M/E = 2:1)		bullet shaped: 17 × 44 nm	
		HU	MnCl2;S; OLA; (M/E = 3:1)		hexagonal: 20–25 nm	
	FCC	HU	Mn(OA/St)2 or Mn(OA) (OH), S, ODE (M/E < 0.5)	250–320 °C	octahedral: 9–30 nm	404
	N.A.	HU	Mn(OA)2; OLA; DDT	280 °C	bullet-shaped: 10–15 nm	371
	N.A.	HU	Mn-(HDX)2 TOA	150 °C	faceted <20 nm	401
	RS	HI	Mn-(DDTC)2 HDA, ODE	250 °C	cubes: 30 nm	405
	RS			180 °C	spherical: 2.5 nm	
	ZB or WZ			150 °C (2 h)	spherical: 2.5 nm	
	WZ			120 °C	wires: 2.5 nm (diameters)	
CuS	M (Ch)	HU	Cu(acac)2; S; OLA (M/E < 2.25)	200–260 °C	spherical: 12 nm	406
	H (Cv)	HU	CuCl; S; OLA; ODE	130–180 °C	nanospheres: 23.2 nm	407
			CuCl; S; OLA; ODE + CuCl, S, OLA (1–3 cycles)		nanoprisms:30–60 nm	
	Non specified	HU	Mn-(HDX)2 TOA	150 °C	mixture of nanorods and nanospheres ~20 nm	401
Cu2S	Chalcocite	HU	Cu-(OA/acac/OAc)2; OLA; DDT	200–230 °C	spherical: 3–20 nm	371,408–411
				140 °C	nanodiscs: 20–50 nm	
	H	HU	Cu-(DTTC); OA, DDT	220 °C	spherical: 6.5 nm	399
	H	HI	Cu(OAc), TOPO, ODE, DDT	160–220 °C	spherical: 3–6 nm; discs: up to 18.2 × 9.6 nm	412
Cu7S4	M	HU	Cu-(DTTC); OA	280 °C	spherical NP: 26 nm	399
Ag2S	FCC	HU	Ag(NO3/OAc); DDT	200–260 °C	spherical: 3–18 nm	409,413
	M	HU	Ag-(DTTC); OA, ODA/OLA, ODE	200 °C	spherical: 10.2 nm	399,414
	M	HU	Ag-(DTTC); OA	200 °C	spherical: 40 nm	414
	M		Ag-(DTTC); OA, TOPO or ODA, ODE		spherical: 20 nm	
	M	HU	Ag-(DTTC); OA, DDT, ODE	130–230 °C	spherical: 2.4–7 nm	415
	M	HI	Ag(MA), S(TMS)2, + Ag(OAc) [for growth]	50–120 °C	spherical: 1.5–4.6 nm	416
	M	HI	Ag(SCOPh), TOP	160 °C	spherical: 25 nm	417
NiS	Rh	HU	Ni(NO3); DDT; M/E = 1:2	150 °C	nanorods: 33 × 8.1 nm; nanoprisms: 6 nm	409,418
	N.A.	HU	Ni-(HDX) TOA	150 °C	mixture of nanorods and nanospheres <20 nm	401
Ni3S4	N.A.	HU	Ni-(NO3); DDT; OA, OLA	250 °C	irregular: 20–50 nm	409,419
Bi2S3	O (Bim)	HU	Bi-(OctA)2; DDT	150 °C	nanorods: 11 × 74 nm	420
				225 °C	nanowires: μm range	
	O (Bim)	HU	Bi-(DDTC)3; OLA, ODE	200 °C	nanoplates: 16 × 80 nm	399
SnS	O	HU	Sn-(DDTC)3; OLA, ODE	300 °C	sheets: 7000 × 3000 × 20 nm	399

Table 7. continued

compound	crystalline phase	method	reagents	temp	nanocrystal shape and size	ref
SnS$_2$	O (Herz)	HI	SnCl$_2$, OA, OLA, DDT	220 °C	sheets: 100 × 100 × 25 nm	421
			SnCl$_2$, OA, OLA, OctT	200 °C	polyhedral: around 100 nm	
			SnCl$_2$, OA, OLA, OctT	150 °C	flowerlike agg, NC range 5 nm	
	H	HU	Sn-(DDTC)$_3$, OA, OLA, ODE	280 °C	nanoplates: 150 × 6 nm	399
EuS	C	HU	Eu(DTC)biPy, OLA, TOP	280 °C	spherical: 5 nm	422
	RS	RS	Eu(HDX/DTC)BiPy, OLA, TOP	220 °C	spherical: 7 nm	
	RS	RS	Eu(HDX/DTC)BiPy, OLA, TOP	280 °C	nanocubes: 20–50 nm	
ZnSe	WZ	HU	Zn(NA)$_2$, Se, OctA, OLA	20–160 °C	spherical: <2 nm	423
	WZ			160–220 °C	spherical: 2–3 nm	
	ZB			>220 °C	rods: diam =2 nm	
	ZB	HU	Zn(St)$_2$, Se, ODE	290 °C	spherical: 2.9–6.2 nm	424
	ZB	HU	Zn(OA)$_2$, TOP/DPP-Se (+DPP/TOP)	310 °C	spherical: 3.1 nm	124
	ZB	HI	Zn$_{10}$Se$_4$(SPh)$_{16}$ HDA	220–280 °C	spherical: 2–5 nm	425
	ZB	HI	Zn(OA)$_2$ Se, ODE	240–330 °C	spherical: 3–8 nm	426
	ZB	HI	Zn$_5$(CO$_3$)$_2$(OH)$_6$ OA, Se, ODE	270 °C	spherical: 3.4 nm	427
	ZB	HI	Zn(OA)$_2$ Se, TOP, ODE	250–317 °C	spherical: 3–7 nm	428
	ZB	HI	Zn(Et)$_2$ HDA, TOP-Se	270 °C	spherical: 6 nm	429
	ZB	HI	Zn(NA)$_2$ Se, OLA, OctA	110–230 °C	spherical: 2–3 nm	423
	ZB	HI	Zn(St)$_2$ Se, NaBH$_4$, OLA	240 °C	spherical: <5 nm	430
	WZ	HI	TOP-EDSC-Zn, TOPO	250 °C	spherical: 3.8–6 nm	431
	ZB	HI	bPhSe-Zn-TMEDA, TOPO	320–385 °C	spherical: 2.7–5 nm	432
Cu$_x$Se	C (Berz)	HU	Cu(St)$_2$, OLA, OA Se, ODE	120–200 °C	4.5–18 nm (Cu:OLA:OA:Se)	433
					hexagonal: 1:2:6:1	
					octadecahedral: 1:2:2:1	
					Pyramidal: 1:6:6:1	
Cu$_2$Se	C	HI	CuCl, OLA, Ph$_2$Se$_2$, ODE	200–300 °C	octahedral: 25–155 nm	434
	C	HU	Cu(NO$_3$), Se, ODA	200 °C	spherical: 10 nm	435
Cu$_7$Se$_4$	C	HI	Cu(DPSe), BH$_4$, DDT	150 °C	irregular shaped aggregate: 100–500 nm	436
Ag$_2$Se	O	HU	Ag(NO$_3$), Se, ODA	200 °C	spherical: 10 nm	435
	O	HU	Ag[(L-HBr)$_2$]BF$_4$, TOP, OA	200 °C	quasispherical: 17 nm (polydisperse)	437
	T	HI	TOP-Ag, TOP-Se/Te, ODA, OA, ODE	130–150 °C	spherical: 2.8–7.5 nm	438
			TOP-AgCl, TOP-Se/Te, ODA, OA, ODE		spherical: 7.5–10.8 nm	
	Unknown phase	HI	AgNO$_3$, Se, NaBH$_4$, OLA	100 °C	15–10 nm	430
	O	HI	Ag(DPSe), BH$_4$, DDT	150 °C	spherical aggregates: 110–170 nm	436
					ellipsoids aggregates: 100 × 200 nm	
Ag$_2$Se–Te	T	HI	TOP-Ag, TOP-Se/Te, ODA, OA, ODE	160–150 °C	spherical: 6.5 nm	439
Co$_2$Se	O (bipyr)	HU	Co[Se$_2$PPr$_2$] HDA	320 °C	spherical: nondetermined	440
SnSe	O (bipyr)	HI	[TMSA]Sn, OLA, TOP-Se + OA (after nucl.)	65–175 °C	spherical: 4–10 nm	441
	O	HI	SnCl$_2$, OA-Se, OLA, OA, ODE	156–170 °C	spherical: 7.5–9.2 nm	421
			SnCl$_2$, OLA-Se, OA, ODE	150–162 °C	nanoplates	
			SnCl$_2$, TOP-Se, OLA, OA, ODE	217 °C	nanosheets	
	O	HI	Sn$_6$O$_4$(OH)$_4$ OLA, OA, Su	110–140 °C	spherical: 7–20 nm Sn/Se = 1:1	442
					Nanocubes: 19.5 nm Sn/Se = 2:1	

Table 7. continued

compound	crystalline phase	method	reagents	temp	nanocrystal shape and size	ref
	O (Sn/Se = 1:1)	HI	SnCl₂, tBu₂Se₂, DDA, DDT	110 °C	24 nm Sn/Se = 1:2	443
	H (Bem) (Sn/Se = 2:1)			180 °C	irregular shape ~19 nm	
NiSe	H	HI	Ni(Se₂PR₂)₂, TOP, HDA/TOPO	200–330 °C	spherical: 3.9–6.2 nm	444
	O	HI	NiCl₂, TOP-Se, HDA	160 °C	star-shaped and amorphous NPs: range 100–500 nm	445
NiSe₂	C	HI	NiCl₂(Se₂C₆H₅)₂, TOP, HDA	160 °C	pseudospherical: 10–15 nm	445
ZnTe	ZB	HI	Core: ZnEt₂, TOP-Te, HDA, ODE.	270 °C	dots: 2.2 nm	446
ZnTe/ ZnSe/ZnS	ZB		Shells: ZnEt₂, TOP-Se/TOP-S, HDA, ODE	220 °C	dots (not specified ~5–6 nm)	
ZnTe	ZB	HI	Zn(St)₂, TBP-Te, ODE (ODA)	300–320 °C; 270–285 °C	dots: 4.4–5.5 nm (without ODA); 5.5–9.0 nm (with ODA)	447
ZnTe/ZnS ZnTe	ZB	HI	Zn(St)₂, Te-TOP/TBP, ODE	270–300 °C	nanoflowers: 18–120 nm (aggr. of NC: 4–7 nm); dots: 9 nm (3 h growth)	448
	O		Zn(St)₂, Te-TOP, ODE	300–330 °C; 180–250 °C	nanorods: 25 × 450 nm; nanoflowers: 20 nm (aggr. of NC 4–7 nm)	
	ZB; O; O; ZB; ZB		Zn(St)₂, Te-TOP/TBP, ODE, OctA/DDA/ODA	180–290 °C; 180–300 °C; 300–270 °C	nanorods: 12 × 160 nm; nanorods: 18 × 300 nm; dots: 7 nm (growth 1 h); dots: 8 nm (OA), 14 nm (ODA); nanoflowers: 60 nm (aggr.of NC: 11 nm) (TOA)	
	ZB	HI	Zn(OAc)₂, TOP-Te + SHy, OA, benzyl ether	250 °C	spherical: 5 nm	449
	ZB	HU	ZnCl₂, TOP-Te (3 injections), OLA, benzyl ether	250 °C	tetrahedral: 5 nm	
	ZB		ZnCl₂, TOP-Te SHy, OLA, benzyl ether	150 °C	tanorods: 5 × 30 nm	
	WZ	HI	Zn(OAc)₂, TOP-Te + SHy, OLA, benzyl ether	160–300 °C	spherical: 3.5–7 nm	450
	WZ	HI	ZnCl₂, TOP-Te, OLA, Li(Et₃BH₄) NW + OLA	160–280 °C; 280 °C	nanorods: 3.5–7 × 21.5–140 nm; nanowires: diameter ~2 nm	451
	ZB	HI	ZnO, OA, OLA, DOPO-Te, PO	310 °C	nanorods: diameter ~3.5 nm; spherical: 7.5 nm	452
	C	HI	Zn(TePh)₂·[TMEDA], TOP, DDA	180–240 °C	spherical: 4.2–5.4 nm	453
	C	HI	Zn(TePh)₂·[TMEDA], DMHA, TOP, DDA	180–240 °C	nanorods: 25 × 200–700 nm	
Cu₂₋ₓTe	H	HI	Cu(acac)₂, TOP-Te, OLA	220 °C; <220 °C	multifaceted NCs: 4.4–8.8 nm; HNCs: 16.8 nm	454
	T	HI	Cu(acac)₂, TOP-Te, OA, DDT + Reduction (DIBAH)	160 °C	multifaceted NC: ~5–10 nm	455
	H	HI	Cu(acac)₂, TOP-Te, OA, DDT	175 °C; 185 °C	hexagonal nanodiscs: 2.2 × 12 nm; hexagonal nanodiscs: 3.2 × 8 nm	456
	T	HI	Cu(acac)₂, DOPO-Te, OA, OLA, PO	160/200 °C	spherical: 4.6/7.4 nm	452
Cu₂Te CuTe/ Cu₂₋ₓTe/ Cu₄Te₃	H	HI	CuCl, TOP-Te, + TOPO (solvent) + OLA (solvent) + OA (solvent)	180 °C; 230–250 °C	nanocubes: 32.8 nm; nanocubes: 54–104 nm; nanosheets (dimensions not specified)	457
SnTe	RS	HI	SnBr₂, TEA, TOP-Se, DMF	50–150 °C	spherical: 2.7–32 nm	458
	RS	HI	Sn(HMDS), TOP-Te, OLA, ODE	90–150 °C	spherical: 4.5–15 nm	459

Table 7. continued

compound	crystalline phase	method	reagents	temp	nanocrystal shape and size	ref
Ag$_2$Te	C	HU	[SnCl$_2$+Li[Et$_3$BH$_4$]+THF], Ph$_2$Te$_2$, Diglyme	165 °C	spherical agg. of NCs ~60 nm (high conc.) star-shaped agg. of needles ~15 × 40 nm (low conc.)	377
	M	HU	AgNO$_3$, TOP, Se,	160–190 °C	hexagonal discs: 20–40 × 5.5–8.1 nm + round discs: 32 × 5.5 nm irregular: size not specified (T > 175 °C)	460
	M	HI	AgNO$_3$, TOP-Te, OLA, DDT	170–190 °C	quasispherical: 5–15 nm	461
				110 °C	nanoplates (irregular)	
	T	HI	Ag(acac), DOPO-Te, OLA	150 °C	spherical: 9.2 nm	452
			Ag(acac), DOPO-Te, OLA, OA	120 °C	nanorods: 11.6 × 18.8 nm	
Bi$_2$Te		HI	Et$_2$BiTeEt, DIPB	100 °C	nanocubes: 100–500 nm	462
Bi$_2$Te$_3$	R	HI	Bi(OAc)$_3$, TOP-Te, OA, DDT	50–150 °C	amorphous (50 °C) nanospheres: 100 nm (NCs ~3–5 nm)	463
Bi$_4$Te$_3$	R	HI	Bi(NMe$_2$)$_3$, Te(SiEt$_3$)$_2$, DIPB (Bi/Te = 2:3)	100 °C	pseudocubic: 40 nm	462
	R	HI	(Et$_2$Bi)$_2$Te, DIPB	80 °C	amorphous aggregates: ~200 nm (composed from NC: 10–40 nm)	462
Sb$_2$Te$_3$	H	HI	Sb(OAc)$_3$, TOP-Te, OA, DDT	50–150 °C	amorphous (50 °C) nanospheres: (NCs ~5–7 nm)	463
	RH	HU	(Et$_2$Sb)$_2$Te, PVP, DIPB	160–200 °C	hexagonal nanoplates: 35 × 200–400 nm	464
	RH	HI	Ph$_2$SbTeR, (R = Ph, Et), TOP, OLA	250–300 °C	hexagonal nanoplates: 20–50 nm ×0,4–2 μm	465
GeTe	Amorphous	HI	GeI$_2$, TOP-Te, TOPO, DDT	250 °C	spherical: ~3.5 nm	466
	Amorphous	HU	Ge-HMDS, TOP-Te, DDT, TOP	250 °C	multifaceted: 8.5 nm	467
			Ge-HMDS, TOP-Te, OLA, TOP	250 °C	multifaceted: 17.4 nm	
			GeCl$_2$-Dioxane, TOP-Te, DDT	180 °C	multifaceted: 102 nm	
	Amorphous	HI	Ge-HMDS, TOP-Te, DDT, OLA	200 °C	spherical: 4.3–27.8 mn	468
			Ge-HMDS, TOP-Te, OLA	170 °C	spherical: 8.7–18.5 nm	
	RH	HI	Ge-HMDS, TOP-Te, OA, PVP-t	250 °C	octohedral: 70–100 nm	469
			Ge-HMDS, TOP-Te, OA, PVP	250 °C	multifaceted: 70–100 nm	
			Ge-HMDS, TOP-Te, NA, PVP/PVP-t	250 °C	2D sheets (triangle, hexagons, quadrilateral: 175–900 nm	
	RH	HI	GeI$_2$, TOP-Te, tBAB, TOP, octylether	180 °C	nanocubes: 1 μm	132

^{a}HU: heat up, HI: hot injection. WZ: wurtzite, ZB: zinc blende, C: cubic, T: tetragonal, H: hexagonal, O: orthorhombic, M: monoclinic, RH: rhombohedral, FCC: face centered cubic, Ch: chalcocite, Cv: covellite, Bim: bismuthinite, Herz: herzenbergite, Berz: berzelianite, Bern: berndtite. NP: nanoparticle, Agg.: aggregates. OLA: oleylamine, TEA: triethanolamine, HDA: hexadecylamine, EDA: ethylenediamine, ODA: octadecylamine, TOA: trioctylamine, DMAB: dimethylamine borane, tBAB: tButylamineborane, OctA: octylamine, TMEDA: tetramethylethylenediamine, DMHA: dimethylhexylamine, DIBAH: diisobutylaluminum hydride, HMDS: hexamethyldisilazane, DPP: diphenylphosphine, TBP: tributylphosphine, TOP: trioctylphosphine, DOP: dioctylphosphine TOPO: trioctylphosphine oxide, DOPO: dioctylphosphine oxide, BiPy: bipyridine, DDA: dodecylamine, SHy: superhydride, OA: oleate/oleic acid, SA: stearic acid, TDPA: tetradecylphosphonic acid, MA: myristic acid, SCOPh: thiobenzoate, ODE: 1-octadecene, PO: Parafin oil, DIPB: diisopropyl benzene, DDT: 1-dodecanethiol, OctT: octanethiol, St: stearate, OAc: acetate, acac: acetylacetonate, NA: nonanoate/nonaoic acid, iPr: isopropyl, Ph: phenyl, Su: selenourea, DTC: dithiocarbamate, DDTC: diethyldithiocarbamate, HTC: hexyldithiocarbamate, EDSC: ethyl(diethyldiselenocarbamato), bPhSe: bis(phenylselenolato), DPSe: 2-(4,6-dimethyl pyrimidyl)selenoate, TMSA: bis(trimethylsilyl)amino, TMAOH: tetramethylammonium hydroxide, CTAB: cetyltrimethylammonium bromide, PVP: polyvinylpyrrolidone, PVP-t: poly(1-vinylpyrrolidone)-graft-(1-triacontene), TMS: trimethylsilyl, HDX: hexadecylxanthate.
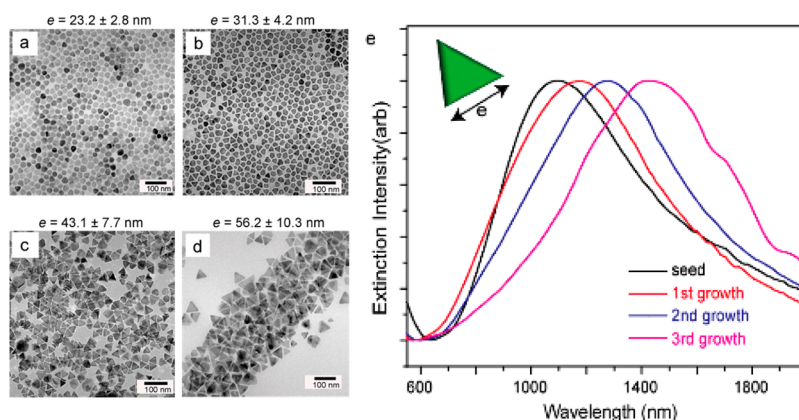
Figure 40. (a−d) TEM images showing the evolution of CuS nanoprisms with increasing number of growth cycles (a−d: from zero to three). (e) Evolution of the NIR extinction intensity as a function of the number of growth cycles. Reproduced with permission from ref 407. Copyright 2015 American Chemical Society.

alternative ME NCs has been intensively studied for ZnE due to the similarities with CdE. Among the first examples, Brus and co-workers used arrested precipitation, where at low temperatures first small crystallites were formed before allowing thermal coagulation.[391] A derivation of this method used stabilizing ligands, which prevented the NCs from aggregation and therefore improved colloidal stability.[392] The amelioration of size and shape control was also attempted using nanoscale micelles: either reverse micelles or normal micelles have been utilized as template or microreactors for the production of small QDs with sizes ranging from 4 to 6 nm.[393,394] Another elegant approach for the formation of ME such as ZnSe consists in ion exchange on presynthesized NCs of another material. Ion exchange is favored in many metal chalcogenides due to the relatively high fractional ionic character of bonding (cf. section 3). As the anions constitute the structural framework the smaller cations show in many compounds sufficient mobility to support this type of reactions.[395] Manna and co-workers used this approach for the synthesis of phase controlled ZnSe NCs and nanorods, through the conversion of CdSe primary particles via a double cation exchange CdSe → Cu_2Se → ZnSe.[396] The synthesis of metal chalcogenide NC has also been performed by means of more exotic strategies such as the use of microorganisms. In one approach, which has been developed mainly for the formation of metal sulfide NCs, the conversion process of sulfate into sulfide ions by enzymes within the cells of funghi, bacteria, or other microorganisms, was used to provide intra- or extra-cellularly the sulfur precursor. Its reaction with soluble metal ions allowed for the formation of insoluble colloidal M_xS_y NCs (M = Zn, Ag, Fe, Bi, Cu, and Mn) with diameters in the range of some nm to some hundreds of nm depending on the material and method, showing narrow size distribution.[397] In the following discussion we will focus on the major body of work developed for the synthesis of metal chalcogenides in organic media, which is essentially derived from the two general methods described in section 3: the hot-injection and the heat-up methods. Table 7 summarizes the different methods and experimental parameters used as well as the mean size and shape obtained.

4.3.2.1. Metal Sulfide NCs. 4.3.2.1.1. Heat-Up Approaches. Contrary to the hot-injection method, the heat-up approach has been widely investigated for the formation of binary metal sulfide NCs. Elemental sulfur is dissolved in an appropriate Lewis base and fatty acid or alkylamine metal complexes are generally applied as precursors. A number of similar methods have been developed for ZnS, MnS and CuS NCs, which mainly differ in regard to the solvent used (oleylamine or 1-octadecene or a mixture of both). In 2003 Hyeon and co-workers proposed a general synthetic procedure for the formation of metal sulfide semiconductor NCs such as ZnS or MnS.[398] In this synthesis the metal precursor was prepared in situ by dissolving the chlorides MCl_2 in oleylamine in the presence of TOPO at 170 °C (Zn) or at 120 °C (Mn). Elemental sulfur "dissolved" in oleylamine was added at room temperature and the reaction was triggered by heating to 340 and 280 °C, respectively, through the release of hydrogen sulfide occurring during the heating of the polysulfides generated in oleylamine (vide supra). This method yielded uniform spherical ZnS NCs with diameters ranging from 8 to 11 nm. According to the authors the addition of TOPO along with oleylamine improved the dispersibility of the obtained particles. In the case of MnS, size and shape control was achieved by modulation of the temperature and the stoichiometry of precursors: a 1:1 molecular ratio of precursors heated up at 240 °C gave rise to rod-shaped NCs with average size of 20 × 37 nm, crystallizing in the wurtzite structure (γ-MnS). The size of these nanorods could be increased up to 60 nm by varying the temperature. When the Mn:S ratio was increased, the wurtzite NCs were found to reach a hexagonal shape with mean diameters of 20−25 nm. The apparent increased reactivity of elemental sulfur in the presence of oleylamine is attributed to the formation of a sulfide-ammonium complex, which acts as a strong Lewis base. The use of elemental sulfur and metal salts in combination with oleylamine has also been applied for synthesizing chalcocite CuS NCs of quasi-spherical shape and a mean diameter of 12 nm.[406] In this case the Cu:S ratio had an influence on the phase purity of the NCs: when the ratio Cu:S was greater than 2.25, pure chalcocite was easier to be obtained. The ratio of Cu:S changed also the phase transformation rate within the NCs: The higher the Cu:S ratio, the slower the phase transformation from α-chalcocite to djurleite. In the majority of other reported heat-up methods, oleic or stearic acid (OA, SA) have been used to generate molecular metal precursors. Metal carboxylate complexes acting as reaction intermediates are easily formed with a large variety of metals, even the softer ones according to Pearson's classification. Fatty acids like OA and SA generally also act as X-type surface ligands and favor isotropic growth of
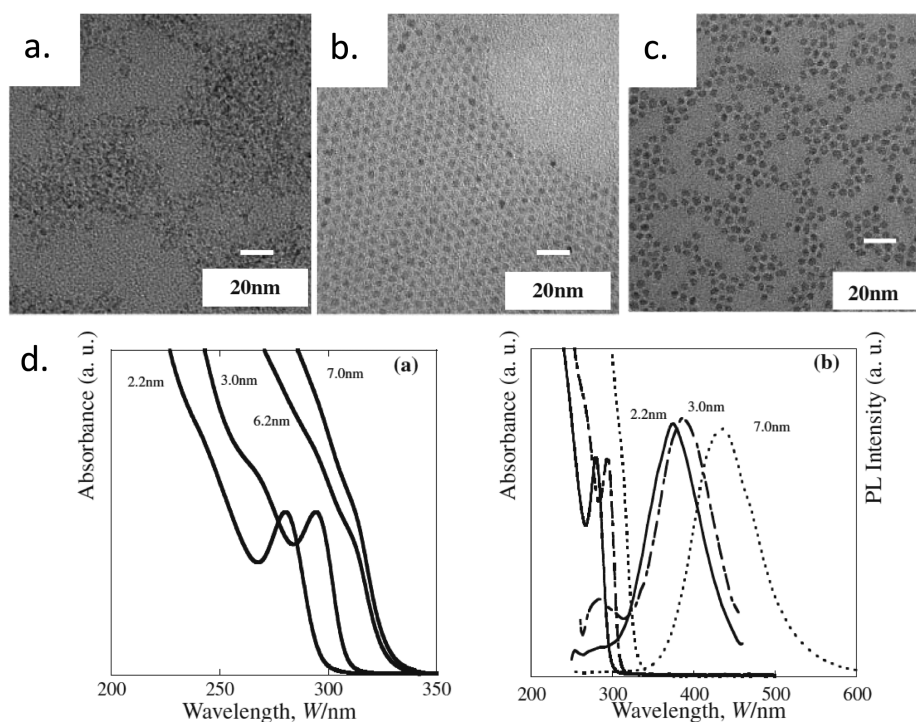
Figure 41. TEM images of ZnS NCs synthesized at 200 °C with 1:1 Zn/S ratio (a) with oleic acid; (b) with OLA as cosurfactant. (c) NCs obtained from a synthesis using a Zn/S ratio of 0.4 at 200 °C and OA. (d) Evolution of the optical properties of the ZnS NCs as a function of their size. Reproduced with permission from ref 402. Copyright 2004 The Japan Institute of Metals.

the nanoparticles. In many cases the addition of neutral L-type donors like TOPO is explored for improving dispersibility but also with the goal of improving the control of size, size distribution and crystalline phase.

In the case of CuS NCs, the precise control of their nanoscale morphology is crucial, as they are known to possess interesting plasmonic properties dependent on their dimensions and composition. Hsu et al. recently developed a heat-up approach for the formation of covellite CuS nanoprisms with tight control of composition and shape.[407] First, CuCl was complexed in in a mixture of OLA and ODE and then sulfur powder was added as such before the heat-up process. The temperature was increased gradually to 130−180 °C, which gave rise to spherical CuS NCs with mean diameters of 23.2 nm (Figure 40a).

These NCs exhibited NIR absorption centered at around 1000 nm. Their addition to a growth solution of CuCl and S in OLA and ODE at 130 °C gave rise to the formation of monodisperse nanoprisms, whose sizes could be increased with the subsequent growth cycles (from 23.2 to 56.2 nm for 1 to 3 cycles as shown Figure 40). The comparison of this approach with the previously described one showed that the presence of ODE helped to achieve a lower size distribution and directed the growth toward prism formation. The NIR absorption was as a function of the NCs' size and varied from 1050 to 1480 nm, making them potential candidates for light focusing and advanced spectroscopy applications. The dispersion of elemental S powder in ODE has also been utilized for the synthesis of MnS NCs. Ponti and co-workers reacted this sulfur source with $Mn(OA)_2$, $Mn(St)_2$ or $Mn(OA)(OH)$ and obtained octahedral-shaped fcc α-MnS nanoparticles of narrow size distribution and 20−30 nm size for reaction temperatures of 300−320 °C and of 9−20 nm for 250−300 °C.[404] The utilization of $Mn(OA)(OH)$, gave rise to smaller NCs than in

the case of $Mn(OA)_2$ with average diameters of 14 and 29 nm, respectively. The Mn:S ratio played a crucial role in this synthesis: for values below 0.5 pure α-MnS was formed, while increasing the Mn:S ratio to >1.7 results in pure MnO nanoparticles. Magnetic measurements on the α-MnS nanoparticles indicated exchange coupling between an antiferromagnetic core and a ferromagnetic shell below the blocking temperature (23 K for 29 nm nanoparticles). Robinson and co-workers proposed another, easily scalable method relying on the use of ammoniumsulfide instead of elemental sulfur.[373] The precursor solution was prepared by mixing $(NH_4)_2S$ with oleylamine for 20 min at room temperature, followed by removal of trace water by means of molecular sieve. This sulfur source was found to be stable for at least 1 h after preparation and showed high reactivity when combined with various metal halides, carboxylates or thiolates. It enabled the use of comparably low reaction temperatures, in some cases room temperature, for the synthesis of metal sulfide NCs showing narrow size distribution and high reaction yield. More specifically, the synthesis of Cu_2S NCs on a scale of several tens of grams has been demonstrated from CuCl in oleylamine, with sizes tunable in the range of 4−8 nm. Using the metal oleates, 3−5 nm CdS, 6−10 nm SnS, 5.5 nm ZnS and 20 × 12 nm anisotropic MnS NCs were synthesized. Reactions using AgCl gave access to 2−3 nm Ag_2S NCs, bismuth dodeca-nethiolate yielded 3−5 nm Bi_2S_3 NCs, albeit with broader size distributions in these last two cases.

Numerous syntheses rely on the use of thiols, in particular dodecanethiol (DDT) as the sulfur source. It has to be noted that DDT can also serve as the solvent and surface ligand in certain reactions. In one of the early examples, the synthesis of monodisperse ZnS NCs has been described by Sumiyama and co-workers.[402] In this method, the zinc was prepared by dissolving $ZnCl_2$ in methanol. S powder dissolved in
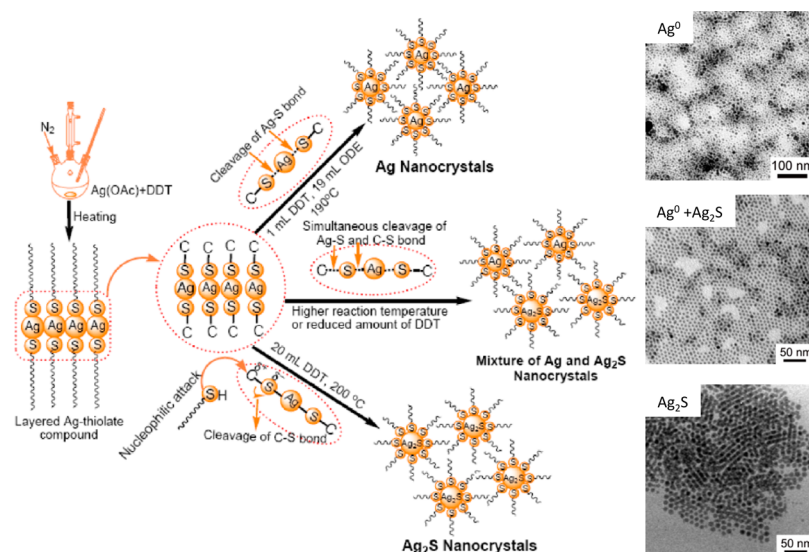
Figure 42. Mechanism proposed for the thermal decomposition of Ag-DDT complexes, leading to Ag nanoparticles and/or Ag$_2$S NCs depending on the reaction temperature and DDT concentration, and TEM images of the samples obtained using the different conditions. Reproduced with permission from ref 409. Copyright 2011 Wiley-VCH Verlag GmbH&Co. KGaA.

dodecanethiol (DDT) was used as the sulfur precursor, DDT also acting as a capping ligand. The nucleation was triggered upon heating in octylether to 180−260 °C. During the subsequent annealing process (3−120h) NCs aggregation was prevented by further addition of cationic or anionic cosurfactants, such as OLA or OA. In both cases monodisperse ZnS NCs have been obtained. In the case of OA the reaction kinetics were slower and therefore gave rise to smaller NCs. Conversely, the use of oleylamine resulted in larger NCs (Figure 41). By varying the annealing temperature and the S/Zn ratio the diameters could be tuned from 2.2 to 7 nm with narrow size distributions. In each case the UV spectra exhibited a narrow exciton band between 280 and 294 nm. Upon irradiation under UV light, the NCs exhibited UV to blue luminescence (maximum emission ranging from 350 to 450 nm; Figure 41d).

Choi et al. have used metal oleate and DDT for the development of a general procedure for the synthesis of uniform metal-sulfide NCs.[371] This synthesis gave rise to monodisperse spherical ZnS and Cu$_2$S as well as bullet-shaped MnS NCs. The preparation of ZnS NCs was performed via a heat-up approach from Zn(OA)$_2$ and DDT in the presence of OLA. The gradual increase of the temperature to 310 °C allowed the formation of zinc blende ZnS NCs with quasi-spherical like shape and average size between 7 and 10 nm. The reaction occurred through a thermolysis mechanism controlled by the thermal degradation of the DDT. Photoexcitation of the NCs at their exciton peak gave rise to band edge emission centered at 350 nm as well as to broad band emission at longer wavelengths attributed to trap states. High quality spherical and disk shaped Cu$_2$S NCs with sizes varying from 7 to 20 nm have been obtained by heating up the reaction mixture to 230 °C for different reaction times. Conversely, disk-shaped NCs were obtained when, after this heating process at 230 °C, aging at 140 °C was carried out for several hours. In a similar way the reaction yielded bullet-shaped MnS NCs of 10−15 nm. Various related studies focused on different metal precursors such as copper acetylacetonate or copper acetate.[408−411] In these examples, by varying the heat-up temperature or aging temperature, spherical NCs with sizes varying between 3 and

10 nm and disk-shaped nanoparticles with diameters between 20 and 50 nm were obtained exhibiting a high size and shape homogeneity. In a similar approach, Peng and co-workers simply heated the thiolate complexes of silver nitrate or the acetate-hydrates of copper, zinc, lead, cadmium and nickel for the facile preparation of the corresponding uniform metal sulfide NCs.[409,413] The main difference with the earlier described DDT-based methods is the fact that the metal salts are not complexed by other surfactants such as oleylamine or oleic acid, but are directly transformed into the metal thiolate complexes. In the case of silver, heating the DDT complex of Ag(NO$_3$) to 200 °C gave rise to monodisperse spherical Ag$_2$S NCs with an average diameter of 3 nm. However, a mixture of Ag$_2$S/Ag^0 has been observed when the temperature was increased. This was attributed to three possible decomposition pathways of the initially formed DDT complex during heating (Figure 42). If either the Ag−S or the C−S bonds are cleaved, exclusively Ag nanoparticles or Ag$_2$S NCs are formed, respectively, while simultaneous cleavage of both bonds at higher temperature leads to a mixture of Ag$_2$S and Ag nanoparticles.

Prior to this work, Korgel et al. had synthesized NiS nanorods and nanotriangles in the mellerite phase from Ni(NO$_3$)$_2$ by means of the solventless thermolysis of the nickel thiolate Ni(DDT)$_2$.[418] Heating to 150 °C to yielded monodisperse rhombohedral nanorods or nanoprisms with sizes of 33 × 8.1 and 6 nm, respectively. The same approach was further extended to the formation of NCs of orthorhombic bismuthinite Bi$_2$S$_3$, a material exhibiting high photoconductivity and hence of interest for photovoltaics.[420] In this work, the reaction of bismuth octanoate with DDT allowed the formation of the alkylthiol monomolecular intermediary and its thermolysis at 150 °C, in the presence of elemental S, gave rise to nanorods with dimension of 11 × 74 nm. The increase of the reaction temperature to 225 °C allowed the acceleration of the decomposition of the precursor provoking strongly anisotropic growth and the formation of micrometric nano-wires.

In conclusion, this general method of decomposition of metal thiolates, which constitute single-molecular precursors as
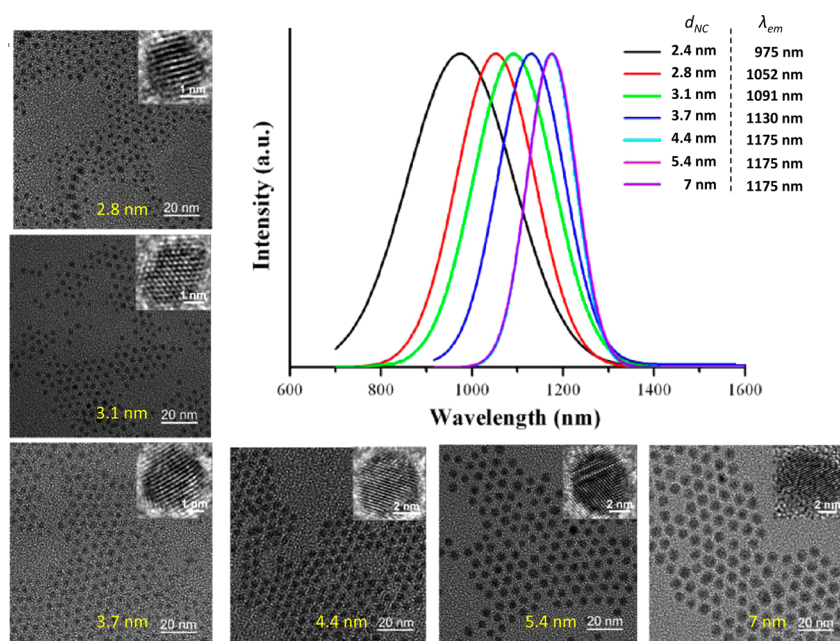
Figure 43. NIR emitting Ag₂S NCs obtained by thermal decomposition of Ag-DDTC in DDT. TEM and HRTEM images of the NC obtained by varying the temperature, with diameters between 2.8 and 7 nm and their respective PL emission spectra. Reproduced with permission from ref 415. Copyright 2014 American Chemical Society.
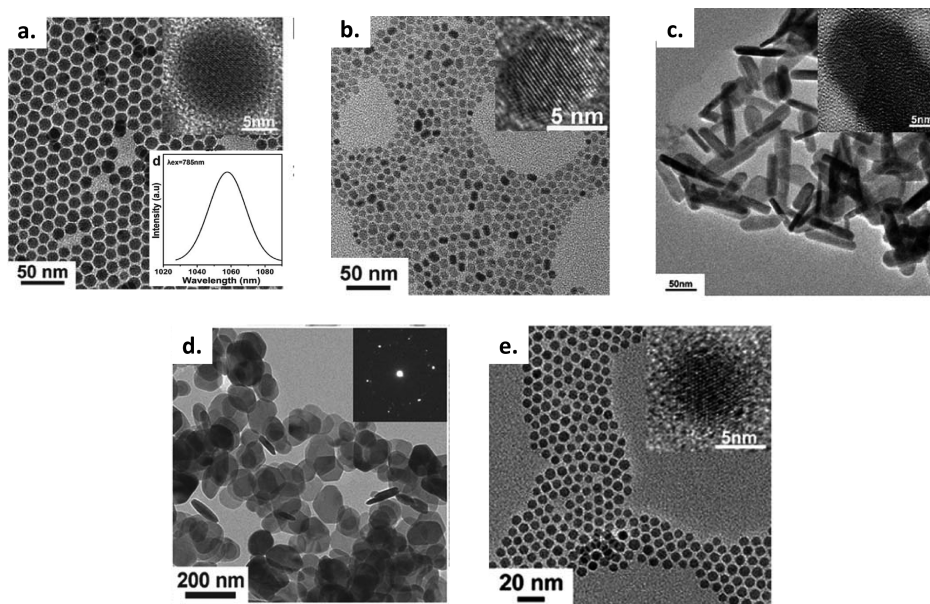

Figure 44. (a) Ag₂S, (b) ZnS, (c) Bi₂S₃, (d) SnS₂, and (e) Cu₂S colloidal NCs obtained through the thermal decomposition of the single-molecular precursors M-(DDTC) (metal diethyldithiocarbamate). Reproduced with permission from ref 399. Copyright 2011 Royal Society of Chemistry.

they contain both the metal and sulfur source, offers a facile and scalable approach for the preparation of a large variety of metal sulfide NCs of controlled size and shape. In accordance with the HSAB principle (cf. section 3), this method utilizing soft S-based Lewis bases, works best in combination with soft or "borderline" Lewis acids, such as Cu^+, Cd^{2+}, Ag^+, Mn^{2+}, Sn^{2+}, Cu^{2+}, Zn^{2+}, and Pb^{2+}, as the resulting complexes exhibit an appropriate bond strength for use in heat-up NC syntheses enabling the temporal separation of nucleation and growth.

In general, single-molecular precursors are of high interest for NC synthesis, as they can eliminate side reactions occurring with separate metal and chalcogenide sources, they are usually

nonpyrophoric in contrast to metal alkyls, and less air-sensitive, i.e. easier to manipulate.[470] Their decomposition and the controlled release of the metal and chalcogen atoms depends on the molecular structure. In the case of the metal sulfides, changing the nature of the S containing coordinating ligand enables the modification of the decomposition kinetics. In addition to thiols, thiourea, or thiocarbamate derivatives have been mainly applied. However, in contrast to the DDT-based syntheses discussed before, these sulfur containing ligands fully decompose during heating, and therefore the use of additional surfactants is mandatory to stabilize the NCs. One example is the heat-up process of metal-thiocarbamate complexes. Shen et
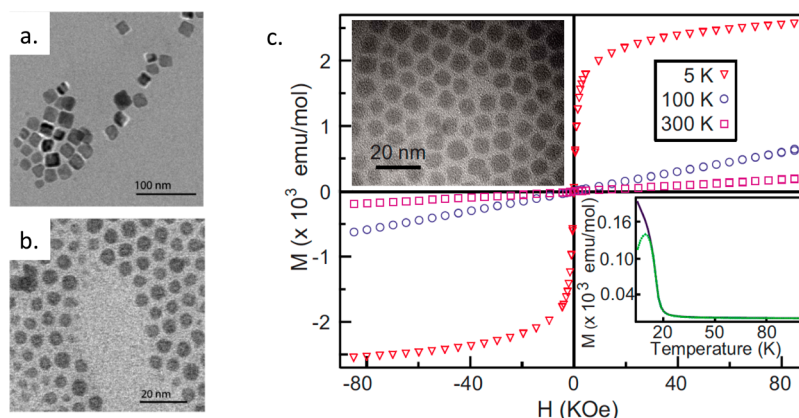
Figure 45. TEM images of EuS NCs obtained from the thermal decomposition of single-molecular precursors in OLA/TOP: (a) reaction of europium diethyldithiocarbamate phenanthroline at 280 °C; (b) reaction of europium diethyldithiocarbamate bipyridine at 200 °C. Reproduced from ref 479. Copyright 2005 American Chemical Society. (c) TEM image of EuS NCs synthesized from europium diethyldithiocarbamate phenanthroline in OLA/TOP at 300 °C and magnetization curves recorded at different temperatures (inset: FC/ZFC curves). Reproduced with permission from ref 476. Copyright 2009 American Institute of Physics.

al. have proposed a generalized synthesis strategy for the formation of various metal sulfide NCs, namely of Ag_2S, ZnS, Bi_2S_3, SnS, SnS_2, as well as of several iron and copper sulfides.[399] In this study, the syntheses are based on the use of nontoxic and air stable metal-diethyldithiocarbamate M-(DDTC) single-molecular precursors together with the additional surfactants OLA and OA. When an equimolar ratio of OA and OLA was used, spherical NCs were obtained with a size around 10 nm, e.g. 10.2 nm Ag_2S through the thermal decomposition of Ag-DDTC. These NCs were in a monoclinic phase and exhibited a band gap of 1.1 eV. Further photophyical studies have shown they possess absorption and emission in the NIR region (centered at 920 and 1058 nm respectively).

The same team had reported before the use of a different surfactant mixture of OA, ODE and octadecylamine for the synthesis of monodisperse, spherical Ag_2S NCs of 10.2 nm size.[414] Using DDT as the surfactant gave access to smaller Ag_2S NCs showing quantum confinement effects.[415] In this method, relying on the decomposition of Ag-DDTC in neat DDT, the variation of the reaction temperature and reaction time allowed the modulation of the size and the composition of the NCs: while the temperature was varied from 130 to 230 °C and the reaction time from 1 to 60 min, the diameters increased gradually from 2.4 to 7 nm (Figure 43). The NIR luminescence shifted from 915 to 1175 nm and a Bohr exciton diameter of 4.4 nm has been estimated. While the PL QY could not be quantified, size-dependent lifetimes in the range of 57−181 ns have been observed. As stated above the thermal decomposition of the M-DDTC complexes has also been used for a variety of other types of NCs: spherical ZnS, Ag_2S and CdS NCs as well as Cu_2S, SnS, SnS_2 and Bi_3S_2 nanoplates and $Fe_{2-x}S$ nanoribbons (Figure 44).[399] In the case of ZnS, luminescent QDs in the wurtzite phase with an average diameter of 9.5 nm were obtained from Zn-$(DDTC)_2$, whereas in the case of CdS, the size was smaller (7.5 nm). In both examples the combined use of OA and OM favored isotropic growth. Conversely, with the other metals investigated anisotropic nanostructures have been obtained: SnS_2 nanoplates with diameters of 150 nm and a thickness of 6 nm crystallizing in a hexagonal phase, $Fe_{1.2}S$ nanoribbons with a width of 15 nm and 80 × 16 nm Bi_2S_3 nanoplates. When only OLA was used in ODE solvent, the thermal degradation of Zn-$(DDTC)_2$ gave rise to ultrathin

hexagonal phased crystalline nanowires with 4.4 nm diameters and 300 nm length. This is due to the selective adsorption of the OLA onto the [100] crystal facet inhibiting isotropic growth.[471] Finally, the use of Cu-$(DDTC)_2$ in neat DDT resulted in the formation of 6 nm spherical QDs (Figure 44e.) whereas the use of OA as the solvent gave rise to larger particles of 26 nm.[399]

It is clear from these methods that the use of metal dithiocarbamate provides an efficient approach for the formation of high quality metal sulfide NCs. However, the simultaneous modulation of size and shape is limited by the decomposition rate of the dithiocarbamate complex. The latter can be influenced by using substitutents different from ethyl on the nitrogen atom, or by replacing the dithiocarbamates by similar compounds, such as for example xanthates (Figure 39). Indeed, similarly as dithiocarbamates, xanthates can easily form air-stable metal complexes. However, the presence of an ester bond in the xanthates can change the ligand decomposition kinetics and therefore the rate of sulfur release. Based on this assumption, Pradhan and co-workers have compared the use of metal-xanthates and metal-dithiocarbamates for the synthesis of various types of NCs, namely ZnS, MnS, NiS, CuS, PbS, CdS and HgS.[401] They showed that the dithiocarbamates possess higher decomposition temperatures than xanthates, which led to NCs of higher polydispersity and with more pronounced defect emission. Comparing the xanthate alkyl chain length showed that shorter substituents (ethyl) led to faster nucleation and growth kinetics than longer ones (hexadecyl). The decomposition temperature strongly depended on the nature of the used solvent. Using hexadecylamine (HDA) allowed the diminution of the reaction temperature from 140 to 70 °C in the case of cadmium hexadecylxanthate and from 170 to 125 °C in the case of cadmium hexadecyldithiocarbamate. The same applies for the zinc precursors. In the case of Mn, Ni, Cu, Pb and Hg, however, the primary amine decomposes the xanthates prior to the formation of the metal sulfide NCs. Therefore, trioctylamine was chosen to replace HDA, albeit the size distribution was broader in these cases. The proposed reaction mechanism is an intramolecular elimination based on the Chugaev reaction and several hypotheses were given concerning the apparent activation of this reaction in the presence of a Lewis base (primary amine). Nonetheless, no
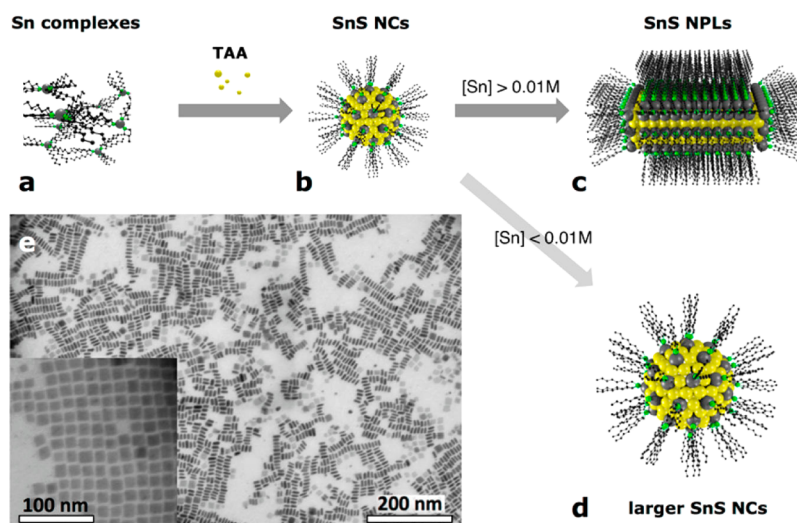
Figure 46. Growth mechanism of square SnS nanoplatelets (c) via the formation of spherical seed nanocyrstals (b). The competing pathway (d) can be suppressed by the proper choice of reaction conditions, giving access to monodisperse nanoplatelets (e, dimensions: 4.4 nm thickness, 14.4 nm edge length). Reproduced with permission from ref 486. Copyright 2015 American Chemical Society.

clear evidence for the formation of carbonyl sulfide (O=C= S) and of the alkene formed in such a reaction has been given. With the goal of fine-tuning the rate of decomposition of these single-molecular precursors, various other substituents such as heterocyclic, alkyl and alkylphenyl dithiocarbamates and xanthates have been investigated.[472,473] II—IV NCs of low size dispersion have been obtained, for example by Onwudiwe et al., who used bipyridyl adducts of Zn(II) and Cd(II) bis (N-phenyldithiocarbamate).[400] The size of the ZnS NCs could be modulated with the growth temperature: diameters of 2.9 and 3.5 nm were obtained at 180 and 220 °C, respectively. The synthesis of SnS NCs has been reported through the thermal decomposition of tin ethylxanthate in octadecylamine yielding rectangular nanoplatelets and a minor fraction of tetrahedron-shaped particles with edge lengths of 20—100 nm.[474] While the former crystallized in the common orthorhombic structure, the latter exhibited the rocksalt phase, previously unobserved for SnS, as evidenced by electron diffraction. The synthesis of NCs of EuS, which is a well-known example of a (concentrated) magnetic semiconductor, has also been realized using thiocarbamate and xanthate derivatives.[475−477] In most cases, diamino-based ligands are used to occupy, in addition to the sulfur containing ligands, the nine sites of the coordination sphere of the lanthanide ion.[422,478] This type of ligand allows not only to adjust the Ln³⁺ to S ratio within the single-molecular precursor, but also to control its decomposition kinetics and hence the size and shape of the formed NCs. In a first study, polyaromatic chelates such as phenanthroline, bipyridine, and other pyridyl derivatives have been used to complex the europium ion. Cubic or close-to-spherical NCs with sizes between 5 and 7 nm were obtained when OLA, TOP and europium diethylcarbamate phenanthroline or bipyridine complexes were used at 280 and 200 °C, respectively (Figure 45).[479]

Conversely, another study has shown that the increase of the synthesis temperature to 240 °C, with the same reagents, gave rise to large particles with average diameters of 20 nm.[480] Summarizing, for the synthesis of metal sulfide NCs, the heat-up approach offers an interesting pathway for the synthesis of high quality NCs, i.e. of low dispersion of size and shape. In many cases, the procedures are applicable to a variety of metals,

show high reaction yields and are easily scalable. On the other hand, as discussed in section 3, in the heat-up method the separation of nucleation and growth is governed by the rate of decomposition/reaction of the precursors. Therefore, a delicate balance for adjusting their reactivity must be found. The hot-injection method can therefore be an interesting alternative for specific materials.

4.3.2.1.2. Hot-Injection Methods. Hot-injection approaches to metal sulfide NCs have mainly been reported for CdS, PbS and ZnS. The metal and S precursors are essentially the same as those used in the heat-up approach, with the metals usually provided as carboxylate complexes. As one example, Zhong et al. injected elemental sulfur solubilized in ODE into a hot solution of CdO and ZnO, complexed with oleic acid in ODE.[481] By alloying CdS with Zn and eventually forming a thin ZnS overlayer, this synthesis addresses the problem that the CdS surface is prone to oxidation leading to deep-trap emission. In another example, Nui et al. have developed CdS and ZnS NC synthesis, using the hot injection of DDT into a solution of zinc oleate.[403] In this method, the zinc oleate precursor was first prepared at 260 °C by dissolution of ZnO with oleic acid in ODE. The nucleation was then triggered though the swift injection of a solution of DDT in ODE affording monodisperse zinc blende ZnS NCs. Using a similar approach Liu et al. synthesized SnS nanosheets, polyhedral nanoparticles and nanoflowers.[421] In this study, SnCl₂ was dispersed in a mixture of OA and OLA and heated. The injection of the alkylthiol (DDT or octanethiol), at various temperatures, gave rise to the formation of NCs showing the above-mentioned morphologies. When carrying out the injection of DDT at 220 °C nanosheets with edge lengths around 100 nm have been obtained. These nanostructures crystallized in the orthorhombic herzenbergite, which is typical for Sn(II)S. Upon decreasing the reaction temperature, the sheet morphology was largely replaced by a polyhedral morphology. Furthermore, the use of octanethiol instead of DDT provoked the formation of NCs with polyhedral shape, albeit in the same crystalline phase. Finally, the authors demonstrated that the use of OLA as the only cosurfactant resulted in the formation of flower-shaped aggregates of quasi-spherical NCs. SnS nanoparticles have also been synthesized by
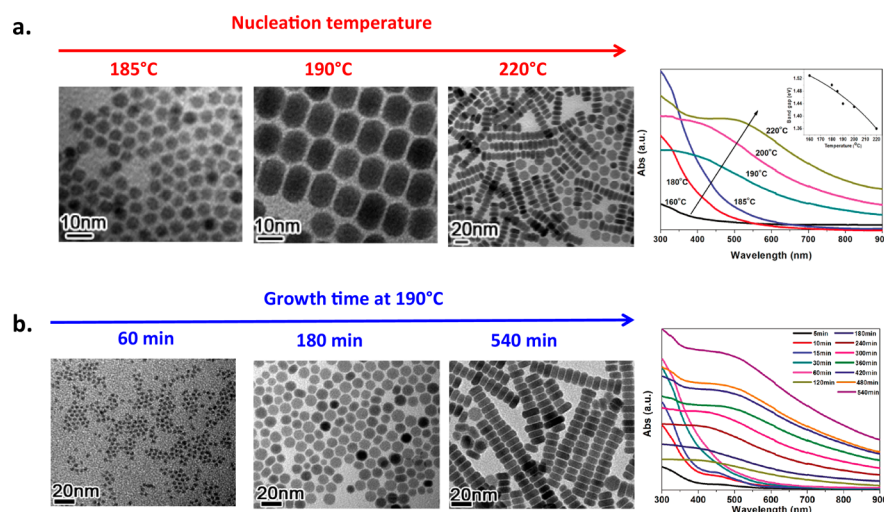
Figure 47. Cu$_2$S NCs obtained by a HI method using DDT as S precursor: size, shape and NIR absorption evolution as a function of (a) the nucleation temperature and (b) the growth time at 190 °C (after injection at 190 °C). Reproduced with permission from ref 412. Copyright 2010 American Chemical Society.

injection of other types of sulfur precursors into the hot solution of the Sn precursor, namely hexamethyldisilathian or bis(trimethylsilyl) sulfide (S(SiMe$_3$)$_2$),[482] thioacetamide (TAA)[483] and elemental sulfur in OLA.[484] Hickey and co-workers injected a solution of TAA in OLA and TOP into a mixture of bis[bis(trimethylsilyl)amino]tin(II), TOP, OA, and ODE at 170 °C.[483] Monodisperse SnS NCs of 7 nm mean size were obtained, and when increasing the OA contents in the reaction mixture a tendency for the formation of larger and triangular-shaped particles was observed. Liu et al. heated SnCl$_2$ in oleylamine to 200 °C and injected S(SiMe$_3$)$_2$ in ODE.[482] By adjusting the injection and growth temperatures, monodisperse SnS nanoparticles in a size range of 6–20 nm could be obtained. De Kergommeaux et al. compared these two protocols with four new ones using different combinations of tin and sulfur precursors.[484] In the best combination resulting in the lowest size distribution (<10%) anhydrous SnCl$_2$ was mixed with ODE, TOP, and OA and heated to 100 °C, before injecting a solution of TAA in OLA and TOP. By changing the reaction temperature from 80 to 180 °C, the particle size could be varied from 5.5 to 19 nm. By means of ^{119}Sn–Mössbauer spectroscopy the spontaneous surface oxidation of the SnS nanoparticles was demonstrated, which occurred regardless of the used synthesis method. Seven nm SnS NCs exposed to air exhibited a Sn(IV):Sn(II) ratio of 40:60, whereas samples kept under inert conditions still showed 20% of Sn(IV), attributed to OA surface ligands. The surface oxidation resulted in the formation of an amorphous oxide layer containing different Sn(IV) and mixed Sn(II)/Sn(IV) species, namely SnS$_2$, Sn$_2$S$_3$ and SnO$_2$. A similar oxidation behavior is observed also in the case of pure tin nanoparticles.[485] When changing the tin precursor from SnCl$_2$ to SnCl$_4$·5H$_2$O, the same hot-injection reaction resulted in the formation of monodisperse square SnS nanoplatelets of 4–15 nm thickness and 15–100 nm edge length, crystallizing as the spherical particles in the orthorhombic herzenbergite phase (space group *Pnma*; Figure 46).[486] Their growth occurred via the assembly of small spherical seed NCs and required a Sn concentration of >0.01 M in the reaction mixture. Replacing in this reaction TAA by elemental sulfur solubilized in OLA as the S source yields 2–3

nm SnS$_2$ NCs with tin in the oxidation state +4.[486] These exhibited the berndtite 4H crystallographic phase.

Wang et al. developed a novel approach for the formation of Cu$_2$S NCs either with a spherical or nanodisc shape based on the use of TOPO as cosurfactant.[412] In this method, injection of DDT at elevated temperature into a solution of Cu(OAc) and TOPO in ODE led to the formation of Cu$_2$S NCs (Figure 47). The formation of small dots of 3–6 nm was detected in the early stages of the reaction, which gradually transformed into discs (up to 18.2 × 9.6 nm) by increasing the nucleation temperature to between 160 and 220 °C.

A second way to tune size and shape of the NCs was by increasing the growth time. Again the shape evolved from spherical dots of 3.1 nm diameter after 60 min to nanodisks with dimensions of 13 × 7.9 nm. Each sample synthesized showed high crystallinity in the Cu$_2$S hexagonal phase and a narrow size distribution. These NCs are good NIR absorbers with size and shape dependent absorption spectra. S(SiMe$_3$)$_2$ decomposes at lower temperatures than DDT. Jiang et al. have developed a two-step hot injection synthesis for the formation of small Ag$_2$S NIR emitting NCs.[487] The first step consisted in initiating the nucleation by injection of S(SiMe$_3$)$_2$ to a myristic acid activated Ag precursor (AgOAc) in a mixture of octylamine and ODE, followed by dropwise addition of a mixture of AgNO$_3$, octylamine and elemental sulfur in toluene to allow the growth (Figure 48). The Ag$_2$S seed NCs crystallized in the monoclinic phase, typical of α-Ag$_2$S. The authors have demonstrated that the NC size was directly linked
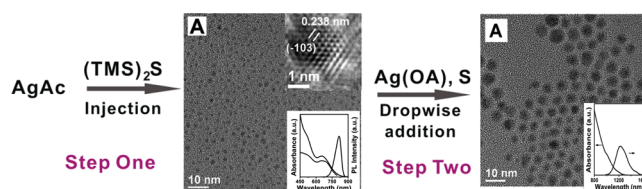

Figure 48. Evolution of Ag$_2$S NCs during a two-step HI synthesis and evolution of their optical properties before and after additional precursor injection (AgAc: silver acetate; TMS: trimethylsilyl; Ag(OA): Ag/octylamine). Reproduced with permission from ref 487. Copyright 2012 American Chemical Society.
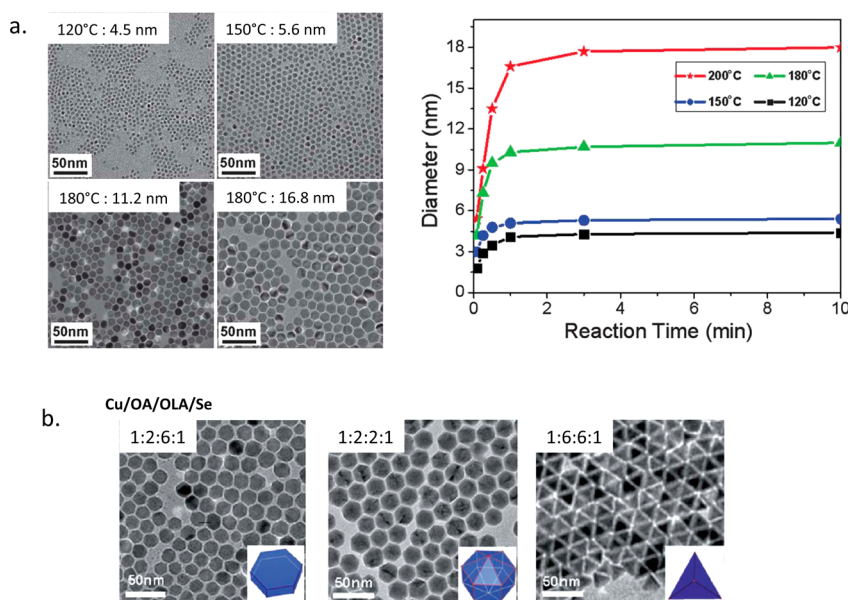
Figure 49. (a) Evolution of the size of Cu$_x$Se NCs as a function of the reaction temperature and reaction time. (b) Evolution of the shape of the NCs as a function of the Cu:OA:OLA:Se ratio. Reproduced with permission from ref 433. Copyright 2011 Royal Society of Chemistry.

to the injection temperature: When the injection temperature was varied from 50 to 120 °C, NCs with diameters varying from 1.5 to 4.6 nm were obtained after the seed-mediated growth of 18 h. This method yielded monodisperse Ag$_2$S NCs exhibiting fluorescence emission in the range of 813−1227 nm.

The hot-injection of single-molecular precursors offers an interesting approach due to the colocalization of both elemental constituents in the same source. An example of MnS NCs synthesis has been described using manganese diethyldithio-carbamate injected into a mixture of hot HDA and ODE.[405] In this study the formation of nanowires has been detected at low temperature (120 °C), whereas increase of the temperature to 180 °C allowed the formation of NCs with a mean diameter of 2.5 nm. Further increase of the temperature leads to the gradual transformation of the dots into nanocubes. The synthesis of Ag$_2$S NCs has been achieved using the single-source precursor Ag(SCOPh), injected into TOP in the absence of activating agents such as alkylamines.[417] This approach allows the sequential release of Ag and then S. Hot injection at 160 °C is affords 25 nm Ag$_2$S nanoparticles, while heating up the mixture from room temperature to 160 °C yields 80 nm Ag nanoparticles.

4.3.2.2. Metal Selenide NCs. Due to the differences in commercial availability and reactivity of the chalcogen precursors, in contrast to the metal sulfides the HI method has been preferentially used in the case of metal selenide NCs. In addition to CdSe, NCs of Zn, Cu and Sn selenides have been intensively studied, while for other materials only few examples exist.

4.3.2.2.1. Heat-Up Approach. In the case of ME materials, the major part of the heat-up approaches has been derived from those initially developed for CdSe and then transferred to ZnSe and eventually to other MSe materials. Although the chemical reactivity of S and Se is similar, NCs of metal sulfides have been much more studied as they benefit from the large variety of S-containing organic compounds, such as alkylthiols, thiourea and carbamates derivatives, the decomposition of which can be finely controlled during the heat-up synthesis. In the case of Se, the precursor library is much more restricted (vide supra).

Zhang et al. confronted the HI and HU approaches using the same precursors.[423] The metal was provided as a fatty acid complex, Zn(NA)$_2$ (NA = nonanoic acid), in an ODE/OLA mixture and Se powder solubilized in octylamine and OLA was the selenium source. When the temperature was varied from 20 to 160 °C in the HU approach the formation of magic-sized ZnSe clusters in the wurtzite phase occurred. Upon further temperature increase, the formation of larger NCs of 2−3 nm size was observed, which showed PL centered around 300 nm. Finally, when the temperature was raised above 220 °C the formation of regular QDs and nanorods occurred exhibiting zinc blende/wurtzite polytypism. The HI approach gave similar results when the corresponding temperatures were used.

Favored by its facile preparation the Se precursor prepared by dispersing Se powder in ODE has been widely applied. Shen et al. used it for the synthesis of high quality Cu$_x$Se NCs (1.58 < x < 1.65) of different shapes.[433] Copper stearate was used as the Cu source and a mixture of OLA and OA as surfactants. All samples obtained from this method exhibited the cubic berzelianite crystalline phase. This approach offered different ways of shape control by varying reaction temperature and growth time (Figure 49a). Under constant heating conditions ramp monodisperse NCs with diameter of 4.5, 5.6, 11.2, and 16.8 nm were obtained, when the end temperature was set to 120, 150, 180, and 200 °C, respectively. In parallel, the shape of the NC could be tuned by varying the ratio Cu-(St)$_2$:OLA:OA:Se leading to hexagonal (1:2:6:1), octadecahe-dral (1:2:2:1), and pyramidal (1:6:6:1) nanoparticles (Figure 49b). Comparison with the HI approach demonstrated the impossibility of size control in that case. Triangular shaped Cu$_2$Se NC have been obtained using similar protocols but replacing OA by stearic acid (SA).[488] Heating a 1:6:6:1 mixture of Cu(St)$_2$:SA:OLA:Se to 220 °C resulted in the formation of NCs with sizes between 2.8 and 12 nm depending on the growth time (5−120 min). The use of SA instead of OA prevented the formation of columnar assemblies of NCs.

O'Brien and co-workers investigated in more detail the role of the zinc carboxylate precursor on the ZnSe NC production.[424] Their synthesis involved heating up of a mixture
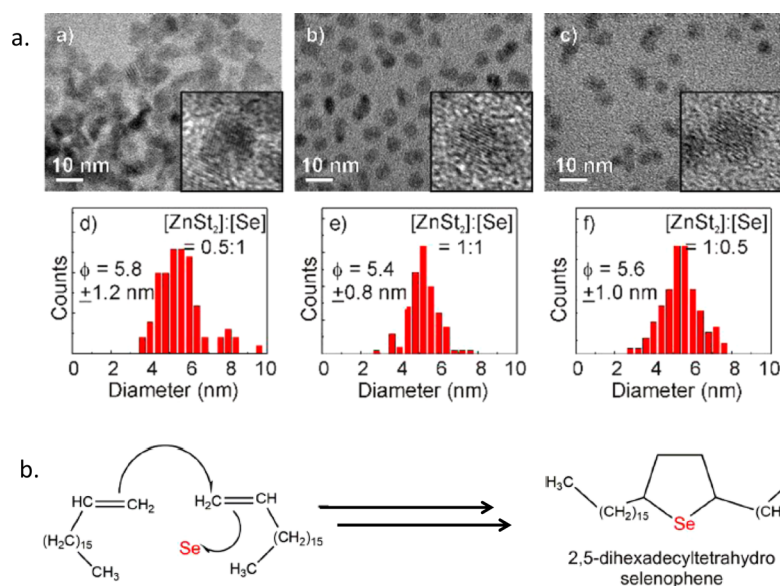
Figure 50. (a) ZnSe NCs obtained from a HU approach varying the Zn(St)$_2$: Se ratio. (b) Proposed reaction between Se and ODE preceding NC formation. Reproduced with permission from ref 424. Copyright 2015 American Chemical Society.

containing Zn(St)$_2$ and Se powder dispersed in ODE to 290 °C. Zn(St)$_2$ acted in this case as both the Zn source and stabilizing ligand for the surface. Spherical ZnS NCs with average diameters of 6, 4.5, and 5 nm were obtained for Zn/Se ratios of 0.5, 1, and 2, respectively (Figure 50a). The authors have also shown that the concentration of Zn(St)$_2$ influenced the morphology of the NC: When an equimolar ratio of Zn and Se was used, the particles were spherical whereas other ratios led to their agglomeration. Previous studies performed on fatty acids used in the synthesis of CdSe NCs,[489,490] showed that the concentration of carboxylates in solution had a large influence on the reaction outcome; if the OA (or SA) concentration was too high, the resulting NCs showed a broad size distribution due to the delayed and prolonged nucleation.

In the proposed reaction mechanism the slow delivery of Se during the growth was due to the reaction of the Se ion with ODE to yield a 2,5-dihexadecyl-tetrahydroselenophene complex prior to the reaction with Zn^{2+} (Figure 50b). This mechanism limited the Se delivery and therefore slowed the growth process, which had also positive effects on the PL properties as it has been shown that Se-rich samples exhibited no luminescence. The obtained stearate stabilized NCs had an average PL QY of 8%.

The activation of elemental selenium in primary amines is another facile way for preparing a Se precursor, even though neither the molecular structure of the latter nor its reaction pathway has been elucidated so far. Wang et al. used Se/OLA in an HI approach for the synthesis of spherical 10 nm Cu$_2$Se and Ag$_2$Se NCs in combination with the metal nitrates.[435] As another alternative selenium source Se powder has been dispersed in alkylphosphines. The use of the secondary phosphine such as diphenylphosphine (DPP) resulted in a higher reactivity of the Se precursor compared to TOP. Yu et al. used this approach in the synthesis of highly luminescent ZnSe QDs.[124] In this example, the DPPSe and TOPSe precursors have been compared. Zn(OA)$_2$ has been reacted either of them in ODE under gradual heating to 310 °C yielding zinc blende ZnSe NCs. With both TOPSe and DPPSe, the presence of free DPP accelerated the initiation of the

nucleation process. The reaction mechanism has been studied by NMR spectroscopy and it was deduced that two main mechanisms occurred (Figure 51). These pathways depended
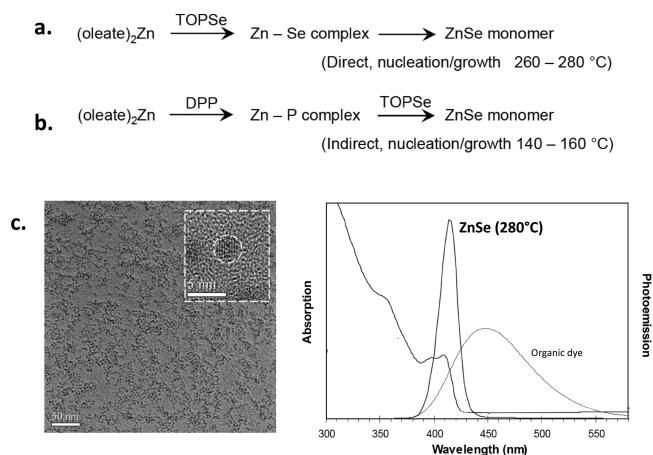
Figure 51. Proposed mechanism for the synthesis of ZnSe from TOPSe and Zn(OA)$_2$ in ODE, (a) in the absence and (b) in the presence of free secondary phosphine (DPP). (c) ZnSe NCs and optical properties of the ZnSe NCs showing a PL QY of 72%. Reproduced with permission from ref 124. Copyright 2011 Royal Society of Chemistry.

on the presence of free phosphine in solution: When only TOP-Se or DDP-Se and Zn(OA)$_2$ were used the synthesis of the ZnSe monomer occurred through a direct nucleation/ growth mechanism via formation of an intermediary Zn−Se-phosphine complex. On the contrary, when free phosphine (TOP, DOP, or DPP) was added to the reaction mixture, an indirect nucleation/growth mechanism occurred and the formation of a Zn-phosphine intermediary complex was detected. The second mechanism resulted in an increase in the reactivity of Zn and Se precursor and has allowed the use of lower temperature for nucleation and growth (160 °C instead of 280 °C).
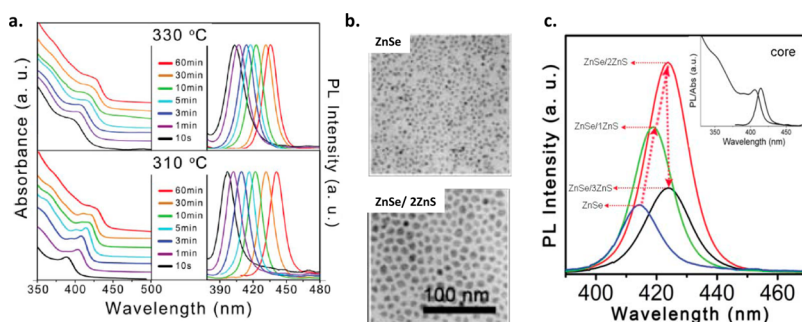
Figure 52. (a) Evolution of the absorption and the PL spectra with reaction time of ZnSe NCs obtained after precursor injection at 310 or 330 °C. (b) TEM images of ZnSe and ZnSe/ZnS core/shell NCs. (c) Evolution of the PL upon ZnS shell growth. Reproduced with permission from ref 426. Copyright 2009 Royal Society of Chemistry.

The use of DPP instead of TOP allowed to further decrease the nucleation and growth temperature from 160 to 120 °C. The obtained zinc blende ZnSe NCs had a mean size of 3.1 nm and a size dispersion of 9%. By varying the size blue luminescence ranging from 360 to 410 nm (QY 66−72% Figure 51c) was achieved.

As in the case of metal sulfide NCs single-source precursors (SSP) have also been explored with the selenides. Cumberland et al. have used the cluster $[Zn_{10}Se_4(SPh)_{16}]^{4-}$ as a single source precursor and HDA as a stabilizing ligand for the synthesis of size tunable small ZnSe QD of narrow size distribution <5%.[425] The diameters were tunable from 2 to 5 nm by varying the temperature from 220 to 280 °C and the approach was easily scalable. Joshi et al. have investigated the facile formation of a new SSP based on the use of 3-benzyl-1-(2-phenylselenyl-ethyl)-3H-imidazole bromide (L), which readily forms complexes with silver.[437] The latter have been applied in the syntheses of Ag_2Se and AgBr NCs. Heating of $Ag[(L-HBr)_2]BF_4$ in the presence of TOP and OA (v:v ratio of 1:2) to 200 °C, gave rise to orthorhombic Ag_2Se with average diameters of 17 nm. The counterions have a certain importance as when the SSP $Ag_2[L_2-Br_2]$ was used in the same conditions, a mixture of AgBr and Ag_2Se particles was obtained. The synthesis of Ni and Co based MSe NCs is delicate using traditional two precursor approaches and gave rise to materials with a limited quality. For this reason, the majority of Co or Ni based NCs were obtained through milling or hydrothermal methods.[440,491] O'Brien and co-workers have originally developed a SSP approach based on the use of metal complexes with dialkyldiselenophosphinates (Se_2PR_2) for Cd based materials[492] and have recently adapted this methods to the synthesis of colloidal $CoSe_2$ NCs.[493] The $Co[Se_2PPr_2]$ precursor was mixed with HDA and the resulting mixture was heated to 320 °C. After 120 min of reaction quasi-spherical $CoSe_2$ NCs were obtained.

As illustrated in the first part of this section, in contrast to the sulfides, the Se precursor library is more restricted. By consequence the fine-tuning of the precursor-to-monomer conversion rate upon temperature increase is more delicate, which explains why most of the synthetic procedures developed for metal selenide NCs rely on the HI rather than the HU approach.

4.3.2.2.2. Hot-Injection Approaches. In the HI approach the same set of Se precursors has been explored as in the case of HU methods albeit with a predominance of TOPSe inspired by the seminal work of Murray and co-workers on CdSe NCs.[95] Hines et al. reported a synthesis using TOPSe or TBPSe as the

selenium and the highly reactive organometallic compound diethylzinc in HDA as the zinc source, respectively.[429] Injection of the Se precursor at 270 °C resulted in the formation of ZB ZnSe NC, with sizes up to 6 nm and PL emission between 365 and 445 nm. The combined use of TOP and HDA provided efficient surface passivation leading to PL QYs of 20−50%. Shen et al. developed a synthesis of highly luminescent ZnSe and ZnSe/ZnS NCs with UV to blue emission and QY up to 70%.[426] $Zn(OA)_2$ and elemental Se powder dispersed in ODE served as the precursors. The authors compared injection of either precursor into the hot solution of the other at 240, 300, or 310 °C. In each case spherical ZnSe NCs with sizes ranging between 3 and 8 nm were obtained. Their range of emission was 390−450 nm with line widths approximately 14−20 nm (fwhm; Figure 52). Interestingly, Zn injection gave NCs of higher quality, with higher QY and narrower emission, than in the case of Se injection. The obtained ZnSe NCs were coated with a ZnS shell using the successive ionic layer adsorption and reaction (SILAR) technique, following a method reported previously for Cd based materials.[494,495] The PL QY reached up to 70% for two ZnS monolayers and decreased to 38% upon growth of the third layer.

Flamee et al. proposed a similar method but replacing $Zn(OA)_2$ with the cluster $Zn_5(CO_3)_2(OH)_6$.[427] More precisely the Se powder, dispersed in ODE, was injected into a hot solution of $Zn_5(CO_3)_2(OH)_6$ in OA and ODE. The obtained NCs exhibited a mean diameter of 3.4 nm. The growth reached saturation after 8 min and the calculated reaction yields were above 90%. Zhang et al. observed the formation of ZnSe magic-sized clusters in a synthesis based on the injection of Se powder dispersed in a mixture of OLA and octylamine into a solution of $Zn(OAc)_2$ complexed with the nonanoic acid at 110, 180, 220, or 230 °C.[423] Our own team developed a straightforward synthesis for ZnSe NCs based on the injection of TOPSe into a hot solution of zinc stearate in ODE.[428] The variation of the temperature between 250 and 315 °C and of the $Zn(St)_2$ concentration from 0.02 to 0.1M, allowed the production of spherical ZB ZnSe NCs with diameters ranging from 3 to 7 nm. The emission spectra exhibited maxima ranging between 390 and 440 nm with narrow line widths of 12.7 to 16.9 nm (fwhm) indicative of narrow size distributions. Several other examples have been reported following similar approaches based on the use of TOPSe or TBPSe leading to spherical, nanorod or nanowire morphologies by varying the temperature and the Se/Zn ratio.[496,497] The syntheses and properties of ZnSe NCs and their core/shell systems reported prior to 2007 have been the object of a dedicated review.[498] Trialkyl phosphines such as

TOP and TBP can also be used to activate the metal precursor if the considered metal center is soft enough as for example in the case of silver, described by Sahu et al.[439] In this method, TOP-Ag was injected at 160 °C into a solution of TOP-Se, ODA, and OA in ODE. 6.5 nm Ag$_2$Se NCs were obtained in the metastable tetragonal phase—bulk Ag$_2$Se exhibits the orthorhombic phase. These NCs exhibited an excellent size dispersion of around 5% (Figure 53) and the same method but using TOPTe could be applied for synthesizing Ag$_2$Te NCs.
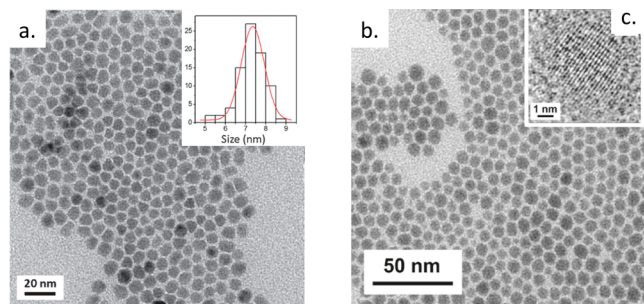

Figure 53. TEM images of Ag$_2$Se (a) and Ag$_2$Te (b) NCs using TOPSe or TOPTe with TOP-Ag. (c) HRTEM image. Reproduced with permission from ref 439. Copyright 2011 American Chemical Society.

This procedure has been slightly modified, which allowed the formation of Ag$_2$Se NC with diameters between 2.8 and 10.8 nm.[438] Diameters below 7.5 nm were synthesized in a similar way to that described before by decreasing the injection temperature to 130 °C and varying the growth time (1−6 min). Diameters larger than 7.5 nm required the utilization of TOP-AgCl and a reaction time of 20 min. The obtained samples exhibited narrow absorption and emission features tunable with size. Importantly the absorption band could be varied from 1.4 to 6.5 μm with increasing size, placing these NCs as interesting alternative to Pb- and Hg-containing mid-IR absorbers. The 2.8 nm NCs exhibited narrow NIR emission centered at 1763 nm with a Stokes shift of 629 nm. TOPSe has also been used for SnSe NC syntheses as in the example of Baumgardner et al., who combined this Se source with bis[bis(trimethylsilyl)-amino]tin.[441] This Sn precursor, dissolved in OLA, was injected into a TOPSe/OLA mixture at temperatures of 65−175 °C, and subsequently OA was injected to quench the nucleation. Quasi-spherical, monodisperse SnSe NCs were obtained with sizes of 4 to 10 nm and a band gap of 1.25 to 0.92 eV. In another approach Liu et al. dissolved Se powder in in different solvents such as TOP, TBP, OLA and OA.[421] The Se precursor was injected into a solution of SnCl$_2$ dissolved in a mixture of OLA, OA, and ODE. The use of OA-Se resulted in spherical NCs with a diameter of 7.5 nm for nucleation/growth temperatures of 156/150 °C. A slight increase of these temperatures to 170/162 °C gave rise to 9.2 nm diameter NCs. Spherical NCs of 7.2 nm diameter were also obtained using OLA-Se with an injection temperature of 150 °C and growth at 146 °C for 30s. With these latter parameters, 2D SnSe nanosheets have been obtained when OLA was replaced by dodecylamine. Also the use of TOPSe or TBPSe as a precursor led to the formation of nanosheets. Wei et al. have developed a method for the synthesis of ZnSe and Ag$_2$Se NCs, using Se in OLA.[430] Se was reduced with sodium borohydride in the presence of OLA producing the reactive hydrophobic precursor. Injection of the latter in a hot solution of Ag(NO$_3$) or Zn(St)$_2$ in OLA, at 100 or 240 °C respectively, triggered the formation of 10−15 nm Ag$_2$Se or <5 nm ZnSe NCs. NaBH$_4$ was employed to facilitate the reduction of elemental selenium in OLA at room temperature, avoiding an extended heating process. Ning et al. used selenourea dispersed in OLA for the synthesis of high quality SnSe NCs with diameters varying from 7 to 20 nm.[442] Sn$_6$O$_4$(OH)$_4$ mixed with OA and OLA acted as the Sn precursor. When a 1:1 ratio was used quasispherical orthorhombic NCs were obtained whose size increased with nucleation temperature from 7.2 nm at 110 °C to 8.4 nm at 140 °C (Figure 54). When changing the Sn/Se ratio to 1:2 or 2:1 nanocubes with sizes of 24 and 19.5 nm have been obtained, respectively (T_{nuc} = 110 °C).

As mentioned in the first part of this section, diorganyl dichalcogenides are another interesting class of chalcogen precursors allowing the control of the reactions kinetics. These compounds can be thermally decomposed either in elemental chalcogen or in monoalkyl-chalcogenide.[499] Wang et al. have used diphenyl diselenide as Se precursor for the synthesis of
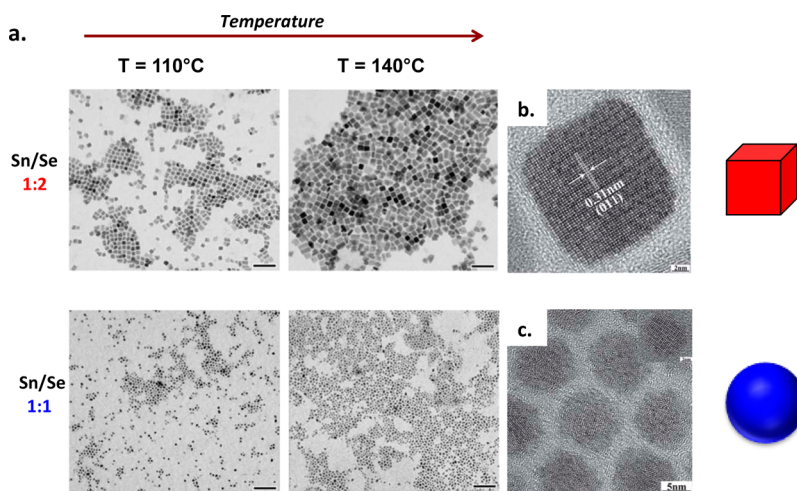

Figure 54. (a) TEM images of SnSe NCs obtained by varying the injection temperature from 110 to 140 °C. Varying the Sn/Se ratio leads to different morphogies. HRTEM images obtained at 140 °C for the (b/c) HRTEM images. Reproduced with permission from ref 442. Copyright 2011 Royal Society of Chemistry.

size-tunable octahedral $Cu_{2-x}Se$ NCs.[434] Ph_2Se_2 was injected into a hot solution combining CuCl and OLA in ODE at temperatures between 200 and 300 °C. Growth for 30 min at 260 °C gave rise to octahedral-shaped NCs in the cubic phase. The size and shape of the particles could be tuned by varying the growth time and reaction temperature: NCs with sizes between 25 and 155 nm were obtained with growth times between 30 s and 60 min (Figure 55). At lower temperature (200 °C) the formation of tetragonal phase Cu_3Se_2 NCs was observed.
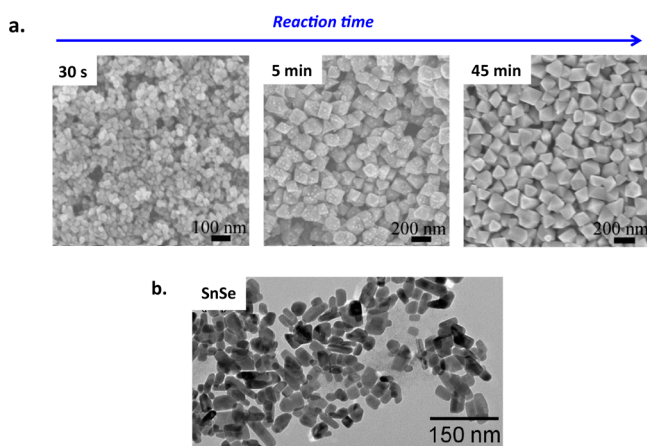

Figure 55. (a) TEM $Cu_{2-x}Se$ NCs obtained during the synthesis with Ph_2Se_2 at 270 °C with growth time of 30 s, 5 min, and 45 min. Reproduced with permission from ref 434. Copyright 2015 American Chemical Society. (b) SnSe NCs obtained from the use of $^tBu_2Se_2$. Reproduced with permission from ref 443. Copyright 2010 American Chemical Society.

Diorganyl dichalcogenides have also been used for the synthesis of SnSe NCs.[443] The reaction of $^tBu_2Se_2$ (di-*tert*-butyl diselenide) with Sn^{2+} (provided as $SnCl_2$) in a mixture containing DDA (dodecylamine) and DDT at 180 °C gave rise to elongated SnSe NCs. For an equimolar Sn/Se ratio the orthorhombic phase was observed while a 2:1 ratio led to the trigonal Berndtite phase. In the original work using the same type of chalcogen precursor performed by Schlecht et al., Sn^0 was reacted with Ph_2Se_2 at 160 °C, which resulted in amorphous NPs.[377] The use of diorganyl dichalcogenides has further been extended to other types of nanostructures, such as ZnSe nano- and microsphere,[500] $MoSe_2$ and WSe_2.[501,502] They are also suitable for the utilization of other techniques such as hydrothermal or microwave assisted methods.

Finally, a number of single-source precursors have been developed for the HI synthesis of metal chalcogenide NCs. In an approach derived from a synthesis developed by O'Brien and co-workers for CdSe NCs,[503] Wakefield et al. injected TOP-ethyl(diethyldiseleno carbamato)zinc into hot TOPO which led to the formation of <6 nm ZnSe NCs.[431] Crystallizing in the wurtzite structure, they exhibited a weak broad emission centered at 446 nm. A more recent example described the use of the bis(phenylselenolato)zinc-tetramethyl-ethylendiamine, which is a better suited ligand for Zn^{2+} ions. Its thermal decomposition led to small, luminescent ZnSe NCs in the zinc blende phase with sizes from 2.7 to 5 nm and PL emission ranging from 351 to 451 nm.[429,432]

More recently, 2-(4,6-dimethylpyrimidyl)selenoate (DPSe) metal complexes were used for the synthesis of coinage metals

selenides.[436] In this method, the M(DPSe) complexes were freshly prepared from metal salts and Na(DPSe) in the presence of BH_4 and CH_2Cl_2. This solution was injected into hot DDT at 150 °C and 30 min growth gave rise to cubic phase Cu_7Se_4 and orthorhombic Ag_2Se NCs. In both cases, spherical shaped aggregated structures were obtained. These structures were composed of irregular shaped NC with diameters of 100–500 nm in the case of Cu_7Se_4 and of a mixture of spherical and ellipsoid shaped particles with sizes of 110–170 nm and 100 × 200 nm respectively, in the case of Ag_2Se. Even if the use of SSP in the described examples did not result in an improvement of the size dispersion as compared to conventional HU or HI methods, they represent an interesting alternative for the synthesis of other types of NCs such as NiSe. Nickel selenide is a p-type semiconductor with a direct band gap of around 2.0 eV. Indeed, as mentioned previously, most of the traditional methods for the synthesis of this material gave rise to highly polydisperse or amorphous nanoparticles. Raftery and co-workers used metal selenophosphinate $M(Se_2PR_2)_2$ (R = iPr, tBu, and Ph) dissolved in TOP and quickly injected into HDA or TOPO at 200, 280, and 330 °C.[444] Once the nucleation was initiated, the growth was continued for 1h. The obtained NCs had diameters from 3.9 to 6.2 nm when the nucleation temperature was varied from 330 to 280 °C. The authors have shown that the length of the alkyl moiety had only a small influence on the size and shape of the NCs. However, the nature of the substitute could direct the crystallization toward different phases: When iPr was used the NCs crystallized in the hexagonal phase, while in the case of tBu orthorhombic NCs were obtained. The use of Se_2PPh_2 gave rise to tetragonal phase $Ni_{12}P_5$ particles. Moloto et al. have developed another method using the SSP $[NiCl_2(Se_2C_6H_5)_2]$ synthesized by reacting diphenyldiselenide with $NiCl_2$.[445] This compound, dispersed in TOP, was injected in HDA at 160 °C and kept at this temperature for 60 min. This single-source approach was also compared to HI methods using $NiCl_2$ and TOPSe or Na_2Se in HDA at 160 °C. The latter gave rise to amorphous materials composed from the aggregation of orthorhombic NiSe particles, the SSP approach lead to the formation of cubic $NiSe_2$ NCs with diameters ranging between 10 and 15 nm. The magnetic properties have not been investigated, however, the authors reported a luminescence emission centered at 400 nm.

4.3.2.3. Metal Telluride NCs. In comparison with their S and Se based homologues, metal telluride NCs have been less developed. Due to the differing reactivity of the tellurium precursors, numerous syntheses based on HU methods gave rise to amorphous or polydispersed samples. Furthermore, many metal tellurides are more sensitive to oxidation than sulfides and selenides. One notable exception is the case of CdTe NCs prepared in aqueous media, which drew tremendous research interest.[504] In contrast to their synthesis in organic solvents, characterized by high air-sensitivity, CdTe NCs prepared from Cd salts and hydrogen or alkali telluride in the presence of hydrophilic thiols in water are extremely stable and show intense fluorescence. The in situ generation of a passivating CdS surface layer is generally invoked to explain this behavior.[505] The majority of synthetic approaches for the preparation of MTe NCs in organic solutions applies the HI approaches. The methods developed for CdTe by Talapin et al. and Wuister et al.,[506,507] which gave rise to high quality NCs with PL QY up to 65%, provided an excellent basis for the development of other metal telluride nanoparticles. These

syntheses used trialkylphosphine telluride as the chalcogenide precursor in the presence of alkylamine. A direct adaptation of this method to ZnTe has been proposed by Bang et al. yielding luminescent ZnTe core as well as ZnTe/ZnSe and ZnTe/ZnSe/ZnS type II core/shell NCs.[446] The injection of a mixture containing both highly reactive $ZnEt_2$ and TOPTe, into a mixture of ODE and HDA at high temperature (270 °C) gave rise to ZB ZnTe QDs with mean diameters of 2.2 nm. The HDA capped ZnTe NCs exhibited no luminescence. Without further purification, they were subsequently coated with ZnSe and/or ZnS shells. In each case, the shell deposition was performed using a one-pot synthesis where TOPSe or bis(trimethylsilyl)sulfur in TOP and $ZnEt_2$ in HDA were added dropwise during 6 h to the colloidal solution of the ZnTe NCs in a HDA/ODE mixture at 200–250 °C. Upon shell deposition, the maximum of emission varied from 500 to 600 nm upon deposition of 1 to 5 ZnSe monolayers due to the type II band alignment with spatial separation of the photogenerated electron–hole pair in the core and shell regions. PL lifetimes of 77 ns and a QY up to 6% were observed. The use of less reactive and easier-to-handle Zn sources has been widely investigated. As in the case of the metal sulfides and selenides, air-stable $Zn(St)_2$ represents an interesting alternative to $ZnEt_2$, which can also act as Z-type surface ligand. Using this Zn source, Park and co-workers studied the shape evolution of ZnTe NCs from nanoflower shaped aggregates to nanorods, as a function of temperature and surfactant nature.[448] In this work, the ZnTe NCs were obtained through the injection of a solution of TOPTe or TBPTe eventually mixed with alkylamine, into a solution containing the metal precursor in ODE at 300 °C. As shown in Figure 56, the variation of the reaction parameters allowed shape control leading to the formation of three different morphologies: nanorods, quantum dots, and flower shaped aggregates of quasispherical NCs. The authors demonstrated that the surfactant nature and concen-

tration variation allowed control over the formation of ZB nanodots and nanoflowers whereas temperature variation enabled the formation of orthorhombic nanorods.

A similar approach has been used by Lincheneau et al. for the synthesis of ZnTe and ZnTe/ZnS QDs.[447] In this work, TBPTe was used and flower-like aggregates were obtained. These aggregates were composed of quasi-spherical NCs with diameters ranging from 4.4 to 9 nm depending on the temperature or the presence of ODE. The presence of ODA or of a higher temperature led to the formation of larger NCs. Conversely, the presence of TOPO in the reaction mixture prevented particle formation. In each case, the obtained NCs exhibited low stability under ambient conditions and no luminescence. They were coated with 2−5 monolayers of ZnS using the SILAR method, which led to a size increase from 5 to 6.1- 9.3 nm (for 2 and 5 monolayers, respectively). While still no luminescence could be detected, the stability was greatly increased from several hours to several months. The obtained samples generated an anodic photocurrent up to 35 nA, making them potential candidates for applications in photovoltaics or photodetectors. SnTe is another material of interest for such types of applications as well as for thermoelectrics. Tilley and co-workers described a facile synthesis of spherical SnTe NCs with tunable size, base on $SnBr_2$ and TOP-Te.[458] In this approach the tin precursor was activated using triethanolamine (TEA) in DMF. A TOPTe solution was injected into this mixture at a comparably low temperature of 50 °C leading to the formation of small SnTe NCs with diameters of 2.7 nm. Their size could be further increased up to 6.5 nm by heating to 150 °C. The size of the particles could be further tuned with the quantity of TEA. Decreasing the quantity of TEA gave rise to smaller NCs due to the decreased stabilization of the Sn-TEA complex by the presence of excess TEA. Changing the amount of TEA thus allowed the control of the remaining monomer reservoir during the growth phase. However, when the quantity of TEA was too small the formation of NCs of irregular shape with diameters up to 32 nm occurred. The obtained samples crystallized in the rocksalt structure and showed an absorption spectrum, which extended to the NIR range. Size control allowed the modulation of the absorption onset from 2270 and 3400 nm. In the case of copper based NCs, the use of $Cu(acac)_2$ represents a widely used Cu^{II} source. It is usually activated in situ by the use of OA or alkylamines. Yang et al. developed a method based on the reaction of $Cu(acac)_2$ with TOP-Te in OLA for the formation of high quality multifaceted plasmonic $Cu_{2-x}Te$ NCs as well as hollow NCs (HNC).[454] Injection of the chalcogen precursor into the solution of the Cu precursor at 220 °C triggered the nucleation. The obtained NCs were monodisperse and multifaceted with mean diameters varying between 4.4 to 8 nm depending on the growth time (up to 1 h; Figure 57). Conversely, HNC were obtained by the Kirkendall effect, using the same parameters but leaving the $Cu(acac)_2$-OLA mixture at temperatures <220 °C prior to injection of TOPTe.

The HNC crystallized in the hexagonal phase and had mean diameters of 16.5 nm (Figure 57c.). The authors envisaged a two-step mechanism for explaining the different morphologies obtained (Figure 57a): heating of the Cu-OLA solution to 220 °C formed Cu_2O NCs, whereas stirring of this solution for 1 h at temperatures below 220 °C provoked the formation of Cu NCs. Upon injection of TOP-Te, these seed particles were transformed into $Cu_{2-x}Te$ NCs and HNCs, respectively. The materials synthesized using this approach exhibited plasmonic
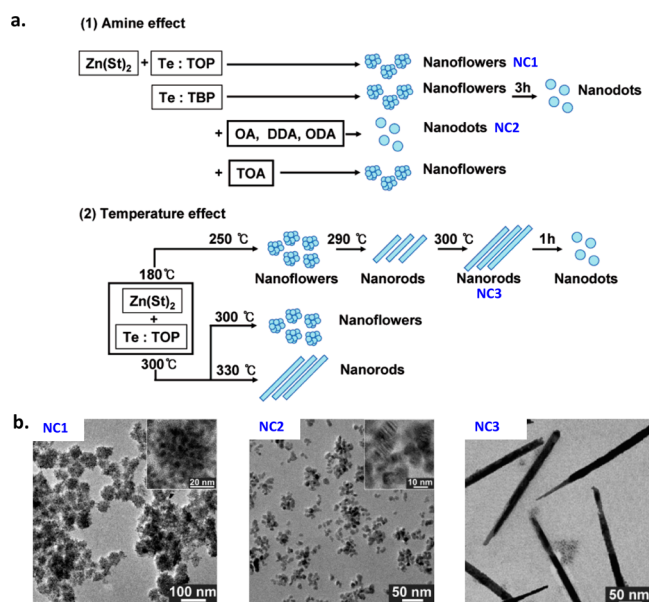

Figure 56. (a) Effect of amine addition and temperature variation on the morphology of ZnTe NCs obtained from a HI synthesis using $Zn(St)_2$ and TOPSe or TBPSe as precursors. (b) TEM images of nanoflower shaped aggregates (NC1), spherical NCs (NC2), and nanorods (NC3). Reproduced with permission from ref 448. Copyright 2007 American Chemical Society.
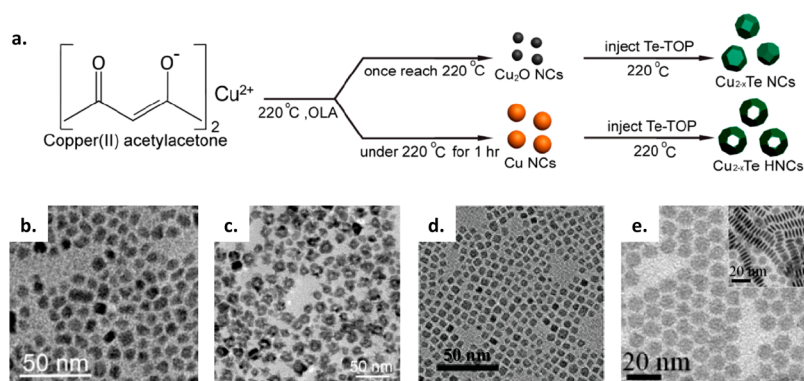
Figure 57. (a) Mechanism proposed for the synthesis of plain and hollow (HNC) $Cu_{2-x}Te$ NCs using TOPTe and $Cu(acac)_2$. (b/c) TEM images of $Cu_{2-x}Te$ faceted NC and HNC obtained in the presence of OLA. (d) Faceted $Cu_{2-x}Te$ NCs obtained in the presence of OA and DDT. (e) Hexagonal shaped $Cu_{2-x}Te$ discs obtained in the presence of OA and DDT. Reproduced with permission from refs 454 and 455. Copyright 2012/2013 American Chemical Society.
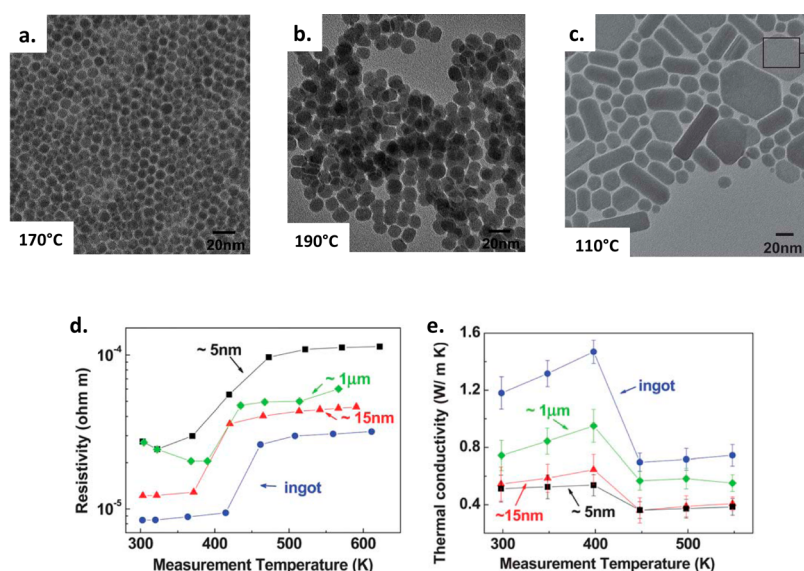
Figure 58. TEM images of Ag_2Te NCs obtained by injecting TOPTe to a mixture of $AgNO_3$, OLA and DDT at 170 °C (a), 190 °C (b), and 110 °C (c), respectively. (d) Resistivity and (e) thermal conductivity as a function of temperature. Reproduced with permission from ref 461. Copyright 2012 Royal Society of Chemistry.

absorption bands centered at 1150 nm for the NCs (with $\varepsilon \approx 2.6 \times 10^7$ M^{-1} cm^{-1}) and at 1200 nm for the HNCs (with $\varepsilon \approx 8.1 \times 10^7$ M^{-1} cm^{-1}). The research on $Cu_{2-x}Te$ particles showing size-tunable plasmonic properties has drawn significant research interest. With the aim of developing quasi-spherical $Cu_{2-x}Te$ NCs showing enhanced tunable IR absorption, Kriegel et al. developed a method based on the combination of the same Cu and Te precursors.[455] However, $Cu(acac)_2$ was dissolved in a mixture of DDT and OA, and the injection of TOP-Te was carried out at 160 °C. After 30 min of growth the obtained NCs exhibited the Cu_2Te stoichiometric phase (Figure 57d.). The authors have shown that the composition of the NCs could be changed from $Cu_{2-x}Te$ ($x > 0$) to Cu_2Te and vice versa through reduction or oxidation, respectively. Changing the composition directly influences the plasmonic absorption properties, as the density of free carriers per volume increases with decreasing copper content. A similar method has been used for the synthesis of hexagonal shaped $Cu_{2-x}Te$ nanodisks and spherical NCs with tight size and shape control by varying the temperature of injection.[456] For temperatures between 175 and 185 °C nanodiscs with average sizes ranging

between 2.2 × 12 nm (175 °C) and 3.2 × 8 nm (185 °C) were obtained (Figure 57e). Conversely, increase and decrease of the reaction temperature to 160 and 200 °C gave rise to the production of spherical NCs with mean diameters of 4.6 and 7.4 nm, respectively. Once the nanodisks were isolated and purified, they were used as templates for the formation of luminescent CdTe nanodisks using cation exchange at higher temperatures. A more recent contribution by Han et al. focused on the influence of the surfactants, namely OLA, OA, TOP and TOPO.[457] At the same time the variation of reaction temperature and of the Cu/Te ratio was investigated. $CuCl_x$ ($x = 1$ and 2) was used as copper source and TOPSe as the chalcogenide precursor. Without the use of any additional surfactants, injection at 230−250 °C gave rise to monodisperse nanocubes with sizes tunable from 54 to 75 nm by changing the temperature and growth time. The size of the nanocubes could also be increased up to 104 nm by increasing the Cu concentration albeit on cost of the narrow size distribution. The shape of the NCs could be tuned with the Cu/Te ratio. It varied from polydisperse irregular shaped particles to monodisperse nanocubes when the Cu/Te changed from 0.5

Figure 59. TEM images and size dispersion of GeTe obtained from the reaction of Ge-HMDS with TOPTe in the presence of DDT (a) and OLA (b) and from the reaction of GeCl$_2$-dioxane with TOPTe in the presence of DDT (c). Reproduced with permission from ref 467. Copyright 2011 American Chemical Society.

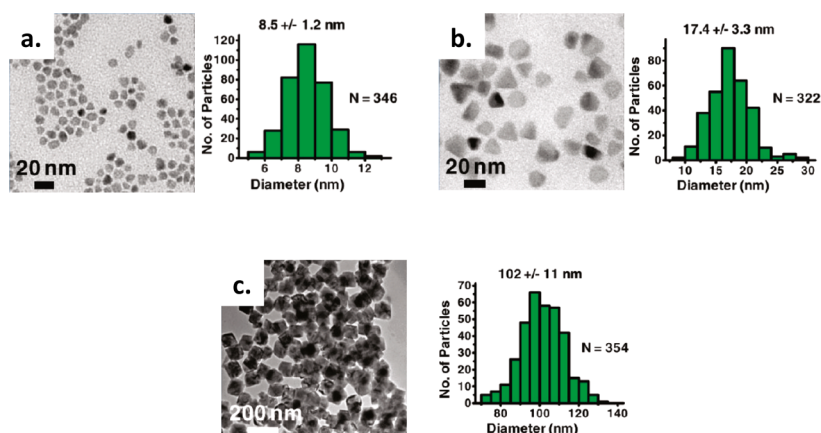to the optimal value of 5. When the reaction was carried out using OLA, TOPO or OA as solvents, Cu$_{2-x}$Te nanosheets, a mixture of Te and CuTe particles or a mixture of Cu$_{1.85}$Te and Cu$_4$Te$_3$ NCs were obtained, respectively. The addition of small amounts of these ligands into TOP broadened the size distribution of the nanocubes. Similar approaches can be applied for Ag$_2$Te NCs. Chen et al. have first described the formation of Ag$_2$Te nanosheets using a HU synthesis.[460] In this approach a mixture containing TOP, Se and AgNO$_3$ heated to 160 °C for 2 h gave rise to nanosheets with either round or hexagonal shape crystallizing in the monoclinic phase. The latter exhibited dimensions of 20−40 nm, while the disc shaped NCs had a mean diameter of 32 nm. In both cases the average thickness was 5.5 nm. The increase of temperature led to bigger NCs but with irregular shapes. Changing the Ag/Se ratio from 2:1 to 1:5 allowed increasing the thickness from 5.5 to 8.1 nm. The electrical conductivity was measured as 102.1 S/cm. In this synthesis TOP acted as both solvent and stabilizer with no addition of other surfactants such as alkylamine or carboxylic acids. Zhou et al. have developed a method for the formation of highly uniform Ag$_2$Te NCs by injecting TOPTe into a mixture containing AgNO$_3$, OLA and DDT.[461] The monodisperse spherical NCs had diameters in the range of 5−15 nm and size modulation was achieved either by changing the temperature or the growth time (Figure 58).

When the injection temperature was decreased to 110 °C nanoplates of irregular shapes and size were produced. The authors suggested that the presence of OLA slowed the nucleation process, leading to the formation of larger NCs. They also demonstrated that DDT acts as a surfactant limiting the growth, as the same synthesis without DDT gave rise to spherical nanoparticles with sizes of ca. 1 μm. The obtained Ag$_2$Te NCs exhibited promising thermoelectrical properties, in particular decreased thermal conductivity as compared to the bulk. The use of DDT has also been investigated in the synthesis of bismuth and antimony telluride NCs, which are also materials of high interest for thermoelectric applications. Kim et al. have developed a simple approach for the synthesis of Bi$_2$Te$_3$ and Sb$_2$Te$_3$ NCs by the injection of a solution of TOPTe in DDT into a mixture of M(OAc)$_3$ (M = Bi or Sb) dissolved in OA, at various temperatures (50, 100, and 150 °C).[463] For both materials, the injection at 50 °C gave rise to amorphous crystalline products. Higher temperatures improved the crystallinity of the samples and gave rise to 100 nm

nanospheres of rhombohedral Bi$_2$Te$_3$ and hexagonal phase Sb$_2$Te$_3$ nanoparticles. These nanoparticles were assemblies of smaller spherical NCs with diameters of 3−5 nm and 5−7 nm, respectively. This approach can be used for the large-scale synthesis of Bi$_2$Te$_3$ and Sb$_2$Te$_3$ based nanostructures for thermoelectric applications. The versatility of TOPTe as a Te source has further been demonstrated in syntheses of GeTe NCs. Milliron and co-workers injected DDT, followed 30 s later by TOPTe, into a solution of GeI$_2$ in TOP and TOPO at 250 °C.[466] The resulting GeTe NCs were amorphous and had mean diameters of 3.5 nm. The use of DDT was mandatory for obtaining nanoparticles of controlled morphology. The authors attributed this to the thiol activation of the GeI$_2$-TOP complex, increasing the reactivity of the germanium precursor. The utilization of other Ge precursors has been explored by Alivisatos and co-workers who compared halide and silylamide compounds: GeCl$_2$ and Ge[N(SiMe$_3$)$_2$]$_2$ (Ge-HMDS).[467] Metal silylamides have meanwhile turned out to be suitable precursors for the precision synthesis of a large variety of semiconductor NCs.[508] Here, the germanium precursor was reacted with TOPTe in the presence of excess of TOP and DDT, or OLA, at 250 °C. When DDT was used, multifaceted NCs with mean diameters of 8.5 nm were obtained, whereas in the case of OLA the diameter increased to 17.4 nm, with narrow size distribution (Figure 59). The use of a GeCl$_2$-dioxane complex with DDT at 180 °C instead of Ge-HMDS gave rise to larger NCs with sizes up to 102 nm. However, while the particles with sizes below 30 nm were monocrystalline, those above 30 nm exhibited multiple crystalline domains.

The same approach, using a lower temperature of 200 °C in the presence of DDT and OLA, yielded smaller GeTe NCs with average diameters of 4.3 nm after 1 min of growth.[468] Extension of the growth time to 2−3 min led to the formation of larger polydispersed NCs with sizes ranging between 9 and 28 nm. When TOPTe was injected into a solution of Ge(HMDS) in OLA at 170 °C, in the absence of DDT, spherical amorphous GeTe NCs were obtained, with diameters ranging from 8.5 to 18.5 nm, tunable with growth time. The use of Ge(HMDS) and TOPTe as precursors, with various surfactants also provides a method for controlling the shape of GeTe NCs. Buck et al. described a polymer assisted method for the controlled growth of faceted GeTe NCs.[469] This approach is similar to the one described previously, except that OA (or nonanoic acid, NA) and poly(vinylpyrrolidone) (PVP)
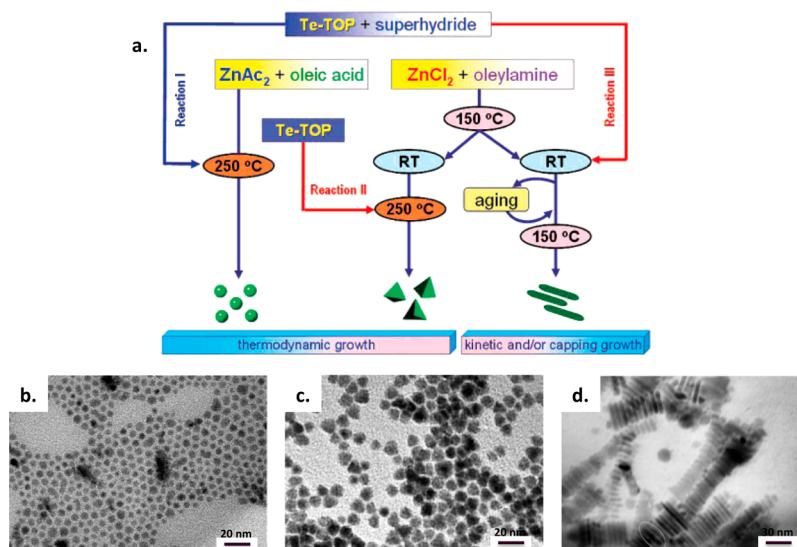
Figure 60. (a) Different approaches for the synthesis of spherical, tetrahedron-, and rod-shaped ZnTe NCs. (b−d) TEM images of the obtained samples. Reproduced with permission from ref 449. Copyright 2008 American Chemical Society.

or poly(1-vinylpyrrolidone)-*graft*-(1-triacontene) (PVP-t) were used as surfactants instead of OLA and DDT. When Ge(HDMS) and the couple OA/PVP-t were reacted with TOPTe at 230 °C, the formation of multifaceted NCs in the rhombohedral crystalline phase was observed. They exhibited octahedral shape with edge lengths ranging from 70 to 100 nm. Conversely, when the same reaction was carried out in the absence of OA, large amorphous NCs were obtained with sizes around 100 nm. These findings were rationalized by the formation of a complex of Ge(HMDS) with protogenic molecules such as OA. The decomposition of the latter slowed down the nucleation kinetics and gave better control of the crystal growth.[509] The same synthetic approach, using OA/PVP at 250 °C also yielded faceted NCs, albeit more polydisperse than with PVP-t. Conversely, the use of NA instead of OA gave rise to the formation of 2D platelets with hexagonal and triangular shapes in the rhombohedral phase. Addition of NaNA led to spherical nanoparticles with average diameter of 90 nm, suggesting that the reactivity of the precursor was decreased by the presence of an extra carboxylate. A further increase of the quantity of NaNA directed the growth toward formation of 2D nanosheets, with lateral dimensions ranging from 175 to 900 nm. The nanosheets exhibited several different morphologies such as triangular, quadrilateral and hexagonal. The use of metal silylamides has been extended to the synthesis of high quality spherical SnTe NCs of narrow size distribution. Kovalenko et al. reacted Sn(HMDS) in ODE with a solution of TOPTe in OLA using the HI method at 150 °C and a growth temperature at 120 °C.[459] The SnTe NCs crystallized in the cubic rocksalt phase and their size could be tuned from 4.5 to 15 nm by adjusting the injection and growth temperatures as well as the concentration of OLA in the reaction mixture. The lowest size distributions were obtained for 90−150 °C enabling the self-assembly of the NC in 3D superlattices. The SnTe NCs showed a band gap of 0.38−0.8 eV and have high potential for application in IR photodetectors. The synthesis of sub-10 nm Bi_2Te_3 is intrinsically difficult due to the high reactivity of bismuth salts with tellurium. Furthermore, bismuth telluride can adopt various compositions complicating the synthesis of phase-pure materials. While direct HI and HU approaches failed, Weller and co-workers proposed an elegant multistep

approach for transforming initially formed bismuth nanoparticles into Bi_2Te_3 by means of TOPTe.[510] Monodisperse Bi nanoparticles of with tunable sizes in the range of 7−40 nm were obtained through the reduction of bismuth acetate by means of oleylamine in the presence of DDT stabilizing ligands. TOPTe was prepared by heating to 220 °C high purity Te powder and distilled TOP in the presence of octadecylphosphonic acid. Bi−Te alloy nanoparticles, which have an approximately 20% larger size than the parent Bi particles, were produced by injecting the Te precursor into the crude colloidal solution of Bi nanoparticles at 60 °C and stirring for 2−3 days. Finally heating at 110 °C for 18 h afforded monodisperse Bi_2Te_3 NCs in the rhombohedral phase, which is accompanied by a change from a spherical to rhombohedral shape.

In addition to these works exploring the chemistry of various metal precursors, attempts have also been made for controlling the reactivity of the Te precursor. One of the first examples has been reported by Zhang et al. in 2008 for the controlled preparation of ZnTe nanotetrahedrons, spherical NCs and nanorods (Figure 60).[449] In this work TOPTe has been used in combination with a superhydride (lithium triethylborohydride), a powerful reducing agent widely applied in organometallic and organic chemistry. As described in the beginning of this section, TOPTe forms an equilibrium with metallic Te.[361] The addition of reducing agents like superhydride is expected to produce an increased amount of reactive $Te^{2−}$ and $TeH^−$ species. In a first approach the HI of the Te precursor into a solution containing $Zn(OAc)_2$ and OA at 250 °C led after few minutes of growth to spherical monodisperse ZB ZnTe NCs with a mean diameter of 5 nm. A second approach consisted in three injections (every 15 min) of neat TOPTe into a solution of $ZnCl_2$ in OLA at 250 °C, which gave rise to tetrahedron shaped NCs with sizes around 5 nm as well. The third method, which led to the formation of nanorods with average sizes of ∼5 × 30 nm consisted in the gradual heating up of the TOPTe/superhydride solution with $ZnCl_2$/OLA to 150 °C and stirring for 3 h. Unlike the two other methods, the third one favors a kinetically controlled growth accompanied by the binding of the capping ligands to specific crystal facets, leading to the formation of uniform nanorods.

This approach has been further optimized by adding OLA to the TOPTe/superhydride mixture, freshly prepared before its injection into the solution of the zinc precursor consisting of $Zn(OAc)_2$ in ODE and OA.[450] After the nucleation at 160 °C, the temperature was further increased to 300 °C for the growth process. The size and shape of the ZnTe NCs could be tuned as a function of the temperature and the quantity of superhydride. Upon injection at 190 °C and using an excess of superhydride with respect to TOPTe, spherical NCs with an average diameter of 3.5 nm were obtained. However, in the presence of an equimolar ratio of hydride, the formation of well-defined nanorods of 3.5 nm diameter was observed. Finally, a smaller amount of superhydride gave rise to small NCs of irregular shapes. The size of the obtained nanorods could be modulated with the growth temperature and time, up to dimensions of 140 × 6.8 nm. The authors reported that the use of superhydride in combination with OLA and TOPTe led to the formation of a mixture of Te^{2-}, Te_2^{2-}, Te_3^{2-}, and higher polytellurides. The observed temperature dependence of NC morphology was ascribed to the different reactivity of Te^{2-} and polytelluride species. At lower temperatures Te^{2-}, being the most reactive species, promotes isotropic growth. Less reactive polytellurides react slower and preferentially with the highly active ($00\bar{1}$) facet, favoring 1D growth at higher temperatures. In a similar synthesis, TOPTe/superhydride was injected in a mixture of $ZnCl_2$ in OLA at 160 °C and heated to 280 °C.[451] ZnTe nanowires in the wurtzite structure with small diameters of 2 nm were obtained. Further heating at 280 °C with OLA during 5 to 60 min led to the formation of nanorods of 4.5 nm diameter via a ripening mechanism. Different reducing agents have been explored in the synthesis of GeTe particles. Using the combination of GeI_2, TOPTe and *t*-butylamine borane (tBAB), Buck et al. synthesized monodisperse GeTe cubes of 1 μm edge length.[132] The nucleation was triggered via injection of tBAB in octylether into a solution of GeI_2 and TOPTe in TOP at 180 °C. The obtained cubes crystallized in the rhombohedral phase typical for the low temperature polymorph of GeTe, which is slightly distorted with respect to the rocksalt structure. As an alternative or additive to tertiary alkylphosphines and phosphine oxides, in recent years their secondary counterparts have become popular in NC synthesis.[139] This was triggered by the fact that, on one hand, their presence as impurities in the former has been revealed and, on the other hand, their influence on reaction mechanisms has been understood.[511] Shen et al. developed a general procedure for the formation of various metal telluride NCs, such as ZnTe, $Cu_{2-x}Te$, and Ag_2Te, with various morphologies. This approach is based on the use of ZnO or metal acetylacetonate and di-*n*-octylphosphine oxide telluride (DOPOTe).[452] In a typical synthesis, DOPOTe was combined with OLA in paraffin oil (in the case of Ag_2Te only OLA was used) and the formation of the NCs was triggered by injection of the metal precursor solution. In the case of ZnTe, ZnO dispersed in OA and ODE was used as Zn source. The nucleation occurred at 310 °C and gave rise to ZB ZnTe nanodots with diameters of 7.5 nm (Figure 61). The same approach was utilized for the synthesis of $Cu_{2-x}Te$ NCs. In this case, the widely applied copper precursor $Cu(acac)_2$, dispersed in OA and OLA, was used. The reaction with DOPO-Te in paraffin oil at 180 °C yielded $Cu_{2-x}Te$ nanocubes of 32.8 nm edge length in the tetragonal phase. When the synthesis was performed with the Ag precursor at 150 °C in the presence of OLA, 9.2 nm Ag_2Te NCs in the tetragonal phase were obtained. Addition of OA to the Ag
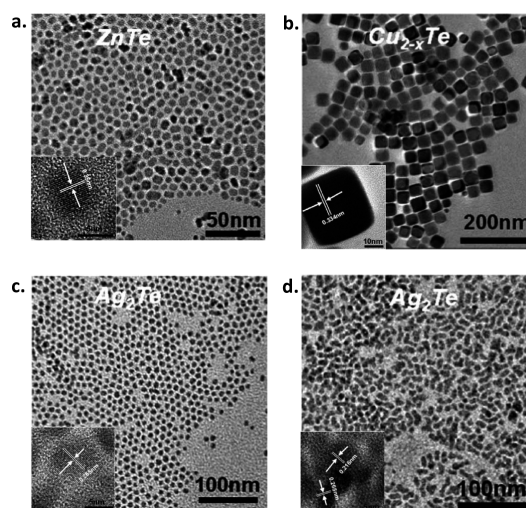
Figure 61. TEM images of spherical ZnTe NCs (a), $Cu_{2-x}Te$ nanocubes (b), and spherical (c) and elongated (d) Ag_2Te NCs obtained by reacting the metal precursors with DOPOTe. Reproduced with permission from ref 452. Copyright 2012 Royal Society of Chemistry.

precursor solution and injection at 120 °C led to the formation of 11.6 × 18.8 nm rod-shaped NCs. The authors suggested that a DOPO-Te intermediate was formed with a P=Te double bond. Starting from this compound, formation of di-*n*-octylphosphinic acid (DOPA) and $Te^{(0)}$ in the presence of oxygen competes with NC formation. Therefore, the absence of oxygen in the reaction mixture is of crucial importance for the successful synthesis. As in the case of the Se-based NCs, the use of diorganyl dichalcogenides offers in principle an interesting way to control the decomposition of the chalcogen precursor and therefore the delivery of tellurium during nucleation and the growth. In an initial approach Schlecht et al. used Ph_2Te_2 for the synthesis of SnTe NCs.[377] In the first step $SnCl_2$ was reduced in the presence of $Li[Et_3BH_4]$ in THF. The obtained nanocrystalline tin was isolated, dispersed in diglyme and mixed with Ph_2Te_2. Gradual heating to 165 °C resulted in the formation of SnTe NCs in the cubic phase. With high precursor concentrations, large agglomerates of particles with an average size of 60 nm were obtained. Conversely, the use of 10-fold smaller concentration provoked the formation of smaller star-shaped aggregates of needles. The needles exhibited average dimensions of 15 × 40 nm. The authors proposed homoleptic cleavage of the Te–Te bond in the course of the reaction preceding Te–C bond cleavage.

Finally, as in the case of the metal sulfides and selenides, single-source precursors (SSP) have applied for the synthesis of M-Te NCs. Cheon and co-workers used the thermolysis of the SSP $Zn(TePh)_2\cdot[TMEDA]$ for the obtention of spherical and rod-shaped ZnTe NCs.[453] The synthesis of spherical NCs with size of 4.2 or 5.4 nm was performed through the injection of the SSP solution in TOP into dodecylamine at 180 or 240 °C, respectively. They crystallized in the cubic phase and exhibited blue luminescence centered at 377 and 451 nm, respectively. When the reaction was carried out with the same parameters but adding dimethylhexylamine (DMHA) to the precursor solution, the formation of rod-like NCs was observed with diameters of 25 nm and lengths varying from 200 to 700 nm. Schultz et al. developed a SSP method for the preparation of Sb_2Te_3 nanoplates (Figure 62).[464] This approach was based on
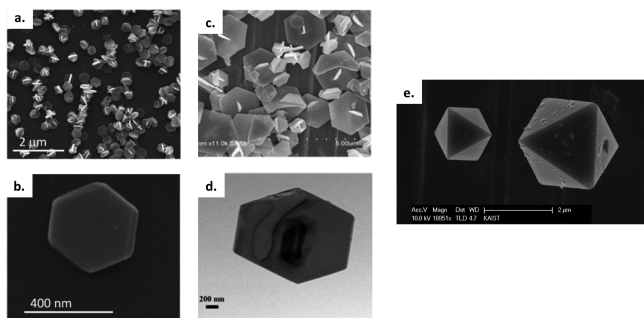
Figure 62. (a/b) Sb_2Te_3 hexagonal nanoplates obtained from the decomposition of $(Et_2Sb)_2Te$ in the presence of PVP-t. Reproduced with permission from ref 464. Copyright 2012 American Chemical Society. (c/d) Sb_2Te_3 nanoplates synthesized by decomposing Ph_2SbTeR (R = Et, Ph) in the presence of OLA and TOP. (e) Bipyramidal Sb NCs resulting from the decomposition of $Ph_2SbTePh$ in absence of OLA and TOP. Reproduced with permission from ref 465. Copyright 2013 Royal Society of Chemistry.

the thermolysis of the SSP $(Et_2Sb)_2Te$ (bis(diethylstibino)-telluride) in the presence of poly(1-vinylpyrrolidone)-*graft*-(1-triacontene) (PVP-t) as capping agent. First, the SSP was synthesized at room temperature through the reaction of tetraethyldistibine Et_4Sb_2 with elemental tellurium in pentane. This compound was then reacted in 1,3-diisopropylbenzene (DIPP) in the presence of PVP-t by heating to 180 °C for 10 h. Hexagonal shaped nanoplates in the rhombohedral phase with average diameters of 400 nm and thickness of 35 nm were obtained using 10 wt % of PVP-t. The quantity of PVP-t strongly influenced the size of the NCs. Their diameters could be tuned from 500 to 200 nm when increasing the quantity of PVP-t from 3 to 50 wt %. Thermoelectric measurements showed that the obtained nanoplates exhibited Seebeck coefficients of around 150 μV/K at ambient temperature, indicating that this SSP approach led to particles with a low concentration of antisite defects.

The synthesis of larger hexagonal Sb_3Te_2 nanoplates was described by Kim and co-workers.[465] Their approach is based on the use of the SSP Ph_2SbTeR (R = Et, Ph). The precursor was synthesized by the reaction of the commercially available Ph_2SbCl with elemental Te in the presence of alkyllithium at room temperature. Sb_3Te_2 NCs were obtained through thermal decomposition of the SSP in the presence of OLA and TOP. The reaction was triggered via injection of TOP in a solution of Ph_2SbTeR in OLA at high temperature (250–300 °C). After 1–2 h of growth, hexagonal nanoplates in the rhombohedral phase were obtained (Figure 62). Their edge lengths varied from 0.4 to 2 μm with thicknesses of 20–50 nm depending on the reaction temperature. When $Ph_2SbTeEt$ was used, the formation of a mixture of Sb_2Te and Sb_3Te_2 NCs (Sb_2Te as predominant phase) was obtained at 250 °C. Increase of the injection temperature to 300 °C gave rise to phase-pure Sb_2Te_3 NCs. In the case of the use of $Ph_2SbTePh$ as SSP, in each case exclusively Sb_2Te_3 was formed. The decomposition of $Ph_2SbTePh$ in the absence of OLA and TOP gave rise to bipyramidal shaped Sb nanoparticles. Within the group IIIA tellurides the heavier homologue Bi_2Te_3 is to date the most important material for use in thermoelectric electrical energy generation in a range close to ambient temperature. SSP methods have been extended to NCs of this material, whose synthesis by conventional HI or HU approaches turned out to be difficult. Schultz and co-workers explored several strategies

for the synthesis of various phases of bismuth telluride, such as BiTe, Bi_2Te, Bi_2Te_3 and Bi_4Te_3.[462] The SSP $(Et_2Bi)_2Te$ and $Et_2BiTeEt$ were chosen as they provide Bi and Te in 2:1 and 1:1 stoichiometric ratios. Therefore, these SSPs were anticipated to give rise to Birich NCs. The syntheses were carried out via thermal decomposition of the SSPs in DIPB (1,3-diisopropylbenzene), or OLA, at 80 and 100 °C for $(Et_2Bi)_2Te$ and $Et_2BiTeEt$, respectively. The decomposition of $(Et_2Bi)_2Te$ at 80 °C gave rise to large aggregates of 200 nm size. These aggregates were composed of rhombohedral phase Bi_4Te_3 NCs with sizes ranging from 10 to 40 nm. Further addition of PVP-t could diminish the level of aggregation of the particles but no narrow size distributions could be obtained. The decomposition of $Et_2BiTeEt$ in OLA gave rise to a mixture of elemental Bi and Bi_2Te NCs. When the reaction was performed in DIPB, phase-pure Bi_2Te NCs were obtained in form of well-defined nanocubes with edge lengths of 100 nm. With increasing reaction time, the particle size reached up to 500 nm. Thus, the thermolyses of these two SSPs resulted in the formation of Birich phases and, unlike in the case of the antimony analogues, the Bi_2Te_3 phase was not detected. This approach was compared with a dual precursor approach, in which a mixture of $Bi(NMe_2)_3$ was reacted with $Te(SiEt_3)_2$ in DIPB at 100 °C using the HI method. In this case Bi/Te ratios of 1:1, 2:3, and 4:3 were explored leading to the selective production of NCs with BiTe, Bi_2Te_3 and Bi_4Te_3 stoichiometry, respectively. In the case of Bi_2Te_3, the NCs were polydisperse with approximately cubic shape and edge lengths of ca. 40 nm.

4.3.3. Ternary and Multinary Metal Chalcogenide NCs. Ternary and multinary chalcogenide semiconductors constitute a large family of materials, which offer the opportunity to influence the band gap not only by changing the size but also by varying the stoichiometry of the constituting elements. Most importantly, they give access to a broad range of semiconductors having band gap energies in the visible and near-infrared range without relying on toxic heavy metals such as Cd, Pb, and Hg. Table 8 lists a number of these compounds, which have been investigated in form of colloidal NCs, and which will be the center of the following section. In recent years reviews on the synthesis and properties of NCs of specific multinary materials appeared,[512,513] as well as a general review on this subject from our group.[369]

Table 8. Properties of Selected Ternary and Quaternary Metal Chalcogenide Materials (at 300 K)

compound	band gap (eV)	crystal structure	space group	lattice parameters
$CuInS_2$	1.53	chalcopyrite	$I–42d$	$a = 5.52$ $c = 11.12$
$CuInSe_2$	1.05	chalcopyrite	$I–42d$	$a = 5.61$ $c = 11.02$
$CuGaSe_2$	1.68	chalcopyrite	$I–42d$	$a = 5.61$ $c = 11.02$
$CuFeS_2$	0.60	chalcopyrite	$I–42d$	$a = 5.28$ $c = 10.41$
$AgInS_2$	1.87	chalcopyrite	$I–42d$	$a = 5.82$ $c = 11.17$
$AgInSe_2$	1.20	chalcopyrite	$I–42d$	$a = 6.10$ $c = 11.69$
Cu_2ZnSnS_4	1.50	kesterite	$I–4$	$a = 5.45$ $c = 10.86$
$Cu_2ZnSnSe_4$	1.02	kesterite	$I–4$	$a = 5.61$ $c = 11.20$

Ternary metal chalcogenides can be conceptually derived from II−VI materials by replacing two divalent metals with one monovalent and one trivalent cation; the quaternary compounds can be derived from the ternary ones by substituting two trivalent cation by one divalent and one tetravalent cation. It should be noted that ternary and multinary semiconductors are of course by no means limited to metal chalcogenides. A number of multinary pnictides is potentially of similar interest, with band gap energies in the range of 0.5−2 eV and absence of toxic heavy metals.[514] An example of this family are II−IV−V$_2$ compounds, such as ZnEP$_2$ (E = Si, Ge, and Sn). However, as a consequence of the more challenging chemical synthesis of metal phosphide NCs as compared to metal chalcogenides, (cf. section 4.2) the preparation of high quality NCs of these compounds has not yet been reported.

In terms of their physical properties, there are marked differences between binary compound semiconductors and their multinary counterparts. First of all the latter present a much larger variety of crystalline phases and they can accommodate in many cases significant off-stoichiometries from the nominal composition. The structural diversity is increasing when going from ternary to quaternary or even more complex systems. Furthermore, for a given composition different crystal structures can be realized, depending on the ordering of the cations in the anion sublattice. When these materials are synthesized in the form of NCs, crystal structures can be stabilized, which are not observed in the bulk. Bulk I−III−VI$_2$ semiconductors generally crystallize in the tetragonal chalcopyrite structure (space group I−42d). This structure, named after the mineral copper iron sulfide, can be derived from the cubic ZnS zinc blende structure by replacing Zn^{2+} ions by Cu$^+$ and In^{3+} ions in an ordered way (Figure 63). The resulting reduced symmetry of the chalcopyrite structure leads to a larger primitive cell (eight atoms vs two in the cubic structure) and to a slight tetragonal lattice distortion with a lattice parameter ratio c/2a of approximately 1.004. When both types of cations are distributed randomly in the cation
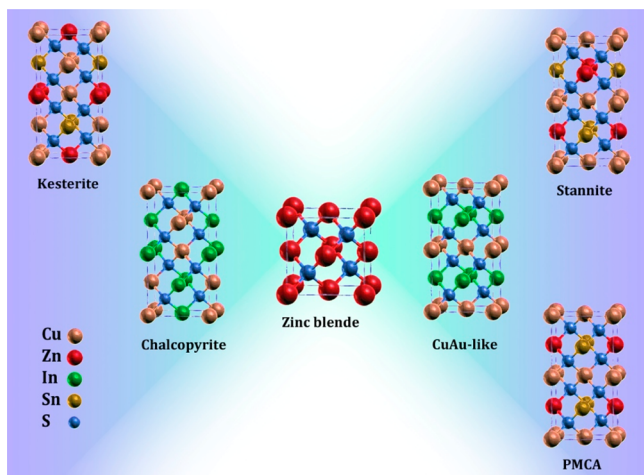
sublattice, the cubic structure is realized. Distinguishing between the chalcopyrite and cubic structure by means of powder X-ray diffraction is a challenging task, as for NCs in a typical size range of 1−20 nm substantial peak broadening occurs, hampering the detection of subtle differences and the accurate determination of the lattice parameters. Particle-to-particle variations in size and composition contribute to this difficulty. In contrast to bulk CuInS$_2$, NCs can also form the hexagonal wurtzite structure (cf. Figure 20). This structure is preferred when the growth of anisotropic nanostructures (e.g., nanorods) is aimed, exploiting the different polarity of specific crystal facets and different reactivity for growth.[513]

Quaternary compounds like Cu$_2$ZnSnS$_4$ (CZTS) or Cu$_2$ZnSnSe$_4$ (CZTSe) adopt in bulk form the tetragonal kesterite (space group I−4) or stannite (space group I−42m) phase (cf. Figure 63). In accordance with the predicted higher thermodynamic stability of the kesterite phase, most examples have been reported to adopt this structure.[516] As in the case of the ternary materials, a hexagonal polytype exists and CZTS NCs crystallizing in the wurtzite structure have been experimentally reported.[517,518] Increasing structural complexity from ternary to quaternary materials augments in principle the chances for cation disorder with three lattice sites. Even though the condition of local charge neutrality tends to counterbalance this effect, theoretical studies revealed the delicate interplay between atomic disorder and the formation of secondary phases.[516] Tight control of the crystalline phase and composition of CZTS and derived materials NCs is of paramount importance for their use in photovoltaics. The formation of secondary phases has been identified as one of the key problems at the origin of the lower power conversion efficiencies observed with kesterites as compared to chalcopyrite materials like CIGS.[519] Simulations have shown that CZTS is the thermodynamically stable phase only for a small domain of chemical potentials, i.e., even slight variations from optimum growth conditions, in particular regarding the Zn contents, favor the formation of secondary sulfide phases like ZnS (Zn-rich conditions) or Cu$_2$SnS$_3$ (Zn-poor conditions).[520] As a further complication these phases are essentially indistinguishable from CZTS by X-ray diffraction (Figure 64); however, they can be evidenced by Raman scattering.

Table 9 gives an overview of the synthesis methods for a large number of different multinary metal chalcogenides. Their detailed discussion would be redundant with section 4.3.2 treating binary metal chalcogenide NCs, due to the fact that the

Figure 63. Structural relationships in ternary and quaternary metal chalcogenides. Kesterite (I−4) is derived from the (201) ordered chalcopyrite structure (space group I−42d), while stannite (space group I−42m) derives from the CuAu (001) ordering. Both structures differ in the ordering of the Cu−Zn sublattice. The PMCA structure (primitive mixed CuAu-like, space group I−4) featuring a 90° rotation of one of the II−IV layers with respect to stannite has been theoretically predicted.[515]

Figure 64. Simulated diffraction patterns (Cu Kα) of kesterite CZTS and of potentially formed, indistinguishable secondary phases. Reproduced with permission from ref 516. Copyright 2012 Wiley-VCH Verlag GmbH & Co. KGaA.

Table 9. Overview of the Chemical Synthesis Methods for Ternary and Quaternary Metal Chalcogenide NCs[a]

material	crystal struct.	precursors, stabilizers and solvents	meth.	diameter (nm), shape	ref
CuInS$_2$	CH	CuI, In(ac)$_3$, DDT	HU	3–8, triangular	521
		CuI, In(ac)$_3$, DDT	HU/A	2	522
		CuI, In(ac)$_3$, S, DDT, DPP	HU	3	529
		CuI, In(ac)$_3$, DDT, ODE	HU	3, spherical	523
		CuI, In(ac)$_3$, DDT, ODE, OA	HU	3–8, triangular	524
		CuI, In(ac)$_3$, DDT, ODE, OA	HU	3	530
		CuI, In(ac)$_3$, DDT, ODE, OA	HU	5	525
		CuI, InI$_3$, S, OLA, TOP, ODE	HU	3–6	531
		CuI, InI$_3$, S, DDT, OLA, ODE	HU	4, spherical	532
		CuI, In(ac)$_3$, DDT, ODE, MA	HI	3	526
		CuI, InCl$_3$, S, OLA	HI	2–4, 5–10, aggregates	533
		CuI, In(NO$_3$)$_3$, HCl, tu, EG	A	100–500 nanospheres	534
		CuCl, InCl$_3$, S, OLA	HU	15–17, spherical	535
		CuCl, InCl$_3$, S, OLA, hexane	HU	3–5	536
		CuCl, InCl$_3$, tu, EtOH	HU/A	1800–2400	537
		CuCl, InCl$_3$, FeCl$_3$, tu, OLA, ODE, OA	HU	20, nanoplates, trigonal	538
		CuCl, In, S, water or benzene	HU/A	15	539
		CuCl, InCl$_3$, Ph$_3$P, NaS(Et), Benzyl(ac)	HI	2–5	540
		CuCl, InCl$_3$, (NH$_4$)$_2$S, DDT, OLA	HI	7, dots (CH) or nanorods (WZ)	541
		CuCl, InCl$_3$, (NH$_4$)$_2$S, DDT, OLA, TOP	HI	7, disks	534
		CuCl$_2$, InCl$_3$, TAA, MPA, water	HU/A	2	542
		CuCl$_2$, In(NO$_3$)$_3$, tu, benzyl(OH)	HU/A	100–200, cubes	543
		Cu(ac), In(ac)$_3$, DDT, ODE	HU	2–5, spherical or nanorods	544
		Cu(ac), In(ac)$_3$, DDT, ODE, OA, TOP	HU	9–12, cubes	545
		Cu(ac), In(NO$_3$)$_3$, TAA, CTAB, EG	HI	80–100, hollow spheres	546
		Cu(ac), InCl$_3$, CS$_2$, HDA, anisole	HI	13–17, polyhedral	547
		Cu(ac)$_2$, In(ac)$_3$, Sn(ac)$_2$Cl$_2$, DDT	HU	polygonal	548
		Cu(ac)$_2$, In(ac)$_3$, DMF, TG, H$_2$S	HI	2	549
		Cu(acac)$_2$, In(acac)$_3$, S, OLA, DCB	HU	20/200, nanotubes	550
		Cu(acac)$_2$, In(acac)$_3$, S, OLA, DCB	HI	8–12, spherical	551
		(Ph$_3$)$_2$CuIn(SEt)$_4$, DOP	HU	500, clusters	552
		(Ph$_3$P)$_2$Cu(μSEt)$_2$In(SEt)$_2$, EDT, Benzyl(ac)	HI	2–4	553
		(Ph$_3$P)$_2$CuIn(SEt)$_4$, hexanethiol, DOP	HU	2–4	554
		(TOP)$_2$CuIn(S(n-Pr) or (t-Bu))$_4$, DOP, benzene, toluene or pentane	HU	2	555
	WZ	Cu(SON(CNPr$_2$)$_2$)$_2$, In(SON(CNPr$_2$)$_2$)$_2$, DDT, OLA, ODE	HU	10, trigonal, spherical, hexagonal	556
		Cu, In, S, EDA	HU/A	20/800, nanorods	557
		CuSe NCs, InCl$_3$, TEG	HU/A	200–400/10–15, nanowires	558
		CuI, In(ac)$_3$, ODE, DDT	HU	10–20, nanoplates	559
		CuI, InCl$_3$, TOOP, TPOP, HDA or OLA, ODE	HU	5	560
		CuI, InCl$_3$, HCl, tu, EG	A	100–500, nanospheres	534
		CuCl, InCl$_3$, DDT, ODE, OA	HU	80–200, nanoplates	561

Table 9. continued

material	crystal struct.	precursors, stabilizers and solvents	meth.	diameter (nm), shape	ref
		CuCl, InCl3, DDT, ODE, OA	HU	200–400, nanoplates	562
		CuCl, InCl3, tu, DEG	HI	80–100, hexagonal nanoplates	563
		CuCl, In(acac)3, DTBDS, DDT, OLA	HI	7, spherical	564
		CuCl2, InCl3, tu, EA	HU/A	flakes or nanoplates	565
		CuCl2, InCl3, DDT, OLA, ODE or OA	HI	pyramids, cones, bullet-shaped, various sizes	566
		Cu(ac), In(ac)3, t-DDT, DDT, OLA, TOPO	HI	elongated, P-shaped, hexagonal, various sizes	567,568
		Cu(ac)2, InCl3, S, OA	HU	3–7 with Cu/In > 1 (Roxbyite phase); 9 with Cu/In = 1; 12–15 with Cu/In < 1	569
		Cu(ac)2, InCl3, tu, parafin, DDT or OLA or OA or OLA+OA	A	5–10	570
		Cu(acac), In(acac)3, t-DDT, DDT, OLA, ODE, TOPO	HI	35, bullet-like	571
		Cu(NO3)2, In(NO3)3, DDT, OLA or/and OA	HU	nanosphere/-rods, various sizes	572
		Cu(NO3)2, In(ac)3, S, OLA, DDT, OA, ODE	HI	3–4	573
		Cu(S2CN(C2H5)2, InCl3, tu, DDT, parafin	A	5–10	570
		[Cu(tu)3]Cl, In2(SO4)3 or In(ac)3, EG	HU	23–28 (Scherrer)	574
		(Ph3P)CuIn(SC(O)Ph)4, DDT, TOPO	HU	nanoplates	575
		Cu(ol), In(ol)3, DDT, OLA	HU	nanorods	576
		[(Me3P)3Cu(SC2H4S)IniPr2], OLA, DOP	HU	5–10 (metastable WZ)	577
	ZB	CuI, In(ac)3, DDT, ODE	HU	10, pyramids	559
		CuI, InCl3, OLA or HDA, ODE, TOOP, TPOP	HU	5	560
		CuCl, InCl3, DDT, ODE, OA	HU	6, triangular pyramids	561
		CuCl, InCl3, DDT, ODE, OA	HU	10, triangular	562
		CuCl2, InCl3, Na2S, 4-bromothiophenol, EtOH	HU/A	2–4	578
		CuCl2, InCl3, S, bis(N-hexyldithiocarbamate)Zn, OLA, ODE, TOP	HI	3	579
		Cu(ac), In(ac)3, S, DDT, OLA, ODE, OA	HI	3–7	580
		Cu(ac), In(ac)3, S, DDT, ODE, OA, TOP, SA	HI	2–20, spherical	581
		Cu(st), In(st)3, S, DDT, ODE	HU	3, spherical	582
		(Ph3P)CuIn(SC(O)Ph)4, DDT, TOPO	HU	5–10, spherical	575
		Cu(S2CNEt2), InCl3, tu, OLA or OA, parafin	A	20	570
	Various	Cu(ac), In(ac)3, S, DDT, t-DDT, OLA, ODE, TOPO	HU	polygonal, WZ/ZB	583
		Cu(ol), In(ol)3, DDT, OLA	HU	biphasic Cu2S-CuInS2	584
		(Ph3P)CuIn(SC(O)Ph)4, DDT, TOPO	HU	spherical and nanoplates	575
		Cu(S2CNEt2), InCl3, tu, OLA, OA, parafin	A	20, nanoplates (spinel CuIn5S8)	570
CuInSe2	CH	CuI, InCl3, Se, ODE, TOOP, TOP, HDA	HU	1–5, spherical	585
		CuI, In(ac)3, Se, DDT, ODE, OA, TBP	HI	3	586
		CuCl, InCl3, Se, EDA	HU/A	80	587
		CuCl, InCl3, Se, EDA	HU	26–45, nanoplates or nanorods	588
		CuCl, InCl3, Se, OLA	HU/A	5	589
		CuCl, InCl3, Se, TOP, TOPO and/or OLA and/or DOPO	HI	10/100 nanowires, 10, spherical	590
		CuCl, InCl3, Se, DDT, ODE, TOP	HI	2–6	591
		CuCl,InCl3, su, OLA	HI	16, trigonal, pyramidal	592

Table 9. continued

material	crystal struct.	precursors, stabilizers and solvents	meth.	diameter (nm), shape	ref
		CuCl,InCl₃, su, OLA	HI	7, spherical	593
		CuCl, InCl₃, Se, LiN(SiMe₃)₂, TOP	HI	3–5, spherical, 5, tetrahedrons	594
		CuCl₂, InCl₃, Se, EDA	HU/A	(3–6) × 30–80, nanowhiskers	595
		CuCl₂, In₂Se₃, NCs, EG	HU	5–21	596
		Cu(ac), In(ac)₃, Se, TOP, OA	HI	nanowires (+Au(Bi) NPs) or particles	597
		Cu(ac)₂ InCl₃, Se, OLA	HI	16, triangular, hexagonal	598
		(PPh₃)₂Cu(SePh)₂In(SePh)₂In(SePh)₂ TOP, OA, Au(Bi) NCs	HU	20/1000 nanowires	597
	WZ	CuCl, In(ac)₃ diphenylselenide, OLA	HI	30, polygonal	599
		Cu(ac), In(ac)₃ Se, OA, TOP, Bi NPs	HU	20/1000 nanowires	600
		Cu(ol), In(ac)₃ diphenylselenide, OLA	HI	21, hexagonal	601
	ZB	CuCl, InCl₃ su, DDT, OLA, ODE, TOP	HU	3–5, triangular or spherical	602
CuInSSe	CH	CuCl, InCl₃ S, Se, OLA	HU	17, faceted	535
		CuCl, InCl₃ S, Se, OLA	HI	14, triangular, hexagonal, spherical	603
		CuCl₂, InCl₃ S, Se, EDA	HU/A	15, aggregated	604
CuFeS₂	CH	Cu[S₂CN(C₂H₅)₂]₂, Fe[S₂CN(C₂H₅)₂]₃, S, TOP, OLA, OA, DCB	HI	12, spherical and 30, pyramidal	605
		[Cu₄(tu)₉](NO₃)₄, FeCl₃, EG	HU	10 nm (Scherrer)	606
	WZ	[Cu₄(tu)₉](NO₃)₄, Fe₂(SO₄)₃, EG	HU	17 nm (Scherrer)	606
CuFeSe₂	CH	Cu(acac)₂ Fe(acac)₃, Ph₂Se₂, OLA, OA	HI	18, quasicubic	607
CuGaS₂	CH	CuCl, Ga, S, water or benzene	HU	35	539
		CuCl, GaCl₃, S, OLA	HI	5–11	608
CuGaSe₂	CH	Cu(ac)₂ Ga(ac)₃ Se, OLA	HI	11	598
	WZ	CuCl, GaCl₃, tu, OLA	HU	30	608
Cu₂SnS₃	KS	CuCl, SnCl₂, NaBH₄Se or Se, TOPO, OLA, DDT or OA	HI	3–16, spherical (NaBH₄Se), 3–17, spherical (Se, DDT), 10, triangular (Se, OA)	609
	H	CuCl, SnCl₂, TOPSe, OLA, TOPO	HI	100–500, nanoplates (klockmannite)	609
	WZ	CuI, Sn(ac)₂, OLA, DDT	HU	30, nanoplates	559
	ZB	CuI, Sn(ac)₂, DDT, ODE	HU	150, pyramids	559
		Cu(acac)₂ Sn(acac)₂, S or DDT, OLA	HU	7 (S) or 9 (DDT)	610
Cu₂SnSₓSe₃₋ₓ	M	CuCl, SnBr₂, Se, S, OLA, DDT	HU		611
Cu₃BiS₃	O	Cu(acac)₂, Bi(NO₃)₃, S, OLA	HI	8–11 (wittichenite)	612
Cu₂GeS₃₋ₓSeₓ	Various	Cu(acac)₂, GeCl₄, S, Se, OLA	HI	10–20	613
Cu₃SbSe₃	O	Cu(acac)₂, Sb(ac)₃, Se, OLA, DMAB	HI	13–18	614

Table 9. continued

material	crystal struct.	precursors, stabilizers and solvents	meth.	diameter (nm), shape	ref
$Cu_xSb_yS_z$	C	CuCl, SbCl₃, OLA, ODE, OA, BTMSS	HI	10/40, nanorods ($Cu_{12}Sb_4S_{13}$, tetrahedrite)	615
				6–18 ($Cu_{12}Sb_4S_{13}$, tetrahedrite)	615
	O	CuCl, SbCl₃, OLA, ODE, OA, BTMSS	HI	50/1000, nanorods ($CuSbS_2$, chalcostibite)	616
	T	Cu(acac)₂, Sb(ac)₃, S, OLA	HI	80 nm, irregular (Cu_3SbS_4, fematinite)	538
$CuIn_xFe_{1-x}S_2$	Various	CuCl, InCl₃, FeCl₃, tu, OLA, ODE, OA	HU	20, nanoplates, CH+WZ	574
		[Cu(tu)₃]Cl, In₂(SO₄)₃ or Fe₂(SO₄)₃ EG	HU	17 (Scherrer), CH+WZ	541
$CuIn_xZn_{1-x}S_2$	CH	CuCl, InCl₃, ZnCl₂, (NH₄)₂S, DDT, OLA	HI	4	538
	Various	CuCl, InCl₃, Zn(ac)₂, tu, OLA	HU	100, CH+WZ	541
$CuIn_xGa_{1-x}S_2$	CH	CuCl, InCl₃, GaCl₃, (NH4)₂S, DDT, OLA	HI	6	553
		(Ph₃P)₂Cu(μSEt)₂In(SEt)₂,In(SEt)₂,(Ph₃P)₂Cu(μSEt)₂Ga(SEt)₂, EDT, benzyl(ac)	HU	3–4	617
	WZ	CuCl, InCl₃, GaCl₃, S, OLA, ODE	HU	13–19	571
		Cu(acac)₂ In(acac)₃ Ga(acac)₃ DDT, t-DDT, OLA	HI	nanorods or tadpoles	551
$CuIn_xGa_{1-x}Se_2$	CH	CuCl, InCl₃, GaCl₃, Se, OLA	HU	spherical	618
		CuCl, InCl₃, Ga(acac)₃, Se, HDA	HI	20, spherical	619
		CuCl, InCl₃, GaCl₃, Se, tetraEG, NaBH₄, EtOH	HU	40–100	620
		CuCl₂, InCl₃, GaCl₃, Se, DEG, PVP, hydrazine	HI	10–20	621
$CuIn_{0.5}B_{0.5}Se_2$	CH	CuCl, InCl₃, BO, Se, diethylenetriamine	HU	70, nanorods	622
$Cu_2Co_xSn_{1-x}Se_3$ $Cu_2Fe_xSn_{1-x}Se_3$	C	CuCl₂, SnCl₄, Co(acac)₂ or Fe(acac)₂, S, DDT, OLA	HI	3–4 (Fe doped) 5–6 (Co doped)	623
$AgInS_2$	CH	AgCl, In, S, EDA	HU/A	10, agglomerates	624
		Ag(ac), In(ac)₃ S, DDT	HU	2–4	625
		AgNO₃, In(ac)₃ DDT, ODE, OA, TOP	HU	10, spherical	626
		AgNO₃ In(ac)₃ S, OLA, ODE, OA, SA	HI	3–5	627
		Agₓ In₍₁₋ₓ₎(S₂CNEt₂)₍₃₋₂ₓ₎, OLA	HU	4–5, spherical	628
	ZB	Ag(ac), In(ac)₃ Na₂S, 1-glutathione, water	HI	3, agglomerates	629
	O	Ag(ac), In(ac)₃ S, OLA, DDT, ODE	HI	4–9 polygonal, 30/300 nanorods	630
		Ag(ac), In(ac)₃ S, DDT, DDA	HI	6, triangular	547
		AgNO₃ InCl₃, CS₂, HDA, anisole	HI	17, rectangular	625
		AgNO₃ In(ac)₃ DDT, ODE, OA, TOP	HU	5, spherical	581
		AgNO₃ In(ac)₃ S, DDT, ODE, OA, TOP, SA	HI	2–10, spherical	631
		AgNO₃ In(NO₃)₃ S, ODA	HU	10/60, nanorods, worm-like	632
		AgNO₃ In(NO₃)₃ (NH₄)₂S, FA	HU	2–6	633
		Ag(S₂CNEt₂), In(S₂CNEt₂)₃ DDT, OA	HU	6/12, 8/16	634
		AgIn[S₂CNEt₂]₄, OLA	HU/A	6, faceted	

Table 9. continued

material	crystal struct.	precursors, stabilizers and solvents	meth.	diameter (nm), shape	ref
AgInSe$_2$	ZB or O	AgIn[S$_2$CN(Et)$_2$]$_4$, OLA	HU	2–6	634
	O	AgNO$_3$, In(st)$_3$, Se, OLA, ODE, OA	HI	24, elongated	635
		(Ph$_3$P)$_2$AgIn(SeCOPh)$_4$, DDT, OLA	HU	50/15, nanorods	636
AgGaS$_2$	CH	AgCl, Ga, S, EDA	HU	6, agglomerates	623
	O	Ag(S$_2$CNEt$_2$), Ga(S$_2$CNEt$_2$)$_3$, DDT or HDT or OLA or HDA	HU	16, pyramidal (DDT), 17, pyramidal (HDT), 18, polyhedral (OLA), 19, polyhedral (HDA)	637
AgSbS$_2$	M	AgNO$_3$, SbCl$_3$, TMS, OLA, OA	HU	5–20 (miargyrite)	638
		AgNO$_3$, Sb(S$_2$CNEt$_2$)$_3$, S, TMS, OLA		20–60 (miargyrite)	
FeCr$_2$S$_4$	C	Fe(acac)$_2$, Cr(acac)$_3$, DDT, OLA	HI	10–15 (daubreelite)	639
FeCr$_2$Se$_4$	M	Fe(acac)$_2$, Cr(acac)$_3$, Se, OLA		60–70	639
ZnIn$_2$S$_4$	H	ZnCl$_2$, In(ac)$_3$, C$_{18}$H$_{33}$NaO$_2$, S or tu, OLA, ODE	HI	2–10, spherical, nanoplates or rectangles	640
ZnIn$_2$Se$_4$	ZB	CuCl$_2$ (dopent), InCl$_3$, Zn(st)$_2$, Se, DDT, OLA, ODE, OA	HI	2–3	641
Cu$_2$ZnSnS$_4$	KS	CuI, SnCl$_4$, Zn(EtXn)$_2$, DDT, OA	HU	5–8	642
		CuI, ZnCl$_2$, SnI$_4$, S, OLA	HI	7–10	643
		CuCl, ZnCl$_2$, SnCl$_2$, S, EDA	HU	200/1000, nanowires	644
		CuCl$_2$, ZnCl$_2$, SnCl$_4$, tu, PVP, EG	HU/A	500, flower-like	645
		CuCl$_2$, ZnCl$_2$, SnCl$_4$, tu, PVP, EG	HU/A	100–150, aggregated	646
		CuCl$_2$, ZnCl$_2$, SnCl$_4$, tu, TMAOH, EG	HU	5–8, aggregated	647
		CuCl$_2$, ZnCl$_2$, SnCl$_4$, tu, OLA, TMAOH, EG	HU/A	aggregated	648
		CuCl$_2$, Zn(ac)$_2$, SnCl$_4$, S, EDA	HU/A	5–32, aggregated	649
		CuCl$_2$, ZnO, SnCl$_4$, S, OLA, ODE	HU/A	15, irregular faceted shape	527
		CuCl$_2$, ZnCl$_2$, SnCl$_4$, S, OLA	HU	7–9	650
		CuCl$_2$, ZnCl$_2$, SnCl$_2$, tu, OLA	HI	22/14, spindle-like	651
		CuCl$_2$, ZnCl$_2$, SnCl$_2$, S, KTB, EtOH	HI	5–8	652
		CuCl$_2$, ZnCl$_2$, SnCl$_2$, Na$_2$S, DEG	HI	10–20	653
		CuCl$_2$, Zn(ac)$_2$, SnCl$_4$, Se(SiEt$_3$)$_2$, ODE, OA	HI	25–30	654
		CuCl$_2$, SnCl$_4$, ZnCl$_2$, Na(ol), S, DDT, OLA, ODE	HI	10–15, spherical	655
		Cu(ac)$_2$, Zn(ac)$_2$, Sn(ac)$_4$, S, DDT	HU	2–3	656
		Cu(ac)$_2$, Zn(ac)$_2$, Sn(ac)$_4$, S, DDT	HU	4	657
		Cu(ac)$_2$, Zn(ac)$_2$, Sn(ac)$_4$, S, OLA	HU	5–6, spherical	658
		Cu(ac)$_2$, ZnCl$_2$, SnCl$_4$, S, OLA	HI	15–25	659
		Cu(ac)$_2$, ZnCl$_2$, SnCl$_2$, TAA, FA	HI	4–6	660
		Cu(ac)$_2$, Zn(ac)$_2$, Sn(ac)$_4$, S, DDT or OLA, ODE, OA	HI	spherical, (yellow ODE-S). Smaller with DDT than with OLA	661
		Cu(acac)$_2$, Zn(ac)$_2$, SnCl$_2$, S, OLA	HU	11, irregular faceted shape	662

Table 9. continued

material	crystal struct.	precursors, stabilizers and solvents	meth.	diameter (nm), shape	ref
		$Cu(acac)_2$, $Zn(ac)_2$, $SnCl_2$, S, OLA	HU	11, irregular faceted shape	663
		$Cu(acac)_2$, $Zn(ac)$, $Sn(ac)_4$, S, OLA, TOPO	HI	13, irregular faceted shape	664
		$Cu(acac)_2$, $Zn(ac)_2$, $SnCl_3$, TAA or S, OLA	HI	6–12	665
		$Cu(acac)_2$, $Zn(ac)_2$, $Sn(ac)_4$, S, OLA, TPP	HI	10–20 (TPP capped); 10–15 (OLA capped)	666
		$Cu(acac)_2$, $ZnCl_2$, $SnCl_2$, S, OLA	HI	10–15, nanoplates	667
		$Cu(acac)_2$, $Zn(ac)_2$, $SnCl_4$, $(TMS)_2S$, OLA, ODE	HI	8–10	668
		$Cu(acac)_2$, $Zn(acac)$, Sn(bis-acac dibromide)$_4$, S, OLA	HI	15–25	669
		$Cu(S_2CNEt_2)_2$, $Zn(S_2CNEt_2)_2$, $Sn(S_2CNEt_2)_4$, OLA	HU	2–7, faceted	670
		$Cu(S_2CNEt_2)_2$, $Zn(S_2CNEt_2)_2$, $Sn(S_2CNEt_2)_4$, OLA, ODE, OA	HI	2 (150 °C) to 40 (340 °C)	671
		$Cu(NO_3)_2$, $Zn(NO_3)_2$, $SnCl_4$, S, OLA	HU	10–15, agglomerated	672
		$Cu(ol)_2$, $Zn(ac)_2$, Sn(ethylhexanoate), DDT or S, OLA, ODE or DCB	HI	2–4 (S + DDT, in DCB); 5–18 (S, in ODE); 2–4 (DDT, in ODE)	518
	WZ	$CuCl_2$, $SnCl_4$, $ZnCl_2$, Na(ol), S, DDT, OLA, ODE	HI	10–15, spherical	655
		$CuCl_2$, $SnCl_4$, $ZnCl_2$, Na(ol), S, DDT, ODE	HI	45, nanorods	655
		$CuCl_2$, $SnCl_4$, $ZnCl_2$, Na(ol), S, DDT, OA	HI	10–15 rice like	655
		$Cu(ac)_2$, $ZnCl_2$, $SnCl_4$, DDT, OLA	HI	12–15	659
		$Cu(acac)_2$, $ZnCl_2$, $SnCl_2$, DDT, OLA	HI	30/10, nanorods	667
		$Cu(acac)_2$, $Zn(ac)_2$, $SnCl_4$, $(TMS)_2S$, OLA, ODE	HI	7–10 (170 °C); 7–12 (190 °C)	668
	ZB	$Cu(S_2CNEt_3)_2$, $Zn(S_2CNEt_2)_2$, $Sn(S_2CNEt_2)_4$, HDT, TOA	HU	15/8, elongated	673
		$CuCl_2$, ZnO, $SnCl_4$, DDT, TDM, OLA, ODE, OLA, THF	HI	12	528
		$CuCl_2$, $ZnCl_2$, $SnCl_4$, DDT, OLA or OA	HI	20/28, prisms (OLA); 14 nm thick nanoplates (OA)	674
		$Cu(ac)_2$, $Zn(ac)_2$, $Sn(ac)_4$, DTBU, S, DDT	HU	10–50, bullet-shaped	657
		$Cu(ac)_2$, $ZnCl_2$, $SnCl_4$, S, OLA	HI	10–20	675
		$Cu(ac)_2$, $Zn(ac)_2$, $Sn(ac)_4$, S, DDT or OLA, ODE, OA	HI	Nanoplates, with (orange ODE-S)	661
		$Cu(acac)$, $Zn(ac)_2$, $Sn(ac)_4$, DDT, t-DDT, ODE, TOPO	HI	35/11, nanorods, bullet-shaped	676
		$Cu(acac)_2$, $Zn(ac)_2$, $SnCl_2$, DDT	HU	10–15, bullets	677
		$Cu(acac)_2$, $Sn(acac)_2$, $Zn(acac)_2$, S or DDT, OLA	HU	9 (S), 5 (DDT)	610
		$Cu(ol)_2$, $Zn(ac)_2$, Sn(ethylhexanoate), DDT, ODE	HU	4–8	518
	O	$CuCl_2$, $ZnCl_2$, $SnCl_2$, TCA, EDA, water	HU/A	20–50, nanoplates, aggregated	678
	Various	$CuCl_2$, $Zn(ac)_2$, $SnCl_2$, tu, OLA	HI	15–18, WZ with minor ZB	679
		$CuCl_2$, $SnCl_4$, $ZnCl_2$, Na(ol), S, DDT, ODE	HI	45, nanorods, WZ+KS	655
		$Cu(ac)_2$, $ZnCl_2$, $SnCl_4$, TAA, OLA	HI	10–100, irregular, WZ+KS	659
		$Cu(acac)_2$ or CuCl, $Zn(ac)_2$ or $ZnCl_2$, $Sn(ac)_4$, DDT, t-DDT, OLA, ODE	HI	various sizes and morphologies; nanorods, bullets, dots	680
$Cu_2ZnSnSe_4$	ST	CuCl, ZnO, $SnCl_4$, SeO_2, ODE, HDA, TDPA	HI	5–30, cubic	681
		$CuCl_2$, $ZnCl_2$, $SnCl_4$, Se, TEA	HU	24, aggregated	682
		$CuCl_2$, $ZnCl_2$, $SnCl_4$, Se, DDT, OLA	HI	3,4, spherical	683

Table 9. continued

material	crystal struct.	precursors, stabilizers and solvents	meth.	diameter (nm), shape	ref
$(Cu_2Sn)_{x/3}Zn_{1-x}S$		$Cu(ac)_2$, $SnCl_2$, $Zn(ac)_2$, Se, OLA	HU	45	684
		$Cu(ac)_2$, $ZnCl_2$, $SnCl_2$, Se, OLA	HI	17, triangular, hexagonal, plate	682
		CuSe NWs, $Zn(ac)_2$, $SnCl_2$, TEG	HU/A	100 μm × 200−400 nm wires	685
	M	CuCl, $Zn(ac)_2$, $SnCl_2$, SeO_2, OLA, ODE	M	20−50	686
	Various	$CuCl_2$, $Zn(ac)_2$, $SnCl_2$, su, OLA	Various	10−15, ZB with minor WZ	679
	ZB	$CuCl_2$, $ZnCl_2$, $SnCl_2$, TCA, OLA, EtOH	HU	3	687
Cu_2ZnFeS_4	CH	CuCl, $ZnCl_2$, $Fe(acac)_3$, S, ODE, (OLA, OA) or (TDPA, TOPO)	HI	10−15, triangular (OLA, OA), 15−20, triangular (TDPA, TOPO)	688
		CuCl, $ZnCl_2$, $Fe(acac)_3$ DDT, ODE, (OLA, OA) or TDPA or TOPO	HI	25−30/6, nanorods (OLA, OA), 35−40, nanoplates (TDPA), 50−80, nanoplates (TOPO)	688
$Cu_2Zn_xFe_{1-x}SnS_4$	Various	$Cu(acac)_2$, $Fe(acac)_2$, $Zn(acac)_2$, $SnCl_2$, S, OLA	HI	10−20, transition from ST to KS at x = 0.4	689
Cu_2FeSnS_4	ST	$Cu(acac)_2$, $Fe(acac)_2$, $SnCl_2$, S, OLA	HI	13, triangular and spherical	690
Cu_2ZnGeS_4	T	$Cu(acac)_2$, $Zn(acac)_2$, $GeCl_2$, S, OLA	HU	8−12	691
	Various	CuI, $ZnCl_2$, $Ge(gly)_2(H_2O)_2$ or $GeCl_4$, CS_2, DDT, OLA	I	5−7, WZ and O	692
$Cu_2ZnGeSe_4$	ST	CuCl, ZnO, $GeCl_4$, Se, ODE, HDA, TDPA	HI	10−25, faceted	693
		CuCl, ZnO, $GeCl_4$, SeO_2, ODE, HDA, TDPA	HI	5−30, triangular	681
	T	$Cu(acac)_2$, $Zn(acac)_2$, $GeCl_2$, Se, OLA	HU	10−15	691
	O	$Cu(S_2CNEt_2)_2$, $GeCl_2$, $Zn(ac)_2$ DDT, OLA	HU	50−80, worm-like	694
$CuInZnS_3$	ZB	$Cu(ac)_2$, $In(ac)_3$, $Zn(ac)_2$, S, DDT, OLA, OA, $Mn(ac)_2$ (dopant)	HU	2−5	695
		CuCl, $InCl_3$, $Zn(ac)_2$, S, DDT, OLA, ODE, OA	HU	3−5, triangular	696
	Various	CuCl, $ZnCl_2$, $InCl_3$, S, DDT, OLA, ODE, OA	HI	2−3, CH, ZB, and WZ	697
Cu_3InSnS_5	WZ	CuCl, $InCl_3$ tu, OLA, DDT	HU	10−12	698
$Cu_2CdSnSe_4$	ST	CuCl, CdO, $SnCl_4$ Se/ODE, HDA, ODPA	HI	10−20, cubes	681,699
$Ag_2ZnSnSe_4$	ST	$Ag(ac)_2$, $SnCl_2$, $Zn(ac)_2$, Se, OLA	HU	65	684

[a]HU: heating-up, HI: hot-injection, A: autoclave, I: injection. CH: chalcopyrite, WZ: wurtzite, ZB: zinc blende, KS: kesterite, ST: stannite, C: Cubic, T: Tetragonal, H: hexagonal, O: orthorhombic, M: monoclinic. OLA: oleylamine, TEA: Triethanolamine, EA: Ethanolamine, HDA: hexadecylamine, EDA: ethylenediamine, HDA: hexadecylamine, ODA: Octadecylamine, TOA: Trioctylamine, TAA: thioacetamide, DMAB: dimethylamine borane. DPP: diphenylphosphine, TBP: Tributylphosphine, TOP: trioctylphosphine, TOPO: trioctylphosphine oxide, TOOP: trioctylphosphite, DOPO: dioctylphosphine oxide, TPOP: triphenylphosphite. OA:oleic acid, SA: stearic acid, TDPA: tetradecylphosphonic acid, ODPA: octadecylphosphonic acid, MA: myristic acid, MPA: mercaptopropionic acid. ODE: octadecene, B: benzene, DCB: dichlorobenzene. EG: ethylene glycol, DEG: diethylene glycol, TEG: triethylene glycol, TG: Thioglycerol. DDT: 1-dodecanethiol, EDT: ethanedithiol, HDT: hexadecanethiol, TDM: Tetradecylmercaptan. ol: oleate, st: stearate, ac: acetate, acac: acetylacetonate, iPr: isopropyl, Ph: phenyl, tu: thiourea, su: selenourea, DBTU: 1,3 dibutylthiourea. TMAOH: tetramethylammonium hydroxide, CTAB: cetyltrimethylammonium bromide, BTMSS: bistrimethylsilyl sulfide, TPP: Triphenylphosphate, DTBDS: ditertbutyldisulfide, TCA: Thiocarbamide, DOP: Dioctylphtalate, PVP: polyvinylpyrrolidone, $Ge(gly)_2(H_2O)_2$: diaquabis(glycolato-O,O)germanium(IV), KTB: $(CH_3)_3COK$, EtXn: Ethyl Xanthate.

fundamental synthetic concepts, metal and chalcogen precursors are identical. The main additional challenge in the synthesis of multinary NCs resides in balancing the reactivity of the different metal precursors, which is a prerequisite for the control of their composition and crystalline phase. Among all compounds, chalcopyrite and kesterite materials have attracted the highest attention. The former show interesting PL properties with QYs exceeding 80% after proper surface passivation, while the latter provide appealing features for use in photovoltaics, thermoelectrics and photocatalysis. DDT and elemental sulfur dissolved in OLA are the main sulfur sources for the preparation of chalcopyrite $CuInS_2$ (CIS) NCs. The soft Lewis base DDT efficiently complexes the soft Lewis acid Cu^+ and can therefore also be used as the stabilizing ligand. In one of the simplest reactions for the synthesis of $CuInS_2$ NCs, DDT acts also as the reaction solvent. Used with copper iodide and indium acetate in a heat-up synthesis, sub-10 nm NCs in the chalcopyrite phase result in close to 1:1:2 stoichiometry and a tunable size with reaction time. In these reactions DDT can be mixed with ODE and oleic acid can be introduced as additional complexing agent for In^{3+}.[521−526] $CuInE_2$ (E = S and Se) nanocrysals in the wurtzite phase have been obtained in syntheses generally comprising amines like OLA, which serves as a co-complexing agent (cf. Table 9). In initial stages of these reactions binary CuE or Cu_2E nanoparticles are formed, which transform subsequently into the ternary hexagonal NCs. Starting from this structure the growth of nanorods and nanowires has been achieved. Likewise the synthesis of quaternary CZTS (and CZTSe) NCs was found to occur via intermediate binary phases, such as Cu_2S or $Cu_{1.94}S$ seeds, while Zn^{2+} and Sn^{4+} ions subsequently diffused into the lattice affording homogeneous CZTS particles.[517] In contrast to CIS syntheses, DDT is not the preferred sulfur source in the preparation of CZTS but rather elemental sulfur dissolved in OLA. By means of a continuous flow reactor Cabot and co-workers produced CZTS nanoparticles of high homogeneity and low size distribution on a gram scale.[527] The same team used a dual thiol approach for preparing CZTS NCs in the wurtzite phase, exhibiting an extremely narrow size distribution, contrasting common believe that multinary NCs are not yet reaching the same standards as binary compounds (Figure 65).[528]
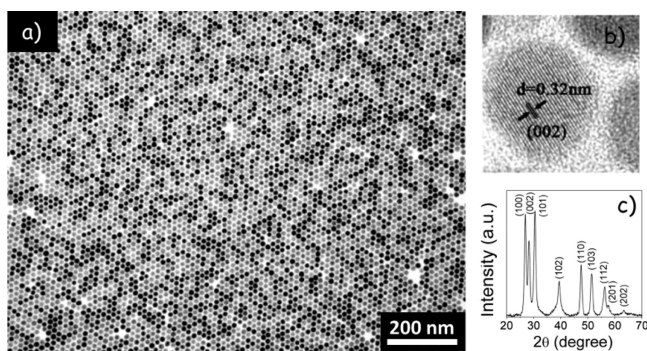

Figure 65. (a) TEM image of monodisperse 12 nm CZTS nanoparticles of 2:1:1:4 elemental stoichiometry. (b) High-resolution image indicating the lattice spacing. (c) X-ray diffractogram showing that the particles crystallize in the metastable wurtzite phase. Reproduced with permission from ref 528. Copyright 2014 American Chemical Society.

5. PERSPECTIVES

Semiconductor NCs of nontoxic or less-toxic elements are a very fertile and burgeoning research field. It is driven on the one hand by the scientific curiosity of the researchers who push further the limits of the understanding of the underlying chemistry and reaction kinetics, which enables the synthesis of novel types of NCs. On the other hand, NCs have demonstrated their potential for improving the performance of optoelectronic devices, in particular those relying on their light emission capacities.[14] Combining narrow, tunable emission peaks with high quantum yield and photostability make QDs ideal phosphors for LED and color conversion applications.[6,700] Used for example as color converters, QDs strongly improve the color-rendering index of white-light emitting diodes and of flat-screen TVs when integrated in the backlighting system.[701,702] Despite their appealing features for use in the fields of photovoltaics and thermoelectrics to date the performance of colloidal NCs lags behind other types of materials. Mastering the surface chemistry, size, shape, crystalline phase and composition are of prime importance for efficient charge transfer and transport in NC solids.[14,703] These challenging tasks have so far only been achieved for Cd- and Pb-based NCs where the charge transport properties are now comparably well understood.[704] The unique properties of semiconductor NCs also generate new applications, which offer exciting possibilities, as for example in the field of nanomedicine. Initially used as diagnostic agents for in vitro and in vivo biological imaging and detection,[21] NCs nowadays evolve toward multifunctional tools in the emerging field of theranostics. As such they can serve as a platform for vectorizing therapeutic agents while showing diagnostic/analytic properties and eventually tailored targeting and cell penetration properties. The use of QDs in this field is still in its infancy, and most reported advances concern metal and/or magnetic nanoparticles.[705,706] The luminescence properties inherent to many types of NCs enable their tracking by fluorescence reflectance imaging (FRI)[707] and in addition further complementary imaging modes can be implemented by appropriate surface functionalization. One example is the surface conjugation of gadolinium complexes on fluorescent QDs, which are efficient contrast agents for magnetic resonance imaging (MRI), leading to dual-mode probes.[708,709] Finally, a field which was at the origin of NC research, photo-electrochemistry for water-splitting and solar fuel generation,[710] comes back into the center of attention with recent advances enabled due to the better understanding of the photocatalytical processes.[711] As one example hydrogen generation with more than 50% external quantum efficiency has been achieved by the simple Ni-decoration of cysteine or mercaptopropionic acid functionalized CdS nanorods.[712] A 100% photon-to-hydrogen production efficiency has been reported very recently by Kalisman et al. using Pt-tipped CdSe spherical core/CdS elongated shell nanorods with a hydroxyl anion-radical redox couple working as hole relay shuttle.[713]

The overwhelming majority of proof-of-concept studies for the aforementioned applications has been reported with the use of Cd- and Pb-based NCs. There is no doubt that these will not be a viable solution for real-life applications in the longer term, due to their (eco-)toxicity. In Europe, derogations from the RoHS directive, which severely limits the use of materials containing these elements in electronic equipment, are currently coming to term. Furthermore, specific regulations

applying to materials of nanometric dimensions regardless of their composition are currently under debate. However, a recent EC statement indicates that this aspect may not be an obstacle, which could be interpreted in a way that the chemical risk prevails over the "nano-risk".[714] As outlined in section 2, risk is a function of hazard and exposure, and the development of safer-by-design NCs is therefore one way to minimize risks. A number of alternative materials have come up in recent years, which are intrinsically less toxic than Cd- or Pb-based QDs. Pnictides and the group IV elemental semiconductors play an important role in this context. III−V compounds and in particular InP-based NCs reach optical properties close to those of well-established types of QDs. Still the emission line width (>40 nm fwhm) and PL QY (generally <80%) require further improvements. Additionally, toxicity concerns and the comparably low Earth abundance of indium[50] are issues related to this material. Materials like Zn_3P_2 could be potential substitutes provided that their optical properties can be improved.[89]

When moving from binary to ternary or multinary compound semiconductors the choice of materials showing narrow direct band gaps without containing toxic heavy metals is significantly enlarged. The most studied by far luminescent material here is $CuInS_2$ eventually containing Zn.[513] Nonetheless, in addition to the above-mentioned issues related to indium, to date no solutions have been found for diminishing the large emission line width of at least 90−100 nm (fwhm) in NCs of this and related (e.g., $AgInS_2$, $CuInSe_2$) materials. The detailed luminescence mechanism is under current debate,[715] however, all descriptions agree on the involvement of intra band gap states. Their distribution in NC ensembles tend to broaden the emission line width, independent from the size distribution of the sample. One possible pathway to circumvent these particle-to-particle variations is the synthesis of precisely controlled crystalline phases occurring in the ternary phase diagram of these compounds. To do so, Yarema and co-workers proposed synthesis methods relying on the use of metal alkyl- or silylamides as precursors.[508] In contrast to the case of binary semiconductors, ternary pnictides have not yet been developed as NCs. This class of materials, $M^{(II)}E^{(IV)}P_2$ like $ZnSiP_2$, $ZnGeP_2$ or $ZnSnP_2$,[716] has recently gained interest as absorber materials for solar cell applications, as $ZnSnP_2$ for example presents a direct band gap ranging from 0.75 to 1.7 eV depending on the crystalline order parameter.[717]

Finally, NCs of the group IV elemental semiconductors Si and Ge have seen impressive improvement of the control of their size and size distribution in the past decade. At the same time "soft-chemical" preparation methods have been elaborated, which no longer rely on extreme reaction conditions in terms of temperature and pressure. Furthermore, easy-to-manipulate and low cost precursors have been applied. On the other hand, their indirect band gap and complex emission mechanisms make it up until now difficult to achieve efficient and narrow fluorescence at precisely controlled wavelengths. Additionally, only a few reports clearly state the obtained absolute fluorescence QYs.

Among the group IV elements, NCs of carbon, Carbon nanodots/C-dots, have been prepared from an intriguingly large variety of naturally occurring starting compounds. Some of these syntheses can be considered as an ultimate green-chemistry approach toward nontoxic types of NCs (cf. Figure 66). There is a growing interest in the application of C-dots since their discovery in 2006, but the understanding of their optical properties is not yet accomplished. In particular, their
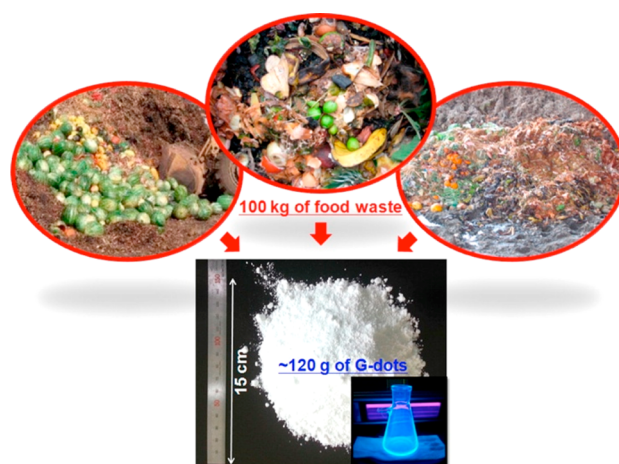

Figure 66. Scheme presenting the large-scale synthesis of fluorescent carbon nanodots by treating 100 kg of food waste in 500 L of 10% ethanol with ultrasound at 40 kHz for 45 min, followed by centrifugation and filtering. Reproduced with permission from ref 718. Copyright 2014 American Chemical Society.

emission shows a strong dependency on the excitation wavelength. Subjects of current research are the control of their emission color, reduction of emission line width, optimization of the PL QY, improvement of the surface passivation and stabilization of the optical properties.

As highlighted, identifying chemical synthesis routes for NCs of alternative nontoxic and Earth-abundant materials remains a challenging task. However, the improved understanding of reaction pathways, as well as some fortunate accidental findings have enabled several breakthroughs. Xia et al. stated in 2008:[719] "At the current stage of development, it is not an exaggeration to say that the chemical synthesis of metal NCs (as well as for other solid materials) remains an art rather than a science". Today this statement has been invalidated partially. Many efforts are currently undertaken for improving the understanding of NCs' nucleation and growth mechanisms and for correlating the precursor-to-monomer conversion rates with the reaction outcome. Although the small dimensions and short time scales characteristic for these processes hamper real-time in situ studies, progress is being made thanks to instrumental developments of dedicated equipment. As an example the development of appropriate liquid cell sample holders now enables the direct observation of NC nucleation and growth in an electron microscope.[120] These studies are completed by ex situ measurements on reaction intermediates and products as well as by simulations of the reaction kinetics.[105] Taken together these efforts aim at the rational design of synthesis methods giving precise control of size, shape and composition. In this context, the understanding of the precursor conversion to monomers has been improved over the last years, both experimentally and theoretically.[358,720] This knowledge allowed the fine-tuning of metal chalcogenide synthesis methods and gave access to monodisperse samples of desired size and quantitative reaction yield. One way to realize this goal consists of the preparation of precursor libraries of smoothly tunable reactivity and hence conversion rates. This has been illustrated at the example of metal sulfide NCs, prepared by using a series of differently substituted thiourea ligands.[106] Similar efforts have been undertaken with pnictogen precursors in the synthesis of III−V NCs.[721] However, the tunability of the precursors was lower and the influence of the precursor-to-

monomer conversion rate on the size and size distribution was less pronounced than in the case of the metal chalcogenide NCs. Insights into the actual structure of the monomers formed would be of great help for further optimization of the synthetic pathways. The broader utilization of existing knowledge in the fields of coordination chemistry and cluster chemistry constitutes another avenue for the rational design of synthesis methods of NCs. A large number of main-group bridged transition metal clusters could be isolated in the form of single-crystals.[722] They represent therefore perfectly monodisperse systems with dimensions in between those of molecular precursors and NCs. Their molecular structures, identified by single-crystal X-ray diffraction, give important information about the binding modes of ligands on the surface and on the existence of coordination patterns differing from bulk materials. Efforts in this direction have recently been made by crystallizing and analyzing an 1.3 nm $In_{37}P_{20}(O_2CCH_2Ph)_{51}$ cluster.[723] Concluding, in view of the progress in this field in the past two decades, it can be expected that the creativity of chemists will face the challenges to bring the quality of alternative nontoxic and Earth-abundant NCs to the same level as it has been achieved for their Cd- and Pb-containing counterparts.

AUTHOR INFORMATION

Corresponding Author
*E-mail: peter.reiss@cea.fr.

Notes
The authors declare no competing financial interest.

Biographies

Peter Reiss is researcher at the Institute of Nanoscience & Cryogenics, CEA Grenoble, and Head of Laboratory of Molecular, Organic and Hybrid Electronics. He graduated (1997) from the University of Karlsruhe, Germany, and earned his Ph.D. in Inorganic Chemistry under the supervision of Prof. Dieter Fenske (2000). During his Ph.D. he investigated nitrogen-bridged transition metal clusters, grown as single crystals. His current research activities focus on colloidal semiconductor nanocrystals and nanowires, in particular their synthesis, surface functionalization, and assembly of these nanoscale building blocks into structurally controlled functional materials. The studied applications range from fluorescent markers for biological labelling and detection over the development of efficient emitters for LEDs and displays to new strategies for nanocrystal based energy conversion (photovoltaics and thermoelectrics) and storage; he is cofounder of the startup company *EnWireS*—silicon nanowires for energy storage.

Marie Carrière received her Ph.D. from AgroParisTech in 2002 and obtained a permanent position at the Atomic Energy Commission (CEA), Saclay, in 2004. In January 2011 she joined CEA-Grenoble, where she currently works as a nanoparticle toxicologist in the Laboratoire Lésions des Acides Nucléiques (Nucleic Acid Lesions) from the Fundamental Research Division, Institute of Nanoscience and Cryogenics. Activities of the group range from the chemistry and detection of DNA damage and DNA repair processes to toxicology and especially genotoxicity of environmental pollutants and drugs. She is also involved in the development of innovative therapeutic approaches using nanoparticles.

Christophe Lincheneau obtained his M.Sc. from University of Bordeaux in supramolecular chemistry and nanoscience. In 2006, he joined the group of Prof. T. Gunnlaugsson at Trinity College, Dublin

where he earned his Ph.D. in Chemistry (2010) focusing on the synthesis and study of lanthanide luminescent architectures. In 2012, he joined the group of Prof. A. Credi at Università di Bologna, where he worked on the synthesis of QDs and organic/inorganic hybrids for optoelectronic applications. Since April 2014, he has been working in the group of Dr. P. Reiss at CEA Grenoble, where his research focused on the synthesis and photophysical studies of InP based QDs and their hybrids with lanthanide complexes.

Louis Vaure received his M.Sc. degree in nanochemistry from Université Grenoble Alpes in 2013. He joined the team of Dr. P. Reiss at CEA Grenoble (INAC/SPrAM) for a 5 months internship, focusing on the synthesis and ligand exchange on ternary chalcogenide nanocrystals. During his Ph.D. in the same team (2013–16) he developed the chemical synthesis of $CuFeS_2$ nanocrystals and explored their thermoelectric properties.

Sudarsan Tamang received his M.Sc. degree in chemistry from North Bengal University, India (2005). Originating from Darjeeling, a small town in the foothills of the Himalayas, he travelled to Grenoble, the city of Alps in France, to pursue his Ph.D. degree. During his Ph.D. research (2009-12) under the supervision of Dr. P. Reiss he focused on the synthesis and bioapplications of NIR-emitting InP based QDs. After coming back to India he joined Sikkim University in 2012 as an assistant professor. He worked as a research fellow in National Chemical Laboratory, Pune, India for two years (supervisor Dr. B. L. V. Prasad) and as a visiting researcher in Korea Institute of Machinery and materials (KIMM), South Korea for one year (supervisor Prof. Sohee Jeong). Currently at Sikkim University, his research focus is on colloidal synthesis, mechanisms of semiconductor nanocrystal formation, surface chemistry, properties, and applications.

ACKNOWLEDGMENTS

REFERENCES

(1) Efros, A. L. Interband Absorption of Light in a Semiconductor Sphere. *Sov. Phys. Semicond.* **1982**, *16*, 772−775.

(2) Ekimov, A.-I.; Onushchenko, A.-A. Quantum Size Effect in Three-Dimensional Microscopic Semiconductor Crystals. *Sov. Phys. JETP* **1981**, *34*, 345−349.

(3) Henglein, A. Photo-Degradation and Fluorescence of Colloidal-Cadmium Sulfide in Aqueous-Solution. *Phys. Chem. Chem. Phys.* **1982**, *86*, 301−305.

(4) Rossetti, R.; Brus, L. Electron-Hole Recombination Emission as a Probe of Surface Chemistry in Aqueous Cadmium Sulfide Colloids. *J. Phys. Chem.* **1982**, *86*, 4470−4472.

(5) Alivisatos, A. P. Semiconductor Clusters, Nanocrystals, and Quantum Dots. *Science* **1996**, *271*, 933−937.

(6) Chen, O.; Wei, H.; Maurice, A.; Bawendi, M.; Reiss, P. Pure Colors from Core−Shell Quantum Dots. *MRS Bull.* **2013**, *38*, 696−702.

(7) Tang, J.; Sargent, E. H. Infrared Colloidal Quantum Dots for Photovoltaics: Fundamentals and Recent Progress. *Adv. Mater.* **2011**, *23*, 12−29.

(8) Murray, C. B.; Kagan, C. R.; Bawendi, M. G. Synthesis and Characterization of Monodisperse Nanocrystals and Close-Packed Nanocrystal Assemblies. *Annu. Rev. Mater. Sci.* **2000**, *30*, 545−610.

(9) El-Sayed, M. A. Small Is Different: Shape-, Size-, and Composition-Dependent Properties of Some Colloidal Semiconductor Nanocrystals. *Acc. Chem. Res.* **2004**, *37*, 326−333.

(10) Talapin, D. V.; Lee, J. S.; Kovalenko, M. V.; Shevchenko, E. V. Prospects of Colloidal Nanocrystals for Electronic and Optoelectronic Applications. *Chem. Rev.* **2010**, *110*, 389−458.

(11) de Mello Donega, C. Synthesis and Properties of Colloidal Heteronanocrystals. *Chem. Soc. Rev.* **2011**, *40*, 1512−1546.

(12) Park, J.; Joo, J.; Kwon, S. G.; Jang, Y.; Hyeon, T. Synthesis of Monodisperse Spherical Nanocrystals. *Angew. Chem., Int. Ed.* **2007**, *46*, 4630−4660.

(13) Kwon, S. G.; Hyeon, T. Formation Mechanisms of Uniform Nanocrystals Via Hot-Injection and Heat-up Methods. *Small* **2011**, *7*, 2685−2702.

(14) Kovalenko, M. V.; Manna, L.; Cabot, A.; Hens, Z.; Talapin, D. V.; Kagan, C. R.; Klimov, V. I.; Rogach, A. L.; Reiss, P.; Milliron, D. J.; et al. Prospects of Nanoscience with Nanocrystals. *ACS Nano* **2015**, *9*, 1012−1057.

(15) Weller, H. Colloidal Semiconductor Q-Particles - Chemistry in the Transition Region between Solid-State and Molecules. *Angew. Chem., Int. Ed. Engl.* **1993**, *32*, 41−53.

(16) Reiss, P. Synthesis of Monodisperse Spherical Semiconductor Nanocrystals of Core and Core/Shell Type in Organic Solvents. In *Semiconductor Nanocrystal Quantum Dots*; Rogach, A. L., Ed.; Springer: New York, 2008; pp 35−72.

(17) Rogach, A. L.; Eychmüller, A.; Hickey, S. G.; Kershaw, S. V. Infrared-Emitting Colloidal Nanocrystals: Synthesis, Assembly, Spectroscopy, and Applications. *Small* **2007**, *3*, 536−557.

(18) Cozzoli, P. D.; Pellegrino, T.; Manna, L. Synthesis, Properties and Perspectives of Hybrid Nanocrystal Structures. *Chem. Soc. Rev.* **2006**, *35*, 1195−1208.

(19) van Embden, J.; Chesman, A. S. R.; Jasieniak, J. J. The Heat-up Synthesis of Colloidal Nanocrystals. *Chem. Mater.* **2015**, *27*, 2246−2285.

(20) Samokhvalov, P.; Artemyev, M.; Nabiev, I. Basic Principles and Current Trends in Colloidal Synthesis of Highly Luminescent Semiconductor Nanocrystals. *Chem. - Eur. J.* **2013**, *19*, 1534−1546.

(21) Pellegrino, T.; Kudera, S.; Liedl, T.; Javier, A. M.; Manna, L.; Parak, W. J. On the Development of Colloidal Nanoparticles Towards Multifunctional Structures and Their Possible Use for Biological Applications. *Small* **2005**, *1*, 48−63.

(22) Bouccara, S.; Sitbon, G.; Fragola, A.; Loriette, V.; Lequeux, N.; Pons, T. Enhancing Fluorescence in Vivo Imaging Using Inorganic Nanoprobes. *Curr. Opin. Biotechnol.* **2015**, *34*, 65−72.

(23) Pino, P. d.; Pelaz, B.; Zhang, Q.; Maffre, P.; Nienhaus, G. U.; Parak, W. J. Protein Corona Formation around Nanoparticles - from the Past to the Future. *Mater. Horiz.* **2014**, *1*, 301−313.

(24) Michalet, X.; Pinaud, F. F.; Bentolila, L. A.; Tsay, J. M.; Doose, S.; Li, J. J.; Sundaresan, G.; Wu, A. M.; Gambhir, S. S.; Weiss, S. Quantum Dots for Live Cells, in Vivo Imaging, and Diagnostics. *Science* **2005**, *307*, 538−544.

(25) Medintz, I. L.; Uyeda, H. T.; Goldman, E. R.; Mattoussi, H. Quantum Dot Bioconjugates for Imaging, Labelling and Sensing. *Nat. Mater.* **2005**, *4*, 435−446.

(26) Shirasaki, Y.; Supran, G. J.; Bawendi, M. G.; Bulovic, V. Emergence of Colloidal Quantum-Dot Light-Emitting Technologies. *Nat. Photonics* **2012**, *7*, 13−23.

(27) Kramer, I. J.; Sargent, E. H. Colloidal Quantum Dot Photovoltaics: A Path Forward. *ACS Nano* **2011**, *5*, 8506−8514.

(28) Kamat, P. V.; Tvrdy, K.; Baker, D. R.; Radich, J. G. Beyond Photovoltaics: Semiconductor Nanoarchitectures for Liquid-Junction Solar Cells. *Chem. Rev.* **2010**, *110*, 6664−6688.

(29) Kamat, P. V. Quantum Dot Solar Cells. Semiconductor Nanocrystals as Light Harvesters. *J. Phys. Chem. C* **2008**, *112*, 18737−18753.

(30) Haxel, G. B.; Boore, S.; Mayfield, S. Rare Earth Elements—Critical Resources for High Technology. *USGS fact sheet* **2002**, 087−02.

(31) Wadia, C.; Alivisatos, A. P.; Kammen, D. M. Materials Availability Expands the Opportunity for Large-Scale Photovoltaics Deployment. *Environ. Sci. Technol.* **2009**, *43*, 2072−2077.

(32) Green, M. A.; Emery, K.; Hishikawa, Y.; Warta, W.; Dunlop, E. D. Solar Cell Efficiency Tables (Version 46). *Prog. Photovoltaics* **2015**, *23*, 805−812.

(33) Zhou, H.; Hsu, W.-C.; Duan, H.-S.; Bob, B.; Yang, W.; Song, T.-B.; Hsu, C.-J.; Yang, Y. CZTS Nanocrystals: A Promising Approach for Next Generation Thin Film Photovoltaics. *Energy Environ. Sci.* **2013**, *6*, 2822−2838.

(34) Hardman, R. A Toxicologic Review of Quantum Dots: Toxicity Depends on Physicochemical and Environmental Factors. *Environ. Health Perspect.* **2006**, *114*, 165−172.

(35) Reiss, P.; Protiere, M.; Li, L. Core/Shell Semiconductor Nanocrystals. *Small* **2009**, *5*, 154−168.

(36) Mélinon, P.; Begin-Colin, S.; Duvail, J. L.; Gauffre, F.; Boime, N. H.; Ledoux, G.; Plain, J.; Reiss, P.; Silly, F.; Warot-Fonrose, B. Engineered Inorganic Core/Shell Nanoparticles. *Phys. Rep.* **2014**, *543*, 163−197.

(37) Ryman-Rasmussen, J. P.; Riviere, J. E.; Monteiro-Riviere, N. A. Penetration of Intact Skin by Quantum Dots with Diverse Physicochemical Properties. *Toxicol. Sci.* **2006**, *91*, 159−65.

(38) Zhang, L. W.; Yu, W. W.; Colvin, V. L.; Monteiro-Riviere, N. A. Biological Interactions of Quantum Dot Nanoparticles in Skin and in Human Epidermal Keratinocytes. *Toxicol. Appl. Pharmacol.* **2008**, *228*, 200−11.

(39) Ryman-Rasmussen, J. P.; Riviere, J. E.; Monteiro-Riviere, N. A. Surface Coatings Determine Cytotoxicity and Irritation Potential of Quantum Dot Nanoparticles in Epidermal Keratinocytes. *J. Invest. Dermatol.* **2007**, *127*, 143−53.

(40) Mortensen, L. J.; Jatana, S.; Gelein, R.; De Benedetto, A.; De Mesy Bentley, K. L.; Beck, L. A.; Elder, A.; Delouise, L. A. Quantification of Quantum Dot Murine Skin Penetration with UVR Barrier Impairment. *Nanotoxicology* **2013**, *7*, 1386−98.

(41) Karabanovas, V.; Zakarevicius, E.; Sukackaite, A.; Streckyte, G.; Rotomskis, R. Examination of the Stability of Hydrophobic (CdSe)-ZnS Quantum Dots in the Digestive Tract of Rats. *Photochem. Photobiol. Sci.* **2008**, *7*, 725−9.

(42) Loginova, Y. F.; Dezhurov, S. V.; Zherdeva, V. V.; Kazachkina, N. I.; Wakstein, M. S.; Savitsky, A. P. Biodistribution and Stability of CdSe Core Quantum Dots in Mouse Digestive Tract Following Per Os Administration: Advantages of Double Polymer/Silica Coated Nanocrystals. *Biochem. Biophys. Res. Commun.* **2012**, *419*, 54−9.

(43) Kabe, I.; Omae, K.; Nakashima, H.; Nomiyama, T.; Uemura, T.; Hosoda, K.; Ishizuka, C.; Yamazaki, K.; Sakurai, H. In Vitro Solubility and in Vivo Toxicity of Indium Phosphide. *J. Occup. Health* **1996**, *38*, 6−12.

(44) Wiecinski, P. N.; Metz, K. M.; Mangham, A. N.; Jacobson, K. H.; Hamers, R. J.; Pedersen, J. A. Gastrointestinal Biodurability of Engineered Nanoparticles: Development of an Assay. *Nanotoxicology* **2009**, *3*, 202−214.

(45) Mohs, A. M.; Duan, H.; Kairdolf, B. A.; Smith, A. M.; Nie, S. Proton-Resistant Quantum Dots: Stability in Gastrointestinal Fluids and Implications for Oral Delivery of Nanoparticle Agents. *Nano Res.* **2009**, *2*, 500−508.

(46) Hsieh, Y.-K.; Hsieh, H.-A.; Hsieh, H.-F.; Wang, T.-H.; Ho, C.-C.; Lin, P.-P.; Wang, C.-F. Using Laser Ablation Inductively Coupled Plasma Mass Spectrometry to Characterize the Biointeractions of Inhaled CdSe Quantum Dots in the Mouse Lungs. *J. Anal. At. Spectrom.* **2013**, *28*, 1396−1401.

(47) Ma-Hock, L.; Brill, S.; Wohlleben, W.; Farias, P. M.; Chaves, C. R.; Tenorio, D. P.; Fontes, A.; Santos, B. S.; Landsiedel, R.; Strauss, V.; et al. Short Term Inhalation Toxicity of a Liquid Aerosol of CdS/

Cd(OH)(2) Core Shell Quantum Dots in Male Wistar Rats. *Toxicol. Lett.* **2012**, *208*, 115−24.

(48) Kirby, P. J.; Shines, C. J.; Taylor, G. J.; Bousquet, R. W.; Price, H. C.; Everitt, J. I.; Morgan, D. L. Pleural Effects of Indium Phosphide in B6C3F1Mice: Nonfibrous Particulate Induced Pleural Fibrosis. *Exp. Lung Res.* **2009**, *35*, 858−82.

(49) NTP, Toxicology and Carcinogenesis Studies of Indium Phosphide (Cas No. 22398-90-7) in F344/N Rats and B6C3F1Mice (Inhalation Studies). 2001; pp 7−340.

(50) IARC, Indium Phosphide. In *Monographs on the Evaluation of the Carcinogenic Risk of Chemicals to Humans*, Cancer., I. A. f. R. o., Ed. World Health Organization: 2006.

(51) Oh, N.; Park, J. H. Endocytosis and Exocytosis of Nanoparticles in Mammalian Cells. *Int. J. Nanomed.* **2014**, *9* (Suppl 1), 51−63.

(52) Lin, G.; Ouyang, Q.; Hu, R.; Ding, Z.; Tian, J.; Yin, F.; Xu, G.; Chen, Q.; Wang, X.; Yong, K. T. In Vivo Toxicity Assessment of Non-Cadmium Quantum Dots in Balb/C Mice. *Nanomedicine* **2015**, *11*, 341−50.

(53) Helle, M.; Cassette, E.; Bezdetnaya, L.; Pons, T.; Leroux, A.; Plenat, F.; Guillemin, F.; Dubertret, B.; Marchal, F. Visualisation of Sentinel Lymph Node with Indium-Based near Infrared Emitting Quantum Dots in a Murine Metastatic Breast Cancer Model. *PLoS One* **2012**, *7*, e44433.

(54) Pons, T.; Pic, E.; Lequeux, N.; Cassette, E.; Bezdetnaya, L.; Guillemin, F.; Marchal, F.; Dubertret, B. Cadmium-Free CuInS$_2$/ZnS Quantum Dots for Sentinel Lymph Node Imaging with Reduced Toxicity. *ACS Nano* **2010**, *4*, 2531−8.

(55) Geys, J.; Nemmar, A.; Verbeken, E.; Smolders, E.; Ratoi, M.; Hoylaerts, M. F.; Nemery, B.; Hoet, P. H. Acute Toxicity and Prothrombotic Effects of Quantum Dots: Impact of Surface Charge. *Environ. Health Perspect.* **2008**, *116*, 1607−13.

(56) Liu, N.; Mu, Y.; Chen, Y.; Sun, H.; Han, S.; Wang, M.; Wang, H.; Li, Y.; Xu, Q.; Huang, P.; Sun, Z. Degradation of Aqueous Synthesized CdTe/ZnS Quantum Dots in Mice: Differential Blood Kinetics and Biodistribution of Cadmium and Tellurium. *Part. Fibre Toxicol.* **2013**, *10*, 37.

(57) Su, Y.; Peng, F.; Jiang, Z.; Zhong, Y.; Lu, Y.; Jiang, X.; Huang, Q.; Fan, C.; Lee, S. T.; He, Y. In Vivo Distribution, Pharmacokinetics, and Toxicity of Aqueous Synthesized Cadmium-Containing Quantum Dots. *Biomaterials* **2011**, *32*, 5855−62.

(58) Yang, R. S.; Chang, L. W.; Wu, J. P.; Tsai, M. H.; Wang, H. J.; Kuo, Y. C.; Yeh, T. K.; Yang, C. S.; Lin, P. Persistent Tissue Kinetics and Redistribution of Nanoparticles, Quantum Dot 705, in Mice: ICP-MS Quantitative Assessment. *Environ. Health Perspect.* **2007**, *115*, 1339−43.

(59) Yeh, T. K.; Wu, J. P.; Chang, L. W.; Tsai, M. H.; Chang, W. H.; Tsai, H. T.; Yang, C. S.; Lin, P. Comparative Tissue Distributions of Cadmium Chloride and Cadmium-Based Quantum Dot 705 in Mice: Safety Implications and Applications. *Nanotoxicology* **2011**, *5*, 91−7.

(60) Choi, H. S.; Liu, W.; Misra, P.; Tanaka, E.; Zimmer, J. P.; Itty Ipe, B.; Bawendi, M. G.; Frangioni, J. V. Renal Clearance of Quantum Dots. *Nat. Biotechnol.* **2007**, *25*, 1165−1170.

(61) Hauck, T. S.; Anderson, R. E.; Fischer, H. C.; Newbigging, S.; Chan, W. C. In Vivo Quantum-Dot Toxicity Assessment. *Small* **2010**, *6*, 138−44.

(62) Ye, L.; Yong, K. T.; Liu, L.; Roy, I.; Hu, R.; Zhu, J.; Cai, H.; Law, W. C.; Liu, J.; Wang, K.; et al. A Pilot Study in Non-Human Primates Shows No Adverse Response to Intravenous Injection of Quantum Dots. *Nat. Nanotechnol.* **2012**, *7*, 453−8.

(63) Fitzpatrick, J. A.; Andreko, S. K.; Ernst, L. A.; Waggoner, A. S.; Ballou, B.; Bruchez, M. P. Long-Term Persistence and Spectral Blue Shifting of Quantum Dots in Vivo. *Nano Lett.* **2009**, *9*, 2736−41.

(64) Gao, X.; Tang, M.; Li, Z.; Zha, Y.; Cheng, G.; Yin, S.; Chen, J.; Ruan, D.-y.; Chen, L.; Wang, M. Streptavidin-Conjugated CdSe/ZnS Quantum Dots Impaired Synaptic Plasticity and Spatial Memory Process. *J. Nanopart. Res.* **2013**, *15*, 1575.

(65) Loginova, Y. F.; Kazachkina, N. I.; Zherdeva, V. V.; Rusanov, A. L.; Shirmanova, M. V.; Zagaynova, E. V.; Sergeeva, E. A.; Dezhurov, S. V.; Wakstein, M. S.; Savitsky, A. P. Biodistribution of Intact Fluorescent CdSe/CdS/ZnS Quantum Dots Coated by Mercaptopropionic Acid after Intravenous Injection into Mice. *J. Biophotonics* **2012**, *5*, 848−59.

(66) Derfus, A. M.; Chan, W. C. W.; Bhatia, S. N. Probing the Cytotoxicity of Semiconductor Quantum Dots. *Nano Lett.* **2004**, *4*, 11−18.

(67) Dollefeld, H.; Hoppe, K.; Kolny, J.; Schilling, K.; Weller, H.; Eychmüller, A. Investigations on the Stability of Thiol Stabilized Semiconductor Nanoparticles. *Phys. Chem. Chem. Phys.* **2002**, *4*, 4747−4753.

(68) Mancini, M. C.; Kairdolf, B. A.; Smith, A. M.; Nie, S. Oxidative Quenching and Degradation of Polymer-Encapsulated Quantum Dots: New Insights into the Long-Term Fate and Toxicity of Nanocrystals in Vivo. *J. Am. Chem. Soc.* **2008**, *130*, 10836−7.

(69) Brunetti, V.; Chibli, H.; Fiammengo, R.; Galeone, A.; Malvindi, M. A.; Vecchio, G.; Cingolani, R.; Nadeau, J. L.; Pompa, P. P. InP/ZnS as a Safer Alternative to CdSe/ZnS Core/Shell Quantum Dots: In Vitro and in Vivo Toxicity Assessment. *Nanoscale* **2013**, *5*, 307−17.

(70) Clift, M. J.; Brandenberger, C.; Rothen-Rutishauser, B.; Brown, D. M.; Stone, V. The Uptake and Intracellular Fate of a Series of Different Surface Coated Quantum Dots in Vitro. *Toxicology* **2011**, *286*, 58−68.

(71) Zhang, L. W.; Monteiro-Riviere, N. A. Mechanisms of Quantum Dot Nanoparticle Cellular Uptake. *Toxicol. Sci.* **2009**, *110*, 138−55.

(72) Martinez-Finley, E. J.; Chakraborty, S.; Fretham, S. J.; Aschner, M. Cellular Transport and Homeostasis of Essential and Nonessential Metals. *Metallomics* **2012**, *4*, 593−605.

(73) Limbach, L. K.; Li, Y.; Grass, R. N.; Brunner, T. J.; Hintermann, M. A.; Müller, M.; Gunther, D.; Stark, W. J. Oxide Nanoparticle Uptake in Human Lung Fibroblasts: Effects of Particle Size, Agglomeration, and Diffusion at Low Concentrations. *Environ. Sci. Technol.* **2005**, *39*, 9370−6.

(74) Ivask, A.; Juganson, K.; Bondarenko, O.; Mortimer, M.; Aruoja, V.; Kasemets, K.; Blinova, I.; Heinlaan, M.; Slaveykova, V.; Kahru, A. Mechanisms of Toxic Action of Ag, ZnO and CuO Nanoparticles to Selected Ecotoxicological Test Organisms and Mammalian Cells in Vitro: A Comparative Review. *Nanotoxicology* **2014**, *8* (Suppl 1), 57−71.

(75) Matovic, V.; Buha, A.; Dukic-Cosic, D.; Bulat, Z. Insight into the Oxidative Stress Induced by Lead and/or Cadmium in Blood, Liver and Kidneys. *Food Chem. Toxicol.* **2015**, *78*, 130−140.

(76) Candeias, S.; Pons, B.; Viau, M.; Caillat, S.; Sauvaigo, S. Direct Inhibition of Excision/Synthesis DNA Repair Activities by Cadmium: Analysis on Dedicated Biochips. *Mutat. Res., Fundam. Mol. Mech. Mutagen.* **2010**, *694*, 53−9.

(77) Chibli, H.; Carlini, L.; Park, S.; Dimitrijevic, N. M.; Nadeau, J. L. Cytotoxicity of InP/ZnS Quantum Dots Related to Reactive Oxygen Species Generation. *Nanoscale* **2011**, *3*, 2552−9.

(78) Green, M.; Howman, E. Semiconductor Quantum Dots and Free Radical Induced DNA Nicking. *Chem. Commun.* **2005**, 121−3.

(79) Ipe, B. I.; Lehnig, M.; Niemeyer, C. M. On the Generation of Free Radical Species from Quantum Dots. *Small* **2005**, *1*, 706−9.

(80) Anas, A.; Akita, H.; Harashima, H.; Itoh, T.; Ishikawa, M.; Biju, V. Photosensitized Breakage and Damage of DNA by CdSe-ZnS Quantum Dots. *J. Phys. Chem. B* **2008**, *112*, 10005−11.

(81) Lin, C. H.; Yang, M. H.; Chang, L. W.; Yang, C. S.; Chang, H.; Chang, W. H.; Tsai, M. H.; Wang, C. J.; Lin, P. Cd/Se/Te-Based Quantum Dot 705 Modulated Redox Homeostasis with Hepatotoxicity in Mice. *Nanotoxicology* **2011**, *5*, 650−63.

(82) Khalil, W. K.; Girgis, E.; Emam, A. N.; Mohamed, M. B.; Rao, K. V. Genotoxicity Evaluation of Nanomaterials: DNA Damage, Micronuclei, and 8-Hydroxy-2-Deoxyguanosine Induced by Magnetic Doped CdSe Quantum Dots in Male Mice. *Chem. Res. Toxicol.* **2011**, *24*, 640−50.

(83) Aye, M.; Di Giorgio, C.; Mekaouche, M.; Steinberg, J. G.; Brerro-Saby, C.; Barthelemy, P.; De Meo, M.; Jammes, Y. Genotoxicity of Intraperitoneal Injection of Lipoamphiphile CdSe/ZnS Quantum Dots in Rats. *Mutat. Res., Genet. Toxicol. Environ. Mutagen.* **2013**, *758*, 48−55.

(84) Cho, S. J.; Maysinger, D.; Jain, M.; Roder, B.; Hackbarth, S.; Winnik, F. M. Long-Term Exposure to CdTe Quantum Dots Causes Functional Impairments in Live Cells. *Langmuir* **2007**, *23*, 1974−80.

(85) Hoshino, A.; Fujioka, K.; Oku, T.; Suga, M.; Sasaki, Y. F.; Ohta, T.; Yasuhara, M.; Suzuki, K.; Yamamoto, K. Physicochemical Properties and Cellular Toxicity of Nanocrystal Quantum Dots Depend on Their Surface Modification. *Nano Lett.* **2004**, *4*, 2163−2169.

(86) Nabiev, I.; Mitchell, S.; Davies, A.; Williams, Y.; Kelleher, D.; Moore, R.; Gun'ko, Y. K.; Byrne, S.; Rakovich, Y. P.; Donegan, J. F.; et al. Nonfunctionalized Nanocrystals Can Exploit a Cell's Active Transport Machinery Delivering Them to Specific Nuclear and Cytoplasmic Compartments. *Nano Lett.* **2007**, *7*, 3452−3461.

(87) Tiwari, D. K.; Jin, T.; Behari, J. Bio-Distribution and Toxicity Assessment of Intravenously Injected Anti-HER2 Antibody Conjugated CdSe/ZnS Quantum Dots in Wistar Rats. *Int. J. Nanomed.* **2011**, *6*, 463−75.

(88) Lison, D.; Laloy, J.; Corazzari, I.; Muller, J.; Rabolli, V.; Panin, N.; Huaux, F.; Fenoglio, I.; Fubini, B. Sintered Indium-Tin-Oxide (ITO) Particles: A New Pneumotoxic Entity. *Toxicol. Sci.* **2009**, *108*, 472−81.

(89) Glassy, B. A.; Cossairt, B. M. Ternary Synthesis of Colloidal Zn$_3$P$_2$ Quantum Dots. *Chem. Commun.* **2015**, *51*, 5283−5286.

(90) Luber, E. J.; Mobarok, M. H.; Buriak, J. M. Solution-Processed Zinc Phosphide (α-Zn$_3$P$_2$) Colloidal Semiconducting Nanocrystals for Thin Film Photovoltaic Applications. *ACS Nano* **2013**, *7*, 8136−8146.

(91) McVey, B. F. P.; Tilley, R. D. Solution Synthesis, Optical Properties, and Bioimaging Applications of Silicon Nanocrystals. *Acc. Chem. Res.* **2014**, *47*, 3045−3051.

(92) Vaughn, D. D., II; Schaak, R. E. Synthesis, Properties and Applications of Colloidal Germanium and Germanium-Based Nanomaterials. *Chem. Soc. Rev.* **2013**, *42*, 2861−2879.

(93) Bhattacharjee, S.; Rietjens, I. M. C. M.; Singh, M. P.; Atkins, T. M.; Purkait, T. K.; Xu, Z.; Regli, S.; Shukaliak, A.; Clark, R. J.; Mitchell, B. S.; et al. Cytotoxicity of Surface-Functionalized Silicon and Germanium Nanoparticles: The Dominant Role of Surface Charges. *Nanoscale* **2013**, *5*, 4870−4883.

(94) Erogbogbo, F.; Yong, K.-T.; Roy, I.; Hu, R.; Law, W.-C.; Zhao, W.; Ding, H.; Wu, F.; Kumar, R.; Swihart, M. T.; et al. In Vivo Targeted Cancer Imaging, Sentinel Lymph Node Mapping and Multi-Channel Imaging with Biocompatible Silicon Nanocrystals. *ACS Nano* **2011**, *5*, 413−423.

(95) Murray, C. B.; Norris, D. J.; Bawendi, M. G. Synthesis and Characterization of Nearly Monodisperse CdE (E = S, Se, Te) Semiconductor Nanocrystallites. *J. Am. Chem. Soc.* **1993**, *115*, 8706−8715.

(96) LaMer, V. K.; Dinegar, R. H. Theory, Production and Mechanism of Formation of Monodispersed Hydrosols. *J. Am. Chem. Soc.* **1950**, *72*, 4847−4854.

(97) Zsigmondy, R. Über Mikroskopische Goldkeime. *Z. Phys. Chem.* **1906**, *56*, 65−76.

(98) Faraday, M. The Bakerian Lecture: Experimental Relations of Gold (and Other Metals) to Light. *Philos. Trans. R. Soc. B* **1857**, *147*, 145−181.

(99) Carbone, L.; Nobile, C.; De Giorg, M.; Sala, F. D.; Morello, G.; Pompa, P.; Hytch, M.; Snoeck, E.; Fiore, A.; Franchini, I. R.; et al. Synthesis and Micrometer-Scale Assembly of Colloidal CdSe/CdS Nanorods Prepared by a Seeded Growth Approach. *Nano Lett.* **2007**, *7*, 2942−2950.

(100) Talapin, D. V.; Nelson, J. H.; Shevchenko, E. V.; Aloni, S.; Sadtler, B.; Alivisatos, A. P. Seeded Growth of Highly Luminescent CdSe/CdS Nanoheterostructures with Rod and Tetrapod Morphologies. *Nano Lett.* **2007**, *7*, 2951−2959.

(101) Becker, R.; Döring, W. Kinetische Behandlung Der Keimbildung in Übersättigten Dämpfen. *Ann. Phys. (Berlin, Ger.)* **1935**, *416*, 719−752.

(102) Callister, W. D., Jr. *Materials Science and Engineering: An Introduction*, 7th ed.; John Wiley & Sons: New York, 2007.

(103) Steckel, J. S.; Yen, B. K. H.; Oertel, D. C.; Bawendi, M. G. On the Mechanism of Lead Chalcogenide Nanocrystal Formation. *J. Am. Chem. Soc.* **2006**, *128*, 13032−13033.

(104) Liu, H.; Owen, J. S.; Alivisatos, A. P. Mechanistic Study of Precursor Evolution in Colloidal Group II−VI Semiconductor Nanocrystal Synthesis. *J. Am. Chem. Soc.* **2007**, *129*, 305−312.

(105) Abe, S.; Čapek, R. K.; De Geyter, B.; Hens, Z. Tuning the Postfocused Size of Colloidal Nanocrystals by the Reaction Rate: From Theory to Application. *ACS Nano* **2012**, *6*, 42−53.

(106) Hendricks, M. P.; Campos, M. P.; Cleveland, G. T.; Jen-La Plante, I.; Owen, J. S. A Tunable Library of Substituted Thiourea Precursors to Metal Sulfide Nanocrystals. *Science* **2015**, *348*, 1226−1230.

(107) Sugimoto, T. Underlying Mechanisms in Size Control of Uniform Nanoparticles. *J. Colloid Interface Sci.* **2007**, *309*, 106−118.

(108) Ostwald, W. Studien Über Die Bildung Und Umwandlung Fester Körper. *Z. Phys. Chem.* **1897**, *22*, 289−330.

(109) Reiss, H. The Growth of Uniform Colloidal Dispersions. *J. Chem. Phys.* **1951**, *19*, 482−487.

(110) Sugimoto, T. Preparation of Monodispersed Colloidal Particles. *Adv. Colloid Interface Sci.* **1987**, *28*, 65−108.

(111) Peng, X.; Wickham, J.; Alivisatos, A. P. Kinetics of II-VI and III-V Colloidal Semiconductor Nanocrystal Growth: "Focusing" of Size Distributions. *J. Am. Chem. Soc.* **1998**, *120*, 5343−5344.

(112) Donega, C. D.; Liljeroth, P.; Vanmaekelbergh, D. Physicochemical Evaluation of the Hot-Injection Method, a Synthesis Route for Monodisperse Nanocrystals. *Small* **2005**, *1*, 1152−1162.

(113) Phillips, J. C. *Bonds and Bands in Semiconductors*; Academic Press Inc.: New York, 1973.

(114) Madelung, O.; Schulz, M.; Weiss, H. *Numerical Data and Functional Relationships in Science and Technology, New Series, Group III: Crystal and Solid State Physics*; Springer: Berlin, 1982; Vol. *III/17b*.

(115) Heath, J. R.; Shiang, J. J. Covalency in Semiconductor Quantum Dots. *Chem. Soc. Rev.* **1998**, *27*, 65−71.

(116) *In-Situ Materials Characterization - across Spatial and Temporal Scales*; Springer: Heidelberg, 2014; Vol. *193*.

(117) Sun, Y. Watching Nanoparticle Kinetics in Liquid. *Mater. Today* **2012**, *15*, 140−147.

(118) Yuk, J. M.; Park, J.; Ercius, P.; Kim, K.; Hellebusch, D. J.; Crommie, M. F.; Lee, J. Y.; Zettl, A.; Alivisatos, A. P. High-Resolution EM of Colloidal Nanocrystal Growth Using Graphene Liquid Cells. *Science* **2012**, *336*, 61−64.

(119) Woehl, T. J.; Evans, J. E.; Arslan, I.; Ristenpart, W. D.; Browning, N. D. Direct in Situ Determination of the Mechanisms Controlling Nanoparticle Nucleation and Growth. *ACS Nano* **2012**, *6*, 8599−8610.

(120) Ngo, T.; Yang, H. Toward Ending the Guessing Game: Study of the Formation of Nanostructures Using in Situ Liquid Transmission Electron Microscopy. *J. Phys. Chem. Lett.* **2015**, *6*, 5051−5061.

(121) Evans, J. E.; Jungjohann, K. L.; Browning, N. D.; Arslan, I. Controlled Growth of Nanoparticles from Solution with in Situ Liquid Transmission Electron Microscopy. *Nano Lett.* **2011**, *11*, 2809−2813.

(122) Ramachandramoorthy, R.; Bernal, R.; Espinosa, H. D. Pushing the Envelope of in Situ Transmission Electron Microscopy. *ACS Nano* **2015**, *9*, 4675−4685.

(123) Dagtepe, P.; Chikan, V.; Jasinski, J.; Leppert, V. J. Quantized Growth of CdTe Quantum Dots; Observation of Magic-Sized CdTe Quantum Dots. *J. Phys. Chem. C* **2007**, *111*, 14977−14983.

(124) Yu, K.; Hrdina, A.; Zhang, X.; Ouyang, J.; Leek, D. M.; Wu, X.; Gong, M.; Wilkinson, D.; Li, C. Highly-Photoluminescent ZnSe Nanocrystals via a Non-Injection-Based Approach with Precursor Reactivity Elevated by a Secondary Phosphine. *Chem. Commun.* **2011**, *47*, 8811−8813.

(125) Sun, Y.; Ren, Y. In Situ Synchrotron X-Ray Techniques for Real-Time Probing of Colloidal Nanoparticle Synthesis. *Part. Part. Syst. Charact.* **2013**, *30*, 399−419.

(126) Liu, Q.; Li, Z.; Okasinski, J. S.; Ren, Y.; Sun, Y. In Situ High-Energy Synchrotron X-Ray Diffraction Revealing Precipitation

Reaction Kinetics of Silver Ions with Mixed Halide Ions. *J. Mater. Chem. C* **2015**, *3*, 7492−7498.

(127) Abecassis, B.; Testard, F.; Spalla, O.; Barboux, P. Probing in Situ the Nucleation and Growth of Gold Nanoparticles by Small-Angle X-Ray Scattering. *Nano Lett.* **2007**, *7*, 1723−1727.

(128) Uehara, M.; Sun, Z. H.; Oyanagi, H.; Yamashita, K.; Fukano, A.; Nakamura, H.; Maeda, H. In Situ Extended X-Ray Absorption Fine Structure Study of Initial Processes in CdSe Nanocrystals Formation Using a Microreactor. *Appl. Phys. Lett.* **2009**, *94*, 063104.

(129) Song, J. X.; Zhang, J.; Xie, Z.; Wei, S. Q.; Pan, Z. Y.; Hu, T. D.; Xie, Y. N. In Situ XAFS Studies on the Growth of ZnSe Quantum Dots. *Nucl. Instrum. Methods Phys. Res., Sect. A* **2010**, *619*, 280−282.

(130) Abécassis, B.; Bouet, C.; Garnero, C.; Constantin, D.; Lequeux, N.; Ithurria, S.; Dubertret, B.; Pauw, B. R.; Pontoni, D. Real-Time in Situ Probing of High-Temperature Quantum Dots Solution Synthesis. *Nano Lett.* **2015**, *15*, 2620−2626.

(131) Song, W.-S.; Lee, H.-S.; Lee, J.; Jang, D.; Choi, Y.; Choi, M.; Yang, H. Amine-Derived Synthetic Approach to Color-Tunable InP/ZnS Quantum Dots with High Fluorescent Qualities. *J. Nanopart. Res.* **2013**, *15*, 1−10.

(132) Buck, M. R.; Sines, I. T.; Schaak, R. E. Liquid-Phase Synthesis of Uniform Cube-Shaped GeTe Microcrystals. *Chem. Mater.* **2010**, *22*, 3236−3240.

(133) Pearson, R. G. Hard and Soft Acids and Bases. *J. Am. Chem. Soc.* **1963**, *85*, 3533.

(134) Zherebetskyy, D.; Scheele, M.; Zhang, Y.; Bronstein, N.; Thompson, C.; Britt, D.; Salmeron, M.; Alivisatos, P.; Wang, L.-W. Hydroxylation of the Surface of PbS Nanocrystals Passivated with Oleic Acid. *Science* **2014**, *344*, 1380−1384.

(135) Green, M. L. H. A New Approach to the Formal Classification of Covalent Compounds of the Elements. *J. Organomet. Chem.* **1995**, *500*, 127−148.

(136) Owen, J. The Coordination Chemistry of Nanocrystal Surfaces. *Science* **2015**, *347*, 615−616.

(137) Wang, F.; Tang, R.; Buhro, W. E. The Trouble with TOPO; Identification of Adventitious Impurities Beneficial to the Growth of Cadmium Selenide Quantum Dots, Rods, and Wires. *Nano Lett.* **2008**, *8*, 3521−3524.

(138) Wang, F.; Buhro, W. E. Morphology Control of Cadmium Selenide Nanocrystals: Insights into the Roles of Di-n-Octylphosphine Oxide (DOPO) and Di-n-Octylphosphinic Acid (DOPA). *J. Am. Chem. Soc.* **2012**, *134*, 5369−5380.

(139) Yu, K.; Liu, X.; Zeng, Q.; Leek, D. M.; Ouyang, J.; Whitmore, K. M.; Ripmeester, J. A.; Tao, Y.; Yang, M. Effect of Tertiary and Secondary Phosphines on Low-Temperature Formation of Quantum Dots. *Angew. Chem., Int. Ed.* **2013**, *52*, 4823−4828.

(140) Owen, J. S.; Park, J.; Trudeau, P.-E.; Alivisatos, A. P. Reaction Chemistry and Ligand Exchange at Cadmium−Selenide Nanocrystal Surfaces. *J. Am. Chem. Soc.* **2008**, *130*, 12279−12281.

(141) Morris-Cohen, A. J.; Donakowski, M. D.; Knowles, K. E.; Weiss, E. A. The Effect of a Common Purification Procedure on the Chemical Composition of the Surfaces of CdSe Quantum Dots Synthesized with Trioctylphosphine Oxide. *J. Phys. Chem. C* **2010**, *114*, 897−906.

(142) Hens, Z.; Martins, J. C. A Solution NMR Toolbox for Characterizing the Surface Chemistry of Colloidal Nanocrystals. *Chem. Mater.* **2013**, *25*, 1211−1221.

(143) Anderson, N. C.; Hendricks, M. P.; Choi, J. J.; Owen, J. S. Ligand Exchange and the Stoichiometry of Metal Chalcogenide Nanocrystals: Spectroscopic Observation of Facile Metal-Carboxylate Displacement and Binding. *J. Am. Chem. Soc.* **2013**, *135*, 18536−18548.

(144) Knittel, F.; Gravel, E.; Cassette, E.; Pons, T.; Pillon, F.; Dubertret, B.; Doris, E. On the Characterization of the Surface Chemistry of Quantum Dots. *Nano Lett.* **2013**, *13*, 5075−5078.

(145) Liu, H. T.; Owen, J. S.; Alivisatos, A. P. Mechanistic Study of Precursor Evolution in Colloidal Group II-VI Semiconductor Nanocrystal Synthesis. *J. Am. Chem. Soc.* **2007**, *129*, 305−312.

(146) Yu, K.; Liu, X.; Zeng, Q.; Yang, M.; Ouyang, J.; Wang, X.; Tao, Y. The Formation Mechanism of Binary Semiconductor Nanomaterials: Shared by Single-Source and Dual-Source Precursor Approaches. *Angew. Chem., Int. Ed.* **2013**, *52*, 11034−11039.

(147) Yu, K.; Liu, X.; Chen, Q. Y.; Yang, H.; Yang, M.; Wang, X.; Wang, X.; Cao, H.; Whitfield, D. M.; Hu, C.; Tao, Y. Mechanistic Study of the Role of Primary Amines in Precursor Conversions to Semiconductor Nanocrystals at Low Temperature. *Angew. Chem., Int. Ed.* **2014**, *53*, 6898−6904.

(148) Dong, A.; Ye, X.; Chen, J.; Kang, Y.; Gordon, T.; Kikkawa, J. M.; Murray, C. B. A Generalized Ligand-Exchange Strategy Enabling Sequential Surface Functionalization of Colloidal Nanocrystals. *J. Am. Chem. Soc.* **2011**, *133*, 998−1006.

(149) Morris-Cohen, A. J.; Donakowski, M. D.; Knowles, K. E.; Weiss, E. A. The Effect of a Common Purification Procedure on the Chemical Composition of the Surfaces of CdSe Quantum Dots Synthesized with Trioctylphosphine Oxide. *J. Phys. Chem. C* **2010**, *114*, 897−906.

(150) King, L. A.; Riley, D. J. Importance of QD Purification Procedure on Surface Adsorbance of QDs and Performance of QD Sensitized Photoanodes. *J. Phys. Chem. C* **2012**, *116*, 3349−3355.

(151) Munro, A. M.; Jen-La Plante, I.; Ng, M. S.; Ginger, D. S. Quantitative Study of the Effects of Surface Ligand Concentration on CdSe Nanocrystal Photoluminescence. *J. Phys. Chem. C* **2007**, *111*, 6220−6227.

(152) Goodwin, E. D.; Diroll, B. T.; Oh, S. J.; Paik, T.; Murray, C. B.; Kagan, C. R. Effects of Post-Synthesis Processing on CdSe Nanocrystals and Their Solids: Correlation between Surface Chemistry and Optoelectronic Properties. *J. Phys. Chem. C* **2014**, *118*, 27097−27105.

(153) Kalyuzhny, G.; Murray, R. W. Ligand Effects on Optical Properties of CdSe Nanocrystals. *J. Phys. Chem. B* **2005**, *109*, 7012−7021.

(154) Guijarro, N.; Lana-Villarreal, T.; Mora-Sero, I.; Bisquert, J.; Gomez, R. CdSe Quantum Dot-Sensitized TiO_2 Electrodes: Effect of Quantum Dot Coverage and Mode of Attachment. *J. Phys. Chem. C* **2009**, *113*, 4208−4214.

(155) Liu, W.; Lee, J.-S.; Talapin, D. V. III-V Nanocrystals Capped with Molecular Metal Chalcogenide Ligands: High Electron Mobility and Ambipolar Photoresponse. *J. Am. Chem. Soc.* **2013**, *135*, 1349−1357.

(156) Luther, J. M.; Law, M.; Song, Q.; Perkins, C. L.; Beard, M. C.; Nozik, A. J. Structural, Optical, and Electrical Properties of Self-Assembled Films of PbSe Nanocrystals Treated with 1,2-Ethanedithiol. *ACS Nano* **2008**, *2*, 271−280.

(157) Green, M. The Nature of Quantum Dot Capping Ligands. *J. Mater. Chem.* **2010**, *20*, 5797−5809.

(158) Li, G.; Shrotriya, V.; Huang, J.; Yao, Y.; Moriarty, T.; Emery, K.; Yang, Y. High-Efficiency Solution Processable Polymer Photovoltaic Cells by Self-Organization of Polymer Blends. *Nat. Mater.* **2005**, *4*, 864−868.

(159) Shen, Y.; Gee, M. Y.; Tan, R.; Pellechia, P. J.; Greytak, A. B. Purification of Quantum Dots by Gel Permeation Chromatography and the Effect of Excess Ligands on Shell Growth and Ligand Exchange. *Chem. Mater.* **2013**, *25*, 2838−2848.

(160) Yu, P.; Beard, M. C.; Ellingson, R. J.; Ferrere, S.; Curtis, C.; Drexler, J.; Luiszer, F.; Nozik, A. J. Absorption Cross-Section and Related Optical Properties of Colloidal InAs Quantum Dots. *J. Phys. Chem. B* **2005**, *109*, 7084−7087.

(161) Hassinen, A.; Moreels, I.; De Nolf, K.; Smet, P. F.; Martins, J. C.; Hens, Z. Short-Chain Alcohols Strip X-Type Ligands and Quench the Luminescence of PbSe and CdSe Quantum Dots, Acetonitrile Does Not. *J. Am. Chem. Soc.* **2012**, *134*, 20705−20712.

(162) Shakeri, B.; Meulenberg, R. W. A Closer Look into the Traditional Purification Process of CdSe Semiconductor Quantum Dots. *Langmuir* **2015**, *31*, 13433−13440.

(163) Hartmann, L.; Kumar, A.; Welker, M.; Fiore, A.; Julien-Rabant, C.; Gromova, M.; Bardet, M.; Reiss, P.; Baxter, P. N. W.; Chandezon,

F.; et al. Quenching Dynamics in CdSe Nanoparticles: Surface-Induced Defects Upon Dilution. *ACS Nano* **2012**, *6*, 9033−9041.

(164) Krueger, K. M.; Al-Somali, A. M.; Falkner, J. C.; Colvin, V. L. Characterization of Nanocrystalline CdSe by Size Exclusion Chromatography. *Anal. Chem.* **2005**, *77*, 3511−3515.

(165) Clarke, S.; Tamang, S.; Reiss, P.; Dahan, M. A Simple and General Route for Monofunctionalization of Fluorescent and Magnetic Nanoparticles Using Peptides. *Nanotechnology* **2011**, *22*, 175103.

(166) Wang, M.; Bardajee, G. R.; Kumar, S.; Nitz, M.; Scholes, G. D.; Winnik, M. A. Preparative Size-Exclusion Chromatography for Purification and Characterization of Colloidal Quantum Dots Bound by Chromophore-Labeled Polymers and Low-Molecular-Weight Chromophores. *J. Chromatogr. A* **2009**, *1216*, 5011−5019.

(167) Park, J.-H.; Gu, L.; von Maltzahn, G.; Ruoslahti, E.; Bhatia, S. N.; Sailor, M. J. Biodegradable Luminescent Porous Silicon Nanoparticles for in Vivo Applications. *Nat. Mater.* **2009**, *8*, 331−336.

(168) Kittel, C. *Introduction to Solid State Physics*, 8th ed.; John Wiley & Sons: Hoboken, NJ, 2005.

(169) Canham, L. T. Silicon Quantum Wire Array Fabrication by Electrochemical and Chemical Dissolution of Wafers. *Appl. Phys. Lett.* **1990**, *57*, 1046−1048.

(170) Li, X. G.; He, Y. Q.; Talukdar, S. S.; Swihart, M. T. Process for Preparing Macroscopic Quantities of Brightly Photoluminescent Silicon Nanoparticles with Emission Spanning the Visible Spectrum. *Langmuir* **2003**, *19*, 8490−8496.

(171) Wilcoxon, J. P.; Samara, G. A.; Provencio, P. N. Optical and Electronic Properties of Si Nanoclusters Synthesized in Inverse Micelles. *Phys. Rev. B: Condens. Matter Mater. Phys.* **1999**, *60*, 2704−2714.

(172) Hessel, C. M.; Reid, D.; Panthani, M. G.; Rasch, M. R.; Goodfellow, B. W.; Wei, J. W.; Fujii, H.; Akhavan, V.; Korgel, B. A. Synthesis of Ligand-Stabilized Silicon Nanocrystals with Size-Dependent Photoluminescence Spanning Visible to near-Infrared Wavelengths. *Chem. Mater.* **2012**, *24*, 393−401.

(173) Cheng, X. Y.; Gondosiswanto, R.; Ciampi, S.; Reece, P. J.; Gooding, J. J. One-Pot Synthesis of Colloidal Silicon Quantum Dots and Surface Functionalization Via Thiol-Ene Click Chemistry. *Chem. Commun.* **2012**, *48*, 11874−11876.

(174) Warner, J. H.; Rubinsztein-Dunlop, H.; Tilley, R. D. Surface Morphology Dependent Photoluminescence from Colloidal Silicon Nanocrystals. *J. Phys. Chem. B* **2005**, *109*, 19064−19067.

(175) Dasog, M.; Yang, Z. Y.; Regli, S.; Atkins, T. M.; Faramus, A.; Singh, M. P.; Muthuswamy, E.; Kauzlarich, S. M.; Tilley, R. D.; Veinot, J. G. C. Chemical Insight into the Origin of Red and Blue Photoluminescence Arising from Freestanding Silicon Nanocrystals. *ACS Nano* **2013**, *7*, 2676−2685.

(176) McVey, B. F.; Tilley, R. D. Solution Synthesis, Optical Properties, and Bioimaging Applications of Silicon Nanocrystals. *Acc. Chem. Res.* **2014**, *47*, 3045−51.

(177) He, Y.; Zhong, Y.; Peng, F.; Wei, X.; Su, Y.; Lu, Y.; Su, S.; Gu, W.; Liao, L.; Lee, S. T. One-Pot Microwave Synthesis of Water-Dispersible, Ultraphoto- and pH-Stable, and Highly Fluorescent Silicon Quantum Dots. *J. Am. Chem. Soc.* **2011**, *133*, 14192−5.

(178) Yang, C.-S.; Bley, R. A.; Kauzlarich, S. M.; Lee, H. W. H.; Delgado, G. R. Synthesis of Alkyl-Terminated Silicon Nanoclusters by a Solution Route. *J. Am. Chem. Soc.* **1999**, *121*, 5191−5195.

(179) Tilley, R. D.; Yamamoto, K. The Microemulsion Synthesis of Hydrophobic and Hydrophilic Silicon Nanocrystals. *Adv. Mater.* **2006**, *18*, 2053−2056.

(180) Zhong, Y.; Peng, F.; Bao, F.; Wang, S.; Ji, X.; Yang, L.; Su, Y.; Lee, S. T.; He, Y. Large-Scale Aqueous Synthesis of Fluorescent and Biocompatible Silicon Nanoparticles and Their Use as Highly Photostable Biological Probes. *J. Am. Chem. Soc.* **2013**, *135*, 8350−6.

(181) Hoffman, M.; Veinot, J. G. C. Understanding the Formation of Elemental Germanium by Thermolysis of Sol-Gel Derived Organogermanium Oxide Polymers. *Chem. Mater.* **2012**, *24*, 1283−1291.

(182) Kovalev, D.; Heckler, H.; Polisski, G.; Koch, F. Optical Properties of Si Nanocrystals. *Phys. Status Solidi B* **1999**, *215*, 871−932.

(183) Delerue, C.; Allan, G.; Lannoo, M. Theoretical Aspects of the Luminescence of Porous Silicon. *Phys. Rev. B: Condens. Matter Mater. Phys.* **1993**, *48*, 11024−11036.

(184) Niquet, Y. M.; Allan, G.; Delerue, C.; Lannoo, M. Quantum Confinement in Germanium Nanocrystals. *Appl. Phys. Lett.* **2000**, *77*, 1182−1184.

(185) Rinck, J.; Schray, D.; Kubel, C.; Powell, A. K.; Ozin, G. A. Size-Dependent Oxidation of Monodisperse Silicon Nanocrystals with Allylphenylsulfide Surfaces. *Small* **2015**, *11*, 335−40.

(186) Mastronardi, M. L.; Hennrich, F.; Henderson, E. J.; Maier-Flaig, F.; Blum, C.; Reichenbach, J.; Lemmer, U.; Kübel, C.; Wang, D.; Kappes, M. M.; Ozin, G. A. Preparation of Monodisperse Silicon Nanocrystals Using Density Gradient Ultracentrifugation. *J. Am. Chem. Soc.* **2011**, *133*, 11928−11931.

(187) Mastronardi, M. L.; Maier-Flaig, F.; Faulkner, D.; Henderson, E. J.; Kübel, C.; Lemmer, U.; Ozin, G. A. Size-Dependent Absolute Quantum Yields for Size-Separated Colloidally-Stable Silicon Nanocrystals. *Nano Lett.* **2012**, *12*, 337−342.

(188) Mochalin, V. N.; Shenderova, O.; Ho, D.; Gogotsi, Y. The Properties and Applications of Nanodiamonds. *Nat. Nanotechnol.* **2011**, *7*, 11−23.

(189) Kroto, H. W.; Heath, J. R.; O'Brien, S. C.; Curl, R. F.; Smalley, R. E. C60: Buckminsterfullerene. *Nature* **1985**, *318*, 162−163.

(190) Rabenau, T.; Simon, A.; Kremer, R. K.; Sohmen, E. The Energy Gaps of Fullerene C60 and C70 Determined from the Temperature Dependent Microwave Conductivity. *Z. Phys. B: Condens. Matter* **1993**, *90*, 69−72.

(191) Iijima, S. Helical Microtubules of Graphitic Carbon. *Nature* **1991**, *354*, 56−58.

(192) Iijima, S.; Ichihashi, T. Single-Shell Carbon Nanotubes of 1-nm Diameter. *Nature* **1993**, *363*, 603−605.

(193) Bethune, D. S.; Klang, C. H.; de Vries, M. S.; Gorman, G.; Savoy, R.; Vazquez, J.; Beyers, R. Cobalt-Catalysed Growth of Carbon Nanotubes with Single-Atomic-Layer Walls. *Nature* **1993**, *363*, 605−607.

(194) Odom, T. W.; Huang, J.-L.; Kim, P.; Lieber, C. M. Atomic Structure and Electronic Properties of Single-Walled Carbon Nanotubes. *Nature* **1998**, *391*, 62−64.

(195) Novoselov, K. S.; Geim, A. K.; Morozov, S. V.; Jiang, D.; Zhang, Y.; Dubonos, S. V.; Grigorieva, I. V.; Firsov, A. A. Electric Field Effect in Atomically Thin Carbon Films. *Science* **2004**, *306*, 666−669.

(196) Balog, R.; Jorgensen, B.; Nilsson, L.; Andersen, M.; Rienks, E.; Bianchi, M.; Fanetti, M.; Laegsgaard, E.; Baraldi, A.; Lizzit, S.; et al. Bandgap Opening in Graphene Induced by Patterned Hydrogen Adsorption. *Nat. Mater.* **2010**, *9*, 315−319.

(197) Zhou, S. Y.; Gweon, G. H.; Fedorov, A. V.; First, P. N.; de Heer, W. A.; Lee, D. H.; Guinea, F.; Castro Neto, A. H.; Lanzara, A. Substrate-Induced Bandgap Opening in Epitaxial Graphene. *Nat. Mater.* **2007**, *6*, 770−775.

(198) Bacon, M.; Bradley, S. J.; Nann, T. Graphene Quantum Dots. *Part. Part. Syst. Charact.* **2014**, *31*, 415−428.

(199) Shen, J.; Zhu, Y.; Yang, X.; Zong, J.; Zhang, J.; Li, C. One-Pot Hydrothermal Synthesis of Graphene Quantum Dots Surface-Passivated by Polyethylene Glycol and Their Photoelectric Conversion under near-Infrared Light. *New J. Chem.* **2012**, *36*, 97−101.

(200) Sk, M. A.; Ananthanarayanan, A.; Huang, L.; Lim, K. H.; Chen, P. Revealing the Tunable Photoluminescence Properties of Graphene Quantum Dots. *J. Mater. Chem. C* **2014**, *2*, 6954−6960.

(201) Zhu, S.; Song, Y.; Zhao, X.; Shao, J.; Zhang, J.; Yang, B. The Photoluminescence Mechanism in Carbon Dots (Graphene Quantum Dots, Carbon Nanodots, and Polymer Dots): Current State and Future Perspective. *Nano Res.* **2015**, *8*, 355−381.

(202) Zhu, S.; Wang, L.; Zhou, N.; Zhao, X.; Song, Y.; Maharjan, S.; Zhang, J.; Lu, L.; Wang, H.; Yang, B. The Crosslink Enhanced Emission (CEE) in Non-Conjugated Polymer Dots: From the Photoluminescence Mechanism to the Cellular Uptake Mechanism and Internalization. *Chem. Commun.* **2014**, *50*, 13845−13848.

(203) Roy, P.; Chen, P.-C.; Periasamy, A. P.; Chen, Y.-N.; Chang, H.-T. Photoluminescent Carbon Nanodots: Synthesis, Physicochemical

Properties and Analytical Applications. *Mater. Today* **2015**, *18*, 447−458.

(204) Kwon, W.; Lee, G.; Do, S.; Joo, T.; Rhee, S.-W. Size-Controlled Soft-Template Synthesis of Carbon Nanodots toward Versatile Photoactive Materials. *Small* **2014**, *10*, 506−513.

(205) Cao, L.; Wang, X.; Meziani, M. J.; Lu, F.; Wang, H.; Luo, P. G.; Lin, Y.; Harruff, B. A.; Veca, L. M.; Murray, D.; et al. Carbon Dots for Multiphoton Bioimaging. *J. Am. Chem. Soc.* **2007**, *129*, 11318−11319.

(206) Hu, S.-L.; Niu, K.-Y.; Sun, J.; Yang, J.; Zhao, N.-Q.; Du, X.-W. One-Step Synthesis of Fluorescent Carbon Nanoparticles by Laser Irradiation. *J. Mater. Chem.* **2009**, *19*, 484−488.

(207) Li, H.; Kang, Z.; Liu, Y.; Lee, S.-T. Carbon Nanodots: Synthesis, Properties and Applications. *J. Mater. Chem.* **2012**, *22*, 24230−24253.

(208) Peng, H.; Travas-Sejdic, J. Simple Aqueous Solution Route to Luminescent Carbogenic Dots from Carbohydrates. *Chem. Mater.* **2009**, *21*, 5563−5565.

(209) Li, H.; He, X.; Liu, Y.; Huang, H.; Lian, S.; Lee, S.-T.; Kang, Z. One-Step Ultrasonic Synthesis of Water-Soluble Carbon Nanoparticles with Excellent Photoluminescent Properties. *Carbon* **2011**, *49*, 605−609.

(210) Zhu, H.; Wang, X.; Li, Y.; Wang, Z.; Yang, F.; Yang, X. Microwave Synthesis of Fluorescent Carbon Nanoparticles with Electrochemiluminescence Properties. *Chem. Commun.* **2009**, 5118−5120.

(211) Wang, X.; Qu, K.; Xu, B.; Ren, J.; Qu, X. Microwave Assisted One-Step Green Synthesis of Cell-Permeable Multicolor Photoluminescent Carbon Dots without Surface Passivation Reagents. *J. Mater. Chem.* **2011**, *21*, 2445−2450.

(212) Sun, Y.-P.; Zhou, B.; Lin, Y.; Wang, W.; Fernando, K. A. S.; Pathak, P.; Meziani, M. J.; Harruff, B. A.; Wang, X.; Wang, H.; et al. Quantum-Sized Carbon Dots for Bright and Colorful Photoluminescence. *J. Am. Chem. Soc.* **2006**, *128*, 7756−7757.

(213) Liu, F.; Jang, M.-H.; Ha, H. D.; Kim, J.-H.; Cho, Y.-H.; Seo, T. S. Facile Synthetic Method for Pristine Graphene Quantum Dots and Graphene Oxide Quantum Dots: Origin of Blue and Green Luminescence. *Adv. Mater.* **2013**, *25*, 3657−3662.

(214) Wang, L.; Zhu, S.-J.; Wang, H.-Y.; Qu, S.-N.; Zhang, Y.-L.; Zhang, J.-H.; Chen, Q.-D.; Xu, H.-L.; Han, W.; Yang, B.; et al. Common Origin of Green Luminescence in Carbon Nanodots and Graphene Quantum Dots. *ACS Nano* **2014**, *8*, 2541−2547.

(215) Hsu, P.-C.; Shih, Z.-Y.; Lee, C.-H.; Chang, H.-T. Synthesis and Analytical Applications of Photoluminescent Carbon Nanodots. *Green Chem.* **2012**, *14*, 917−920.

(216) Veinot, J. G. Synthesis, Surface Functionalization, and Properties of Freestanding Silicon Nanocrystals. *Chem. Commun.* **2006**, 4160−8.

(217) Vaughn, D. D., II; Schaak, R. E. Synthesis, Properties and Applications of Colloidal Germanium and Germanium-Based Nanomaterials. *Chem. Soc. Rev.* **2013**, *42*, 2861−2879.

(218) Tilley, R. D.; Warner, J. H.; Yamamoto, K.; I, M.; Fujimori, H. Micro-Emulsion Synthesis of Monodisperse Surface Stabilized Silicon Nanocrystals. *Chem. Commun.* **2005**, 1833−1835.

(219) Warner, J. H.; Hoshino, A.; Yamamoto, K.; Tilley, R. D. Water-Soluble Photoluminescent Silicon Quantum Dots. *Angew. Chem., Int. Ed.* **2005**, *44*, 4550−4554.

(220) Shiohara, A.; Prabakar, S.; Faramus, A.; Hsu, C. Y.; Lai, P. S.; Northcote, P. T.; Tilley, R. D. Sized Controlled Synthesis, Purification, and Cell Studies with Silicon Quantum Dots. *Nanoscale* **2011**, *3*, 3364−3370.

(221) Rosso-Vasic, M.; Spruijt, E.; van Lagen, B.; De Cola, L.; Zuilhof, H. Alkyl-Functionalized Oxide-Free Silicon Nanoparticles: Synthesis and Optical Properties. *Small* **2008**, *4*, 1835−1841.

(222) Shiohara, A.; Hanada, S.; Prabakar, S.; Fujioka, K.; Lim, T. H.; Yamamoto, K.; Northcote, P. T.; Tilley, R. D. Chemical Reactions on Surface Molecules Attached to Silicon Quantum Dots. *J. Am. Chem. Soc.* **2010**, *132*, 248−253.

(223) Zhong, Y.; Sun, X.; Wang, S.; Peng, F.; Bao, F.; Su, Y.; Li, Y.; Lee, S.-T.; He, Y. Facile, Large-Quantity Synthesis of Stable, Tunable-Color Silicon Nanoparticles and Their Application for Long-Term Cellular Imaging. *ACS Nano* **2015**, *9*, 5958−5967.

(224) Heath, J. R. A Liquid-Solution-Phase Synthesis of Crystalline Silicon. *Science* **1992**, *258*, 1131−3.

(225) Henderson, E. J.; Kelly, J. A.; Veinot, J. G. C. Influence of $HSiO_{1.5}$ Sol-Gel Polymer Structure and Composition on the Size and Luminescent Properties of Silicon Nanocrystals. *Chem. Mater.* **2009**, *21*, 5426−5434.

(226) Holmes, J. D.; Ziegler, K. J.; Doty, R. C.; Pell, L. E.; Johnston, K. P.; Korgel, B. A. Highly Luminescent Silicon Nanocrystals with Discrete Optical Transitions. *J. Am. Chem. Soc.* **2001**, *123*, 3743−3748.

(227) Li, Z. F.; Ruckenstein, E. Water-Soluble Poly(Acrylic Acid) Grafted Luminescent Silicon Nanoparticles and Their Use as Fluorescent Biological Staining Labels. *Nano Lett.* **2004**, *4*, 1463−1467.

(228) Littau, K. A.; Szajowski, P. J.; Müller, A. J.; Kortan, A. R.; Brus, L. E. A Luminescent Silicon Nanocrystal Colloid Via a High-Temperature Aerosol Reaction. *J. Phys. Chem.* **1993**, *97*, 1224−1230.

(229) Erogbogbo, F.; Yong, K. T.; Roy, I.; Xu, G. X.; Prasad, P. N.; Swihart, M. T. Biocompatible Luminescent Silicon Quantum Dots for Imaging of Cancer Cells. *ACS Nano* **2008**, *2*, 873−878.

(230) Wilcoxon, J. P.; Provencio, P. P.; Samara, G. A. Synthesis and Optical Properties of Colloidal Germanium Nanocrystals. *Phys. Rev. B: Condens. Matter Mater. Phys.* **2001**, *64*, 035417.

(231) Lee, H.; Kim, M. G.; Choi, C. H.; Sun, Y. K.; Yoon, C. S.; Cho, J. Surface-Stabilized Amorphous Germanium Nanoparticles for Lithium-Storage Material. *J. Phys. Chem. B* **2005**, *109*, 20719−20723.

(232) Carolan, D.; Doyle, H. Efficient One-Pot Synthesis of Monodisperse Alkyl-Terminated Colloidal Germanium Nanocrystals. *J. Nanopart. Res.* **2014**, *16*, 2721.

(233) Carolan, D.; Doyle, H. Germanium Nanocrystals as Luminescent Probes for Rapid, Sensitive and Label-Free Detection of Fe^{3+} Ions. *Nanoscale* **2015**, *7*, 5488−94.

(234) Carolan, D.; Doyle, H. Size Controlled Synthesis of Germanium Nanocrystals: Effect of Ge Precursor and Hydride Reducing Agent. *J. Nanomater.* **2015**, *2015*, 1−9.

(235) Carolan, D.; Doyle, H. Size and Emission Color Tuning in the Solution Phase Synthesis of Highly Luminescent Germanium Nanocrystals. *J. Mater. Chem. C* **2014**, *2*, 3562−3568.

(236) Zhang, Y. P.; Karatutlu, A.; Ersoy, O.; Little, W.; Cibin, G.; Dent, A.; Sapelkin, A. Structure and Effects of Annealing in Colloidal Matrix-Free Ge Quantum Dots. *J. Synchrotron Radiat.* **2015**, *22*, 105−112.

(237) Karatutlu, A.; Song, M. Y.; Wheeler, A. P.; Ersoy, O.; Little, W. R.; Zhang, Y. P.; Puech, P.; Boi, F. S.; Luklinska, Z.; Sapelkin, A. V. Synthesis and Structure of Free-Standing Germanium Quantum Dots and Their Application in Live Cell Imaging. *RSC Adv.* **2015**, *5*, 20566−20573.

(238) Kornowski, A.; Giersig, M.; Vogel, R.; Chemseddine, A.; Weller, H. Nanometer-Sized Colloidal Germanium Particles - Wet-Chemical Synthesis, Laser-Induced Crystallization and Particle Growth. *Adv. Mater.* **1993**, *5*, 634−636.

(239) Wu, J. H.; Sun, Y. G.; Zou, R. J.; Song, G. S.; Chen, Z. G.; Wang, C. R.; Hu, J. Q. One-Step Aqueous Solution Synthesis of Ge Nanocrystals from GeO_2 Powders. *CrystEngComm* **2011**, *13*, 3674−3677.

(240) Li, F.; Wang, J.; Sun, S.; Wang, H.; Tang, Z.; Nie, G. Facile Synthesis of pH-Sensitive Germanium Nanocrystals with High Quantum Yield for Intracellular Acidic Compartment Imaging. *Small* **2015**, *11*, 1954−61.

(241) Chiu, H. W.; Chervin, C. N.; Kauzlarich, S. M. Phase Changes in Ge Nanoparticles. *Chem. Mater.* **2005**, *17*, 4858−4864.

(242) Heath, J. R.; Shiang, J. J.; Alivisatos, A. P. Germanium Quantum Dots - Optical-Properties and Synthesis. *J. Chem. Phys.* **1994**, *101*, 1607−1615.

(243) Purkait, T. K.; Swarnakar, A. K.; De Los Reyes, G. B.; Hegmann, F. A.; Rivard, E.; Veinot, J. G. One-Pot Synthesis of Functionalized Germanium Nanocrystals from a Single Source Precursor. *Nanoscale* **2015**, *7*, 2241−4.

(244) Vaughn, D. D., II; Bondi, J. F.; Schaak, R. E. Colloidal Synthesis of Air-Stable Crystalline Germanium Nanoparticles with Tunable Sizes and Shapes. *Chem. Mater.* **2010**, *22*, 6103−6108.

(245) Shirahata, N. Solution-Processable White-Light-Emitting Germanium Nanocrystals. *J. Solid State Chem.* **2014**, *214*, 74−78.

(246) Xue, D. J.; Wang, J. J.; Wang, Y. Q.; Xin, S.; Guo, Y. G.; Wan, L. J. Facile Synthesis of Germanium Nanocrystals and Their Application in Organic-Inorganic Hybrid Photodetectors. *Adv. Mater.* **2011**, *23*, 3704−3707.

(247) Muthuswamy, E.; Zhao, J.; Tabatabaei, K.; Amador, M. M.; Holmes, M. A.; Osterloh, F. E.; Kauzlarich, S. M. Thiol-Capped Germanium Nanocrystals: Preparation and Evidence for Quantum Size Effects. *Chem. Mater.* **2014**, *26*, 2138−2146.

(248) Muthuswamy, E.; Iskandar, A. S.; Amador, M. M.; Kauzlarich, S. M. Facile Synthesis of Germanium Nanoparticles with Size Control: Microwave Versus Conventional Heating. *Chem. Mater.* **2013**, *25*, 1416−1422.

(249) Holmes, A. L.; Hütges, J.; Reckmann, A.; Muthuswamy, E.; Meerholz, K.; Kauzlarich, S. M. Probing Electronics as a Function of Size and Surface of Colloidal Germanium Nanocrystals. *J. Phys. Chem. C* **2015**, *119*, 5671−5678.

(250) Ruddy, D. A.; Johnson, J. C.; Smith, E. R.; Neale, N. R. Size and Bandgap Control in the Solution-Phase Synthesis of near-Infrared-Emitting Germanium Nanocrystals. *ACS Nano* **2010**, *4*, 7459−7466.

(251) Henderson, E. J.; Hessel, C. M.; Veinot, J. G. C. Synthesis and Photoluminescent Properties of Size-Controlled Germanium Nanocrystals from Phenyl Trichlorogermane-Derived Polymers. *J. Am. Chem. Soc.* **2008**, *130*, 3624−3632.

(252) Taylor, B. R.; Kauzlarich, S. M.; Delgado, G. R.; Lee, H. W. H. Solution Synthesis and Characterization of Quantum Confined Ge Nanoparticles. *Chem. Mater.* **1999**, *11*, 2493−2500.

(253) Gerion, D.; Zaitseva, N.; Saw, C.; Casula, M. F.; Fakra, S.; Van Buuren, T.; Galli, G. Solution Synthesis of Germanium Nanocrystals: Success and Open Challenges. *Nano Lett.* **2004**, *4*, 597−602.

(254) Lu, X. M.; Korgel, B. A.; Johnston, K. P. Synthesis of Germanium Nanocrystals in High Temperature Supercritical CO_2. *Nanotechnology* **2005**, *16*, S389−S394.

(255) Zaitseva, N.; Dai, Z. R.; Grant, C. D.; Harper, J.; Saw, C. Germanium Nanocrystals Synthesized in High-Boiling-Point Organic Solvents. *Chem. Mater.* **2007**, *19*, 5174−5178.

(256) Wu, H. P.; Ge, M. Y.; Yao, C. W.; Wang, Y. W.; Zeng, Y. W.; Wang, L. N.; Zhang, G. Q.; Jiang, J. Z. Blue Emission of Ge Nanocrystals Prepared by Thermal Decomposition. *Nanotechnology* **2006**, *17*, 5339−5343.

(257) Gerung, H.; Bunge, S. D.; Boyle, T. J.; Brinker, C. J.; Han, S. M. Anhydrous Solution Synthesis of Germanium Nanocrystals from the Germanium(II) Precursor Ge[N(SiMe$_3$)$_2$]$_2$. *Chem. Commun.* **2005**, 1914−1916.

(258) Sen, S. S.; Roesky, H. W.; Stern, D.; Henn, J.; Stalke, D. High Yield Access to Silylene RSiCl (R = PhC(N-*t*Bu)$_2$) and Its Reactivity toward Alkyne: Synthesis of Stable Disilacyclobutene. *J. Am. Chem. Soc.* **2010**, *132*, 1123−1126.

(259) Thimer, K. C.; Al-Rafia, S. M.; Ferguson, M. J.; McDonald, R.; Rivard, E. Donor/Acceptor Stabilization of Ge(II) Dihydride. *Chem. Commun.* **2009**, 7119−21.

(260) Swarnakar, A. K.; McDonald, S. M.; Deutsch, K. C.; Choi, P.; Ferguson, M. J.; McDonald, R.; Rivard, E. Application of the Donor-Acceptor Concept to Intercept Low Oxidation State Group 14 Element Hydrides Using a Wittig Reagent as a Lewis Base. *Inorg. Chem.* **2014**, *53*, 8662−8671.

(261) Wilcoxon, J. P.; Provencio, P. P.; Samara, G. A. Synthesis and Optical Properties of Colloidal Germanium Nanocrystals. *Phys. Rev. B: Condens. Matter Mater. Phys.* **2001**, *64*, 035417.

(262) Lianos, P.; Thomas, J. K. Cadmium-Sulfide of Small Dimensions Produced in Inverted Micelles. *Chem. Phys. Lett.* **1986**, *125*, 299−302.

(263) Pileni, M. P. Nanosized Particles Made in Colloidal Assemblies. *Langmuir* **1997**, *13*, 3266−3276.

(264) Wilcoxon, J. P.; Samara, G. A.; Provencio, P. N. Erratum: Optical and Electronic Properties of Si Nanoclusters Synthesized in Inverse Micelles [Phys. Rev. B 60, 2704 (1999)]. *Phys. Rev. B: Condens. Matter Mater. Phys.* **2007**, *76*, 199903.

(265) Tilley, R. D.; Warner, J. H.; Yamamoto, K.; Matsui, I.; Fujimori, H. Micro-Emulsion Synthesis of Monodisperse Surface Stabilized Silicon Nanocrystals. *Chem. Commun.* **2005**, 1833−1835.

(266) Yoffe, A. D. Low-Dimensional Systems: Quantum Size Effects and Electronic Properties of Semiconductor Microcrystallites (Zero-Dimensional Systems) and Some Quasi-Two-Dimensional Systems. *Adv. Phys.* **1993**, *42*, 173−262.

(267) Thuy, U. T. D.; Liem, N. Q.; Thanh, D. X.; Protiere, M.; Reiss, P. Optical Transitions in Polarized CdSe, CdSe/ZnSe, and CdSe/CdS/ZnS Quantum Dots Dispersed in Various Polar Solvents. *Appl. Phys. Lett.* **2007**, *91*, 241908.

(268) Wilcoxon, J. P.; Provencio, P. P.; Samara, G. A. Erratum: Synthesis and Optical Properties of Colloidal Germanium Nanocrystals [Phys. Rev. B 64, 035417 (2001)]. *Phys. Rev. B: Condens. Matter Mater. Phys.* **2007**, *76*, 199904.

(269) Bostedt, C.; van Buuren, T.; Willey, T. M.; Franco, N.; Terminello, L. J.; Heske, C.; Möller, T. Strong Quantum-Confinement Effects in the Conduction Band of Germanium Nanocrystals. *Appl. Phys. Lett.* **2004**, *84*, 4056−4058.

(270) Chou, N. H.; Oyler, K. D.; Motl, N. E.; Schaak, R. E. Colloidal Synthesis of Germanium Nanocrystals Using Room-Temperature Benchtop Chemistry. *Chem. Mater.* **2009**, *21*, 4105−4107.

(271) Mourdikoudis, S.; Liz-Marzán, L. M. Oleylamine in Nanoparticle Synthesis. *Chem. Mater.* **2013**, *25*, 1465−1476.

(272) Ghosh, B.; Ogawara, M.; Sakka, Y.; Shirahata, N. Reductant-Free Colloidal Synthesis of near-Ir Emitting Germanium Nanocrystals: Role of Primary Amine. *J. Nanosci. Nanotechnol.* **2014**, *14*, 2204−2210.

(273) Dag, Ö.; Henderson, E. J.; Ozin, G. A. Synthesis of Nanoamorphous Germanium and Its Transformation to Nanocrystalline Germanium. *Small* **2012**, *8*, 921−929.

(274) Hench, L. L.; West, J. K. The Sol-Gel Process. *Chem. Rev.* **1990**, *90*, 33−72.

(275) Hessel, C. M.; Henderson, E. J.; Veinot, J. G. C. Hydrogen Silsesquioxane: A Molecular Precursor for Nanocrystalline Si−SiO$_2$ Composites and Freestanding Hydride-Surface-Terminated Silicon Nanoparticles. *Chem. Mater.* **2006**, *18*, 6139−6146.

(276) Schäfer, H.; Eisenmann, B.; Müller, W. Zintl Phases: Transitions between Metallic and Ionic Bonding. *Angew. Chem., Int. Ed. Engl.* **1973**, *12*, 694−712.

(277) Bley, R. A.; Kauzlarich, S. M. A Low-Temperature Solution Phase Route for the Synthesis of Silicon Nanoclusters. *J. Am. Chem. Soc.* **1996**, *118*, 12461−12462.

(278) Neiner, D.; Chiu, H. W.; Kauzlarich, S. M. Low-Temperature Solution Route to Macroscopic Amounts of Hydrogen Terminated Silicon Nanoparticles. *J. Am. Chem. Soc.* **2006**, *128*, 11016−11017.

(279) Atkins, T. M.; Cassidy, M. C.; Lee, M.; Ganguly, S.; Marcus, C. M.; Kauzlarich, S. M. Synthesis of Long T1 Silicon Nanoparticles for Hyperpolarized 29Si Magnetic Resonance Imaging. *ACS Nano* **2013**, *7*, 1609−1617.

(280) Wang, L.; Lin, N.; Zhou, J.; Zhu, Y.; Qian, Y. Silicon Nanoparticles Obtained Via a Low Temperature Chemical ″Metathesis″ Synthesis Route and Their Lithium-Ion Battery Properties. *Chem. Commun.* **2015**, *51*, 2345−2348.

(281) Yang, C. S.; Kauzlarich, S. M.; Wang, Y. C. Synthesis and Characterization of Germanium/Si-Alkyl and Germanium/Silica Core-Shell Quantum Dots. *Chem. Mater.* **1999**, *11*, 3666−3670.

(282) Wilson, W. L.; Szajowski, P. F.; Brus, L. E. Quantum Confinement in Size-Selected, Surface-Oxidized Silicon Nanocrystals. *Science* **1993**, *262*, 1242−1244.

(283) Heath, J. R. Covalency in Semiconductor Quantum Dots. *Chem. Soc. Rev.* **1998**, *27*, 65−71.

(284) Guo, Q.; Kato, O.; Yoshida, A. Thermal Stability of Indium Nitride Single Crystal Films. *J. Appl. Phys.* **1993**, *73*, 7969−7971.

(285) Kuno, M. *Introductory Nanoscience*; Garland Science: New York, 2011.

(286) Lucovsky, G.; Martin, R. M.; Burstein, E. Localized Effective Charges in Diatomic Crystals. *Phys. Rev. B* **1971**, *4*, 1367−1374.

(287) Rogach, A. *Semiconductor Nanocrystal Quantum Dots: Synthesis, Assembly, Spectroscopy and Applications*; Springer: New York, 2008.

(288) Yasushi, N.; Yoshiki, S.; Tomohiro, Y. Rf-Molecular Beam Epitaxy Growth and Properties of InN and Related Alloys. *Jpn. J. Appl. Phys.* **2003**, *42*, 2549.

(289) Nakamura, S. The Roles of Structural Imperfections in Ingan-Based Blue Light-Emitting Diodes and Laser Diodes. *Science* **1998**, *281*, 956−961.

(290) Bai, Y.-J.; Liu, Z.-G.; Xu, X.-G.; Cui, D.-L.; Hao, X.-P.; Feng, X.; Wang, Q.-L. Preparation of InN Nanocrystals by Solvo-Thermal Method. *J. Cryst. Growth* **2002**, *241*, 189−192.

(291) Wu, C.; Li, T.; Lei, L.; Hu, S.; Liu, Y.; Xie, Y. Indium Nitride from Indium Iodide at Low Temperatures: Synthesis and Their Optical Properties. *New J. Chem.* **2005**, *29*, 1610−1615.

(292) Xiao, J.; Xie, Y.; Tang, R.; Luo, W. Benzene Thermal Conversion to Nanocrystalline Indium Nitride from Sulfide at Low Temperature. *Inorg. Chem.* **2003**, *42*, 107−111.

(293) Xiong, Y.; Xie, Y.; Li, Z.; Li, X.; Zhang, R. Aqueous Synthesis of Group IIIA Nitrides at Low Temperature. *New J. Chem.* **2004**, *28*, 214−217.

(294) Palomaki, P. K. B.; Miller, E. M.; Neale, N. R. Control of Plasmonic and Interband Transitions in Colloidal Indium Nitride Nanocrystals. *J. Am. Chem. Soc.* **2013**, *135*, 14142−14150.

(295) Greenberg, M. R.; Chen, W.; Pulford, B. N.; Smolyakov, G. A.; Jiang, Y.-B.; Bunge, S. D.; Boyle, T. J.; Osinski, M. *Proc. SPIE* **2005**, 68−76.

(296) Chen, Z.; Li, Y.; Cao, C.; Zhao, S.; Fathololoumi, S.; Mi, Z.; Xu, X. Large-Scale Cubic Inn Nanocrystals by a Combined Solution- and Vapor-Phase Method under Silica Confinement. *J. Am. Chem. Soc.* **2012**, *134*, 780−783.

(297) Xie, Y.; Qian, Y.; Wang, W.; Zhang, S.; Zhang, Y. A Benzene-Thermal Synthetic Route to Nanocrystalline Gan. *Science* **1996**, *272*, 1926−1927.

(298) Sardar, K.; Rao, C. N. R. New Solvothermal Routes for Gan Nanocrystals. *Adv. Mater.* **2004**, *16*, 425−429.

(299) Mićić, O. I.; Ahrenkiel, S. P.; Bertram, D.; Nozik, A. J. Synthesis, Structure, and Optical Properties of Colloidal GaN Quantum Dots. *Appl. Phys. Lett.* **1999**, *75*, 478−480.

(300) Janik, J. F.; Wells, R. L. Gallium Imide, {Ga(NH)$_{3/2}$}$_n$, a New Polymeric Precursor for Gallium Nitride Powders. *Chem. Mater.* **1996**, *8*, 2708−2711.

(301) Pan, G.; Kordesch, M. E.; Van Patten, P. G. New Pyrolysis Route to Gan Quantum Dots. *Chem. Mater.* **2006**, *18*, 3915−3917.

(302) Manz, A.; Birkner, A.; Kolbe, M.; Fischer, R. A. Solution Synthesis of Colloidal Gallium Nitride at Unprecedented Low Temperatures. *Adv. Mater.* **2000**, *12*, 569−573.

(303) Guzelian, A. A.; Katari, J. E. B.; Kadavanich, A. V.; Banin, U.; Hamad, K.; Juban, E.; Alivisatos, A. P.; Wolters, R. H.; Arnold, C. C.; Heath, J. R. Synthesis of Size-Selected, Surface-Passivated Inp Nanocrystals. *J. Phys. Chem.* **1996**, *100*, 7212−7219.

(304) Mićić, O. I.; Sprague, J.; Lu, Z.; Nozik, A. J. Highly Efficient Band-Edge Emission from InP Quantum Dots. *Appl. Phys. Lett.* **1996**, *68*, 3150−3152.

(305) Adam, S.; Talapin, D. V.; Borchert, H.; Lobo, A.; McGinley, C.; de Castro, A. R. B.; Haase, M.; Weller, H.; Möller, T. The Effect of Nanocrystal Surface Structure on the Luminescence Properties: Photoemission Study of HF-Etched InP Nanocrystals. *J. Chem. Phys.* **2005**, *123*, 084706.

(306) Mićić, O. I.; Smith, B. B.; Nozik, A. J. Core-Shell Quantum Dots of Lattice-Matched ZnCdSe$_2$ Shells on InP Cores: Experiment and Theory. *J. Phys. Chem. B* **2000**, *104*, 12149−12156.

(307) Haubold, S.; Haase, M.; Kornowski, A.; Weller, H. Strongly Luminescent InP/ZnS Core−Shell Nanoparticles. *ChemPhysChem* **2001**, *2*, 331−334.

(308) Lim, J.; Park, M.; Bae, W. K.; Lee, D.; Lee, S.; Lee, C.; Char, K. Highly Efficient Cadmium-Free Quantum Dot Light-Emitting Diodes

(309) Lim, J.; Bae, W. K.; Lee, D.; Nam, M. K.; Jung, J.; Lee, C.; Char, K.; Lee, S. InP@ZnSeS, Core@Composition Gradient Shell Quantum Dots with Enhanced Stability. *Chem. Mater.* **2011**, *23*, 4459−4463.

(310) Kim, S.; Kim, T.; Kang, M.; Kwak, S. K.; Yoo, T. W.; Park, L. S.; Yang, I.; Hwang, S.; Lee, J. E.; Kim, S. K.; et al. Highly Luminescent InP/GaP/ZnS Nanocrystals and Their Application to White Light-Emitting Diodes. *J. Am. Chem. Soc.* **2012**, *134*, 3804−3809.

(311) Thuy, U. T. D.; Reiss, P.; Liem, N. Q. Luminescence Properties of in(Zn)P Alloy Core/ZnS Shell Quantum Dots. *Appl. Phys. Lett.* **2010**, *97*, 193104.

(312) Thuy, U. T. D.; Maurice, A.; Liem, N. Q.; Reiss, P. Europium Doped in(Zn)P/ZnS Colloidal Quantum Dots. *Dalton Trans.* **2013**, *42*, 12606.

(313) Li, L.; Reiss, P. One-Pot Synthesis of Highly Luminescent InP/ZnS Nanocrystals without Precursor Injection. *J. Am. Chem. Soc.* **2008**, *130*, 11588−11589.

(314) Huang, K.; Demadrille, R.; Silly, M. G.; Sirotti, F.; Reiss, P.; Renault, O. Internal Structure of InP/ZnS Nanocrystals Unraveled by High-Resolution Soft X-Ray Photoelectron Spectroscopy. *ACS Nano* **2010**, *4*, 4799−4805.

(315) Xie, R.; Battaglia, D.; Peng, X. Colloidal InP Nanocrystals as Efficient Emitters Covering Blue to near-Infrared. *J. Am. Chem. Soc.* **2007**, *129*, 15432−15433.

(316) Xu, S.; Ziegler, J.; Nann, T. Rapid Synthesis of Highly Luminescent InP and InP/ZnS Nanocrystals. *J. Mater. Chem.* **2008**, *18*, 2653−2656.

(317) Battaglia, D.; Peng, X. Formation of High Quality InP and InAs Nanocrystals in a Noncoordinating Solvent. *Nano Lett.* **2002**, *2*, 1027−1030.

(318) Protiere, M.; Reiss, P. Amine-Induced Growth of an In$_2$O$_3$ Shell on Colloidal InP Nanocrystals. *Chem. Commun.* **2007**, 2417−2419.

(319) Li, L.; Protiere, M.; Reiss, P. Economic Synthesis of High Quality Inp Nanocrystals Using Calcium Phosphide as the Phosphorus Precursor. *Chem. Mater.* **2008**, *20*, 2621−2623.

(320) Cros-Gagneux, A.; Delpech, F.; Nayral, C.; Cornejo, A.; Coppel, Y.; Chaudret, B. Surface Chemistry of InP Quantum Dots: A Comprehensive Study. *J. Am. Chem. Soc.* **2010**, *132*, 18147−18157.

(321) Virieux, H.; Le Troedec, M.; Cros-Gagneux, A.; Ojo, W.-S.; Delpech, F.; Nayral, C.; Martinez, H.; Chaudret, B. InP/ZnS Nanocrystals: Coupling NMR and XPS for Fine Surface and Interface Description. *J. Am. Chem. Soc.* **2012**, *134*, 19701−19708.

(322) Allen, P. M.; Walker, B. J.; Bawendi, M. G. Mechanistic Insights into the Formation of InP Quantum Dots. *Angew. Chem., Int. Ed.* **2010**, *49*, 760−762.

(323) Gary, D. C.; Cossairt, B. M. Role of Acid in Precursor Conversion During InP Quantum Dot Synthesis. *Chem. Mater.* **2013**, *25*, 2463−2469.

(324) Joung, S.; Yoon, S.; Han, C.-S.; Kim, Y.; Jeong, S. Facile Synthesis of Uniform Large-Sized InP Nanocrystal Quantum Dots Using Tris(*Tert*-Butyldimethylsilyl)Phosphine. *Nanoscale Res. Lett.* **2012**, *7*, 93.

(325) Harris, D. K.; Bawendi, M. G. Improved Precursor Chemistry for the Synthesis of III-V Quantum Dots. *J. Am. Chem. Soc.* **2012**, *134*, 20211−20213.

(326) Song, W.-S.; Lee, H.-S.; Lee, J.; Jang, D.; Choi, Y.; Choi, M.; Yang, H. Amine-Derived Synthetic Approach to Color-Tunable InP/ZnS Quantum Dots with High Fluorescent Qualities. *J. Nanopart. Res.* **2013**, *15*, 1−10.

(327) Yang, S. J.; Oh, J. H.; Kim, S.; Yang, H.; Do, Y. R. Realization of InP/ZnS Quantum Dots for Green, Amber and Red Down-Converted Leds and Their Color-Tunable, Four-Package White Leds. *J. Mater. Chem. C* **2015**, *3*, 3582−3591.

(328) Jang, E.-P.; Yang, H. Utilization of Solvothermally Grown InP/ZnS Quantum Dots as Wavelength Converters for Fabrication of

White Light-Emitting Diodes. *J. Nanosci. Nanotechnol.* **2013**, *13*, 6011−6015.

(329) Tessier, M. D.; Dupont, D.; De Nolf, K.; De Roo, J.; Hens, Z. Economic and Size-Tunable Synthesis of InP/ZnE (E = S, Se) Colloidal Quantum Dots. *Chem. Mater.* **2015**, *27*, 4893−4898.

(330) Green, M. Solution Routes to III-V Semiconductor Quantum Dots. *Curr. Opin. Solid State Mater. Sci.* **2002**, *6*, 355−363.

(331) Fan, G.; Wang, C.; Fang, J. Solution-Based Synthesis of III-V Quantum Dots and Their Applications in Gas Sensing and Bio-Imaging. *Nano Today* **2014**, *9*, 69−84.

(332) Liu, Z.; Kumbhar, A.; Xu, D.; Zhang, J.; Sun, Z.; Fang, J. Coreduction Colloidal Synthesis of III−V Nanocrystals: The Case of InP. *Angew. Chem.* **2008**, *120*, 3596−3598.

(333) Tamang, S.; Beaune, G.; Texier, I.; Reiss, P. Aqueous Phase Transfer of InP/ZnS Nanocrystals Conserving Fluorescence and High Colloidal Stability. *ACS Nano* **2011**, *5*, 9392−9402.

(334) Lauth, J.; Strupeit, T.; Kornowski, A.; Weller, H. A Transmetalation Route for Colloidal GaAs Nanocrystals and Additional III-V Semiconductor Materials. *Chem. Mater.* **2013**, *25*, 1377−1383.

(335) Mac Dougall, J. E.; Eckert, H.; Stucky, G. D.; Herron, N.; Wang, Y.; Moller, K.; Bein, T.; Cox, D. Synthesis and Characterization of Group III-V Semiconductor Clusters: Gallium Phosphide GaP in Zeolite Y. *J. Am. Chem. Soc.* **1989**, *111*, 8006−8007.

(336) Mićić, O. I.; Sprague, J. R.; Curtis, C. J.; Jones, K. M.; Machol, J. L.; Nozik, A. J.; Giessen, H.; Fluegel, B.; Mohs, G.; Peyghambarian, N. Synthesis and Characterization of InP, GaP, and GaInP₂ Quantum Dots. *J. Phys. Chem.* **1995**, *99*, 7754−7759.

(337) Beberwyck, B. J.; Alivisatos, A. P. Ion Exchange Synthesis of III-V Nanocrystals. *J. Am. Chem. Soc.* **2012**, *134*, 19977−19980.

(338) Guzelian, A. A.; Banin, U.; Kadavanich, A. V.; Peng, X.; Alivisatos, A. P. Colloidal Chemical Synthesis and Characterization of InAs Nanocrystal Quantum Dots. *Appl. Phys. Lett.* **1996**, *69*, 1432−1434.

(339) Xie, R.; Peng, X. Synthetic Scheme for High-Quality InAs Nanocrystals Based on Self-Focusing and One-Pot Synthesis of InAs-Based Core−Shell Nanocrystals. *Angew. Chem., Int. Ed.* **2008**, *47*, 7677−7680.

(340) Clark, M. D.; Kumar, S. K.; Owen, J. S.; Chan, E. M. Focusing Nanocrystal Size Distributions Via Production Control. *Nano Lett.* **2011**, *11*, 1976−1980.

(341) Baldan, A. Review Progress in Ostwald Ripening Theories and Their Applications to Nickel-Base Superalloys Part I: Ostwald Ripening Theories. *J. Mater. Sci.* **2002**, *37*, 2171−2202.

(342) Thessing, J.; Qian, J.; Chen, H.; Pradhan, N.; Peng, X. Interparticle Influence on Size/Size Distribution Evolution of Nanocrystals. *J. Am. Chem. Soc.* **2007**, *129*, 2736−2737.

(343) Chen, Y.; Johnson, E.; Peng, X. Formation of Monodisperse and Shape-Controlled MnO Nanocrystals in Non-Injection Synthesis: Self-Focusing Via Ripening. *J. Am. Chem. Soc.* **2007**, *129*, 10937−10947.

(344) Cao; Banin, U. Growth and Properties of Semiconductor Core/Shell Nanocrystals with InAs Cores. *J. Am. Chem. Soc.* **2000**, *122*, 9692−9702.

(345) Zimmer, J. P.; Kim, S.-W.; Ohnishi, S.; Tanaka, E.; Frangioni, J. V.; Bawendi, M. G. Size Series of Small Indium Arsenide-Zinc Selenide Core-Shell Nanocrystals and Their Application to in Vivo Imaging. *J. Am. Chem. Soc.* **2006**, *128*, 2526−2527.

(346) Kim, S.-W.; Zimmer, J. P.; Ohnishi, S.; Tracy, J. B.; Frangioni, J. V.; Bawendi, M. G. Engineering InAsₓP₁₋ₓ/InP/ZnSe III-V Alloyed Core/Shell Quantum Dots for the near-Infrared. *J. Am. Chem. Soc.* **2005**, *127*, 10526−10532.

(347) Xie, R.; Chen, K.; Chen, X.; Peng, X. InAs/InP/ZnSe Core/Shell/Shell Quantum Dots as near-Infrared Emitters: Bright, Narrow-Band, Non-Cadmium Containing, and Biocompatible. *Nano Res.* **2008**, *1*, 457−464.

(348) Weissleder, R. A Clearer Vision for in Vivo Imaging. *Nat. Biotechnol.* **2001**, *19*, 316−317.

(349) Allen, P. M.; Liu, W.; Chauhan, V. P.; Lee, J.; Ting, A. Y.; Fukumura, D.; Jain, R. K.; Bawendi, M. G. InAs(ZnCdS) Quantum Dots Optimized for Biological Imaging in the near-Infrared. *J. Am. Chem. Soc.* **2010**, *132*, 470−471.

(350) Choi, H. S.; Liu, W.; Misra, P.; Tanaka, E.; Zimmer, J. P.; Ipe, B. I.; Bawendi, M. G.; Frangioni, J. V. Renal Clearance of Quantum Dots. *Nat. Biotechnol.* **2007**, *25*, 1165−1170.

(351) Schaller, R. D.; Pietryga, J. M.; Klimov, V. I. Carrier Multiplication in Inas Nanocrystal Quantum Dots with an Onset Defined by the Energy Conservation Limit. *Nano Lett.* **2007**, *7*, 3469−3476.

(352) Evans, C. M.; Castro, S. L.; Worman, J. J.; Raffaelle, R. P. Synthesis and Use of Tris(Trimethylsilyl)Antimony for the Preparation of InSb Quantum Dots. *Chem. Mater.* **2008**, *20*, 5727−5730.

(353) Zhang, J.; Zhang, D. Synthesis and Growth Kinetics of High Quality Inas Nanocrystals Using in Situ Generated AsH₃ as the Arsenic Source. *CrystEngComm* **2010**, *12*, 591−594.

(354) Maurice, A.; Haro, M. L.; Hyot, B.; Reiss, P. Synthesis of Colloidal Indium Antimonide Nanocrystals Using Stibine. *Part. Part. Syst. Charact.* **2013**, *30*, 828−831.

(355) Liu, W.; Chang, A. Y.; Schaller, R. D.; Talapin, D. V. Colloidal InSb Nanocrystals. *J. Am. Chem. Soc.* **2012**, *134*, 20258−20261.

(356) Yarema, M.; Kovalenko, M. V. Colloidal Synthesis of InSb Nanocrystals with Controlled Polymorphism Using Indium and Antimony Amides. *Chem. Mater.* **2013**, *25*, 1788−1792.

(357) Tamang, S.; Kim, K.; Choi, H.; Kim, Y.; Jeong, S. Synthesis of Colloidal InSb Nanocrystals Via in Situ Activation of InCl₃. *Dalton Trans.* **2015**, *44*, 16923−16928.

(358) García-Rodríguez, R.; Hendricks, M. P.; Cossairt, B. M.; Liu, H.; Owen, J. S. Conversion Reactions of Cadmium Chalcogenide Nanocrystal Precursors. *Chem. Mater.* **2013**, *25*, 1233−1249.

(359) Capps, K. B.; Wixmerten, B.; Bauer, A.; Hoff, C. D. Thermochemistry of Sulfur Atom Transfer. Enthalpies of Reaction of Phosphines with Sulfur, Selenium, and Tellurium, and of Desulfurization of Triphenylarsenic Sulfide, Triphenylantimony Sulfide, and Benzyl Trisulfide. *Inorg. Chem.* **1998**, *37*, 2861−2864.

(360) Zingaro, R. A.; McGlothin, R. E. Some Phosphines, Phosphine Sulfides, and Phosphine Selenides. *J. Chem. Eng. Data* **1963**, *8*, 226−229.

(361) Zingaro, R. A.; Steeves, B. H.; Irgolic, K. Phosphine Tellurides. *J. Organomet. Chem.* **1965**, *4*, 320−323.

(362) García-Rodríguez, R.; Liu, H. Mechanistic Study of the Synthesis of CdSe Nanocrystals: Release of Selenium. *J. Am. Chem. Soc.* **2012**, *134*, 1400−1403.

(363) Steigerwald, M. L.; Sprinkle, C. R. Application of Phosphine Tellurides to the Preparation of Group II-VI (2−16) Semiconductor Materials. *Organometallics* **1988**, *7*, 245−246.

(364) Thomson, J. W.; Nagashima, K.; Macdonald, P. M.; Ozin, G. A. From Sulfur−Amine Solutions to Metal Sulfide Nanocrystals: Peering into the Oleylamine−Sulfur Black Box. *J. Am. Chem. Soc.* **2011**, *133*, 5036−5041.

(365) Li, Z.; Ji, Y.; Xie, R.; Grisham, S. Y.; Peng, X. Correlation of CdS Nanocrystal Formation with Elemental Sulfur Activation and Its Implication in Synthetic Development. *J. Am. Chem. Soc.* **2011**, *133*, 17248−17256.

(366) Tamang, S.; Lincheneau, C.; Hermans, Y.; Jeong, S.; Reiss, P. Chemistry of InP Nanocrystal Syntheses. *Chem. Mater.* **2016**, *28*, 2491−2506.

(367) Jasieniak, J.; Bullen, C.; van Embden, J.; Mulvaney, P. Phosphine-Free Synthesis of CdSe Nanocrystals. *J. Phys. Chem. B* **2005**, *109*, 20665−20668.

(368) Bullen, C.; van Embden, J.; Jasieniak, J.; Cosgriff, J. E.; Mulder, R. J.; Rizzardo, E.; Gu, M.; Raston, C. L. High Activity Phosphine-Free Selenium Precursor Solution for Semiconductor Nanocrystal Growth. *Chem. Mater.* **2010**, *22*, 4135−4143.

(369) Aldakov, D.; Lefrancois, A.; Reiss, P. Ternary and Quaternary Metal Chalcogenide Nanocrystals: Synthesis, Properties and Applications. *J. Mater. Chem. C* **2013**, *1*, 3756−3776.

(370) Yang, Z.; Smetana, A. B.; Sorensen, C. M.; Klabunde, K. J. Synthesis and Characterization of a New Tiara Pd(II) Thiolate Complex, $[Pd(SC_{12}H_{25})_2]_6$, and Its Solution-Phase Thermolysis to Prepare Nearly Monodisperse Palladium Sulfide Nanoparticles. *Inorg. Chem.* **2007**, *46*, 2427–2431.

(371) Choi, S.-H.; An, K.; Kim, E.-G.; Yu, J. H.; Kim, J. H.; Hyeon, T. Simple and Generalized Synthesis of Semiconducting Metal Sulfide Nanocrystals. *Adv. Funct. Mater.* **2009**, *19*, 1645–1649.

(372) Querner, C.; Reiss, P.; Bleuse, J.; Pron, A. Chelating Ligands for Nanocrystals' Surface Functionalization. *J. Am. Chem. Soc.* **2004**, *126*, 11574–11582.

(373) Zhang, H.; Hyun, B.-R.; Wise, F. W.; Robinson, R. D. A Generic Method for Rational Scalable Synthesis of Monodisperse Metal Sulfide Nanocrystals. *Nano Lett.* **2012**, *12*, 5856–5860.

(374) Chen, O.; Chen, X.; Yang, Y.; Lynch, J.; Wu, H.; Zhuang, J.; Cao, Y. C. Synthesis of Metal–Selenide Nanocrystals Using Selenium Dioxide as the Selenium Precursor. *Angew. Chem., Int. Ed.* **2008**, *47*, 8638–8641.

(375) Detty, M. R.; Seidler, M. D. Bis(Trialkylsilyl) Chalcogenides. 1. Preparation and Reduction of Group Via Oxides. *J. Org. Chem.* **1982**, *47*, 1354–1356.

(376) Brutchey, R. L. Diorganyl Dichalcogenides as Useful Synthons for Colloidal Semiconductor Nanocrystals. *Acc. Chem. Res.* **2015**, *48*, 2918–2926.

(377) Schlecht, S.; Budde, M.; Kienle, L. Nanocrystalline Tin as a Preparative Tool: Synthesis of Unprotected Nanoparticles of SnTe and SnSe and a New Route to $(PhSe)_4Sn$. *Inorg. Chem.* **2002**, *41*, 6001–6005.

(378) Guo, Y.; Alvarado, S. R.; Barclay, J. D.; Vela, J. Shape-Programmed Nanofabrication: Understanding the Reactivity of Dichalcogenide Precursors. *ACS Nano* **2013**, *7*, 3616–3626.

(379) Ekimov, A. I.; Onushchenko, A. A. Quantum Size Effect in Three-Dimensional Microscopic Semiconductor Crystals. *JETP Lett.* **1981**, *34*, 345–349.

(380) Efros, A. L.; Efros, A. L. Interband Absorption of Light in a Semiconductor Sphere. *Sov. Phys.-Semicond.* **1982**, *16*, 772–775.

(381) Brus, L. E. Electron–Electron and Electron-Hole Interactions in Small Semiconductor Crystallites: The Size Dependence of the Lowest Excited Electronic State. *J. Chem. Phys.* **1984**, *80*, 4403–4409.

(382) Anikeeva, P. O.; Halpert, J. E.; Bawendi, M. G.; Bulović, V. Quantum Dot Light-Emitting Devices with Electroluminescence Tunable over the Entire Visible Spectrum. *Nano Lett.* **2009**, *9*, 2532–2536.

(383) Choi, J. J.; Lim, Y.-F.; Santiago-Berrios, M. E. B.; Oh, M.; Hyun, B.-R.; Sun, L.; Bartnik, A. C.; Goedhart, A.; Malliaras, G. G.; Abruña, H. D.; Wise, F. W.; Hanrath, T. Pbse Nanocrystal Excitonic Solar Cells. *Nano Lett.* **2009**, *9*, 3749–3755.

(384) Sukhovatkin, V.; Hinds, S.; Brzozowski, L.; Sargent, E. H. Colloidal Quantum-Dot Photodetectors Exploiting Multiexciton Generation. *Science* **2009**, *324*, 1542–1544.

(385) Konstantatos, G.; Howard, I.; Fischer, A.; Hoogland, S.; Clifford, J.; Klem, E.; Levina, L.; Sargent, E. H. Ultrasensitive Solution-Cast Quantum Dot Photodetectors. *Nature* **2006**, *442*, 180–183.

(386) Murray, C. B.; Kagan, C. R.; Bawendi, M. G. Self-Organization of CdSe Nanocrystallites into Three-Dimensional Quantum Dot Superlattices. *Science* **1995**, *270*, 1335–1338.

(387) Singh, N.; Mulrooney, R. C.; Kaur, N.; Callan, J. F. A Nanoparticle Based Chromogenic Chemosensor for the Simultaneous Detection of Multiple Analytes. *Chem. Commun.* **2008**, 4900–4902.

(388) Chan, W. C. W.; Nie, S. Quantum Dot Bioconjugates for Ultrasensitive Nonisotopic Detection. *Science* **1998**, *281*, 2016–2018.

(389) Medintz, I. L.; Uyeda, H. T.; Goldman, E. R.; Mattoussi, H. Quantum Dot Bioconjugates for Imaging, Labelling and Sensing. *Nat. Mater.* **2005**, *4*, 435–446.

(390) Dubertret, B.; Skourides, P.; Norris, D. J.; Noireaux, V.; Brivanlou, A. H.; Libchaber, A. In Vivo Imaging of Quantum Dots Encapsulated in Phospholipid Micelles. *Science* **2002**, *298*, 1759–1762.

(391) Chestnoy, N.; Hull, R.; Brus, L. E. Higher Excited Electronic States in Clusters of ZnSe, CdSe, and ZnS: Spin-Orbit, Vibronic, and Relaxation Phenomena. *J. Chem. Phys.* **1986**, *85*, 2237–2242.

(392) Shavel, A.; Gaponik, N.; Eychmüller, A. Efficient UV-Blue Photoluminescing Thiol-Stabilized Water-Soluble Alloyed ZnSe(S) Nanocrystals. *J. Phys. Chem. B* **2004**, *108*, 5905–5908.

(393) Quinlan, F. T.; Kuther, J.; Tremel, W.; Knoll, W.; Risbud, S.; Stroeve, P. Reverse Micelle Synthesis and Characterization of ZnSe Nanoparticles. *Langmuir* **2000**, *16*, 4049–4051.

(394) Georgios, N. K.; Nga-Leung, L.; Robert, M.; Athos, P.; Paschalis, A.; Mountziaris, T. J. Water-Based Synthesis of ZnSe Nanostructures Using Amphiphilic Block Copolymer Stabilized Lyotropic Liquid Crystals as Templates. *Nanotechnology* **2006**, *17*, 3121.

(395) Moon, G. D.; Ko, S.; Min, Y.; Zeng, J.; Xia, Y.; Jeong, U. Chemical Transformations of Nanostructured Materials. *Nano Today* **2011**, *6*, 186–203.

(396) Li, H.; Zanella, M.; Genovese, A.; Povia, M.; Falqui, A.; Giannini, C.; Manna, L. Sequential Cation Exchange in Nanocrystals: Preservation of Crystal Phase and Formation of Metastable Phases. *Nano Lett.* **2011**, *11*, 4964–4970.

(397) Raouf Hosseini, M.; Nasiri Sarvi, M. Recent Achievements in the Microbial Synthesis of Semiconductor Metal Sulfide Nanoparticles. *Mater. Sci. Semicond. Process.* **2015**, *40*, 293–301.

(398) Joo, J.; Na, H. B.; Yu, T.; Yu, J. H.; Kim, Y. W.; Wu, F.; Zhang, J. Z.; Hyeon, T. Generalized and Facile Synthesis of Semiconducting Metal Sulfide Nanocrystals. *J. Am. Chem. Soc.* **2003**, *125*, 11100–11105.

(399) Shen, S.; Zhang, Y.; Peng, L.; Xu, B.; Du, Y.; Deng, M.; Xu, H.; Wang, Q. Generalized Synthesis of Metal Sulfide Nanocrystals from Single-Source Precursors: Size, Shape and Chemical Composition Control and Their Properties. *CrystEngComm* **2011**, *13*, 4572–4579.

(400) Onwudiwe, D. C.; Strydom, C. A. The Bipyridine Adducts of n-Phenyldithiocarbamato Complexes of Zn(II) and Cd(II); Synthesis, Spectral, Thermal Decomposition Studies and Use as Precursors for ZnS and CdS Nanoparticles. *Spectrochim. Acta, Part A* **2015**, *135*, 1080–1089.

(401) Pradhan, N.; Katz, B.; Efrima, S. Synthesis of High-Quality Metal Sulfide Nanoparticles from Alkyl Xanthate Single Precursors in Alkylamine Solvents. *J. Phys. Chem. B* **2003**, *107*, 13843–13854.

(402) Kuzuya, T.; Tai, Y.; Yamamuro, S.; Hihara, T.; Peng, D. L.; Sumiyama, K. Synthesis of Zinc Sulfide Nanocrystals and Fabrication of Nanocrystal Superlattice. *Mater. Trans.* **2004**, *45*, 2650–2652.

(403) Niu, J.; Xu, W.; Shen, H.; Li, S.; Wang, H.; Li, L. S. Synthesis of CdS, ZnS and CdS/ZnS Core/Shell Nanocrystals Using Dodecanthiol. *Bull. Korean Chem. Soc.* **2012**, *33*, 393–397.

(404) Puglisi, A.; Mondini, S.; Cenedese, S.; Ferretti, A. M.; Santo, N.; Ponti, A. Monodisperse Octahedral Α-MnS and MnO Nanoparticles by the Decomposition of Manganese Oleate in the Presence of Sulfur. *Chem. Mater.* **2010**, *22*, 2804–2813.

(405) Jun, Y.-w.; Jung, Y.-y.; Cheon, J. Architectural Control of Magnetic Semiconductor Nanocrystals. *J. Am. Chem. Soc.* **2002**, *124*, 615–619.

(406) Lotfipour, M.; Machani, T.; Rossi, D. P.; Plass, K. E. A-Chalcocite Nanoparticle Synthesis and Stability. *Chem. Mater.* **2011**, *23*, 3032–3038.

(407) Hsu, S.-W.; Ngo, C.; Bryks, W.; Tao, A. R. Shape Focusing During the Anisotropic Growth of CuS Triangular Nanoprisms. *Chem. Mater.* **2015**, *27*, 4957–4963.

(408) Larsen, T. H.; Sigman, M.; Ghezelbash, A.; Doty, R. C.; Korgel, B. A. Solventless Synthesis of Copper Sulfide Nanorods by Thermolysis of a Single Source Thiolate-Derived Precursor. *J. Am. Chem. Soc.* **2003**, *125*, 5638–5639.

(409) Zhuang, Z.; Lu, X.; Peng, Q.; Li, Y. A Facile "Dispersion–Decomposition" Route to Metal Sulfide Nanocrystals. *Chem. - Eur. J.* **2011**, *17*, 10445–10452.

(410) Sigman, M. B.; Ghezelbash, A.; Hanrath, T.; Saunders, A. E.; Lee, F.; Korgel, B. A. Solventless Synthesis of Monodisperse Cu_2S

Nanorods, Nanodisks, and Nanoplatelets. *J. Am. Chem. Soc.* **2003**, *125*, 16050−16057.

(411) Aiwei, T.; Shengchun, Q.; Kai, L.; Yanbing, H.; Feng, T.; Jie, C.; Yongsheng, W.; Zhanguo, W. One-Pot Synthesis and Self-Assembly of Colloidal Copper(I) Sulfide Nanocrystals. *Nanotechnology* **2010**, *21*, 285602.

(412) Wang, Y.; Hu, Y.; Zhang, Q.; Ge, J.; Lu, Z.; Hou, Y.; Yin, Y. One-Pot Synthesis and Optical Property of Copper(I) Sulfide Nanodisks. *Inorg. Chem.* **2010**, *49*, 6601−6608.

(413) Aiwei, T.; Yu, W.; Haihang, Y.; Chao, Z.; Chunhe, Y.; Xu, L.; Hongshang, P.; Fujun, Z.; Yanbing, H.; Feng, T. Controllable Synthesis of Silver and Silver Sulfide Nanocrystals Via Selective Cleavage of Chemical Bonds. *Nanotechnology* **2013**, *24*, 355602.

(414) Du, Y.; Xu, B.; Fu, T.; Cai, M.; Li, F.; Zhang, Y.; Wang, Q. Near-Infrared Photoluminescent Ag₂S Quantum Dots from a Single Source Precursor. *J. Am. Chem. Soc.* **2010**, *132*, 1470−1471.

(415) Zhang, Y.; Liu, Y.; Li, C.; Chen, X.; Wang, Q. Controlled Synthesis of Ag₂S Quantum Dots and Experimental Determination of the Exciton Bohr Radius. *J. Phys. Chem. C* **2014**, *118*, 4918−4923.

(416) Zhong, X.; Liu, S.; Zhang, Z.; Li, L.; Wei, Z.; Knoll, W. Synthesis of High-Quality CdS, ZnS, and ZnₓCd₁₋ₓS Nanocrystals Using Metal Salts and Elemental Sulfur. *J. Mater. Chem.* **2004**, *14*, 2790−2794.

(417) Tang, Q.; Yoon, S. M.; Yang, H. J.; Lee, Y.; Song, H. J.; Byon, H. R.; Choi, H. C. Selective Degradation of Chemical Bonds: From Single-Source Molecular Precursors to Metallic Ag and Semiconducting Ag₂S Nanocrystals Via Instant Thermal Activation. *Langmuir* **2006**, *22*, 2802−2805.

(418) Ghezelbash, A.; Sigman, M. B.; Korgel, B. A. Solventless Synthesis of Nickel Sulfide Nanorods and Triangular Nanoprisms. *Nano Lett.* **2004**, *4*, 537−542.

(419) Zhuang, Z.; Peng, Q.; Wang, X.; Li, Y. Tetrahedral Colloidal Crystals of Ag₂S Nanocrystals. *Angew. Chem.* **2007**, *119*, 8322−8325.

(420) Sigman, M. B.; Korgel, B. A. Solventless Synthesis of Bi₂S₃ (Bismuthinite) Nanorods, Nanowires, and Nanofabric. *Chem. Mater.* **2005**, *17*, 1655−1660.

(421) Liu, X.; Li, Y.; Zhou, B.; Wang, X.; Cartwright, A. N.; Swihart, M. T. Shape-Controlled Synthesis of SnE (E = S, Se) Semiconductor Nanocrystals for Optoelectronics. *Chem. Mater.* **2014**, *26*, 3515−3521.

(422) Mirkovic, T.; Hines, M. A.; Nair, P. S.; Scholes, G. D. Single-Source Precursor Route for the Synthesis of EuS Nanocrystals. *Chem. Mater.* **2005**, *17*, 3451−3456.

(423) Zhang, L.-J.; Shen, X.-C.; Liang, H.; Yao, J.-T. Multiple Families of Magic-Sized ZnSe Quantum Dots Via Noninjection One-Pot and Hot-Injection Synthesis. *J. Phys. Chem. C* **2010**, *114*, 21921−21927.

(424) Banski, M.; Afzaal, M.; Malik, M. A.; Podhorodecki, A.; Misiewicz, J.; O'Brien, P. Special Role for Zinc Stearate and Octadecene in the Synthesis of Luminescent Znse Nanocrystals. *Chem. Mater.* **2015**, *27*, 3797−3800.

(425) Cumberland, S. L.; Hanif, K. M.; Javier, A.; Khitrov, G. A.; Strouse, G. F.; Woessner, S. M.; Yun, C. S. Inorganic Clusters as Single-Source Precursors for Preparation of CdSe, ZnSe, and CdSe/ZnS Nanomaterials. *Chem. Mater.* **2002**, *14*, 1576−1584.

(426) Shen, H.; Wang, H.; Li, X.; Niu, J. Z.; Wang, H.; Chen, X.; Li, L. S. Phosphine-Free Synthesis of High Quality ZnSe, ZnSe/ZnS, and Cu-, Mn-Doped ZnSe Nanocrystals. *Dalton Trans.* **2009**, 10534−10540.

(427) Flamee, S.; Dierick, R.; Cirillo, M.; Van Genechten, D.; Aubert, T.; Hens, Z. Synthesis of Metal Selenide Colloidal Nanocrystals by the Hot Injection of Selenium Powder. *Dalton Trans.* **2013**, *42*, 12654−12661.

(428) Reiss, P.; Quemard, G.; Carayon, S.; Bleuse, J.; Chandezon, F.; Pron, A. Luminescent ZnSe Nanocrystals of High Color Purity. *Mater. Chem. Phys.* **2004**, *84*, 10−13.

(429) Hines, M. A.; Guyot-Sionnest, P. Bright UV-Blue Luminescent Colloidal ZnSe Nanocrystals. *J. Phys. Chem. B* **1998**, *102*, 3655−3657.

(430) Wei, Y.; Yang, J.; Lin, A. W. H.; Ying, J. Y. Highly Reactive Se Precursor for the Phosphine-Free Synthesis of Metal Selenide Nanocrystals. *Chem. Mater.* **2010**, *22*, 5672−5677.

(431) Azad Malik, M.; Zulu, M. M.; O'Brien, P.; Wakefield, G. Single-Source Molecular Precursors for the Deposition of Zinc Selenide Quantum Dots. *J. Mater. Chem.* **1998**, *8*, 1885−1888.

(432) Jun, Y.-w.; Koo, J.-E.; Cheon, J. One-Step Synthesis of Size Tuned Zinc Selenide Quantum Dots a Temperature Controlled Molecular Precursor Approach. *Chem. Commun.* **2000**, 1243−1244.

(433) Shen, H.; Wang, H.; Yuan, H.; Ma, L.; Li, L. S. Size-, Shape-, and Assembly-Controlled Synthesis of Cu₂₋ₓSe Nanocrystals via a Non-Injection Phosphine-Free Colloidal Method. *CrystEngComm* **2012**, *14*, 555−560.

(434) Wang, D.-S.; Zheng, W.; Hao, C.-H.; Peng, Q.; Li, Y.-D. A Synthetic Method for Transition-Metal Chalcogenide Nanocrystals. *Chem. - Eur. J.* **2009**, *15*, 1870−1875.

(435) Wang, W.; Zhang, L.; Chen, G.; Jiang, J.; Ding, T.; Zuo, J.; Yang, Q. Cu₂₋ₓSe Nanooctahedra: Controllable Synthesis and Optoelectronic Properties. *CrystEngComm* **2015**, *17*, 1975−1981.

(436) Sharma, R. K.; Wadawale, A.; Kedarnath, G.; Manna, D.; Ghanty, T. K.; Vishwanadh, B.; Jain, V. K. Synthesis, Structures and DFT Calculations of 2-(4,6-Dimethyl Pyrimidyl)Selenolate Complexes of Cu(I), Ag(I) and Au(I) and Their Conversion into Metal Selenide Nanocrystals. *Dalton Trans.* **2014**, *43*, 6525−6535.

(437) Joshi, H.; Sharma, K. N.; Singh, V. V.; Singh, P.; Singh, A. K. Selenium Containing Imidazolium Salt in Designing Single Source Precursors for Silver Bromide and Selenide Nano-Particles. *Dalton Trans.* **2013**, *42*, 2366−2370.

(438) Sahu, A.; Khare, A.; Deng, D. D.; Norris, D. J. Quantum Confinement in Silver Selenide Semiconductor Nanocrystals. *Chem. Commun.* **2012**, *48*, 5458−5460.

(439) Sahu, A.; Qi, L.; Kang, M. S.; Deng, D.; Norris, D. J. Facile Synthesis of Silver Chalcogenide (Ag₂E; E = Se, S, Te) Semiconductor Nanocrystals. *J. Am. Chem. Soc.* **2011**, *133*, 6509−6512.

(440) Zhang, W.; Yang, Z.; Liu, J.; Hui, Z.; Yu, W.; Qian, Y.; Zhou, G.; Yang, L. A Hydrothermal Synthesis of Orthorhombic Nanocrystal-line Cobalt Diselenide CoSe₂. *Mater. Res. Bull.* **2000**, *35*, 2403−2408.

(441) Baumgardner, W. J.; Choi, J. J.; Lim, Y.-F.; Hanrath, T. Snse Nanocrystals: Synthesis, Structure, Optical Properties, and Surface Chemistry. *J. Am. Chem. Soc.* **2010**, *132*, 9519−9521.

(442) Ning, J.; Xiao, G.; Jiang, T.; Wang, L.; Dai, Q.; Zou, B.; Liu, B.; Wei, Y.; Chen, G.; Zou, G. Shape and Size Controlled Synthesis and Properties of Colloidal IV-VI SnSe Nanocrystals. *CrystEngComm* **2011**, *13*, 4161−4166.

(443) Franzman, M. A.; Schlenker, C. W.; Thompson, M. E.; Brutchey, R. L. Solution-Phase Synthesis of SnSe Nanocrystals for Use in Solar Cells. *J. Am. Chem. Soc.* **2010**, *132*, 4060−4061.

(444) Maneeprakorn, W.; Nguyen, C. Q.; Malik, M. A.; O'Brien, P.; Raftery, J. Synthesis of the Nickel Selenophosphinates [Ni(Se₂PR₂)₂] (R = ipr, tbu and ph) and Their Use as Single Source Precursors for the Deposition of Nickel Phosphide or Nickel Selenide Nanoparticles. *Dalton Trans.* **2009**, 2103−2108.

(445) Moloto, N.; Moloto, M. J.; Coville, N. J.; Sinha Ray, S. Optical and Structural Characterization of Nickel Selenide Nanoparticles Synthesized by Simple Methods. *J. Cryst. Growth* **2009**, *311*, 3924−3932.

(446) Bang, J.; Park, J.; Lee, J. H.; Won, N.; Nam, J.; Lim, J.; Chang, B. Y.; Lee, H. J.; Chon, B.; Shin, J.; et al. ZnTe/ZnSe (Core/Shell) Type-II Quantum Dots: Their Optical and Photovoltaic Properties. *Chem. Mater.* **2010**, *22*, 233−240.

(447) Lincheneau, C.; Amelia, M.; Oszajca, M.; Boccia, A.; D'Orazi, F.; Madrigale, M.; Zanoni, R.; Mazzaro, R.; Ortolani, L.; Morandi, V.; et al. Synthesis and Properties of Znte and ZnTe/ZnS Core/Shell Semiconductor Nanocrystals. *J. Mater. Chem. C* **2014**, *2*, 2877−2886.

(448) Lee, S. H.; Kim, Y. J.; Park, J. Shape Evolution of ZnTe Nanocrystals: Nanoflowers, Nanodots, and Nanorods. *Chem. Mater.* **2007**, *19*, 4670−4675.

(449) Zhang, J.; Sun, K.; Kumbhar, A.; Fang, J. Shape-Control of ZnTe Nanocrystal Growth in Organic Solution. *J. Phys. Chem. C* **2008**, *112*, 5454−5458.

(450) Zhang, J.; Jin, S.; Fry, H. C.; Peng, S.; Shevchenko, E.; Wiederrecht, G. P.; Rajh, T. Synthesis and Characterization of Wurtzite ZnTe Nanorods with Controllable Aspect Ratios. *J. Am. Chem. Soc.* **2011**, *133*, 15324−15327.

(451) Jia, G.; Banin, U. A General Strategy for Synthesizing Colloidal Semiconductor Zinc Chalcogenide Quantum Rods. *J. Am. Chem. Soc.* **2014**, *136*, 11121−11127.

(452) Shen, H.; Jiang, X.-D.; Wang, S.; Fu, Y.; Zhou, C.; Li, L. S. Facile Preparation of Metal Telluride Nanocrystals Using Di-n-Octylphosphine Oxide (DOPO) as an Air-Stable and Less Toxic Alternative to the Common Tri-Alkylphosphines. *J. Mater. Chem.* **2012**, *22*, 25050−25056.

(453) Jun, Y.-w.; Choi, C.-S.; Cheon, J. Size and Shape Controlled ZnTe Nanocrystals with Quantum Confinement Effect. *Chem. Commun.* **2001**, 101−102.

(454) Yang, H.-J.; Chen, C.-Y.; Yuan, F.-W.; Tuan, H.-Y. Designed Synthesis of Solid and Hollow $Cu_{2-x}Te$ Nanocrystals with Tunable near-Infrared Localized Surface Plasmon Resonance. *J. Phys. Chem. C* **2013**, *117*, 21955−21964.

(455) Kriegel, I.; Jiang, C.; Rodríguez-Fernández, J.; Schaller, R. D.; Talapin, D. V.; da Como, E.; Feldmann, J. Tuning the Excitonic and Plasmonic Properties of Copper Chalcogenide Nanocrystals. *J. Am. Chem. Soc.* **2012**, *134*, 1583−1590.

(456) Li, H.; Brescia, R.; Povia, M.; Prato, M.; Bertoni, G.; Manna, L.; Moreels, I. Synthesis of Uniform Disk-Shaped Copper Telluride Nanocrystals and Cation Exchange to Cadmium Telluride Quantum Disks with Stable Red Emission. *J. Am. Chem. Soc.* **2013**, *135*, 12270−12278.

(457) Han, C.; Li, Z.; Li, W.-j.; Chou, S.-l.; Dou, S.-x. Controlled Synthesis of Copper Telluride Nanostructures for Long-Cycling Anodes in Lithium Ion Batteries. *J. Mater. Chem. A* **2014**, *2*, 11683−11690.

(458) Xu, Y.; Al-Salim, N.; Hodgkiss, J. M.; Tilley, R. D. Solution Synthesis and Optical Properties of Snte Nanocrystals. *Cryst. Growth Des.* **2011**, *11*, 2721−2723.

(459) Kovalenko, M. V.; Heiss, W.; Shevchenko, E. V.; Lee, J.-S.; Schwinghammer, H.; Alivisatos, A. P.; Talapin, D. V. SnTe Nanocrystals: A New Example of Narrow-Gap Semiconductor Quantum Dots. *J. Am. Chem. Soc.* **2007**, *129*, 11354−11355.

(460) Chen, S.; Lee, S. TOP as Ligand and Solvent to Synthesize Silver Telluride Nanosheets. *Mater. Res. Bull.* **2015**, *71*, 30−36.

(461) Zhou, W.; Zhao, W.; Lu, Z.; Zhu, J.; Fan, S.; Ma, J.; Hng, H. H.; Yan, Q. Preparation and Thermoelectric Properties of Sulfur Doped Ag_2Te Nanoparticles Via Solvothermal Methods. *Nanoscale* **2012**, *4*, 3926−3931.

(462) Bendt, G.; Weber, A.; Heimann, S.; Assenmacher, W.; Prymak, O.; Schulz, S. Wet-Chemical Synthesis of Different Bismuth Telluride Nanoparticles Using Metal Organic Precursors - Single Source Vs. Dual Source Approach. *Dalton Trans.* **2015**, *44*, 14272−14280.

(463) Kim, H.-J.; Lee, K.-J.; Kim, S.-J.; Han, M.-K. A Simple and Quick Chemical Synthesis of Nanostructured Bi_2Te_3, Sb_2Te_3, and $Bi_xSb_{2-X}Te_3$. *Bull. Korean Chem. Soc.* **2010**, *31*, 1123−1127.

(464) Schulz, S.; Heimann, S.; Friedrich, J.; Engenhorst, M.; Schierning, G.; Assenmacher, W. Synthesis of Hexagonal Sb_2Te_3 Nanoplates by Thermal Decomposition of the Single-Source Precursor $(Et_2Sb)_2Te$. *Chem. Mater.* **2012**, *24*, 2228−2234.

(465) Gupta, G.; Kim, J. Facile Synthesis of Hexagonal Sb_2Te_3 Nanoplates Using Ph_2SbTeR (R = Et, Ph) Single Source Precursors. *Dalton Trans.* **2013**, *42*, 8209−8211.

(466) Caldwell, M. A.; Raoux, S.; Wang, R. Y.; Philip Wong, H. S.; Milliron, D. J. Synthesis and Size-Dependent Crystallization of Colloidal Germanium Telluride Nanoparticles. *J. Mater. Chem.* **2010**, *20*, 1285−1291.

(467) Polking, M. J.; Zheng, H.; Ramesh, R.; Alivisatos, A. P. Controlled Synthesis and Size-Dependent Polarization Domain Structure of Colloidal Germanium Telluride Nanocrystals. *J. Am. Chem. Soc.* **2011**, *133*, 2044−2047.

(468) Arachchige, I. U.; Soriano, R.; Malliakas, C. D.; Ivanov, S. A.; Kanatzidis, M. G. Amorphous and Crystalline GeTe Nanocrystals. *Adv. Funct. Mater.* **2011**, *21*, 2737−2743.

(469) Buck, M. R.; Biacchi, A. J.; Popczun, E. J.; Schaak, R. E. Polymer-Assisted Synthesis of Colloidal Germanium Telluride Nano-Octahedra, Nanospheres, and Nanosheets. *Chem. Mater.* **2013**, *25*, 2163−2171.

(470) Afzaal, M.; Malik, M. A.; O'Brien, P. Chemical Routes to Chalcogenide Materials as Thin Films or Particles with Critical Dimensions with the Order of Nanometres. *J. Mater. Chem.* **2010**, *20*, 4031−4040.

(471) Zhang, Y.; Xu, H.; Wang, Q. Ultrathin Single Crystal ZnS Nanowires. *Chem. Commun.* **2010**, *46*, 8941−8943.

(472) Mthethwa, T.; Pullabhotla, V. S. R. R.; Mdluli, P. S.; Wesley-Smith, J.; Revaprasadu, N. Synthesis of Hexadecylamine Capped CdS Nanoparticles Using Heterocyclic Cadmium Dithiocarbamates as Single Source Precursors. *Polyhedron* **2009**, *28*, 2977−2982.

(473) Lazell, M.; Nørager, S. J.; O'Brien, P.; Revaprasadu, N. The Use of Dithio- and Diselenocarbamates as Precursors to Nanoscale Materials. *Mater. Sci. Eng., C* **2001**, *16*, 129−133.

(474) Rabkin, A.; Samuha, S.; Abutbul, R. E.; Ezersky, V.; Meshi, L.; Golan, Y. New Nanocrystalline Materials: A Previously Unknown Simple Cubic Phase in the SnS Binary System. *Nano Lett.* **2015**, *15*, 2174−2179.

(475) Supitcha, T.; Yasuchika, H.; Katsuhisa, T.; Koji, F.; Kazuyuki, H.; Yuji, W.; Shozo, Y. First Observation of Faraday Effect of EuS Nanocrystals in Polymer Thin Films. *Jpn. J. Appl. Phys.* **2003**, *42*, L876.

(476) Selinsky, R. S.; Keavney, D. J.; Bierman, M. J.; Jin, S. Element-Specific Magnetometry of EuS Nanocrystals. *Appl. Phys. Lett.* **2009**, *95*, 202501.

(477) Mauger, A.; Godart, C. The Magnetic, Optical, and Transport Properties of Representatives of a Class of Magnetic Semiconductors: The Europium Chalcogenides. *Phys. Rep.* **1986**, *141*, 51−176.

(478) Ivanov, R. A.; Korsakov, I. E.; Formanovskii, A. A.; Paramonov, S. E.; Kuz'mina, N. P.; Kaul, A. R. Heteroligand Lanthanide Dialkyldithiocarbamate Complexes with 1,10-Phenanthroline: A New Approach to Synthesis and Application for the Preparation of Sulfides. *Russ. J. Coord. Chem.* **2002**, *28*, 670−672.

(479) Zhao, F.; Sun, H.-L.; Gao, S.; Su, G. Magnetic Properties of EuS Nanoparticles Synthesized by Thermal Decomposition of Molecular Precursors. *J. Mater. Chem.* **2005**, *15*, 4209−4214.

(480) Regulacio, M. D.; Bussmann, K.; Lewis, B.; Stoll, S. L. Magnetic Properties of Lanthanide Chalcogenide Semiconducting Nanoparticles. *J. Am. Chem. Soc.* **2006**, *128*, 11173−11179.

(481) Zhong, X. H.; Feng, Y. Y.; Knoll, W.; Han, M. Y. Alloyed $Zn_xCd_{1-x}S$ Nanocrystals with Highly Narrow Luminescence Spectral Width. *J. Am. Chem. Soc.* **2003**, *125*, 13559−13563.

(482) Liu, H.; Liu, Y.; Wang, Z.; He, P. Facile Synthesis of Monodisperse, Size-Tunable SnS Nanoparticles Potentially for Solar Cell Energy Conversion. *Nanotechnology* **2010**, *21*, 105707.

(483) Hickey, S. G.; Waurisch, C.; Rellinghaus, B.; Eychmüller, A. Size and Shape Control of Colloidally Synthesized IV-VI Nano-particulate Tin(II) Sulfide. *J. Am. Chem. Soc.* **2008**, *130*, 14978−14979.

(484) de Kergommeaux, A.; Faure-Vincent, J.; Pron, A.; de Bettignies, R.; Malaman, B.; Reiss, P. Surface Oxidation of Tin Chalcogenide Nanocrystals Revealed by Sn-119-Mössbauer Spectroscopy. *J. Am. Chem. Soc.* **2012**, *134*, 11659−11666.

(485) Protesescu, L.; Rossini, A. J.; Kriegner, D.; Valla, M.; de Kergommeaux, A.; Walter, M.; Kravchyk, K. V.; Nachtegaal, M.; Stangl, J.; Malaman, B.; et al. Unraveling the Core−Shell Structure of Ligand-Capped Sn/SnO_x Nanoparticles by Surface-Enhanced Nuclear Magnetic Resonance, Mössbauer, and X-Ray Absorption Spectroscopies. *ACS Nano* **2014**, *8*, 2639−2648.

(486) de Kergommeaux, A.; Lopez-Haro, M.; Pouget, S.; Zuo, J.-M.; Lebrun, C.; Chandezon, F.; Aldakov, D.; Reiss, P. Synthesis, Internal Structure and Formation Mechanism of Monodisperse Tin Sulfide Nanoplatelets. *J. Am. Chem. Soc.* **2015**, *137*, 9943−9952.

(487) Jiang, P.; Tian, Z.-Q.; Zhu, C.-N.; Zhang, Z.-L.; Pang, D.-W. Emission-Tunable near-Infrared Ag_2S Quantum Dots. *Chem. Mater.* **2012**, *24*, 3−5.

(488) Tian, G.; Zhao, T.; Niu, J.; Shen, H.; Li, L. S. Synthesis and Self-Assembly of Triangular $Cu_{2-x}Se$ Nanocrystals. *RSC Adv.* **2014**, *4*, 39547−39551.

(489) Bullen, C. R.; Mulvaney, P. Nucleation and Growth Kinetics of CdSe Nanocrystals in Octadecene. *Nano Lett.* **2004**, *4*, 2303−2307.

(490) Yu, W. W.; Peng, X. Formation of High-Quality CdS and Other II−VI Semiconductor Nanocrystals in Noncoordinating Solvents: Tunable Reactivity of Monomers. *Angew. Chem., Int. Ed.* **2002**, *41*, 2368−2371.

(491) Zhuang, Z.; Peng, Q.; Zhuang, J.; Wang, X.; Li, Y. Controlled Hydrothermal Synthesis and Structural Characterization of a Nickel Selenide Series. *Chem. - Eur. J.* **2006**, *12*, 211−217.

(492) Trindade, T.; O'Brien, P. A Single Source Approach to the Synthesis of CdSe Nanocrystallites. *Adv. Mater.* **1996**, *8*, 161−163.

(493) Maneeprakorn, W.; Malik, M. A.; O'Brien, P. The Preparation of Cobalt Phosphide and Cobalt Chalcogenide (CoX, X = S, Se) Nanoparticles from Single Source Precursors. *J. Mater. Chem.* **2010**, *20*, 2329−2335.

(494) Battaglia, D.; Li, J. J.; Wang, Y.; Peng, X. Colloidal Two-Dimensional Systems: CdSe Quantum Shells and Wells. *Angew. Chem., Int. Ed.* **2003**, *42*, 5035−5039.

(495) Shen, H.; Wang, H.; Tang, Z.; Niu, J. Z.; Lou, S.; Du, Z.; Li, L. S. High Quality Synthesis of Monodisperse Zinc-Blende CdSe and CdSe/ZnS Nanocrystals with a Phosphine-Free Method. *CrystEngComm* **2009**, *11*, 1733−1738.

(496) Cozzoli, P. D.; Manna, L.; Curri, M. L.; Kudera, S.; Giannini, C.; Striccoli, M.; Agostiano, A. Shape and Phase Control of Colloidal ZnSe Nanocrystals. *Chem. Mater.* **2005**, *17*, 1296−1306.

(497) Fanfair, D. D.; Korgel, B. A. Twin-Related Branching of Solution-Grown Znse Nanowires. *Chem. Mater.* **2007**, *19*, 4943−4948.

(498) Reiss, P. ZnSe Based Colloidal Nanocrystals: Synthesis, Shape Control, Core/Shell, Alloy and Doped Systems. *New J. Chem.* **2007**, *31*, 1843−1852.

(499) Chu, J. Y. C.; Lewicki, J. W. Thermal Decomposition of Bis(Diphenylmethyl) Diselenide. *J. Org. Chem.* **1977**, *42*, 2491−2493.

(500) Tyrrell, S.; Behrendt, G.; Liu, Y.; Nockemann, P. Zinc Selenide Nano- and Microspheres Via Microwave-Assisted Ionothermal Synthesis. *RSC Adv.* **2014**, *4*, 36110−36116.

(501) Jung, W.; Lee, S.; Yoo, D.; Jeong, S.; Miró, P.; Kuc, A.; Heine, T.; Cheon, J. Colloidal Synthesis of Single-Layer MSe_2 (M = Mo, W) Nanosheets Via Anisotropic Solution-Phase Growth Approach. *J. Am. Chem. Soc.* **2015**, *137*, 7266−7269.

(502) Antunez, P. D.; Webber, D. H.; Brutchey, R. L. Solution-Phase Synthesis of Highly Conductive Tungsten Diselenide Nanosheets. *Chem. Mater.* **2013**, *25*, 2385−2387.

(503) Trindade, T.; O'Brien, P.; Zhang, X.-M. Synthesis of CdS and CdSe Nanocrystallites Using a Novel Single-Molecule Precursors Approach. *Chem. Mater.* **1997**, *9*, 523−530.

(504) Rogach, A. L.; Franzl, T.; Klar, T. A.; Feldmann, J.; Gaponik, N.; Lesnyak, V.; Shavel, A.; Eychmüller, A.; Rakovich, Y. P.; Donegan, J. F. Aqueous Synthesis of Thiol-Capped CdTe Nanocrystals: State-of-the-Art. *J. Phys. Chem. C* **2007**, *111*, 14628−14637.

(505) Reiss, P.; Philippot, C. Synthesis of Inorganic Nanocrystals for Biological Fluorescence Imaging. In *Frontiers of Nanoscience*; De la Fuente, J.; Grazu, V., Eds.; Elsevier: Amsterdam, The Netherlands, 2012; Vol. 4, pp 81−114.

(506) Wuister, S. F.; Swart, I.; van Driel, F.; Hickey, S. G.; de Mello Donegá, C. Highly Luminescent Water-Soluble Cdte Quantum Dots. *Nano Lett.* **2003**, *3*, 503−507.

(507) Talapin, D. V.; Haubold, S.; Rogach, A. L.; Kornowski, A.; Haase, M.; Weller, H. A Novel Organometallic Synthesis of Highly Luminescent CdTe Nanocrystals. *J. Phys. Chem. B* **2001**, *105*, 2260−2263.

(508) Yarema, M.; Caputo, R.; Kovalenko, M. V. Precision Synthesis of Colloidal Inorganic Nanocrystals Using Metal and Metalloid Amides. *Nanoscale* **2013**, *5*, 8398−8410.

(509) Caulton, K. G.; Hubert-Pfalzgraf, L. G. Synthesis, Structural Principles and Reactivity of Heterometallic Alkoxides. *Chem. Rev.* **1990**, *90*, 969−995.

(510) Scheele, M.; Oeschler, N.; Meier, K.; Kornowski, A.; Klinke, C.; Weller, H. Synthesis and Thermoelectric Characterization of Bi_2Te_3 Nanoparticles. *Adv. Funct. Mater.* **2009**, *19*, 3476−3483.

(511) Evans, C. M.; Evans, M. E.; Krauss, T. D. Mysteries of Topse Revealed: Insights into Quantum Dot Nucleation. *J. Am. Chem. Soc.* **2010**, *132*, 10973−10975.

(512) Zhong, H.; Bai, Z.; Zou, B. Tuning the Luminescence Properties of Colloidal I−III−VI Semiconductor Nanocrystals for Optoelectronics and Biotechnology Applications. *J. Phys. Chem. Lett.* **2012**, *3*, 3167−3175.

(513) Kolny-Olesiak, J.; Weller, H. Synthesis and Application of Colloidal $CuInS_2$ Semiconductor Nanocrystals. *ACS Appl. Mater. Interfaces* **2013**, *5*, 12221−12237.

(514) Madelung, O.; Rössler, U.; Schulz, M. *Semiconductors - Ternary Compounds, Organic Semiconductors*; Springer: Berlin, 2000; Vol. 41E.

(515) Chen, S.; Gong, X. G.; Walsh, A.; Wei, S.-H. Crystal and Electronic Band Structure of Cu_2ZnSnX_4 (X = S and Se) Photovoltaic Absorbers: First-Principles Insights. *Appl. Phys. Lett.* **2009**, *94*, 041903.

(516) Walsh, A.; Chen, S.; Wei, S.-H.; Gong, X.-G. Kesterite Thin-Film Solar Cells: Advances in Materials Modelling of Cu_2ZnSnS_4. *Adv. Energy Mater.* **2012**, *2*, 400−409.

(517) Li, M.; Zhou, W.-H.; Guo, J.; Zhou, Y.-L.; Hou, Z.-L.; Jiao, J.; Zhou, Z.-J.; Du, Z.-L.; Wu, S.-X. Synthesis of Pure Metastable Wurtzite CZTS Nanocrystals by Facile One-Pot Method. *J. Phys. Chem. C* **2012**, *116*, 26507−26516.

(518) Gabka, G.; Bujak, P.; Gryszel, M.; Ostrowski, A.; Malinowska, K.; Zukowska, G. Z.; Agnese, F.; Pron, A.; Reiss, P. Synthesis and Surface Chemistry of High Quality Wurtzite and Kesterite Cu_2ZnSnS_4 Nanocrystals Using Tin(II) 2-Ethylhexanoate as a New Tin Source. *Chem. Commun.* **2015**, *51*, 12985−12988.

(519) Du, H.; Yan, F.; Young, M.; To, B.; Jiang, C.-S.; Dippo, P.; Kuciauskas, D.; Chi, Z.; Lund, E. A.; Hancock, C.; Hlaing OO, W. M.; Scarpulla, M. A.; Teeter, G. Investigation of Combinatorial Coevaporated Thin Film Cu_2ZnSnS_4. I. Temperature Effect, Crystalline Phases, Morphology, and Photoluminescence. *J. Appl. Phys.* **2014**, *115*, 173502.

(520) Nagoya, A.; Asahi, R.; Wahl, R.; Kresse, G. Defect Formation and Phase Stability of Cu_2ZnSnS_4 Photovoltaic Material. *Phys. Rev. B: Condens. Matter Mater. Phys.* **2010**, *81*, 113202.

(521) Li, L.; Pandey, A.; Werder, D. J.; Khanal, B. P.; Pietryga, J. M.; Klimov, V. I. Efficient Synthesis of Highly Luminescent Copper Indium Sulfide-Based Core/Shell Nanocrystals with Surprisingly Long-Lived Emission. *J. Am. Chem. Soc.* **2011**, *133*, 1176−1179.

(522) Song, W. S.; Yang, H. *Appl. Phys. Lett.* **2012**, *100*, 183104.

(523) Li, L.; Daou, T.; Texier, I.; Tran, T.; Liem, N.; Reiss, P. Highly Luminescent $CuInS_2$/ZnS Core/Shell Nanocrystals: Cadmium-Free Quantum Dots for in Vivo Imaging. *Chem. Mater.* **2009**, *21*, 2422−2429.

(524) Zhong, H.; Lo, S. S.; Mirkovic, T.; Li, Y.; Ding, Y.; Li, Y.; Scholes, G. D. Noninjection Gram-Scale Synthesis of Monodisperse Pyramidal $CuInS_2$ Nanocrystals and Their Size-Dependent Properties. *ACS Nano* **2010**, *4*, 5253−5262.

(525) Chen, B.; Zhong, H.; Zhang, W.; Tan, Z. a.; Li, Y.; Yu, C.; Zhai, T.; Bando, Y.; Yang, S.; Zou, B. Highly Emissive and Color-Tunable $CuInS_2$-Based Colloidal Semiconductor Nanocrystals: Off-Stoichiometry Effects and Improved Electroluminescence Performance. *Adv. Funct. Mater.* **2012**, *22*, 2081−2088.

(526) Park, J.; Kim, S.-W. $CuInS_2$/ZnS Core/Shell Quantum Dots by Cation Exchange and Their Blue-Shifted Photoluminescence. *J. Mater. Chem.* **2011**, *21*, 3745−3750.

(527) Shavel, A.; Cadavid, D.; Ibáñez, M.; Carrete, A.; Cabot, A. Continuous Production of Cu_2ZnSnS_4 Nanocrystals in a Flow Reactor. *J. Am. Chem. Soc.* **2012**, *134*, 1438−1441.

(528) Yu, X.; Shavel, A.; An, X.; Luo, Z.; Ibáñez, M.; Cabot, A. Cu_2ZnSnS_4-Pt and Cu_2ZnSnS_4-Au Heterostructured Nanoparticles for

Photocatalytic Water Splitting and Pollutant Degradation. *J. Am. Chem. Soc.* **2014**, *136*, 9236−9239.

(529) Yu, K.; Ng, P.; Ouyang, J.; Zaman, M. B.; Abulrob, A.; Baral, T. N.; Fatehi, D.; Jakubek, Z. J.; Kingston, D.; Wu, X.; et al. Low-Temperature Approach to Highly Emissive Copper Indium Sulfide Colloidal Nanocrystals and Their Bioimaging Applications. *ACS Appl. Mater. Interfaces* **2013**, *5*, 2870−2880.

(530) Speranskaya, E. S.; Beloglazova, N. V.; Abe, S.; Aubert, T.; Smet, P. F.; Poelman, D.; Goryacheva, I. Y.; De Saeger, S.; Hens, Z. Hydrophilic, Bright CuInS$_2$ Quantum Dots as Cd-Free Fluorescent Labels in Quantitative Immunoassay. *Langmuir* **2014**, *30*, 7567−7575.

(531) Nakamura, H.; Kato, W.; Uehara, M.; Nose, K.; Omata, T.; Otsuka-Yao-Matsuo, S.; Miyazaki, M.; Maeda, H. Tunable Photoluminescence Wavelength of Chalcopyrite CuInS$_2$-Based Semiconductor Nanocrystals Synthesized in a Colloidal System. *Chem. Mater.* **2006**, *18*, 3330−3335.

(532) Uehara, M.; Watanabe, K.; Tajiri, Y.; Nakamura, H.; Maeda, H. Synthesis of CuInS$_2$ Fluorescent Nanocrystals and Enhancement of Fluorescence by Controlling Crystal Defect. *J. Chem. Phys.* **2008**, *129*, 134709.

(533) Pein, A.; Baghbanzadeh, M.; Rath, T.; Haas, W.; Maier, E.; Amenitsch, H.; Hofer, F.; Kappe, C. O.; Trimmel, G. Investigation of the Formation of CuInS$_2$ Nanoparticles by the Oleylamine Route: Comparison of Microwave-Assisted and Conventional Syntheses. *Inorg. Chem.* **2011**, *50*, 193−200.

(534) Yu, C.; Zhang, L.; Tian, L.; Liu, D.; Chen, F.; Wang, C. Synthesis and Formation Mechanism of CuInS$_2$ Nanocrystals with a Tunable Phase. *CrystEngComm* **2014**, *16*, 9596−9602.

(535) Chiang, M.-Y.; Chang, S.-H.; Chen, C.-Y.; Yuan, F.-W.; Tuan, H.-Y. Quaternary CuIn(S$_{1−x}$Se$_x$)2 Nanocrystals: Facile Heating-up Synthesis, Band Gap Tuning, and Gram-Scale Production. *J. Phys. Chem. C* **2011**, *115*, 1592−1599.

(536) Li, T. L.; Teng, H. S. Solution Synthesis of High-Quality CuInS$_2$ Quantum Dots as Sensitizers for TiO$_2$ Photoelectrodes. *J. Mater. Chem.* **2010**, *20*, 3656−3664.

(537) Das, K.; Panda, S. K.; Gorai, S.; Mishra, P.; Chaudhuri, S. Effect of Cu/In Molar Ratio on the Microstructural and Optical Properties of Microcrystalline CuInS$_2$ Prepared by Solvothermal Route. *Mater. Res. Bull.* **2008**, *43*, 2742−2750.

(538) Vahidshad, Y.; Tahir, M. N.; Zad, A. I.; Mirkazemi, S. M.; Ghazemzadeh, R.; Tremel, W. Structural and Optical Properties of Fe and Zn Substituted CuInS$_2$ Nanoparticles Synthesized by a One-Pot Facile Method. *J. Mater. Chem. C* **2015**, *3*, 889−898.

(539) Lu, Q.; Hu, J.; Tang, K.; Qian, Y.; Zhou, G.; Liu, X. Synthesis of Nanocrystalline CuMS$_2$ (M = In or Ga) through a Solvothermal Process. *Inorg. Chem.* **2000**, *39*, 1606−1607.

(540) Sun, C.; Cevher, Z.; Zhang, J.; Gao, B.; Shum, K.; Ren, Y. One-Pot Synthesis and Characterization of Chalcopyrite CuInS$_2$ Nanoparticles. *J. Mater. Chem. A* **2014**, *2*, 10629−10633.

(541) Perera, S. D.; Zhang, H.; Ding, X.; Nelson, A.; Robinson, R. D. Nanocluster Seed-Mediated Synthesis of CuInS$_2$ Quantum Dots, Nanodisks, Nanorods, and Doped Zn-CuInGaS$_2$ Quantum Dots. *J. Mater. Chem. C* **2015**, *3*, 1044−1055.

(542) Liu, S.; Zhang, H.; Qiao, Y.; Su, X. One-Pot Synthesis of Ternary CuInS$_2$ Quantum Dots with near-Infrared Fluorescence in Aqueous Solution. *RSC Adv.* **2012**, *2*, 819−825.

(543) Yu, C.; Yu, J. C.; Wen, H.; Zhang, C. A Mild Solvothermal Route for Preparation of Cubic-Like CuInS$_2$ Crystals. *Mater. Lett.* **2009**, *63*, 1984−1986.

(544) Zhong, H. Z.; Zhou, Y.; Ye, M. F.; He, Y. J.; Ye, J. P.; He, C.; Yang, C. H.; Li, Y. F. Controlled Synthesis and Optical Properties of Colloidal Ternary Chalcogenide CuInS$_2$ Nanocrystals. *Chem. Mater.* **2008**, *20*, 6434−6443.

(545) Tang, X.; Cheng, W.; Choo, E. S. G.; Xue, J. Synthesis of CuInS$_2$-ZnS Alloyed Nanocubes with High Luminescence. *Chem. Commun.* **2011**, *47*, 5217−5219.

(546) Zhang, A.; Ma, Q.; Lu, M.; Yu, G.; Zhou, Y.; Qiu, Z. Copper−Indium Sulfide Hollow Nanospheres Synthesized by a Facile Solution-Chemical Method. *Cryst. Growth Des.* **2008**, *8*, 2402−2405.

(547) Du, W. M.; Qian, X. F.; Yin, J.; Gong, Q. Shape- and Phase-Controlled Synthesis of Monodisperse, Single-Crystalline Ternary Chalcogenide Colloids through a Convenient Solution Synthesis Strategy. *Chem. - Eur. J.* **2007**, *13*, 8840−8846.

(548) He, J.-J.; Zhou, W.-H.; Li, M.; Hou, Z.-L.; Du, Y.-F.; Wu, S.-X. One-Pot Route for Preparation of Monodisperse CuInS$_2$ Nanocrystals. *Mater. Lett.* **2012**, *66*, 96−98.

(549) Zhang, J.; Sun, W.; Yin, L.; Miao, X.; Zhang, D. One-Pot Synthesis of Hydrophilic CuInS$_2$ and CuInS$_2$-ZnS Colloidal Quantum Dots. *J. Mater. Chem. C* **2014**, *2*, 4812−4817.

(550) Shi, L.; Pei, C.; Li, Q. Ordered Arrays of Shape Tunable CuInS$_2$ Nanostructures, from Nanotubes to Nano Test Tubes and Nanowires. *Nanoscale* **2010**, *2*, 2126−2130.

(551) Panthani, M. G.; Akhavan, V.; Goodfellow, B.; Schmidtke, J. P.; Dunn, L.; Dodabalapur, A.; Barbara, P. F.; Korgel, B. A. Synthesis of CuInS$_2$, CuInSe$_2$, and Cu(In$_x$Ga$_{1−x}$)Se$_2$ (CIGS) Nanocrystal "Inks" for Printable Photovoltaics. *J. Am. Chem. Soc.* **2008**, *130*, 16770−16777.

(552) Castro, S. L.; Bailey, S. G.; Raffaelle, R. P.; Banger, K. K.; Hepp, A. F. Nanocrystalline Chalcopyrite Materials (CuInS$_2$ and CuInSe$_2$) Via Low-Temperature Pyrolysis of Molecular Single-Source Precursors. *Chem. Mater.* **2003**, *15*, 3142−3147.

(553) Sun, C. V.; Gardner, J. S.; Long, G.; Bajracharya, C.; Thurber, A.; Punnoose, A.; Rodriguez, R. G.; Pak, J. J. Controlled Stoichiometry for Quaternary CuIn$_x$Ga$_{1−x}$S$_2$ Chalcopyrite Nanoparticles from Single-Source Precursors Via Microwave Irradiation. *Chem. Mater.* **2010**, *22*, 2699−2701.

(554) Castro, S. L.; Bailey, S. G.; Raffaelle, R. P.; Banger, K. K.; Hepp, A. F. Synthesis and Characterization of Colloidal CuInS$_2$ Nanoparticles from a Molecular Single-Source Precursor. *J. Phys. Chem. B* **2004**, *108*, 12429−12435.

(555) Nairn, J. J.; Shapiro, P. J.; Twamley, B.; Pounds, T.; von Wandruszka, R.; Fletcher, T. R.; Williams, M.; Wang, C. M.; Norton, M. G. Preparation of Ultrafine Chalcopyrite Nanoparticles Via the Photochemical Decomposition of Molecular Single-Source Precursors. *Nano Lett.* **2006**, *6*, 1218−1223.

(556) Abdelhady, A. L.; Malik, M. A.; O'Brien, P. Iso-Propylthiobiuret-Copper and Indium Complexes as Novel Precursors for Colloidal Synthesis of CuInS$_2$ Nanoparticles. *J. Mater. Chem.* **2012**, *22*, 3781−3785.

(557) Jiang, Y.; Wu, Y.; Mo, X.; Yu, W.; Xie, Y.; Qian, Y. Elemental Solvothermal Reaction to Produce Ternary Semiconductor CuInE$_2$ (E = S, Se) Nanorods. *Inorg. Chem.* **2000**, *39*, 2964−2965.

(558) Xu, J.; Lee, C.-S.; Tang, Y.-B.; Chen, X.; Chen, Z.-H.; Zhang, W.-J.; Lee, S.-T.; Zhang, W.; Yang, Z. Large-Scale Synthesis and Phase Transformation of CuSe, CuInSe$_2$, and CuInSe$_2$/CuInS$_2$ Core/Shell Nanowire Bundles. *ACS Nano* **2010**, *4*, 1845−1850.

(559) Chang, J.; Waclawik, E. R. Controlled Synthesis of CuInS$_2$, Cu$_2$SnS$_3$ and Cu$_2$ZnSnS$_4$ Nano-Structures: Insight into the Universal Phase-Selectivity Mechanism. *CrystEngComm* **2013**, *15*, 5612−5619.

(560) Nose, K.; Soma, Y.; Omata, T.; Otsuka-Yao-Matsuo, S. Synthesis of Ternary CuInS$_2$ Nanocrystals; Phase Determination by Complex Ligand Species. *Chem. Mater.* **2009**, *21*, 2607−2613.

(561) Gong, F.; Tian, S.; Liu, B.; Xiong, D.; Zhao, X. Oleic Acid Assisted Formation Mechanism of CuInS$_2$ Nanocrystals with Tunable Structures. *RSC Adv.* **2014**, *4*, 36875−36881.

(562) Liu, Z.; Wang, L.; Hao, Q.; Wang, D.; Tang, K.; Zuo, M.; Yang, Q. Facile Synthesis and Characterization of CuInS$_2$ Nanocrystals with Different Structures and Shapes. *CrystEngComm* **2013**, *15*, 7192−7198.

(563) Sheng, X.; Wang, L.; Luo, Y.; Yang, D. Synthesis of Hexagonal Structured Wurtzite and Chalcopyrite CuInS$_2$ Via a Simple Solution Route. *Nanoscale Res. Lett.* **2011**, *6*, 562.

(564) Norako, M. E.; Franzman, M. A.; Brutchey, R. L. Growth Kinetics of Monodisperse Cu−In−S Nanocrystals Using a Dialkyl Disulfide Sulfur Source. *Chem. Mater.* **2009**, *21*, 4299−4304.

(565) Qi, Y.; Liu, Q.; Tang, K.; Liang, Z.; Ren, Z.; Liu, X. Synthesis and Characterization of Nanostructured Wurtzite CuInS$_2$: A New Cation Disordered Polymorph of CuInS$_2$. *J. Phys. Chem. C* **2009**, *113*, 3939−3944.

(566) Bao, N.; Qiu, X.; Wang, Y.-H. A.; Zhou, Z.; Lu, X.; Grimes, C. A.; Gupta, A. Facile Thermolysis Synthesis of CuInS$_2$ Nanocrystals with Tunable Anisotropic Shape and Structure. *Chem. Commun.* **2011**, *47*, 9441−9443.

(567) Kruszynska, M.; Knipper, M.; Kolny-Olesiak, J.; Borchert, H.; Parisi, J. Charge Transfer in Blends of P3HT and Colloidally Prepared CuInS$_2$ Nanocrystals. *Thin Solid Films* **2011**, *519*, 7374−7377.

(568) Kruszynska, M.; Borchert, H.; Parisi, J.; Kolny-Olesiak, J. Synthesis and Shape Control of CuInS$_2$ Nanoparticles. *J. Am. Chem. Soc.* **2010**, *132*, 15976−15986.

(569) Wang, X.; Swihart, M. T. Controlling the Size, Shape, Phase, Band Gap, and Localized Surface Plasmon Resonance of Cu$_{2-x}$S and Cu$_x$In$_y$S Nanocrystals. *Chem. Mater.* **2015**, *27*, 1786−1791.

(570) Lei, S.; Wang, C.; Liu, L.; Guo, D.; Wang, C.; Tang, Q.; Cheng, B.; Xiao, Y.; Zhou, L. Spinel Indium Sulfide Precursor for the Phase-Selective Synthesis of Cu-In-S Nanocrystals with Zinc-Blende, Wurtzite, and Spinel Structures. *Chem. Mater.* **2013**, *25*, 2991−2997.

(571) Wang, Y.-H. A.; Zhang, X.; Bao, N.; Lin, B.; Gupta, A. Synthesis of Shape-Controlled Monodisperse Wurtzite CuIn$_x$Ga$_{1−x}$S$_2$ Semiconductor Nanocrystals with Tunable Band Gap. *J. Am. Chem. Soc.* **2011**, *133*, 11072−11075.

(572) Lu, X.; Zhuang, Z.; Peng, Q.; Li, Y. Controlled Synthesis of Wurtzite CuInS$_2$ Nanocrystals and Their Side-by-Side Nanorod Assemblies. *CrystEngComm* **2011**, *13*, 4039−4045.

(573) Yong, K. T.; Roy, I.; Hu, R.; Ding, H.; Cai, H. X.; Zhu, J.; Zhang, X. H.; Bergey, E. J.; Prasad, P. N. Synthesis of Ternary CuInS(2)/ZnS Quantum Dot Bioconjugates and Their Applications for Targeted Cancer Bioimaging. *Integr. Biol.* **2010**, *2*, 121−129.

(574) Gusain, M.; Kumar, P.; Nagarajan, R. Wurtzite CuInS$_2$: Solution Based One Pot Direct Synthesis and Its Doping Studies with Non-Magnetic Ga^{3+} and Magnetic Fe^{3+} Ions. *RSC Adv.* **2013**, *3*, 18863−18871.

(575) Batabyal, S. K.; Tian, L.; Venkatram, N.; Ji, W.; Vittal, J. J. Phase-Selective Synthesis of CuInS$_2$ Nanocrystals. *J. Phys. Chem. C* **2009**, *113*, 15037−15042.

(576) Connor, S. T.; Hsu, C. M.; Weil, B. D.; Aloni, S.; Cui, Y. Phase Transformation of Biphasic Cu$_2$S-CuInS$_2$ to Monophasic CuInS$_2$ Nanorods. *J. Am. Chem. Soc.* **2009**, *131*, 4962−4966.

(577) Cholula-Diaz, J. L.; Wagner, G.; Friedrich, D.; Oeckler, O.; Krautscheid, H. Synthesis of CuInS$_2$ Nanocrystals from a Molecular Complex - Characterization of the Orthorhombic Domain Structure. *Dalton Trans.* **2015**, *44*, 14227−14234.

(578) Yue, W.; Han, S.; Peng, R.; Shen, W.; Geng, H.; Wu, F.; Tao, S.; Wang, M. CuInS$_2$ Quantum Dots Synthesized by a Solvothermal Route and Their Application as Effective Electron Acceptors for Hybrid Solar Cells. *J. Mater. Chem.* **2010**, *20*, 7570−7578.

(579) Pons, T.; Pic, E.; Lequeux, N.; Cassette, E.; Bezdetnaya, L.; Guillemin, F.; Marchal, F.; Dubertret, B. Cadmium-Free CuInS(2)/ZnS Quantum Dots for Sentinel Lymph Node Imaging with Reduced Toxicity. *ACS Nano* **2010**, *4*, 2531−2538.

(580) Zhang, J.; Xie, R.; Yang, W. A Simple Route for Highly Luminescent Quaternary Cu-Zn-In-S Nanocrystal Emitters. *Chem. Mater.* **2011**, *23*, 3357−3361.

(581) Xie, R. G.; Rutherford, M.; Peng, X. G. Formation of High-Quality I-III-VI Semiconductor Nanocrystals by Tuning Relative Reactivity of Cationic Precursors. *J. Am. Chem. Soc.* **2009**, *131*, 5691−5697.

(582) Zhang, W.; Zhong, X. Facile Synthesis of ZnS−CuInS$_2$-Alloyed Nanocrystals for a Color-Tunable Fluorochrome and Photocatalyst. *Inorg. Chem.* **2011**, *50*, 4065−4072.

(583) Kruszynska, M.; Borchert, H.; Parisi, J.; Kolny-Olesiak, J. Investigations of Solvents and Various Sulfur Sources Influence on the Shape-Controlled Synthesis of CuInS$_2$ Nanocrystals. *J. Nanopart. Res.* **2011**, *13*, 5815−5824.

(584) Choi, S. H.; Kim, E. G.; Hyeon, T. One-Pot Synthesis of Copper-Indium Sulfide Nanocrystal Heterostructures with Acorn, Bottle, and Larva Shapes. *J. Am. Chem. Soc.* **2006**, *128*, 2520−2521.

(585) Nose, K.; Omata, T.; Otsuka-Yao-Matsuo, S. Colloidal Synthesis of Ternary Copper Indium Diselenide Quantum Dots and Their Optical Properties. *J. Phys. Chem. C* **2009**, *113*, 3455−3460.

(586) Zhong, H.; Wang, Z.; Bovero, E.; Lu, Z.; van Veggel, F. C. J. M.; Scholes, G. D. Colloidal CuInSe$_2$ Nanocrystals in the Quantum Confinement Regime: Synthesis, Optical Properties, and Electroluminescence. *J. Phys. Chem. C* **2011**, *115*, 12396−12402.

(587) Chen, H.; Yu, S.-M.; Shin, D.-W.; Yoo, J.-B. Solvothermal Synthesis and Characterization of Chalcopyrite CuInSe$_2$ Nanoparticles. *Nanoscale Res. Lett.* **2010**, *5*, 217−223.

(588) Wu, C.-C.; Shiau, C.-Y.; Ayele, D. W.; Su, W.-N.; Cheng, M.-Y.; Chiu, C.-Y.; Hwang, B.-J. Rapid Microwave-Enhanced Solvothermal Process for Synthesis of CuInSe$_2$ Particles and Its Morphologic Manipulation. *Chem. Mater.* **2010**, *22*, 4185−4190.

(589) Du, C.-F.; You, T.; Jiang, L.; Yang, S.-Q.; Zou, K.; Han, K.-L.; Deng, W.-Q. Controllable Synthesis of Ultrasmall CuInSe$_2$ Quantum Dots for Photovoltaic Application. *RSC Adv.* **2014**, *4*, 33855−33860.

(590) Wark, S. E.; Hsia, C.-H.; Luo, Z.; Son, D. H. Surfactant Effect on the Formation of CuInSe$_2$ Nanowires in Solution Phase Synthesis. *J. Mater. Chem.* **2011**, *21*, 11618−11625.

(591) Zhong, H.; Li, Y.; Ye, M.; Zhu, Z.; Zhou, Y.; Yang, C.; Li, Y. A Facile Route to Synthesize Chalcopyrite CuInSe$_2$ Nanocrystals in Non-Coordinating Solvent. *Nanotechnology* **2007**, *18*, 025602.

(592) Koo, B.; Patel, R. N.; Korgel, B. A. Synthesis of CuInSe$_2$ Nanocrystals with Trigonal Pyramidal Shape. *J. Am. Chem. Soc.* **2009**, *131*, 3134−3135.

(593) de Kergommeaux, A.; Fiore, A.; Bruyant, N.; Chandezon, F.; Reiss, P.; Pron, A.; de Bettignies, R.; Faure-Vincent, J. Synthesis of Colloidal CuInSe$_2$ Nanocrystals Films for Photovoltaic Applications. *Sol. Energy Mater. Sol. Cells* **2011**, *95*, S39−S43.

(594) Yarema, O.; Bozyigit, D.; Rousseau, I.; Nowack, L.; Yarema, M.; Heiss, W.; Wood, V. Highly Luminescent, Size- and Shape-Tunable Copper Indium Selenide Based Colloidal Nanocrystals. *Chem. Mater.* **2013**, *25*, 3753−3757.

(595) Li, B.; Xie, Y.; Huang, J.; Qian, Y. Synthesis by a Solvothermal Route and Characterization of CuInSe$_2$ Nanowhiskers and Nanoparticles. *Adv. Mater.* **1999**, *11*, 1456−1459.

(596) Min, Y.; Moon, G. D.; Park, J.; Park, M.; Jeong, U. Surfactant-Free CuInSe$_2$ Nanocrystals Transformed from In2Se$_3$ Nanoparticles and Their Application for a Flexible UV Photodetector. *Nanotechnology* **2011**, *22*, 465604.

(597) Wooten, A. J.; Werder, D. J.; Williams, D. J.; Casson, J. L.; Hollingsworth, J. A. Solution-Liquid-Solid Growth of Ternary Cu-In-Se Semiconductor Nanowires from Multiple- and Single-Source Precursors. *J. Am. Chem. Soc.* **2009**, *131*, 16177−16188.

(598) Tang, J.; Hinds, S.; Kelley, S. O.; Sargent, E. H. Synthesis of Colloidal CuGaSe$_2$, CuInSe$_2$, and Cu(InGa)Se$_2$ Nanoparticles. *Chem. Mater.* **2008**, *20*, 6906−6910.

(599) Norako, M. E.; Brutchey, R. L. Synthesis of Metastable Wurtzite CuInSe$_2$ Nanocrystals. *Chem. Mater.* **2010**, *22*, 1613−1615.

(600) Steinhagen, C.; Akhavan, V. A.; Goodfellow, B. W.; Panthani, M. G.; Harris, J. T.; Holmberg, V. C.; Korgel, B. A. Solution−Liquid−Solid Synthesis of CuInSe$_2$ Nanowires and Their Implementation in Photovoltaic Devices. *ACS Appl. Mater. Interfaces* **2011**, *3*, 1781−1785.

(601) Wang, J.-J.; Wang, Y.-Q.; Cao, F.-F.; Guo, Y.-G.; Wan, L.-J. Synthesis of Monodispersed Wurtzite Structure CuInSe$_2$ Nanocrystals and Their Application in High-Performance Organic-Inorganic Hybrid Photodetectors. *J. Am. Chem. Soc.* **2010**, *132*, 12218−12221.

(602) Cassette, E.; Pons, T.; Bouet, C.; Helle, M.; Bezdetnaya, L.; Marchal, F.; Dubertret, B. Synthesis and Characterization of near-Infrared Cu-In-Se/ZnS Core/Shell Quantum Dots for in Vivo Imaging. *Chem. Mater.* **2010**, *22*, 6117−6124.

(603) Zou, Y.; Li, D.; Yang, D. Colloidal Synthesis of Monodisperse Quaternary CuInSSe Nanocrystals. *Mater. Chem. Phys.* **2012**, *132*, 865−869.

(604) Xiao, J.; Xie, Y.; Xiong, Y.; Tang, R.; Qian, Y. A Mild Solvothermal Route to Chalcopyrite Quaternary Semiconductor CuIn(SeS) Nanocrystallites. *J. Mater. Chem.* **2001**, *11*, 1417−1420.

(605) Wang, Y.-H. A.; Bao, N.; Gupta, A. Shape-Controlled Synthesis of Semiconducting CuFeS₂ Nanocrystals. *Solid State Sci.* **2010**, *12*, 387−390.

(606) Kumar, P.; Uma, S.; Nagarajan, R. Precursor Driven One Pot Synthesis of Wurtzite and Chalcopyrite CuFeS₂. *Chem. Commun.* **2013**, *49*, 7316−7318.

(607) Wang, W.; Jiang, J.; Ding, T.; Wang, C.; Zuo, J.; Yang, Q. Alternative Synthesis of CuFeSe₂ Nanocrystals with Magnetic and Photoelectric Properties. *ACS Appl. Mater. Interfaces* **2015**, *7*, 2235−2241.

(608) Chang, S.-H.; Chiu, B.-C.; Gao, T.-L.; Jheng, S.-L.; Tuan, H.-Y. Selective Synthesis of Copper Gallium Sulfide (CuGaS₂) Nanostructures of Different Sizes, Crystal Phases, and Morphologies. *CrystEngComm* **2014**, *16*, 3323−3330.

(609) Wang, X.; Liu, X.; Yin, D.; Ke, Y.; Swihart, M. T. Size-, Shape-, and Composition-Controlled Synthesis and Localized Surface Plasmon Resonance of Copper Tin Selenide Nanocrystals. *Chem. Mater.* **2015**, *27*, 3378−3388.

(610) Park, Y.; Jin, H.; Park, J.; Kim, S. Simultaneous Phase and Size Control in the Synthesis of Cu₂SnS₃ and Cu₂ZnSnS₄ Nanocrystals. *CrystEngComm* **2014**, *16*, 8642−8645.

(611) Liang, Q.; Han, L.; Deng, X.; Yao, C.; Meng, J.; Liu, X.; Meng, J. Compositionally Tunable Cu₂Sn(SₓSe₁₋ₓ)(3) Nanocrystals: Facile Direct Solution-Phase Synthesis, Characterization, and Scalable Procedure. *CrystEngComm* **2014**, *16*, 4001−4007.

(612) Yan, C.; Gu, E.; Liu, F.; Lai, Y.; Li, J.; Liu, Y. Colloidal Synthesis and Characterizations of Wittichenite Copper Bismuth Sulphide Nanocrystals. *Nanoscale* **2013**, *5*, 1789−1792.

(613) Yang, C.; Zhou, B.; Miao, S.; Yang, C.; Cai, B.; Zhang, W.-H.; Xu, X. Cu₂Ge(S₃₋ₓSeₓ) Colloidal Nanocrystals: Synthesis, Characterization, and Composition-Dependent Band Gap Engineering. *J. Am. Chem. Soc.* **2013**, *135*, 5958−5961.

(614) Liu, Y.; Yang, J.; Gu, E.; Cao, T.; Su, Z.; Jiang, L.; Yan, C.; Hao, X.; Liu, F.; Liu, Y. Colloidal Synthesis and Characterisation of Cu₃SbSe₃ Nanocrystals. *J. Mater. Chem. A* **2014**, *2*, 6363−6367.

(615) van Embden, J.; Latham, K.; Duffy, N. W.; Tachibana, Y. Near-Infrared Absorbing Cu₁₂Sb₄S₁₃ and Cu₃SbS₄ Nanocrystals: Synthesis, Characterization, and Photoelectrochemistry. *J. Am. Chem. Soc.* **2013**, *135*, 11562−11571.

(616) Suehiro, S.; Horita, K.; Yuasa, M.; Tanaka, T.; Fujita, K.; Ishiwata, Y.; Shimanoe, K.; Kida, T. Synthesis of Copper-Antimony-Sulfide Nanocrystals for Solution processed Solar Cells. *Inorg. Chem.* **2015**, *54*, 7840−7845.

(617) Dilena, E.; Xie, Y.; Brescia, R.; Prato, M.; Maserati, L.; Krahne, R.; Paolella, A.; Bertoni, G.; Povia, M.; Moreels, I.; et al. CuInₓGa₁₋ₓS₂ Nanocrystals with Tunable Composition and Band Gap Synthesized Via a Phosphine-Free and Scalable Procedure. *Chem. Mater.* **2013**, *25*, 3180−3187.

(618) Ahmadi, M.; Pramana, S. S.; Xi, L.; Boothroyd, C.; Lam, Y. M.; Mhaisalkar, S. Evolution Pathway of CIGSe Nanocrystals for Solar Cell Applications. *J. Phys. Chem. C* **2012**, *116*, 8202−8209.

(619) Der Wu, J.; Ting Wang, L.; Gau, C. Synthesis of CuInGaSe₂ Nanoparticles by Modified Polyol Route. *Sol. Energy Mater. Sol. Cells* **2012**, *98*, 404−408.

(620) Li, J.; Jin, Z.; Liu, T.; Wang, J.; Wang, D.; Lai, J.; Du, H.; Cui, L. Ternary and Quaternary Chalcopyrite Cu(In₁₋ₓGaₓ)Se₂ Nanocrystals: Organoalkali-Assisted Diethylene Glycol Solution Synthesis and Band-Gap Tuning. *CrystEngComm* **2013**, *15*, 7327−7338.

(621) Chen, L.-J.; Liao, J.-D.; Chuang, Y.-J.; Fu, Y.-S. Synthesis and Characterization of Cu(InₓB₁₋ₓ)Se₂ Nanocrystals for Low-Cost Thin Film Photovoltaics. *J. Am. Chem. Soc.* **2011**, *133*, 3704−3707.

(622) Liu, Y.; Yao, D.; Yao, S.; Zhao, J.; Zhang, H.; Tian, W.; Yang, B. Phosphine-Free Synthesis of Heavy Co²⁺- and Fe²⁺-Doped Cu₂SnSe₃ Nanocrystals by Virtue of Alkylthiol-Assistant Se Powder Dissolution. *J. Mater. Chem. A* **2013**, *1*, 2748−2751.

(623) Hu, J.; Lu, Q.; Tang, K.; Qian, Y.; Hu, J.; Lu, Q.; Tang, K.; Qian, Y.; Zhou, G.; Liu, X. Solvothermal Reaction Route to Nanocrystalline Semiconductors AgMS₂ (M = Ga, In). *Chem. Commun.* **1999**, 1093−1094.

(624) Hamanaka, Y.; Ozawa, K.; Kuzuya, T. Enhancement of Donor-Acceptor Pair Emissions in Colloidal AgIn₂ Quantum Dots with High Concentrations of Defects. *J. Phys. Chem. C* **2014**, *118*, 14562−14568.

(625) Tang, X.; Yu, K.; Xu, Q.; Choo, E. S. G.; Goh, G. K. L.; Xue, J. Synthesis and Characterization of AgInS₂-ZnS Heterodimers with Tunable Photoluminescence. *J. Mater. Chem.* **2011**, *21*, 11239−11243.

(626) Liu, L.; Hu, R.; Roy, I.; Lin, G.; Ye, L.; Reynolds, J. L.; Liu, J.; Liu, J.; Schwartz, S. A.; Zhang, X.; et al. Synthesis of Luminescent near-Infrared AgInS₂ Nanocrystals as Optical Probes for in Vivo Applications. *Theranostics* **2013**, *3*, 109−115.

(627) Dai, M.; Ogawa, S.; Kameyama, T.; Okazaki, K.-i.; Kudo, A.; Kuwabata, S.; Tsuboi, Y.; Torimoto, T. Tunable Photoluminescence from the Visible to near-Infrared Wavelength Region of Non-Stoichiometric AgIn₂ Nanoparticles. *J. Mater. Chem.* **2012**, *22*, 12851−12858.

(628) Luo, Z.; Zhang, H.; Huang, J.; Zhong, X. One-Step Synthesis of Water-Soluble AgInS₂ and ZnS−AgInS₂ Composite Nanocrystals and Their Photocatalytic Activities. *J. Colloid Interface Sci.* **2012**, *377*, 27−33.

(629) Peng, S.; Zhang, S.; Mhaisalkar, S. G.; Ramakrishna, S. Synthesis of AgInS₂ Nanocrystal Ink and Its Photoelectrical Application. *Phys. Chem. Chem. Phys.* **2012**, *14*, 8523−8529.

(630) Ogawa, T.; Kuzuya, T.; Hamanaka, Y.; Sumiyama, K. Synthesis of Ag-In Binary Sulfide Nanoparticles-Structural Tuning and Their Photoluminescence Properties. *J. Mater. Chem.* **2010**, *20*, 2226−2231.

(631) Wang, D. S.; Zheng, W.; Hao, C. H.; Peng, Q.; Li, Y. D. General Synthesis of I-III-VI₂ Ternary Semiconductor Nanocrystals. *Chem. Commun.* **2008**, 2556−2558.

(632) Kadlag, K. P.; Patil, P.; Rao, M. J.; Datta, S.; Nag, A. Luminescence and Solar Cell from Ligand-Free Colloidal AgInS₂ Nanocrystals. *CrystEngComm* **2014**, *16*, 3605−3612.

(633) Deng, M.; Shen, S.; Wang, X.; Zhang, Y.; Xu, H.; Zhang, T.; Wang, Q. Controlled Synthesis of AgInS₂ Nanocrystals and Their Application in Organic-Inorganic Hybrid Photodetectors. *CrystEngComm* **2013**, *15*, 6443−6447.

(634) Feng, Z.; Dai, P.; Ma, X.; Zhan, J.; Lin, Z. Monodispersed Cation-Disordered Cubic AgInS₂ Nanocrystals with Enhanced Fluorescence. *Appl. Phys. Lett.* **2010**, *96*, 013104.

(635) Bai, T.; Li, C.; Li, F.; Zhao, L.; Wang, Z.; Huang, H.; Chen, C.; Han, Y.; Shi, Z.; Feng, S. A Simple Solution-Phase Approach to Synthesize High Quality Ternary AgInSe2 and Band Gap Tunable Quaternary AgIn(S₁₋ₓSeₓ)(2) Nanocrystals. *Nanoscale* **2014**, *6*, 6782−6789.

(636) Ng, M. T.; Boothroyd, C. B.; Vittal, J. J. One-Pot Synthesis of New-Phase AgInSe₂ Nanorods. *J. Am. Chem. Soc.* **2006**, *128*, 7118−7119.

(637) Fan, C.-M.; Regulacio, M. D.; Ye, C.; Lim, S. H.; Zheng, Y.; Xu, Q.-H.; Xu, A.-W.; Han, M.-Y. Colloidal Synthesis and Photocatalytic Properties of Orthorhombic AgGaS₂ Nanocrystals. *Chem. Commun.* **2014**, *50*, 7128−7131.

(638) Zhou, B.; Li, M.; Wu, Y.; Yang, C.; Zhang, W.-H.; Li, C. Monodisperse AgSbS₂ Nanocrystals: Size-Control Strategy, Large-Scale Synthesis, and Photoelectrochemistry. *Chem. - Eur. J.* **2015**, *21*, 11143−11151.

(639) Mao, X.; Lee, J. Facile Synthesis of Phase-Pure FeCr₂Se₄ and FeCr₂S₄ Nanocrystals Via a Wet Chemistry Method. *J. Mater. Chem. C* **2014**, *2*, 3744−3749.

(640) Peng, S.; Li, L.; Wu, Y.; Jia, L.; Tian, L.; Srinivasan, M.; Ramakrishna, S.; Yan, Q.; Mhaisalkar, S. G. Size- and Shape-Controlled Synthesis of ZnIn₂S₄ Nanocrystals with High Photo-catalytic Performance. *CrystEngComm* **2013**, *15*, 1922−1930.

(641) Ke, J.; Li, X.; Zhao, Q.; Shi, Y.; Chen, G. A Novel Approach to Synthesize Ultrasmall Cu Doped Zn-In-Se Nanocrystal Emitters in a Colloidal System. *Nanoscale* **2014**, *6*, 3403−3409.

(642) Chesman, A. S. R.; Duffy, N. W.; Peacock, S.; Waddington, L.; Webster, N. A. S.; Jasieniak, J. J. Non-Injection Synthesis of Cu₂ZnSnS₄ Nanocrystals Using a Binary Precursor and Ligand Approach. *RSC Adv.* **2013**, *3*, 1017−1020.

(643) Rath, T.; Haas, W.; Pein, A.; Saf, R.; Maier, E.; Kunert, B.; Hofer, F.; Resel, R.; Trimmel, G. Synthesis and Characterization of Copper Zinc Tin Chalcogenide Nanoparticles: Influence of Reactants on the Chemical Composition. *Sol. Energy Mater. Sol. Cells* **2012**, *101*, 87−94.

(644) Shi, L.; Pei, C.; Xu, Y.; Li, Q. Template-Directed Synthesis of Ordered Single-Crystalline Nanowires Arrays of Cu_2ZnSnS_4 and $Cu_2ZnSnSe_4$. *J. Am. Chem. Soc.* **2011**, *133*, 10328−10331.

(645) Zhou, Y.-L.; Zhou, W.-H.; Li, M.; Du, Y.-F.; Wu, S.-X. Hierarchical Cu_2ZnSnS_4 Particles for a Low-Cost Solar Cell: Morphology Control and Growth Mechanism. *J. Phys. Chem. C* **2011**, *115*, 19632−19639.

(646) Zhou, Y.-L.; Zhou, W.-H.; Du, Y.-F.; Li, M.; Wu, S.-X. Sphere-Like Kesterite Cu_2ZnSnS_4 Nanoparticles Synthesized by a Facile Solvothermal Method. *Mater. Lett.* **2011**, *65*, 1535−1537.

(647) Zaberca, O.; Gillorin, A.; Durand, B.; Chane-Ching, J. Y. A General Route to the Synthesis of Surfactant-Free, Solvent-Dispersible Ternary and Quaternary Chalcogenide Nanocrystals. *J. Mater. Chem.* **2011**, *21*, 6483−6486.

(648) Zaberca, O.; Oftinger, F.; Chane-Ching, J. Y.; Datas, L.; Lafond, A.; Puech, P.; Balocchi, A.; Lagarde, D.; Marie, X. Surfactant-Free CZTS Nanoparticles as Building Blocks for Low-Cost Solar Cell Absorbers. *Nanotechnology* **2012**, *23*, 185402.

(649) Cao, M.; Shen, Y. A Mild Solvothermal Route to Kesterite Quaternary Cu_2ZnSnS_4 Nanoparticles. *J. Cryst. Growth* **2011**, *318*, 1117−1120.

(650) Saha, S. K.; Guchhait, A.; Pal, A. J. Cu_2ZnSnS_4 (CZTS) Nanoparticle Based Nontoxic and Earth-Abundant Hybrid pn-Junction Solar Cells. *Phys. Chem. Chem. Phys.* **2012**, *14*, 8090−8096.

(651) Wei, M.; Du, Q.; Wang, D.; Liu, W.; Jiang, G.; Zhu, C. Synthesis of Spindle-Like Kesterite Cu_2ZnSnS_4 Nanoparticles Using Thiorea as Sulfur Source. *Mater. Lett.* **2012**, *79*, 177−179.

(652) Gao, Y.; Yang, H.; Zhang, Y.; Li, J.; Zhao, H.; Feng, J.; Sun, J.; Zheng, Z. Facile Non-Injection Synthesis of High Quality CZTS Nanocrystals. *RSC Adv.* **2014**, *4*, 17667−17670.

(653) Dong, H.; Schnabel, T.; Ahlswede, E.; Feldmann, C. Polyol-Mediated Synthesis of $Cu_2ZnSn(S,Se)(4)$ Kesterite Nanoparticles and Their Use in Thin-Film Solar Cells. *Solid State Sci.* **2014**, *29*, 52−57.

(654) Jin, C.; Ramasamy, P.; Kim, J. Facile Hot-Injection Synthesis of Stoichiometric $Cu_2ZnSnSe_4$ Nanocrystals Using Bis(Triethylsilyl) Selenide. *Dalton Trans.* **2014**, *43*, 9481−9485.

(655) Zhang, X.; Guo, G.; Ji, C.; Huang, K.; Zha, C.; Wang, Y.; Shen, L.; Gupta, A.; Bao, N. Efficient Thermolysis Route to Monodisperse Cu_2ZnSnS_4 Nanocrystals with Controlled Shape and Structure. *Sci. Rep.* **2014**, *4*.10.1038/srep05086

(656) Nishi, H.; Kuwabata, S.; Torimoto, T. Composition-Dependent Photoelectrochemical Properties of Nonstoichiometric Cu_2ZnSnS_4 Nanoparticles. *J. Phys. Chem. C* **2013**, *117*, 21055−21063.

(657) Nishi, H.; Nagano, T.; Kameyama, T.; Kuwabata, S.; Torimoto, T. Well-Controlled Synthesis of Wurtzite-Type Cu_2ZnSnS_4 Nanoparticles Using Multiple Sulfur Sources Via a Two-Step Heating Process. *CrystEngComm* **2015**, *17*, 174−182.

(658) Kameyama, T.; Osaki, T.; Okazaki, K.-i.; Shibayama, T.; Kudo, A.; Kuwabata, S.; Torimoto, T. Preparation and Photoelectrochemical Properties of Densely Immobilized Cu_2ZnSnS_4 Nanoparticle Films. *J. Mater. Chem.* **2010**, *20*, 5319−5324.

(659) Li, Z.; Lui, A. L. K.; Lam, K. H.; Xi, L.; Lam, Y. M. Phase-Selective Synthesis of Cu_2ZnSnS_4 Nanocrystals Using Different Sulfur Precursors. *Inorg. Chem.* **2014**, *53*, 10874−10880.

(660) Huang, T. J.; Yin, X.; Tang, C.; Qi, G.; Gong, H. A Low-Cost, Ligand Exchange-Free Strategy to Synthesize Large-Grained Cu_2ZnSnS_4 Thin-Films without a Fine-Grain Underlayer from Nanocrystals. *J. Mater. Chem. A* **2015**, *3*, 17788−17796.

(661) Zou, Y.; Su, X.; Jiang, J. Phase-Controlled Synthesis of Cu_2ZnSnS_4 Nanocrystals: The Role of Reactivity between Zn and S. *J. Am. Chem. Soc.* **2013**, *135*, 18377−18384.

(662) Yang, H.; Jauregui, L. A.; Zhang, G.; Chen, Y. P.; Wu, Y. Nontoxic and Abundant Copper Zinc Tin Sulfide Nanocrystals for Potential High-Temperature Thermoelectric Energy Harvesting. *Nano Lett.* **2012**, *12*, 540−545.

(663) Steinhagen, C.; Panthani, M. G.; Akhavan, V.; Goodfellow, B.; Koo, B.; Korgel, B. A. Synthesis of Cu_2ZnSnS_4 Nanocrystals for Use in Low-Cost Photovoltaics. *J. Am. Chem. Soc.* **2009**, *131*, 12554−12556.

(664) Riha, S. C.; Parkinson, B. A.; Prieto, A. L. Solution-Based Synthesis and Characterization of Cu_2ZnSnS_4 Nanocrystals. *J. Am. Chem. Soc.* **2009**, *131*, 12054−12055.

(665) An, P.; Liang, Z.; Xu, X.; Wang, X.; Jin, H.; Wang, N.; Wang, J.; Zhu, F. A Heating-up Method for the Synthesis of Pure Phase Kesterite Cu_2ZnSnS_4 Nanocrystals Using a Simple Coordinating Sulphur Precursor. *RSC Adv.* **2015**, *5*, 6879−6885.

(666) Kim, Y.; Woo, K.; Kim, I.; Cho, Y. S.; Jeong, S.; Moon, J. Highly Concentrated Synthesis of Copper-Zinc-Tin-Sulfide Nanocrystals with Easily Decomposable Capping Molecules for Printed Photovoltaic Applications. *Nanoscale* **2013**, *5*, 10183−10188.

(667) Zhou, B.; Xia, D.; Wang, Y. Phase-Selective Synthesis and Formation Mechanism of CZTS Nanocrystals. *RSC Adv.* **2015**, *5*, 70117−70126.

(668) Cattley, C. A.; Cheng, C.; Fairclough, S. M.; Droessler, L. M.; Young, N. P.; Warner, J. H.; Smith, J. M.; Assender, H. E.; Watt, A. A. R. Low Temperature Phase Selective Synthesis of Cu_2ZnSnS_4 Quantum Dots. *Chem. Commun.* **2013**, *49*, 3745−3747.

(669) Guo, Q.; Hillhouse, H. W.; Agrawal, R. Synthesis of Cu_2ZnSnS_4 Nanocrystal Ink and Its Use for Solar Cells. *J. Am. Chem. Soc.* **2009**, *131*, 11672−11673.

(670) Khare, A.; Wills, A. W.; Ammerman, L. M.; Norris, D. J.; Aydil, E. S. Size Control and Quantum Confinement in Cu_2ZnSnS_4 Nanocrystals. *Chem. Commun.* **2011**, *47*, 11721−11723.

(671) Chernomordik, B. D.; Beland, A. E.; Trejo, N. D.; Gunawan, A. A.; Deng, D. D.; Mkhoyan, K. A.; Aydil, E. S. Rapid Facile Synthesis of Cu_2ZnSnS_4 Nanocrystals. *J. Mater. Chem. A* **2014**, *2*, 10389−10395.

(672) Yang, X.; Xu, J.; Xi, L.; Yao, Y.; Yang, Q.; Chung, C. Y.; Lee, C.-S. Microwave-Assisted Synthesis of Cu_2ZnSnS_4 Nanocrystals as a Novel Anode Material for Lithium Ion Battery. *J. Nanopart. Res.* **2012**, *14*, 1−6.

(673) Regulacio, M. D.; Ye, C.; Lim, S. H.; Bosman, M.; Ye, E.; Chen, S.; Xu, Q.-H.; Han, M.-Y. Colloidal Nanocrystals of Wurtzite-Type Cu_2ZnSnS_4: Facile Noninjection Synthesis and Formation Mechanism. *Chem. - Eur. J.* **2012**, *18*, 3127−3131.

(674) Lu, X.; Zhuang, Z.; Peng, Q.; Li, Y. Wurtzite Cu_2ZnSnS_4 Nanocrystals: A Novel Quaternary Semiconductor. *Chem. Commun.* **2011**, *47*, 3141−3143.

(675) Engberg, S.; Li, Z.; Lek, J. Y.; Lam, Y. M.; Schou, J. Synthesis of Large CZTSe Nanoparticles through a Two-Step Hot-Injection Method. *RSC Adv.* **2015**, *5*, 96593−96600.

(676) Singh, A.; Geaney, H.; Laffir, F.; Ryan, K. M. Colloidal Synthesis of Wurtzite Cu_2ZnSnS_4 Nanorods and Their Perpendicular Assembly. *J. Am. Chem. Soc.* **2012**, *134*, 2910−2913.

(677) Liao, H.-C.; Jao, M.-H.; Shyue, J.-J.; Chen, Y.-F.; Su, W.-F. Facile Synthesis of Wurtzite Copper-Zinc-Tin Sulfide Nanocrystals from Plasmonic Djurleite Nuclei. *J. Mater. Chem. A* **2013**, *1*, 337−341.

(678) Jiang, H.; Dai, P.; Feng, Z.; Fan, W.; Zhan, J. Phase Selective Synthesis of Metastable Orthorhombic Cu_2ZnSnS_4. *J. Mater. Chem.* **2012**, *22*, 7502−7506.

(679) Li, Y.; Han, Q.; Kim, T. W.; Shi, W. Synthesis of Wurtzite-Zinc blende Cu_2AnSnS_4 and $Cu_2ZnSnSe_4$ Nanocrystals: Insight into the Structural Selection of Quaternary and Ternary Compounds Influenced by Binary Nuclei. *Nanoscale* **2014**, *6*, 3777−3785.

(680) Coughlan, C.; Ryan, K. M. Complete Study of the Composition and Shape Evolution in the Synthesis of Cu_2ZnSnS_4 (CZTS) Semiconductor Nanocrystals. *CrystEngComm* **2015**, *17*, 6914−6922.

(681) Ibáñez, M.; Zamani, R.; Li, W.; Shavel, A.; Arbiol, J.; Morante, J. R.; Cabot, A. Extending the Nanocrystal Synthesis Control to Quaternary Compositions. *Cryst. Growth Des.* **2012**, *12*, 1085−1090.

(682) Wei, H.; Guo, W.; Sun, Y.; Yang, Z.; Zhang, Y. Hot-Injection Synthesis and Characterization of Quaternary $Cu_2ZnSnSe_4$ Nanocrystals. *Mater. Lett.* **2010**, *64*, 1424−1426.

(683) Liu, Y.; Yao, D.; Shen, L.; Zhang, H.; Zhang, X.; Yang, B. Alkylthiol-Enabled Se Powder Dissolution in Oleylamine at Room Temperature for the Phosphine-Free Synthesis of Copper-Based Quaternary Selenide Nanocrystals. *J. Am. Chem. Soc.* **2012**, *134*, 7207−7210.

(684) Wei, K.; Nolas, G. S. Synthesis and Characterization of Nanostructured Stannite $Cu_2ZnSnSe_4$ and $Ag_2ZnSnSe_4$ for Thermoelectric Applications. *ACS Appl. Mater. Interfaces* **2015**, *7*, 9752−9757.

(685) Li, Z. Q.; Shi, J. H.; Liu, Q. Q.; Chen, Y. W.; Sun, Z.; Yang, Z.; Huang, S. M. Large-Scale Growth of $Cu_2ZnSnSe_4$ and $Cu_2ZnSnSe_4$/Cu_2ZnSnS_4 Core/Shell Nanowires. *Nanotechnology* **2011**, *22*, 265615.

(686) Chen, D.; Zhao, Y.; Chen, Y.; Wang, B.; Wang, Y.; Zhou, J.; Liang, Z. Hot-Injection Synthesis of Cu-Doped $Cu_2ZnSnSe_4$ Nanocrystals to Reach Thermoelectric ZT of 0.70 at 450 Degrees C. *ACS Appl. Mater. Interfaces* **2015**, *7*, 24403−24408.

(687) Dai, P.; Shen, X.; Lin, Z.; Feng, Z.; Xu, H.; Zhan, J. Band-Gap Tunable $(Cu_2Sn)_{x/3}Zn_{1-x}S$ Nanoparticles for Solar Cells. *Chem. Commun.* **2010**, *46*, 5749−5751.

(688) Dalui, A.; Khan, A. H.; Pradhan, B.; Pradhan, J.; Satpati, B.; Acharya, S. Facile Synthesis of Composition and Morphology Modulated Quaternary CuZnFeS Colloidal Nanocrystals for Photovoltaic Application. *RSC Adv.* **2015**, *5*, 97485−97494.

(689) Huang, C.; Chan, Y.; Liu, F.; Tang, D.; Yang, J.; Lai, Y.; Li, J.; Liu, Y. Synthesis and Characterization of Multicomponent $Cu_2(Fe_xZn_{1-x})SnS_4$ Nanocrystals with Tunable Band Gap and Structure. *J. Mater. Chem. A* **2013**, *1*, 5402−5407.

(690) Yan, C.; Huang, C.; Yang, J.; Liu, F.; Liu, J.; Lai, Y.; Li, J.; Liu, Y. Synthesis and Characterizations of Quaternary Cu_2FeSnS_4 Nanocrystals. *Chem. Commun.* **2012**, *48*, 2603−2605.

(691) Shi, L.; Yin, P. Phosphate-Free Synthesis, Optical Absorption and Photoelectric Properties of Cu_2ZnGeS_4 and $Cu_2ZnGeSe_4$ Uniform Nanocrystals. *Dalton Trans.* **2013**, *42*, 13607−13611.

(692) Chesman, A. S. R.; van Embden, J.; Della Gaspera, E.; Duffy, N. W.; Webster, N. A. S.; Jasieniak, J. J. Cu_2ZnGeS_4 Nanocrystals from Air-Stable Precursors for Sintered Thin Film Alloys. *Chem. Mater.* **2014**, *26*, 5482−5491.

(693) Ibáñez, M.; Zamani, R.; LaLonde, A.; Cadavid, D.; Li, W.; Shavel, A.; Arbiol, J.; Morante, J. R.; Gorsse, S.; Snyder, G. J.; Cabot, A. $Cu_2ZnGeSe_4$ Nanocrystals: Synthesis and Thermoelectric Properties. *J. Am. Chem. Soc.* **2012**, *134*, 4060−4063.

(694) Fan, C.-M.; Regulacio, M. D.; Ye, C.; Lim, S. H.; Lua, S. K.; Xu, Q.-H.; Dong, Z.; Xu, A.-W.; Han, M.-Y. Colloidal Nanocrystals of Orthorhombic Cu_2ZnGeS_4: Phase-Controlled Synthesis, Formation Mechanism and Photocatalytic Behavior. *Nanoscale* **2015**, *7*, 3247−3253.

(695) Peng, L.; Li, D.; Zhang, Z.; Huang, K.; Zhang, Y.; Shi, Z.; Xie, R.; Yang, W. Large-Scale Synthesis of Single-Source, Thermally Stable, and Dual-Emissive Mn-Doped Zn-Cu-In-S Nanocrystals for Bright White Light-Emitting Diodes. *Nano Res.* **2015**, *8*, 3316−3331.

(696) Liu, Z.; Tang, A.; Wang, M.; Yang, C.; Teng, F. Heating-up Synthesis of Cadimum-Free and Color-Tunable Quaternary and Five-Component Cu-In-Zn-S-Based Semiconductor Nanocrystals. *J. Mater. Chem. C* **2015**, *3*, 10114−10120.

(697) Xiang, W.-D.; Yang, H.-L.; Liang, X.-J.; Zhong, J.-S.; Wang, J.; Luo, L.; Xie, C.-P. Direct Synthesis of Highly Luminescent Cu-Zn-In-S Quaternary Nanocrystals with Tunable Photoluminescence Spectra and Decay Times. *J. Mater. Chem. C* **2013**, *1*, 2014−2020.

(698) Cui, Y.; Wang, G.; Pan, D. Colloidal Synthesis and Optical Properties of Metastable Wurtzite I_3-III-IV-VI_5 (Cu_3InSnS_5) Nanocrystals. *CrystEngComm* **2013**, *15*, 10459−10463.

(699) Ibáñez, M.; Cadavid, D.; Zamani, R.; García-Castelló, N.; Izquierdo-Roca, V.; Li, W.; Fairbrother, A.; Prades, J. D.; Shavel, A.; Arbiol, J.; et al. Composition Control and Thermoelectric Properties of Quaternary Chalcogenide Nanocrystals: The Case of Stannite $Cu_2CdSnSe_4$. *Chem. Mater.* **2012**, *24*, 562−570.

(700) Talapin, D. V.; Steckel, J. Quantum Dot Light-Emitting Devices. *MRS Bull.* **2013**, *38*, 685−691.

(701) Jang, E.; Jun, S.; Jang, H.; Lim, J.; Kim, B.; Kim, Y. White-Light-Emitting Diodes with Quantum Dot Color Converters for Display Backlights. *Adv. Mater.* **2010**, *22*, 3076−3080.

(702) Zhuang, Z.; Guo, X.; Liu, B.; Hu, F.; Li, Y.; Tao, T.; Dai, J.; Zhi, T.; Xie, Z.; Chen, P.; et al. High Color Rendering Index Hybrid III-Nitride/Nanocrystals White Light-Emitting Diodes. *Adv. Funct. Mater.* **2016**, *26*, 36−43.

(703) Boles, M. A.; Ling, D.; Hyeon, T.; Talapin, D. V. The Surface Science of Nanocrystals. *Nat. Mater.* **2016**, *15*, 141−153.

(704) Kagan, C. R.; Murray, C. B. Charge Transport in Strongly Coupled Quantum Dot Solids. *Nat. Nanotechnol.* **2015**, *10*, 1013−1026.

(705) Ling, D.; Park, W.; Park, S.-j.; Lu, Y.; Kim, K. S.; Hackett, M. J.; Kim, B. H.; Yim, H.; Jeon, Y. S.; Na, K.; Hyeon, T. Multifunctional Tumor pH-Sensitive Self-Assembled Nanoparticles for Bimodal Imaging and Treatment of Resistant Heterogeneous Tumors. *J. Am. Chem. Soc.* **2014**, *136*, 5647−5655.

(706) Ling, D.; Xia, H.; Park, W.; Hackett, M. J.; Song, C.; Na, K.; Hui, K. M.; Hyeon, T. pH-Sensitive Nanoformulated Triptolide as a Targeted Therapeutic Strategy for Hepatocellular Carcinoma. *ACS Nano* **2014**, *8*, 8027−8039.

(707) Ntziachristos, V. Fluorescence Molecular Imaging. *Annu. Rev. Biomed. Eng.* **2006**, *8*, 1−33.

(708) Stasiuk, G. J.; Tamang, S.; Imbert, D.; Poillot, C.; Giardiello, M.; Tisseyre, C.; Barbier, E. L.; Fries, P. H.; de Waard, M.; Reiss, P.; et al. Cell-Permeable Ln(III) Chelate-Functionalized InP Quantum Dots as Multimodal Imaging Agents. *ACS Nano* **2011**, *5*, 8193−8201.

(709) Stasiuk, G. J.; Tamang, S.; Imbert, D.; Gateau, C.; Reiss, P.; Fries, P.; Mazzanti, M. Optimizing the Relaxivity of Gd(III) Complexes Appended to InP/ZnS Quantum Dots by Linker Tuning. *Dalton Trans.* **2013**, *42*, 8197−8200.

(710) Nozik, A. J. Photoelectrochemistry: Applications to Solar Energy Conversion. *Annu. Rev. Phys. Chem.* **1978**, *29*, 189−222.

(711) Gimbert-Suriñach, C.; Albero, J.; Stoll, T.; Fortage, J.; Collomb, M.-N.; Deronzier, A.; Palomares, E.; Llobet, A. Efficient and Limiting Reactions in Aqueous Light-Induced Hydrogen Evolution Systems Using Molecular Catalysts and Quantum Dots. *J. Am. Chem. Soc.* **2014**, *136*, 7655−7661.

(712) Simon, T.; Bouchonville, N.; Berr, M. J.; Vaneski, A.; Adrović, A.; Volbers, D.; Wyrwich, R.; Döblinger, M.; Susha, A. S.; Rogach, A. L.; et al. Redox Shuttle Mechanism Enhances Photocatalytic H_2 Generation on Ni-Decorated CdS nanorods. *Nat. Mater.* **2014**, *13*, 1013−1018.

(713) Kalisman, P.; Nakibli, Y.; Amirav, L. Perfect Photon-to-Hydrogen Conversion Efficiency. *Nano Lett.* **2016**, *16*, 1776−1781.

(714) Tajani, A. Substance Identification of Nanomaterials Not Key to Ensuring Their Safe Use. *Nat. Nanotechnol.* **2013**, *8*, 306−307.

(715) Leach, A. D. P.; Macdonald, J. E. Optoelectronic Properties of $CuInS_2$ Nanocrystals and Their Origin. *J. Phys. Chem. Lett.* **2016**, *7*, 572−583.

(716) Mughal, S. A.; Payne, A. J.; Ray, B. Preparation and Phase Studies of the Ternary Semiconducting Compounds $ZnSnP_2$, $ZnGeP_2$, $ZnSiP_2$, $CdGeP_2$, and $CdSiP_2$. *J. Mater. Sci.* **1969**, *4*, 895−901.

(717) Scanlon, D. O.; Walsh, A. Bandgap Engineering of $ZnSnP_2$ for High-Efficiency Solar Cells. *Appl. Phys. Lett.* **2012**, *100*, 251911.

(718) Park, S. Y.; Lee, H. U.; Park, E. S.; Lee, S. C.; Lee, J.-W.; Jeong, S. W.; Kim, C. H.; Lee, Y.-C.; Huh, Y. S.; Lee, J. Photoluminescent Green Carbon Nanodots from Food-Waste-Derived Sources: Large-Scale Synthesis, Properties, and Biomedical Applications. *ACS Appl. Mater. Interfaces* **2014**, *6*, 3365−3370.

(719) Xia, Y.; Xiong, Y.; Lim, B.; Skrabalak, S. E. Shape-Controlled Synthesis of Metal Nanocrystals: Simple Chemistry Meets Complex Physics. *Angew. Chem., Int. Ed.* **2009**, *48*, 60−103.

(720) Hens, Z.; Čapek, R. K. Size Tuning at Full Yield in the Synthesis of Colloidal Semiconductor Nanocrystals, Reaction Simulations and Experimental Verification. *Coord. Chem. Rev.* **2014**, *263−264*, 217−228.

(721) Franke, D.; Harris, D. K.; Xie, L.; Jensen, K. F.; Bawendi, M. G. The Unexpected Influence of Precursor Conversion Rate for III−V Quantum Dots. *Angew. Chem.* **2015**, *127*, 14507−14511.

(722) Schmid, G. *Clusters and Colloids: From Theory to Applications*; VCH Verlagsgesellschaft mbH: Weinheim, Germany, 1994.

(723) Gary, D. C.; Flowers, S. E.; Kaminsky, W.; Petrone, A.; Li, X.; Cossairt, B. M. Single-Crystal and Electronic Structure of a 1.3 nm Indium Phosphide Nanocluster. *J. Am. Chem. Soc.* **2016**, *138*, 1510− 1513.